Università degli Studi di Torino
Facoltà di Scienze M.F.N.

Corso di Dottorato in Fisica Sperimentale
XVIII Ciclo

Settori scientifico-disciplinare FIS/04
FISICA NUCLEARE E SUBNUCLEARE

Beam and ageing tests of Resistive Plate Chambers for the ALICE Muon Spectrometer

Francesca Poggio

Relatore:
Dott. Alfredo Musso

Referee:
Prof. Salvatore Nuzzo

Coordinatore del corso:
Prof. Ezio Menichetti
Prof. Stefano Sciuto

Anni Accademici: 2002/2003 - 2003/2004 - 2004/2005

Al Monviso,
che sposerei se fosse un uomo,
e a Carletto,
che per fortuna non è una montagna.

"Un buon lettore è raro quanto un bravo scrittore" Jorge Luis Borges

Contents

List of Figures

List of Tables

Sommario

Questa tesi riporta i risultati ottenuti con test su fascio e con test di invecchiamento effettuati sui rivelatori per il Sistema di Trigger dello Spettrometro di coppie di muoni dell'esperimento ALICE, le Resistive Plate Chambers (RPC).

ALICE (A Large Ion Collider Experiment) è l'unico esperimento a LHC dedicato allo studio delle collisioni tra ioni pesanti. Investigherà la predetta transizione di fase a uno stato deconfinato, detto Plasma di Gluoni e Quark (QGP), la quale dovrebbe avvenire per densità di energia di 1-3 GeV/fm^3, corrispondenti a temperature critiche di 150-200 MeV.

La produzione delle risonanze pesanti J/ψ e Υ costituisce una delle osservabili sperimentali più promettenti dell'avvenuta formazione del QGP, in quanto è sensibile al mezzo attraversato, vale a dire a seconda che quest'ultimo si trovi in uno stato confinato o deconfinato. La produzione di queste risonanze pesanti sarà misurata attraverso il canale di decadimento in due muoni dallo Spettrometro di coppie di muoni dell'esperimento ALICE.

Il Sistema di Trigger dello Spettrometro ha il compito di selezionare muoni con momento trasverso superiore a una soglia fissata, in modo tale da discriminare le coppie di muoni provenienti dal decadimento delle risonanze pesanti dai muoni di fondo prodotti nei decadimenti di pioni e kaoni. I rivelatori utilizzati saranno le Resistive Plate Chambers (RPC) con elettrodi di bakelite a bassa resistività (1–8$\times$10^9 Ω·cm) per ottimizzare la tenuta al flusso di particelle incidenti; le camere saranno equipaggiate con un'elettronica di Front End con un discriminatore a doppia soglia (10/80 mV) sviluppato per migliorare la risoluzione temporale.

Il programma dell'esperimento ALICE prevede acquisizioni di dati con diversi sistemi di collisione per i primi dieci anni di operazioni: Pb–Pb e altri sistemi di ioni pesanti per 1 mese/anno (10^6 s di tempo effettivo di presa dati) e 8 mesi/anno di collisioni protone–protone (10^7 s di tempo effettivo di presa dati); ne conseguono diverse condizioni di lavoro e diversi vincoli riguardanti il funzionamento delle RPC.

Test precedenti, effettuati su prototipi di dimensioni ridotte, hanno di-

mostrato che i requisiti per il programma di collisioni tra ioni pasanti, sia in termini di comportamento (risoluzione paziale eccellente, 2.5 mm per strip con passo 1 cm, bassa *cluster size*, 1.5 per strip con passo 1 cm e risoluzione temporale di 1 ns) che in termini di tempo di vita del rivelatore (100 Mhits/cm^2, corrispondenti a 50 mC/cm^2, per le camere più irradiate e per dieci anni di acquisizione), sono totalmente soddisfatti utilizzando RPC che lavorino con una miscela di gas streamer (50.5% Ar, 41.3% $C_2H_2F_4$, 7.2% C_4H_{10}, 1% SF_6, umidità relativa RH=50%).

La situazione è differente per le collisioni protone–protone: i requisiti per la risoluzione spaziale sono meno stringenti, tuttavia i tassi di conteggio aspettati sono più alti a causa del fondo dovuto alle interazioni tra le particelle del fascio e particelle residue nei tubi di fascio. I tassi di conteggio, insieme alla durata dell'acquisizione dell'ordine di 10^7 s per anno, forniscono un requisito sulla durata di vita delle RPC di 100 Mhit/cm^2 per le camere più irradiate e per un anno di acquisizione. Il valore è un ordine di grandezza più grande di quello ottenuto per le collisioni tra ioni pesanti. In base agli aspetti specifici delle collisioni p–p, è stato investigato un nuovo regime di lavoro detto avalanche altamente saturato, o maxi–avalanche, con proprietà di invecchiamento migliori sebbene con una cluster size maggiore. Lo studio iniziale è stato volto a verificare che fosse possibile lavorare con la stessa elettronica di Front End prevista per il modo streamer (che non prevede uno stadio di amplificazione) semplicemente abbassando la soglia al minimo valore possibile (10 mV). Test preliminari con raggi cosmici mostrano che è possibile operare le RPC in regime maxi–avalanche ($\sim$90% $C_2H_2F_4$, 10% C_4H_{10} e diverse percentuali di SF_6, RH=50%) ottenendo un comportamento stabile.

Con la miscela streamer e quella maxi–avalanche sono stati effettuati test su fascio e test di invecchiamento. I test sono stati eseguiti su prototipi di piccole dimensioni (50×50 cm^2), così come su RPC di dimensioni finali, campionando tra le camere appartenenti alla pre–produzione e alla produzione finale. Attenzione speciale è stata rivolta alla verifica dell'uniformità del comportamento su tutta l'area attiva delle RPC e della loro stabilità durante lunghi periodi di irradiazione.

I risultati del test con la miscela streamer confermano quelli ottenuti con i prototipi di dimensioni ridotte. Per quanto concerne gli studi di invecchiamento, il test è stato effettuato su una camera della pre–produzione e, dopo protratto funzionamento (equivalente a 100 Mhit/cm^2), il rivelatore ha mostrato un lieve aumento della corrente fino a valori di 13 μA, mentre i conteggi di fondo sono rimasti minori di 0.4 Hz/cm^2. Una leggera perdita di efficienza è stata riscontrata ad alti rate (60 Hz/cm^2), mentre l'efficienza a

rate simili a quelli dei raggi cosmici rimane costante (97%) per l'intera dirata del test. Inoltre, un test su fascio in regime streamer è stato effettuato su tre camere della produzione finale: le RPC hanno un comportameto uniforme sull'intera area attiva (efficienza=98%) e questo comportamento è del tutto simile per tutte le camere sottoposte a test.

Il test su fascio con la miscela maxi–avalanche dimostra che è possibile utilizzare la stessa elettronica di Front End prevista per il regime streamer: il comportameto ottenuto rispetta i requisiti per le collisioni protone–protone. Il test di invecchiamento effettuato su prototipi di dimensioni ridotte è attualmente in corso. Al momento, sono stati integrati 550 Mhit/cm^2 senza osservare segni di invecchiamento, quali aumento della corrente o perdita di efficienza; l'efficienza è stabile al 95%.

Nella prima parte di questa tesi, sono riportati i modelli teorici che predicono a descrivono la fase di QGP e le osservabili per studiare ogni fase della collisione ione–ione e per ottenere una completa caratterizzazione degli eventi (Capitolo 1). L'esperimento ALICE e lo Spettrometro di coppie di muoni sono illustrati nei Capitoli 2 e 3.

Nel Capitolo 4 vengono descritti il principio di funzionamento e lo sviluppo storico delle RPC, mentre nel Capitolo 5 sono forniti i dettagli specifici riguardanti le RPC per l'esperimento ALICE. L'ultima parte di questa tesi (Capitoli 6 e 7) è dedicata ai risultati sperimentali dei test su fascio e dei test di invecchiamento.

Abstract

This thesis illustrates the results of beam and ageing tests performed on the detectors for the Trigger System of the ALICE Muon Spectrometer, the Resistive Plate Chambers (RPC).

ALICE (A Large Ion Collider Experiment) is the LHC experiment dedicated to the study of the heavy–ion collisions. It will investigate the predicted phase transition to the deconfined state called Quark Gluon Plasma (QGP) expected at an energy density of 1-3 GeV/fm^3, corresponding to a critical temperature of 150-200 MeV. The production of heavy quarkonium states is one of the most promising probes of the QGP formation since it is sensitive to the medium, so that for deconfined matter the production pattern will be different from the case of confined matter. J/ψ and Υ production will be measured via their dimuon decay channel by the ALICE Muon Forward Spectrometer.

The Trigger System of the Muon Spectrometer has to select events with muons having transverse momentum higher than a fixed threshold, in order to trigger on muon pairs coming from the quarkonia decays rejecting background muons from pion and kaon decays. The trigger detectors will be single gap Resistive Plate Chambers (RPC) with low–resistivity bakelite electrodes (1–8×10^9 Ω·cm) to cope with the required rate capability; they will equipped with Front End Electronics (FEE) with A DUaL Threshold discriminator (10/80 mV) especially developed to improve the time resolution.

Data taking for different colliding systems are foreseen in the ALICE program during the first ten years of operation: Pb–Pb and other heavy–ion systems for 1 month/year (10^6 s of effective data taking) and p–p collisions during about 8 month/year (10^7 s of effective data taking); this results in different working conditions and different constraints for the RPC operation.

Previous tests on small RPC prototypes have shown that the requirements for heavy–ion data taking, both in term of performance (excellent position resolution, 2.5 mm for 1 cm wide strips, low cluster size, 1.5 for 1 cm wide strips, and 1 ns time resolution) and of lifetime (100 Mhits/cm^2, i.e. 50 mC/cm^2 , for the most irradiated chambers over ten year), are ful-

filled by operating the RPCs in streamer mode (50.5% Ar, 41.3% $C_2H_2F_4$, 7.2% C_4H_{10}, 1% SF_6, Relative Humidity=50%).

The situation is different for the p–p program: the constraint on the position resolution is less stringent but the higher expected rate due to the background from the interactions between beam and residual gas, coupled with a data taking of the order of 10^7 s per year, leads to a requirement on the detector lifetime (for the most irradiated chambers) of 100 Mhit/cm^2 per year, that is one order of magnitude greater with respect to the heavy–ion data taking. According to the specific aspects of p–p data taking, a new running mode, called highly–saturated avalanche, with better ageing properties but with larger cluster size, has been investigated in order to verify the possibility to work with the same FEE foreseen for the streamer mode (which does not include an amplification stage) simply by lowering the threshold to the minimum possible value (10 mV). Preliminary tests with cosmic rays show that a stable behaviour in highly–saturated avalanche mode ($\sim$90% $C_2H_2F_4$, 10% C_4H_{10} and different percentages of SF_6, RH=50%) can be achieved.

With the streamer and with the maxi–avalanche gas mixture we have performed beam and ageing tests. The tests have been carried out with small RPC prototypes (50×50 cm^2) as well as with full-size RPCs sampling pre–production and final–production chambers. Special attention has been put to check the uniformity of the performances on the whole active surface of the RPCs and their stability during long irradiation periods.

The results of the tests with the streamer gas mixture confirm the performance obtained with the small RPC prototypes. Concerning the ageing, a pre–production RPC has been tested and, after protracted operation (equivalent to 100 Mhit/cm^2), the detector has shown a slight current increase up to 13 μA, while the dark rate remains lower than 0.4 Hz/cm^2. A slight efficiency loss has been found with high rate (60 Hz/cm^2), while the efficiency with cosmic–like rate is 97% for the whole test period. Furthermore, a beam test in streamer mode performed on three final–production RPCs shows that the chambers have a uniform behaviour over the whole active area (efficiency at 98%) and that this behaviour is quite the same for all the tested RPCs.

The beam test in maxi–avalanche mode demonstrates that it is possible to use the same FEE foreseen for the streamer mode: the obtained performance cope with the p–p collision requirements. The ageing test carried out on small prototypes is presently in progress. Up to now, 550 Mhits/cm^2 have been integrated without observing any ageing effects, such as dark current increase or efficiency loss; the efficiency is stable at 95%.

In the first part of this thesis are reported the theoretical models that predict and describe the QGP phase and the observables to study each phase of the ion-ion collisions and to achieve a global characterization of the events (Chapter 1). The ALICE experiment and the Muon Forward Spectrometer are illustrated in Chapter 2 and 3.

In Chapter 4 are described the working principle and the historical development of RPCs, while specific aspects concerning the ALICE RPCs are given in Chapter 5. The last part of this thesis (Chapter 6 and 7) is devoted to the experimental results of beam and ageing tests.

Chapter 1

QGP: theoretical predictions and experimental expectations

"So there must be an ultimate limit
to bodies, beyond perception by our
senses. This limit is without parts,
is the smallest possible thing.
It can never exist by itself, but only
as a primordial part of a larger body,
from which no force can tear it loose."
Titus Lucretius Carus, *De rerum natura*

1.1 Introduction

High-energy physics has established and validated over the last decades a detailed, though still incomplete, theory of elementary particles and their fundamental interactions, called the Standard Model. Applying and extending the Standard Model to complex and dynamically evolving systems of finite size is the aim of ultra-relativistic heavy-ion physics. The focus of heavy-ion physics is to study and understand how collective phenomena and macroscopic properties, involving many degrees of freedom, emerge from the microscopic laws of elementary-particle physics. Specifically, heavy-ion physics addresses these questions in the sector of strong interactions by studying nuclear matter under conditions of extreme density and temperature.

The most striking case of a collective bulk phenomenon predicted by the Standard Model is the occurrence of phase transitions in quantum fields at

characteristic energy densities. This affects crucially our current understanding of both the structure of the Standard Model at low energy and of the evolution of the early Universe. According to Big-Bang cosmology, the Universe evolved from an initial state of extreme energy density to its present state through rapid expansion and cooling, thereby traversing the series of phase transitions predicted by the Standard Model. Global features of our Universe like baryon asymmetry or the large scale structure (galaxy distribution) are believed to be linked to characteristic properties of these phase transitions.

Lattice calculations of Quantum ChromoDynamics (QCD), the theory of strong interactions, predict that at a critical temperature of $\sim$170 MeV, corresponding to an energy density of $\epsilon_c \sim$1 GeV/fm^3, nuclear matter undergoes a phase transition to a deconfined state of quarks and gluons, the Quark Gluon Plasma (QGP). In addition, chiral symmetry is approximately restored and quark masses are reduced from their large effective values in hadronic matter to their small bare ones.

Similarly to water, nuclear matter exists in different phases as a function of temperature and density. A schematic phase diagram of strongly interacting matter is shown in Fig. 1.1 where different phases can be distinguished:

- a 'liquid' phase, given by the atomic nuclei (ρ=0.17 nucleon/fm^3) at low temperature;
- the 'gaseous' phase, which correspond to the hadronic phase coming from nuclei excitation;
- the 'solid' phase, which is represented by a high compressed cold matter, as it may exist in the interior of neutron stars;
- the 'plasma' phase, at high temperature and/or density, identifiable with a quark-gluon deconfined matter;
- a colour 'superconductor' phase, expected at very high densities and low temperatures, beyond the confinement transition.

The ALICE experiment is one of the four experiment at the Large Hadron Collider (LHC) at CERN; the other three experiments (ATLAS, CMS and LHCb) will acquire data mainly during proton–proton collision, while ALICE is the only one specifically designed for heavy–ion collisions. The nucleon–nucleon centre-of-mass energy for collisions of the heaviest ions at the LHC ($\sqrt{s}$=5.5 TeV) will exceed that available at RHIC by a factor of about 30, opening up a new physics domain for an accurate study of the phase transition in the hot and dense hadronic matter environment.

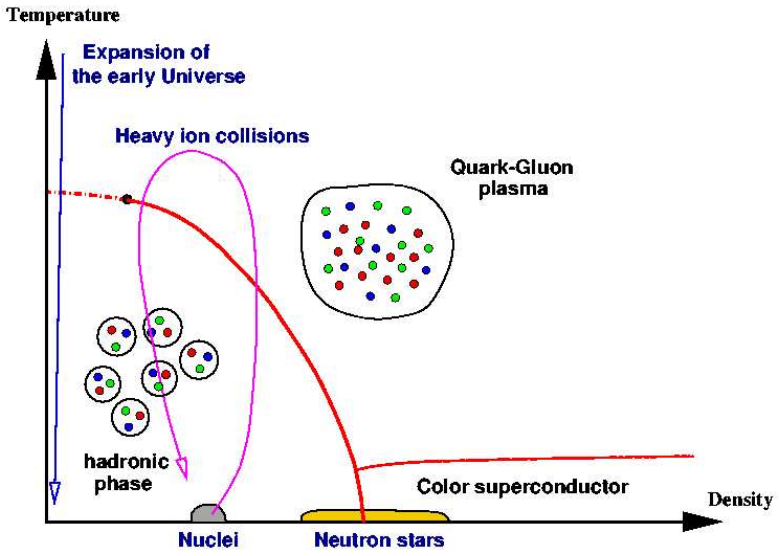

Fig. 1.1: Phase diagram of strongly interacting matter.

1.2 States of matter in QCD

The Quantum ChromoDynamics (QCD) affirm that nucleons, and more generally all strongly interacting particles (hadrons), are bound states of quark. The quark are point–like and confined in their hadron by the binding potential $V_0(r)$ which increases linearly with the quark separation r:

$$V_0(r) \sim \sigma r \tag{1.1}$$

where the string tension σ measures the energy per unit separation distance. Hence an infinite amount of energy would be needed to isolate a quark; it cannot exist by itself, and it is therefore not possible to split an isolated hadron into its quark constituent.

To get a first idea of what the quark infrastructure of elementary particles implies for the behaviour of matter at extreme density, a very simple picture, reported in Fig. 1.2, can be considered. If nucleons, with their intrinsic spatial extension, were at the same time elementary and incompressible, then a state of close packing would constitute the high–density limit of matter. On the other hand, composite nucleons made up of point-like quarks will start to overlap with increasing density, until eventually each quark finds within its immediate vicinity a considerable number of other quarks. It has no way to identify which of these had been its partners in a specific nucleon at some previous state of lower density. Beyond a certain point, the concept of a

hadron thus loses its meaning; at extreme density, we are quite naturally led to a medium whose basic constituents are unbound quarks [1].

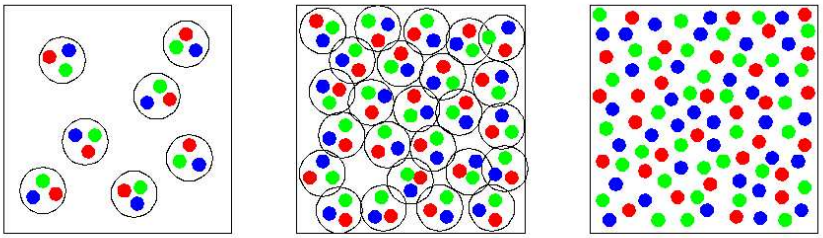

Fig. 1.2: Strongly interacting matter as nuclear matter at a density of closely packed nucleons (a) and as quark matter at much higher density (b).

On the theoretical side, studies of statistical QCD, in particular through computer simulations, have confirmed the transition from hadronic matter to a plasma of unbound quarks and gluons.

The interaction of quarks in QCD is based on their intrinsic colour charge, and in a dense medium this charge can be screened in much the same way as an electric charge. Hadrons are colour–neutral bound states of coloured quarks; hence dilute hadronic matter is a colour insulator. At sufficiently high density, however, we expect colour screening to set in, so that the potential becomes:

$$V(r) \simeq \sigma r[\frac{1 - exp(-\mu r)}{\mu r}] \tag{1.2}$$

where μ is the color screening mass, it is also the inverse of the screening radius for color charges and it decreases as the charge density of the medium increases. The resulting exponential damping of the binding force will remove all long-range effects and in a sufficiently dense medium hadrons will melt as shown in Fig. 1.2. Colour screening will thus transform a colour insulator into a colour conductor, turning hadronic matter into a quark plasma. The transition from insulator to conductor by charge screening is a collective effect, so that we expect a phase transition at the point of plasma formation.

When atomic matter is transformed from an insulator into a conductor, the effective mass of the conduction electrons is changed, similarly, the effective quark mass is expected to change between the confined and the deconfined phase. When confined in hadrons, the basic quarks 'dress' themselves with gluons to acquire an effective constituent quark mass of about

300 MeV (1/3 of the proton or 1/2 of the ρ meson mass). On the other hand, the basic bare quarks in the QCD Lagrangian are almost massless, so that the mass of the constituent quarks in the confined phase must be generated spontaneously through the confinement interaction. Hence it is likely that when deconfinement occurs, this additional mass is 'lost' and the quarks revert to their intrinsic 'bare' mass. This mass shift transition is often referred to as chiral symmetry restoration, since a Lagrangian with massless fermions possesses chiral symmetry.

At low temperature and high density, the quark triplets in nucleons, once deconfined, might choose to recombine into massive coloured quark pairs ('diquarks') [4], similar to Cooper pairs in QED. When the density is increased further, the diquarks would break up into the massless basic quarks. This results in a three–phase picture of strongly interacting matter, as reported in Fig. 1.1, with hadronic matter as confined phase, then deconfinement, followed by a phase consisting of massive coloured diquark systems, and finally, after chiral symmetry restoration, a plasma of coloured massless quarks and gluons. Such a three–phase structure would correspond to the succession of insulator, superconductor and conductor in atomic matter.

1.2.1 Critical behaviour in QCD

Lattice QCD calculations suggest the existence of a phase transition for temperatures higher than a critical value; however these results are limited to a vanishing baryochemical potential μ_b (quantity related to the barion–number density), namely they cover the region explored by the RHIC and LHC experiments.

The thermodynamics asserts that a phase transition is associated with a critical behaviour. Hadronic matter shows different forms of critical behaviour that can be described in term of symmetry breaking. Let us investigate the nature of the symmetries of the QCD Lagrangian $L(\mathrm{m}_q)$. In $L(\mathrm{m}_q)$ the bare quark mass m_q is an open parameter. Two cases assume particular importance:

1. $\mathrm{m}_q = \infty$

2. $\mathrm{m}_q = 0$.

The first variable to consider is the deconfinement measure given by the Polyakov loop [2, 3]:

$$L(T) \sim \lim_{r\to\infty} exp\{-V(r)/T\}, \tag{1.3}$$

where $V(r)$ is the potential between a static quark–antiquark pair separated by a distance r. In the limit of large input quark mass, QCD reduces to pure SU(3) gauge theory, invariant under a global Z_3 symmetry. In the same limit ($m_q = \infty$), $V(\infty) = \infty$ in the confined phase, so that L=0. Colour screening, on the other hand, makes $V(r)$ finite at large r, so that in the deconfined phase, L does not vanish. It thus becomes an 'order parameter', that is the parameter that provides a measure of the state of the system under this symmetry: it vanishes for Z_3 symmetric states and becomes finite when Z_3 is spontaneously broken.

The temperature dependence of the Polyakov loop is sketched in Fig. 1.3.

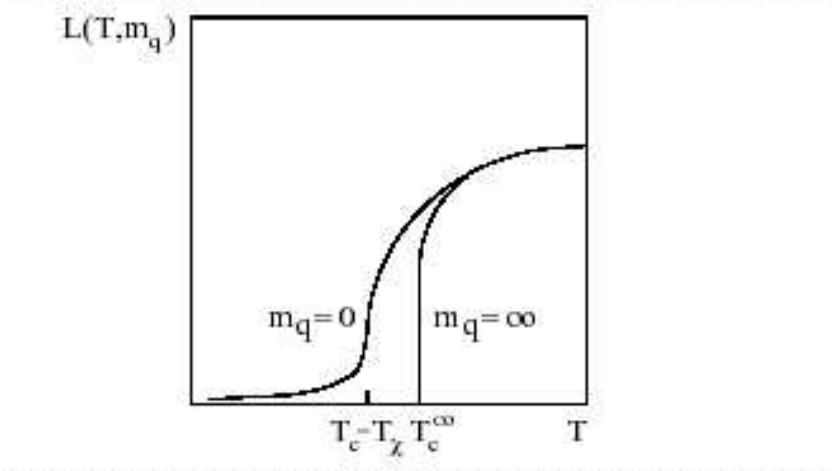

Fig. 1.3: Temperature dependence of the Polyakov loop for $m_q = \infty$ and two-flavour QCD with $m_q = 0$.

Fig. 1.4 shows recent lattice results for L(T) and the corresponding susceptibility $\chi_L(T) \sim < L^2 > - < L >^2$: L(T) undergoes the expected sudden increase from a small confinement to a much larger deconfinement value. The sharp peak of $\chi_L(T)$ defines quite well the transition temperature T_c.

The next quantity to consider is the effective quark mass; it is measured by the expectation value of the corresponding term in the Lagrangian, $\bar{\psi}\psi(T)$. In the limit of vanishing current quark mass, the Lagrangian becomes chirally symmetric and $\bar{\psi}\psi(T)$ the corresponding order parameter. In the confined phase, with effective constituent quark masses $M_q \sim 0.3$ GeV, this chiral symmetry is spontaneously broken, while in the deconfined phase, at high enough temperature, its restoration is expected.

The behaviour of $\bar{\psi}\psi(T)$ and the corresponding susceptibility $\chi_m(T) \sim \delta\bar{\psi}\psi(T)/\delta m_q$ are shown in Fig. 1.5, calculated for the same case as above in Fig. 1.4. We note here the expected sudden drop of the effective quark

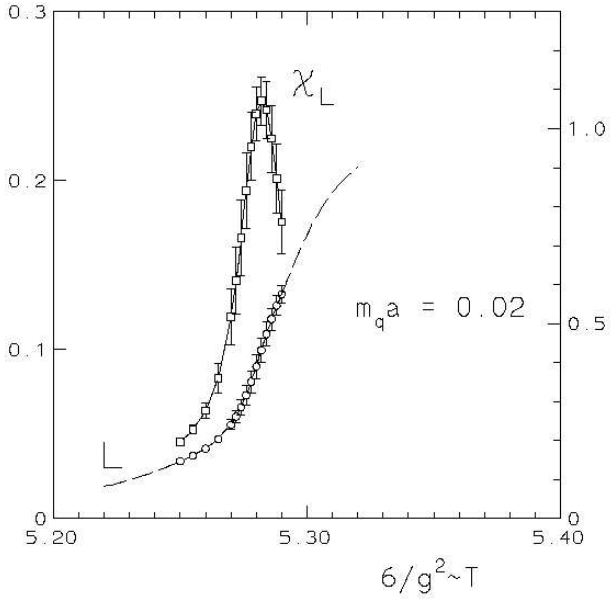

Fig. 1.4: Temperature dependence of the Polyakov loop and of the corresponding susceptibility in two-flavour QCD [4].

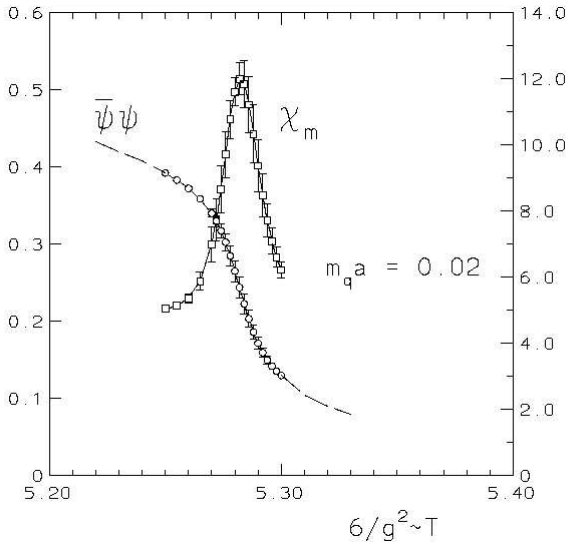

Fig. 1.5: Temperature dependence of the chiral condensate $\bar{\psi}\psi$ and of the corresponding susceptibility in two-flavour QCD [4].

mass and the associated sharp peak in the susceptibility. The temperature at which this occurs coincides with that obtained through the deconfinement measure. We therefore conclude that at vanishing baryon number density, quark deconfinement and shift from constituent to current quark mass coincide.

We thus obtain for μ_B=0 a rather well defined phase structure, consisting of a confined phase for T<T_c, with L(T)=0 and $\bar{\psi}\psi$(T)≠0, and a deconfined phase for T>T_c with L(T)≠0 and $\bar{\psi}\psi$(T)=0. The underlying symmetries associated to the critical behaviour at T=T_c, the Z_3 symmetry of deconfinement and the chiral symmetry of the quark mass shift, become exact in the limits $m_q = \infty$ and m_q=0, respectively. In the real world, both symmetries are only approximate.

Considering a thermodynamical approach, using the QCD Lagrangian it is possible to define the corresponding partition function Z(T,V) to calculate all thermodynamical observables:

$$\epsilon = (T^2/V)\left(\frac{\delta lnZ}{\delta T}\right)_V \tag{1.4}$$

for energy density, and

$$p = T\left(\frac{\delta lnZ}{\delta V}\right)_T \tag{1.5}$$

for pressure. Recent results of a calculation of p/T^4 and ϵ/T^4 as a function of temperature are shown in Fig. 1.6. The important feature is the rapid change in a narrow temperature range around $T \sim 170MeV$, that could be interpreted as a released latent heat associated to the colour deconfinement. The Stephan-Boltzmann values, indicated in the picture with arrows in the right-side ordinate, that represent the behaviour for an ideal gas, are not reached due to the effective 'thermal' masses m_{th} of quarks and gluons, with $m_{th} \sim gT$ [5]. The difference between $3p$ and ϵ in the region $T_c < T < 2T_c$ is presumably related with a difference between physical vacuum and QCD in-medium ground state [6]: while for a ideal gas of massless pions we expect $\epsilon - 3p = 0$, in the case of an ideal QGP we expect $\epsilon - 3p = 4B$, where B is the so-called bag pressure that takes into account the above cited difference [7].

Finally we turn to the value of the transition temperature. Since QCD (in the limit of massless quarks) does not contain any dimensional parameters, T_c can only be obtained in physical units by expressing it in terms of some other known observable which can also be calculated on the lattice, such as the ρ mass, the proton mass, or the string tension. In the continuum limit, all

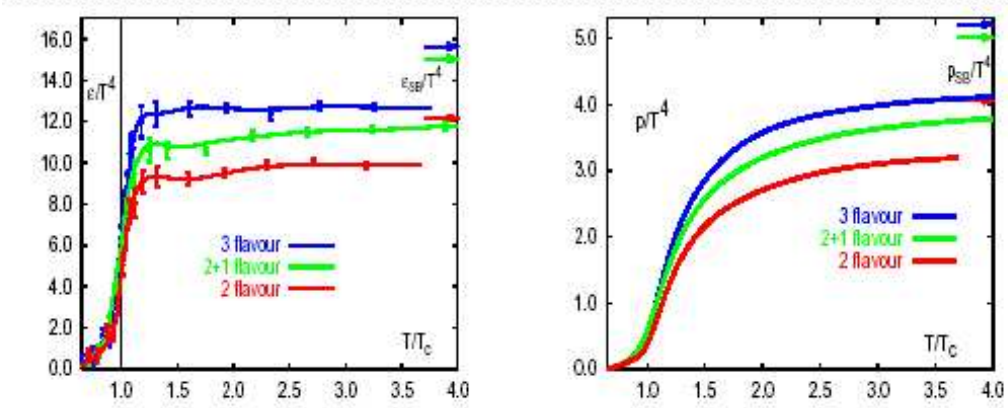

Fig. 1.6: Energy density (left) and pressure (right) temperature dependence in QCD with 3 and 2 degenerate quark flavour as well as with 2 light and a heavier quark. Arrows indicate the Stephan-Boltzmann limit for an ideal quark-gluon gas.

different ways should lead to the same result. Within the present accuracy, they define the uncertainty so far still inherent in the lattice evaluation of QCD. Using the ρ mass to fix the scale leads to T_c ~0.15 GeV, while the string tension still allows values as large as T_c ~0.20 GeV. This means that energy densities of some 1-2 GeV/fm^3 are needed to produce a medium of deconfined quarks and gluons.

In summary, finite temperature lattice QCD at μ_B=0 shows that:

- there is a deconfinement transition coincident with an associated shift in the effective quark mass at T_c ~0.15–0.20 GeV;
- the transition is accompanied by a sudden increase in the energy density ('latent heat of deconfinement') from a small hadronic value to a much larger value near that of an ideal QGP.

1.2.2 Deconfinement and chiral symmetry restoration

The relation between these two transition phenomena has been quite puzzling all along; the reason why they should, at least for μ_B=0, occur at the same temperature can be explained by a comparison between the temperature dependence of the Polyakov loop (see Fig. 1.3) and the magnetization in the Ising model (see Fig. 1.7).

It suggests that the quark mass constitutes an effective external field in QCD that can be expressed by a combination of bare quark mass, chiral mass

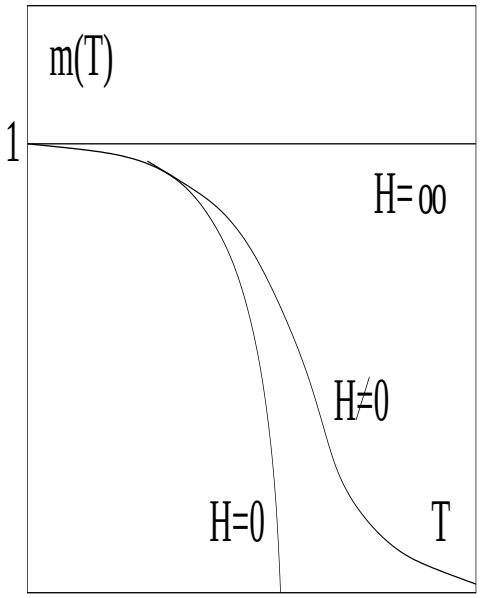

Fig. 1.7: Magnetization in the Ising model with and without external magnetic field.

and thermal mass:

$$H \sim \frac{1}{m_q + c_1 \langle \bar{\psi}\psi \rangle^{1/3} + c_2 g T}. \tag{1.6}$$

We can deduce:

- for $m_q \to \infty$, $H \to 0$, that is the pure gauge theory limit;
- for $m_q \to 0$, $\langle \bar{\psi}\psi \rangle$ is the crucial term, since the thermal mass at low temperature is very small

$$H = \left\{ \begin{array}{ll} \text{small} & \text{if } T \leq T_\chi \ (\langle \bar{\psi}\psi \rangle \text{ large}); \\ \text{large} & \text{if } T > T_\chi \ (\langle \bar{\psi}\psi \rangle \text{ small}). \end{array} \right\}$$

as reported in Fig. 1.8 with T_χ corresponding to the chiral restoration point.

We thus have essentially two limiting situations:

- for large m_q, H is always very small, so that deconfinement is determined by an approximate spontaneous symmetry breaking at $T = T_c$.
- for small m_q, H becomes large when $\langle \bar{\psi}\psi \rangle$ vanishes; H then aligns the Polyakov loops, resulting in deconfinement at $T=T_\chi$.

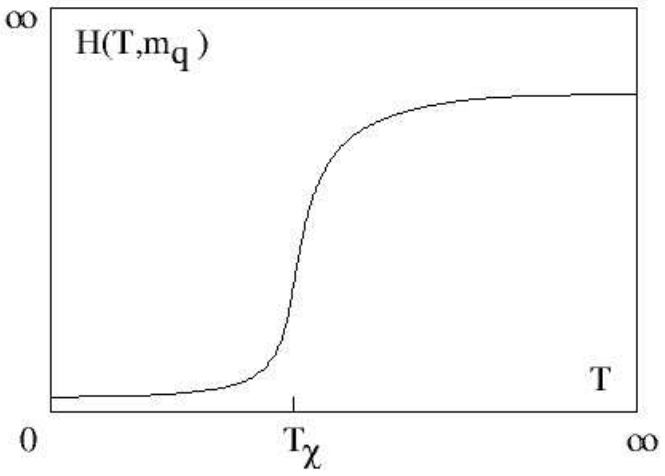

Fig. 1.8: The expected temperature dependence of the effective external field in full QCD.

Deconfinement is thus due to *spontaneous* Z_3 symmetry breaking only in the large m_q limit. For small m_q, that symmetry is broken *explicitly* by the effective external field H which becomes large when $\langle\bar{\psi}\psi\rangle \to 0$. Hence deconfinement and chiral symmetry restoration coincide.

These are the two limit cases for what we call "thermal" critical behaviour of nuclear matter, while the nature of the transition for $0<m_q<\infty$ is not manifest. The discontinuity of L(T) at T_c^∞ cannot disappear immediately for $m_q<\infty$, but it holds until a value m_q^0. So we have a "thermal" critical behaviour, connected with the confined–deconfined matter transition, for $m_q=0$ and for $m_q^0 \leq m_q \leq \infty$, while stays undefined the definition of deconfinement in the rest of the mass range, where the rapid variation in a narrow temperature interval (called rapid cross–over) is not accompanied by a spontaneous symmetry breaking, neither by a singular behaviour of thermodynamical observables. This is indicated in Fig. 1.9 in the T–m_q plane.

1.2.3 Deconfinement and percolation theory

Once the density of constituents becomes so high that several hadrons have considerable overlap, there is no mechanism to partition the quark constituents into color–neutral bound states. Instead, there appear clusters much larger than hadrons, within which colour is not confined. This suggests that deconfinement is related to cluster formation, and since that is the central topic of percolation theory, possible connection between percolation and deconfinement seems very likely.

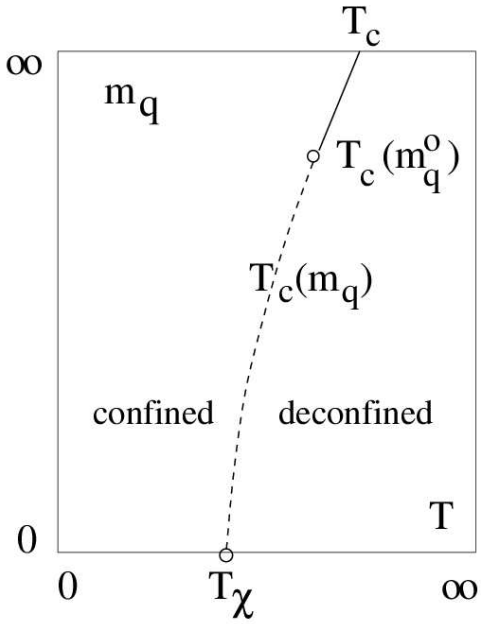

Fig. 1.9: The phase structure of nuclear matter.

In percolation theory, one considers a system of extended geometric objects, such as spheres, which can overlap; percolation is said to occur when, with increasing density, a connected cluster begins to span the entire system. If the interior of the spheres is coloured, such a cluster signals the onset of colour conductivity and hence of deconfinement.

For spin systems without external field, the thermal magnetization transition can be equivalently described as a percolation transition of suitably defined cluster [8]. For non–vanishing external field, magnetization never vanishes and there is no more thermal critical behaviour, however the percolation transition persists and the critical behaviour remains.

The resulting phase diagram in the T–H^{-1} plane is shown in Fig. 1.10: here the dashed line, the so–called Kertész line [9], is defined as the line of geometrical critical behaviour obtained from cluster percolation.

Comparing this result to the T–m_q diagram of QCD, it is possible to make the hypothesis that deconfinement for $0<m_q<\infty$ corresponds to Kertész line of QCD.

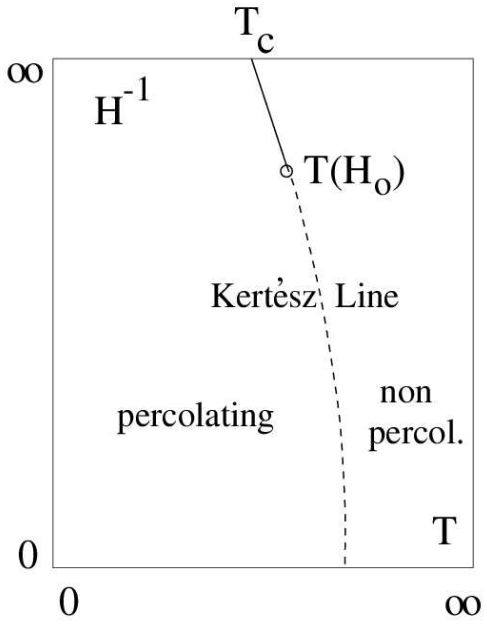

Fig. 1.10: The phase diagram in the T–H^{-1} plane.

1.3 The QGP in ultra relativistic heavy-ion collision: production and evolution

Ultra-relativistic heavy-ion collisions are the tool to obtain the extreme temperature and energy density conditions needed to have the production of a deconfined matter.

To attend to formation of QGP in laboratory, different conditions have to be fulfilled [10]:

- the dimensions of the system have to be large with respect to the range of the strong interaction, that is around 1 fm, and it has to be made of many particles, to allow a description with macroscopic variables;
- the lifetime of the system has to be larger than the typical relaxation times ($\tau >> 1$ fm/c) to reach the equilibrium, in order to use a thermodynamical approach. On the other hand, the equilibrium can be reached only in a sufficiently interacting system, so that the number of collisions per particle must be larger than one;
- as previous illustrated, the QCD predicts that the energy density needed for the QGP formation is of the order ϵ_c=1-3 GeV/fm^3, corresponding to a temperature T_c ~150-200 MeV and/or to a net baryon density

$\rho_c \sim 5 \div 10 \rho_0$, where ρ_0=0.17 nucleon/fm^3 is the density of the atomic nuclei.

After all, we deduce that in a heavy–ion collision a large amount of energy should be released in a small region of space and in a short time duration.

Characteristics of high energy heavy–ion collisions are determined by different parameters:

- **The impact parameter *b*.** As illustrated in Fig. 1.11, it provides the information about the centrality of the collision separating the nucleons into participants with primary nucleon–nucleon collisions, and spectators, which proceed quite unaffected along the original direction. The energy released in the collision increases with the number of participants, so that the most interesting collisions are the central interactions between heavy-ions.

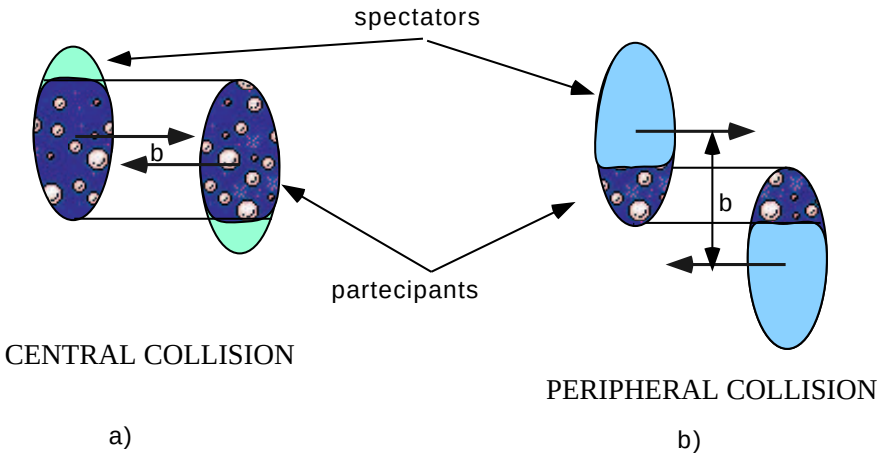

Fig. 1.11: Schematic view of a central (a) and peripheral (b) heavy-ion collision.

- **The rapidity distribution** of particles emitted in the collision[1]. It depends on the stopping level that is due to the energy of the colliding nuclei. If the energy is low, the two nuclei will remain intact, simply 'bouncing off' each other. With increasing energy, they will penetrate each other with the production of a highly excited nuclear matter, at

[1]The rapidity of a particle with velocity v_l in the z-direction is defined by the following expression:

$$y = \frac{1}{2} \times ln \left(\frac{1+\beta_l}{1-\beta_l} \right) \text{ with } \beta_l = \frac{v_l}{c}$$

high baryon density, which rapidly breaks up into nuclear fragments and some mesons. When the energy is higher, as is the case at LHC, the nuclei become 'transparent' due to relativistic effects: they pass through each other leaving a 'vapour trail', at zero baryon density, which eventually decays into hadrons [1]. For the last situation, in the centre-of-mass system, we can expect a rapidity distribution as the one indicated in Fig. 1.12: at the beginning, target and projectile take up the rapidity regions $y = \pm y_0$, where y_0 depends on the incident energy, after the collision the incident nuclei fragments remain at $\pm y_0$ and the excited fireball is in the central rapidity region, namely at $y = 0$.

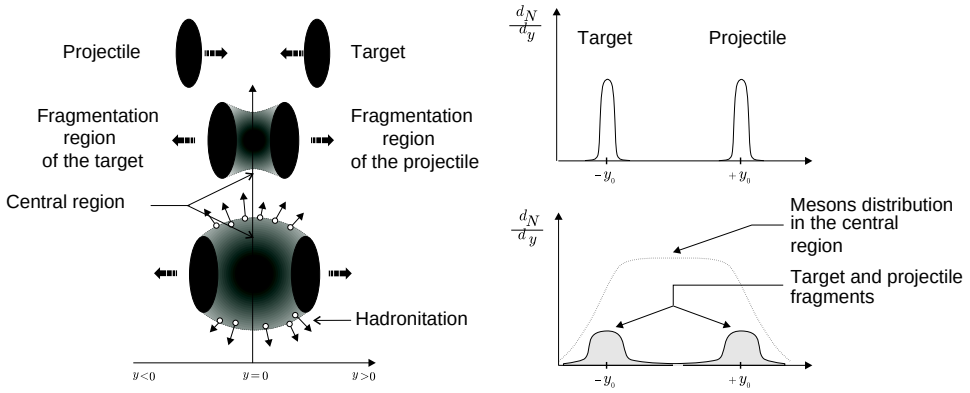

Fig. 1.12: Representation of a central nucleus-nucleus collision as a function of the rapidity.

As it appears in Fig. 1.11 and 1.12, the colliding nuclei are Lorentz-contracted, so that all the primary nucleon-nucleon collisions take place in a small region of space (the size of the contracted nuclei) and in a short time interval ($\sim$ 1 fm/c). This means that, if the energy density reaches the critical value ϵ_c, all the conditions listed at the beginning of the paragraph needed for the QGP formation are satisfied. On the basis of this assumption, we can study the space–time evolution of the fireball, illustrated in Fig. 1.13 following a model due to J. D. Bjorken [11]. The main steps of the process that leads from the initial collision to hadronization and freeze–out are:

- Pre-equilibrium ($\tau \leq$1 fm/c). The initial partons scatter among each other giving rise to an abundant production of quarks and gluons.
- Quark gluon plasma ($\tau \sim$10 fm/c). The quark gluon gas evolves into thermal equilibrium: the QGP is formed and starts expanding.

- Mixed phase. The QGP, while expanding, starts converting into a hadron gas.

- Hadronization ($\tau \sim$20 fm/c). As far as the system expands, its temperature decreases till quarks and gluons are again confined in hadrons.

- Freeze-out. Hadrons decouple from the gas, thus becoming free.

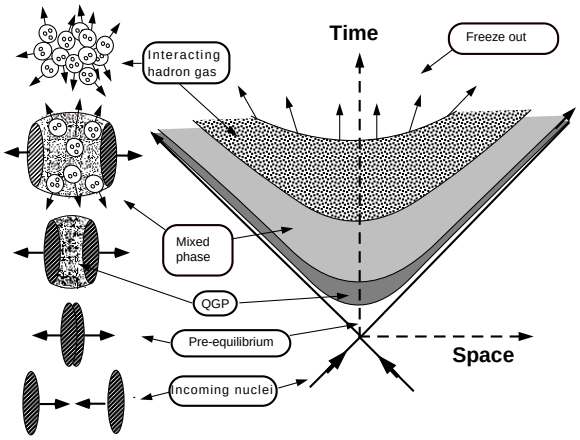

Fig. 1.13: Space-time evolution of a heavy-ion collision according to the Bjorken model.

The very short lasting time of QGP (only few 10^{-23} s), together with the interdiction to detect free quarks, do not allow to directly measure the transition. Nevertheless, impossibility are indirectly provided by a series of "probes", specifically thought to test different aspects of the medium. In the following, a short overview of such signals will be presented.

1.4 Experimental signatures of QGP

The phase transitions are critical behaviours, and the general way to probe such behaviours consists in finding the transition point and determine how the system and its observables change from one side to the other. In the case of complex phenomena, such as the QGP formation, different observables can be used in order to investigate different aspects of the same system, in many phases of its evolution.

1.4.1 Initial conditions

The centrality of the collision can be deduced from the measurement of several observables: the particle multiplicity, the transverse energy carried out by produced particles, the zero degree energy carried forward by spectator nucleons. The correlation between these observables and the value of the impact parameter is made via event generators or via theoretical models, as the Glauber theory.

The particle multiplicity allows also the calculation of the initial energy density of the produced medium. The simplest model [11] assumes that the finally observed hadrons have emerged from an initial interaction volume in free flow, i.e., without any collective motion. The resulting initial energy density is:

$$\epsilon = \left(\frac{dN_h}{dy}\right)_{y=0} \frac{w_h}{\pi R_A^2 \tau_0}, \tag{1.7}$$

where $(dN_h/dy)_{y=0}$ is the number of secondary hadrons emitted per unit rapidity at mid-rapidity, w_h is their average energy, πR_A^2 is the transverse overlapping area of the two nuclei and τ_0 is the time that represents the longitudinal size of the initial volume. In Fig. 1.14 ϵ as function of centrality measured by NA50 experiment in Pb-Pb collisions at $\sqrt{s} = 17$ GeV is shown.

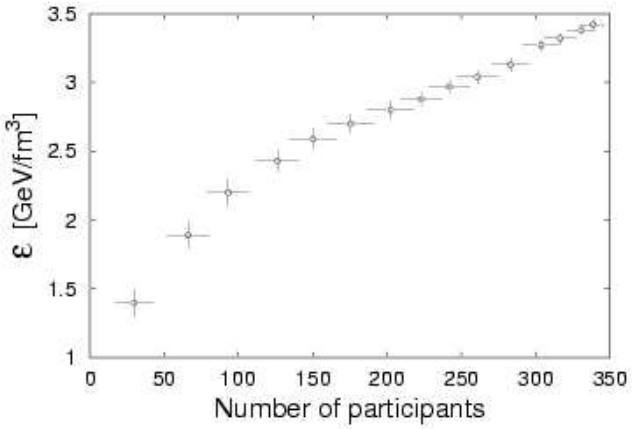

Fig. 1.14: Centrality dependence of the energy density in Pb-Pb collisions at $\sqrt{s}$=17 GeV [12].

Before looking at the attainable energy densities, let us note where nucleus-nucleus collision experiments reaching the range of interest can actually be performed. The only laboratories providing sufficiently energetic nuclear

beams are the Brookhaven National Laboratory (BNL) near New York (USA) and the European Organization for Nuclear Research (CERN) in Geneva (Switzerland). Both began experimentation in 1986, using existing accelerators. BNL had the alternating gradient synchrotron (AGS), designed for 30 GeV/c proton beams, CERN the super proton synchrotron (SPS) for 450 GeV/c protons. The injectors available at that time allowed only the acceleration of nuclei containing equal numbers of protons and neutrons (A = 2Z), so that the beams were restricted to light ions (A<40). Both laboratories have in the meantime built new injectors, allowing the acceleration of arbitrarily heavy nuclei in AGS and SPS.

From then, energy and luminosity of the ion beams have grown: at BNL, the relativistic heavy ion collider (RHIC) operates since 2000; at CERN, the large hadron collider (LHC) is planned for 2007 and it will allow to study Pb-Pb collisions at $\sqrt{s} \sim 5.5$ TeV per nucleon pair.

A new facility, SIS200, for the investigation of the behaviour of nuclear matter at low temperature and high density has been proposed at the Gesellschaft fùr Schwerionenforschung laboratory (GSI); it will accelerate heavy-ion beams with energies up to 30 GeV/nucleon.

Machine	Start	Type	Beam	$\sqrt{s}$ [GeV/A]
BNL-AGS	1986	Fixed Target	^{28}Si	5
CERN-SPS	1986	Fixed Target	^{16}O,^{32}S	19
BNL-AGS	1992	Fixed Target	^{197}Au	5
CERN-SPS	1994	Fixed Target	^{208}Pb	17
BNL-RHIC	2000	Collider	^{197}Au	200
CERN-LHC	$\sim$ 2007	Collider	^{208}Pb	5000
GSI-SIS200	$\sim$ 2008	Fixed Target	^{92+}U	$\sim$ 7.5

Tab. 1.1: Experimental facilities for high energy nuclear collisions with the indication of the beams and of the centre-of-mass energy values.

The available and planned facilities are summarized in Table 1.1 with corresponding energy density values.

Charged particle multiplicity

The average charged-particle multiplicity per rapidity unit is the most fundamental 'day–one' observable as, from the experimental side, it fixes the main unknown in the detector performance; the charged-particle multi-

plicity per unit rapidity largely determines the accuracy with which many observables can be measured.

The charged particle multiplicity, N_{ch}, is one of the global observables, it tells us which fraction of the collision energy is inelastically transferred to the secondary particles. Moreover, as shown above, the rapidity density, dN_{ch}/dy is used in the calculation of the energy density, then it is fundamental to know the other observables. On the theoretical side, it is connected to the properties of the medium produced in the collision and allows to distinguish the mechanisms of particle production.

For this, it is useful to study the charged particle multiplicity per participant pair, $(dN_{ch}/d\eta)/\frac{1}{2}N_{part}$. In Fig. 1.15, are reported the experimental values updated to the new results from RHIC. We can see that the A–A collisions produce more particles, normalized to the participant pairs, than the p–p collisions at the same energy, so that they cannot be described as independent nucleon-nucleon collisions. However, the multiplicity measured at RHIC appears much smaller than theoretical predictions.

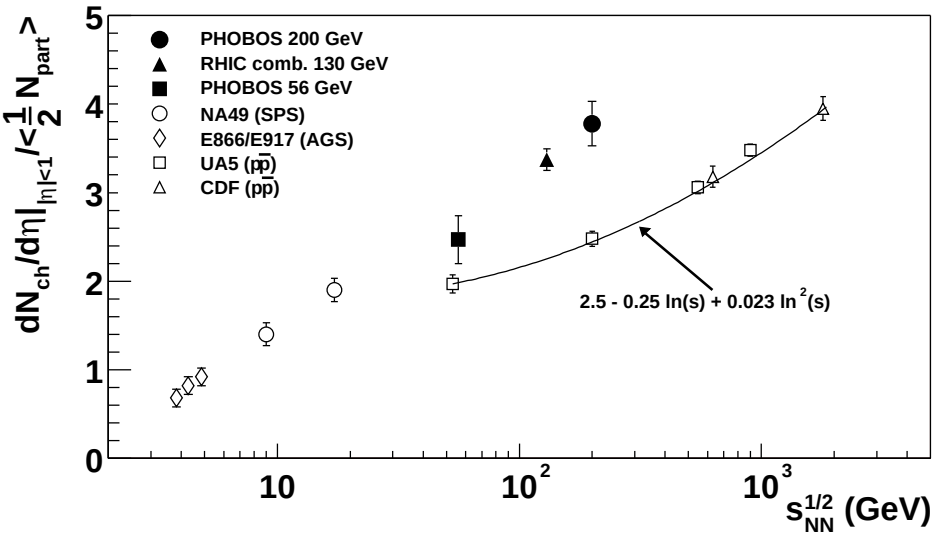

Fig. 1.15: Energy dependence of the charged particle rapidity density per participant pair in p–p, $p-\overline{p}$ and A–A. RHIC data refers to mid-rapidity Au-Au collisions at $\sqrt{s}$=20, 130 and 200 GeV [13].

Theoretical models of particle productions, which investigate the variation of $dN_{ch}/d\eta$ with N_{part} at a fixed collision energy, can be classified in two classes.

The first class is the one of the eikonal models of hadron production. In these models, one assumes that the multiplicity measured in p–p collisions at some energy $\sqrt{s}$ is composed of a fraction $X(s)$ coming from 'hard' processes, and a remaining $1 - X(s)$ coming from 'soft' processes. In nuclear collisions, the multiplicity will also have two components: the 'soft' component which scales with the number of binary collisions, and the 'hard' component proportional to the number of participants. As a result, for A–A collisions we have:

$$\frac{dN_{ch}^{AA}}{d\eta} = [(1 - X(S))\langle N_{part}\rangle + X(s)\langle N_{coll}\rangle] \frac{dN_{ch}^{NN}}{d\eta}. \qquad (1.8)$$

The HIJING model [14] follows this approach including also additional physics effects (jet quenching and nuclear shadowing) and predicts a linear rise of $dN_{ch}/d\eta/\frac{1}{2}N_{part}$ as a function of N_{part}.

The other class of calculations is based on the parton saturation model. An example is given by the EKRT model [15] that introduces a geometry–dependent saturation scale in the parton density due to the large production in a small volume, especially at high energy. This formulation leads to a slow decrease of $(dN_{ch}/d\eta)/\frac{1}{2}N_{part}$ as a function of N_{part}.

As shown in Fig. 1.16, neither models do reproduce properly the experimental values measured by PHENIX at $\sqrt{s} = 130\ GeV$.

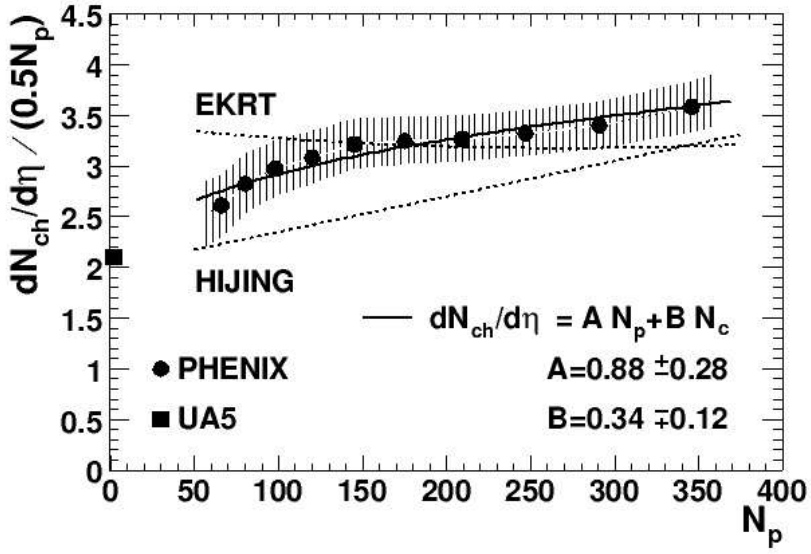

Fig. 1.16: PHENIX results for the centrality dependence of the charged particle rapidity density per participant pair in collisions at $\sqrt{s}$=130 GeV [16].

Kharzeev and Nardi [17] proposed a calculation for the centrality depen-

dence of particle multiplicity both in eikonal approach and in the framework of the parton saturation. In the first case, they do not take into account the physics effects of the HIJING model; in the second one, they consider a saturation of partons in the initial wave function of nuclei and not of the produced partons, as in the EKRT model. In both cases, the important assumption is that the role of hard processes in particle production increases at collider energies, leading to a regime of high parton densities.

The two Kharzeev and Nardi formulations give an almost identical behaviour, with multiplicity per participant increasing as a function of centrality. They agree very well with the most recent results from RHIC, shown in Fig. 1.17, where the rise of the slope of the data at higher centre-of-mass energies can be observed, confirming the predicted increase of the hard processes with $\sqrt{s}$.

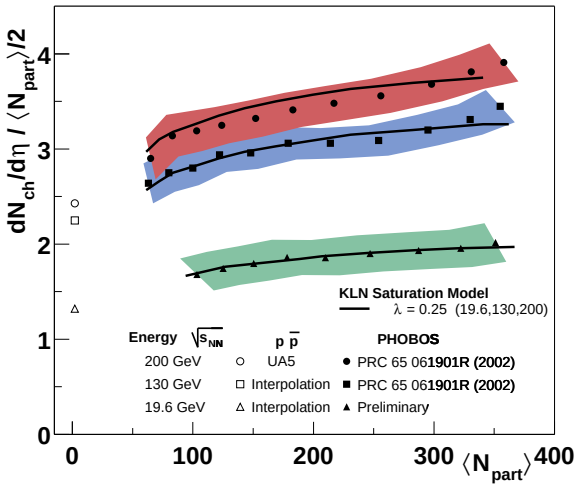

Fig. 1.17: Centrality dependence of the charged particle rapidity density per participant pair at mid-rapidity Au-Au collisions at $\sqrt{s}$=20, 130 and 200 GeV [13].

1.4.2 The QGP phase

The basis for a QGP is the high parton density in the early stages after the collision; this effectively screens all confining long–range forces, so that only short–range interactions remain. Any deconfinement probe must therefore:

- be hard enough to resolve sub–hadronic scales;
- be able to distinguish confinement and deconfinement;

- be present in the early stage of the evolution;
- retain the information throughout the subsequent evolution.

The last point requires that probes should not be in thermal equilibrium with later evolution stages, since this would lead to a loss of memory of the previous stages.

So far, two types of probes satisfying these conditions fully or in part have been considered.

- **External** probes are produced essentially by primary collisions, before the existence of any medium. Their observed behaviour can indicate whether the subsequent medium was deconfined or not. The most important observables are the production of quarkonium states and the energy loss or attenuation of hard jets.
- **Internal** probes are produced by the QGP itself. Since they must leave the medium without being affected by its subsequent states, they should undergo only weak or electromagnetic interactions after their formation. Thus the main candidates are thermal dileptons and photons.

Quarkonium suppression

In the QGP, quarkonium suppression is expected to occur owing to the shielding of the $c\bar{c}$ binding potential by colour screening, leading to the breakup of the quarkonium states, first the ψ' and χ_c, and finally the J/ψ itself. For the much higher energies of nuclear collisions at the LHC, the Υ family will also be copiously produced and any possible Υ suppression pattern can be studied in detail. This signature will be treated in detail in Section 1.5.

Jet quenching

The role of jets as a deconfinement probe was first proposed in 1982 by Bjorken. He stressed that a "high-p_t quark or gluon might lose tens of GeV of its initial transverse momentum while plowing through quark-gluon plasma produced in its local environment".

The partonic energy loss grows quadratically with the in–medium path length and is proportional to the gluon density, hence the observation of jet quenching in heavy ion collisions can be accounted as a proof of deconfinement.

It is clear that, in order to notice a "quenching", comparisons with jets in ordinary matter have to be performed. An important benchmark for fragmentation function of jets will be provided by analysis of p–p collisions.

Thermal dileptons and photons

Owing to their small coupling, photons, once produced, do not interact with the surrounding matter and can thus provide information on the state of matter at the time of their formation.

The production of photons in the different stages of heavy–ion collision can be summarized qualitatively as follows:

1. Early in the collisions, so-called "prompt" photons are produced by parton–parton scattering in the primary nucleus–nucleus collisions. An important background to such photons is the decay $\pi^0 \to \gamma\gamma$.

2. In the following stage of the collision, a QGP is expected to be formed with a temperature up to 1 GeV. Photons are radiated off by the quarks which undergo collisions with other quarks and gluons in the thermal bath. The energy spectrum of these photons is exponentially suppressed, but should extend up to several GeV.

3. The plasma expands and cools. At the critical temperature, a hadronic phase is formed, during which photons can be produced in hadron rescattering or in resonance decays. The mechanism continues until the resonances cease to interact, that means until the freeze-out temperature ($\sim$ 100 MeV) is reached. Photons produced in this phase will have energies between few hundred MeV and several GeV.

4. Finally, after freeze-out, further photons can be produced by the decay of π^0's, η's and higher resonances. Their energy lies in the range of up to few hundred MeV.

The prompt photons of phase one constitutes an "irreducible" background to thermal photons of phase two and three. Such background has to be kept under control, for example via comparison to the p–p benchmark. The occurrence of an excess in thermal photons (after background subtraction) in the few GeV range, would be a clear indication of a thermalized medium.

Lepton pair production shows analogies with the photon generation. In fact, they are emitted throughout the evolution of the system, and with the same stages described above.

The prompt contribution to the continuum in the dilepton mass range above pair mass $M \sim 2$ GeV is dominated by semileptonic decays of heavy flavor mesons and by the Drell-Yan process. The latter was particularly important in previous experiments, not as a deconfinement probe, but because it gives information on the initial state. Its prediction were usually adopted as a benchmark in heavy ion collisions, as it is affected only by ordinary nuclear matter effects, but it is not modified by the formation of a hot dense system. However, in the LHC, it is overwhelmed by heavy quark decays, which dominate the lepton pair continuum between the J/ψ and the Z^0 peaks.

1.4.3 Probes of the equation of state

The basic idea behind this class of signatures is the identification of modifications in the dependence of energy density (ϵ), pressure (P) and entropy density (s) of superdense hadronic matter on temperature T and baryochemical potential μ_B. A rapid rise in the ratios ϵ/T^4 or s/T^4 is, indeed, an evidence of a first–order phase transition.

The observables related to such quantities, obtainable through an analysis of the particle spectra, are the average transverse momentum and the charged particle multiplicity per rapidity unit or transverse energy per rapidity unit at mid-rapidities. In particular, a first–order transition should manifest itself through a saturation of the average transverse momentum during the mixed phase.

Particle spectra can provide information about another class of phenomena related to the equation of state: the flow. With this term is meant a collective motion of particles, superimposed to the thermal one. The flow is directly related to the pressure gradient, and can quantify the effective equation of state of the matter.

1.4.4 Signatures of chiral symmetry restoration

The expected restoration of the chiral–symmetry in the QGP could provide a change of quark and hadron masses close to the transition point. The corresponding observables will be a modification on the low mass dilepton spectra and an increment in the strangeness production.

Low mass dilepton

The study of the dilepton mass spectrum at low masses, i.e. less than 1.5 GeV, allows to get informations about the in–medium modifications of

light vector mesons properties (mass and width). In particular, the ρ meson plays a key role because its e^+e^- decay is a factor of $\sim$10 (5) larger than the one of the ω (Φ) and because it decays in the very early stages of the collision, thus carrying information on the hottest stages of the evolution. In proton–nucleus collisions the invariant mass spectrum is quite well reproduced by the standard cocktail of hadronic decays. On the contrary, the dielectron spectrum measured by the NA45 at CERN SPS for S–Au and Pb–Au collisions, shown in Fig. 1.18, differs considerably from the expected yield and shape due to the known hadronic sources: the signal is enhanced by a factor 2.6 in the mass window 250-700 MeV/c^2, just below the ρ peak.

This can be interpreted as the result of two effects. First, the ρ mass shift expected in a deconfined medium due to the chiral–symmetry restoration, which could also indicate that the ρ and its chiral partner (a_1) become degenerate. Second, the peak broadening due to strong rescattering in a dense hadronic medium.

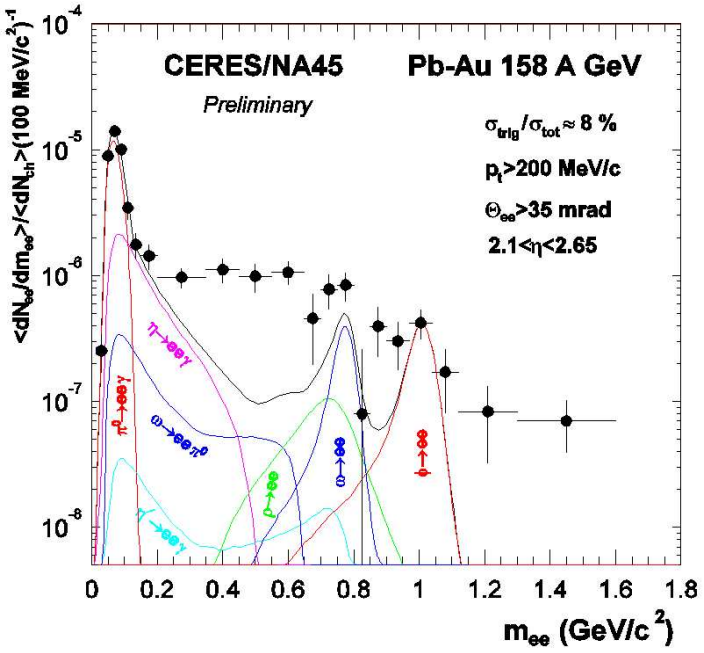

Fig. 1.18: Dielectron mass spectrum in Pb–Au collisions at $\sqrt{s}$=17 GeV compared to the expected contributions (solid line) from hadronic cocktail [18].

Strangeness enhancement

In p–p collisions, the production of particles containing strange quarks is strongly suppressed, as compared to the production of hadrons with u and d quarks. The suppression, probably due to the higher mass of the $s\bar{s}$ pair, increases with the strangeness content of the particles.

In heavy–ion collisions, the production of s quarks is expected to be favored with respect to p–p collisions, due to the reduction of its mass to $\sim$150 MeV because of chiral symmetry restoration, and it is also favored by the Pauli blocking, due to the large density of u and d quarks. In this case the strange hadron yield derives from two independent reaction steps following each other in time:

1. in a deconfined QGP, strange quark pairs ($s\bar{s}$) can be copiously produced through gluon–gluon fusion, while in hadronic gas $s\bar{s}$ pairs have to be produced via pairs of strange hadrons with higher production thresholds;

2. the initial s and $\bar{s}$ survive the process of fireball expansion, thus resulting, at hadronization, in an unusually high yield of strange and multi-strange (anti)baryon abundance.

In the following hadronization, quark recombination leads to emergence of particles such as $\Xi(ssq)$ and $\bar{\Omega}(\bar{s}\bar{s}\bar{s})$, which otherwise could only very rarely be produced, as well as to a global increase of the strange particles production.

The described enhancement as a function of the centrality of collision has been already observed [19] in experiments such as NA57 at SPS, as it is clearly shown in figure 1.19.

It is trivial to stress the importance of measuring strange production even in p–A and p–p collisions, as the enhancement can be noticed only in comparison with such data.

1.5 Heavy quarkonia suppression

Heavy quarkonia suppression is indicated as the major probe for the phase transition to QGP.

During the pre-equilibrium phase, processes of hard scattering among partons lead to production of heavy quarks c, $\overline{c}$, $b, \overline{b}$. Later, they can interact with light quarks to form D and $\overline{D}$ (open charm), or B and $\overline{B}$ (open beauty) mesons, otherwise $c\overline{c}$ and $b\overline{b}$ pairs can propagate respectively as J/ψ (hidden charm) or as Υ (hidden beauty). According to a theory due to Matsui and

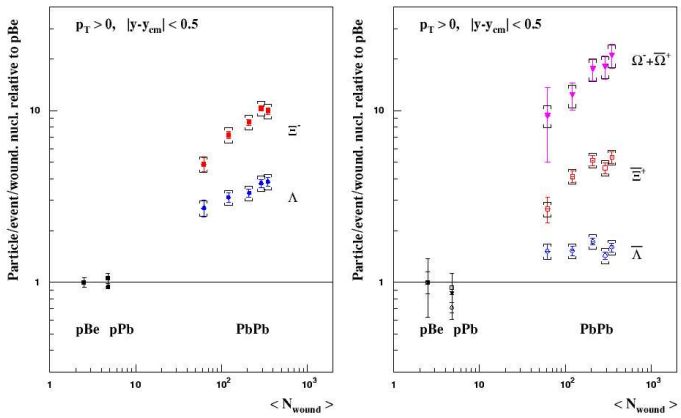

Fig. 1.19: Centrality dependence of hyperon enhancements at 158 A GeV/c [20]

Satz [21], J/ψ and Υ production is sensitive to the nature of the created medium: in a deconfined phase and over a certain temperature they would melt through color screening. Therefore, a suppression of heavy resonances production in nuclear collisions, with respect to the yields from p-p collisions, would indicate the formation of QGP.

Heavy quarkonia production can be studied via leptonic decays which are easy to tag.

Charmonium production in heavy-ion collisions has been measured at the SPS, in particular by the NA50 collaboration by means of a dimuon spectrometer. The J/ψ mesons are identified by the invariant mass of the measured muon pairs and their yields are normalized to the number of Drell-Yan pairs, which are produced proportionally to the number of hard collisions.

The interpretation of experimental data requires a comprehension of the theoretical framework that involve heavy quarkonia in general.

J/ψ and Υ are the 1^3S_1 bound states (in the $n^{2S+1}L_J$ form) of $c\overline{c}$ and $b\overline{b}$ pairs, respectively. They can be produced directly by $gg \rightarrow\ c\overline{c}$ ($b\overline{b}$) or $q\overline{q} \rightarrow c\overline{c}$ ($b\overline{b}$) processes, otherwise they can come from the decay of the corresponding excited states.

Because of the large charm quark mass, the quarkonium spectra can be calculated with good precision by means of the Schrödinger equation:

$$[2m_{c(b)} + \frac{1}{m_{c(b)}}\Delta^2 + V(r)]\Psi_{n,l} = M_{n,l}\Psi_{n,l}, \tag{1.9}$$

where $V(r) = \sigma r - \alpha/r$ contains the confining long–distance σr and a Coulomb–like short–distance term α/r. For different values of the quantum numbers n and l, the masses $M_{n,l}$ and the wave functions $\Psi_{n,l}$ for different

quarkonium states are determined in term of the constants $m_{c(b)}$, σ and α.

The value of J/ψ and Υ masses indicate that the decay into open charm or beauty is forbidden due to the mass of pairs of D mesons ($2M_D$=3.740 GeV/c^2) and B mesons ($2M_B$=10.558 GeV/c^2), so that the quarkonium states can decay only into light hadrons and leptons.

The quarkonium production in a nucleon–nucleon collision can be divided in two steps: first, a $q\overline{q}$ pair is created, generally not in a colour singlet state; then, this pair neutralizes its colour by emission or absorption of gluons. There are several models that differ in the description of the latter step. I will refer to the colour octet model [22, 23] that allows the interpretation of some charmonium production data.

The basis of the colour octet model is that a quark–antiquark state can be decomposed in the following way:

$$|\Psi\rangle = a_0|(q\overline{q})_1\rangle + a_1|(q\overline{q})_8 g\rangle + a_2|(q\overline{q})_1 gg\rangle + a_3|(q\overline{q})_8 gg\rangle + ... \qquad (1.10)$$

namely into a pure $(q\overline{q})_1$ colour singlet component, plus a $(q\overline{q})_8$ colour octet component and a gluon, and so on. At high energy, the second term becomes the most important in the quarkonium production: the $(q\overline{q})_8$ pair will interact with a gluon to form a pre-resonant state and, only after some time (that depends on gluon energy) the quarkonium state is formed. The important feature is that the pre–resonant $(q\overline{q})$ state has the same characteristics (size and lifetime) for the different quarkonium states.

In proton–nucleus and nucleus–nucleus collisions, the heavy quarkonia production can suffer a suppression due to the nuclear absorption, the so–called "normal" suppression. In terms of the colour octet model, at high energy, we can expect that the pre–resonance propagates through the nuclear matter and undergoes interaction with both target and projectile nucleons. The degree of suppression depends on the thickness of nuclear matter traversed by the pre–resonance. This means that J/ψ and ψ' should undergo the same amount of 'normal' suppression, as confirmed by the data from NA38 collaboration [24].

In the picture of a pre-resonant "normal" absorption, the cross–section for J/ψ production in p–A and A–B collisions can be parametrized as a function of the cross–section in p–p collisions:

$$\sigma_{pA} = \sigma_{pp} A^{\alpha}, \qquad (1.11)$$

where α accounts for nuclear effects and $\alpha < 1$ indicates absorption by nucleons. While data collected at the SPS in p–p, p–A and light ion collisions

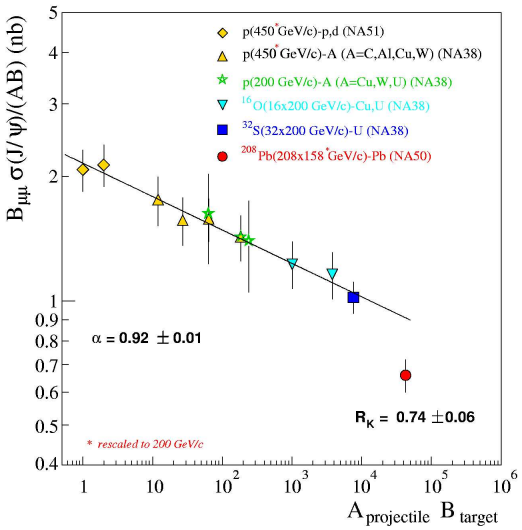

Fig. 1.20: J/ψ cross section as a function of the product of the projectile and target atomic mass number.

agree with this parametrization, the J/ψ yield in Pb–Pb collisions is much lower than the one expected from such a parametrization, as can be seen in Fig. 1.20.

Moreover, in Fig. 1.21 is reported the number of produced J/ψ as a function of the density energy ϵ measured by the NA50 collaboration: for ϵ >2.5 GeV/fm^3 the number of J/ψ, with respect to the number of expected ones, decreases, while for lower energy density the "normal" behaviour is followed. In the same picture, a multi-steps pattern can be observed.

These features can be reproduced in a deconfinement scenario.

According to the Schrödinger equation 1.9, quarkonia radii are much smaller than those of usual hadrons: $r_{J/\psi} = 0.2$ fm and $r_\Upsilon = 0.1$ fm, in contrast to about 1 fm for light $q\overline{q}$ state radii.

By comparing the bound state radii to the colour screening radius r(T)=μ^{-1} (see Section 1.2), one can obtain the temperature (T_d) expected for dissociation of each state. In Table 1.2, results for the dissociation temperatures obtained by lattice studies are listed [25]. We can see that only J/ψ, Υ, χ_b and Υ' states have a dissociation temperature above the deconfinement critical temperature T_c. However, the states J/ψ', χ_c, Υ'', χ_b' may decay in open charm/beauty, rather than undergo a dissociation, because of the decrease of open charm/beauty threshold in a hot but still confined medium.

By putting together the fractions of quarkonium ground state production originated from higher excitations, and the temperature or energy density at

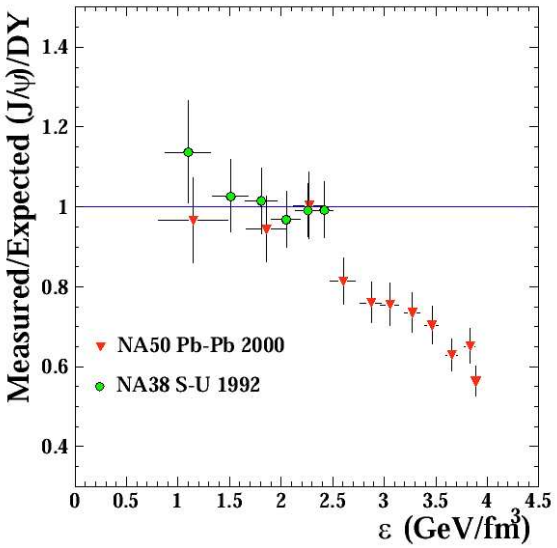

Fig. 1.21: Results of NA38 and NA50 experiments: the number of J/ψ produced depends on the density energy ϵ with a sharp suppression after ϵ >2.5 GeV/fm^3.

Resonance	Binding Energy (MeV)	T_d/T_c	$\mu(T_c)/\mu(T_d)$
J/ψ	640	1.10	0.91
χ_c(1P)	250	0.74	*
J/ψ'(2S)	60	0.1-0.2	*
Υ	1100	2.31	0.43
χ_b(1P)	670	1.13	0.88
Υ'(2S)	550	1.10	0.91
χ_b(2P)	305	0.83	*
Υ''(3S)	200	0.75	*

Tab. 1.2: Binding energy and dissociation parameters of different quarkonium states [25, 26].

which a given excitation dissolves (or decays) (Table 1.2), the suppression patterns of Fig. 1.22 and Fig. 1.23 are obtained.

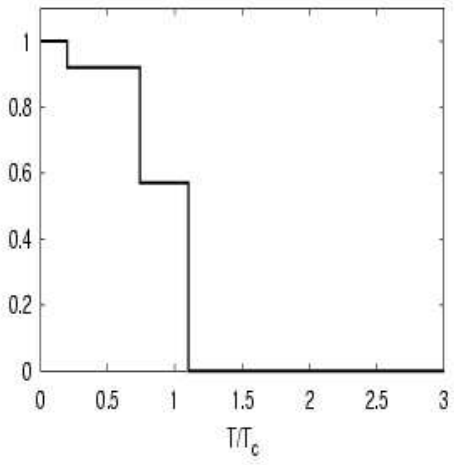

Fig. 1.22: The J/ψ suppression pattern [26].

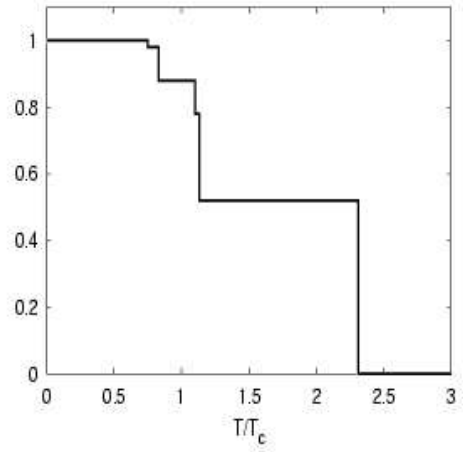

Fig. 1.23: The Υ suppression pattern [26].

Fig. 1.22 offers the interpretation of the NA50 data shown in Fig. 1.21: the first step is due to the disappearance of the χ_c mesons, which is responsible for about 30-40% of the indirect J/ψ, while the second step is due to the dissociation of the directly produced J/ψ that are more tightly bound.

Other models attribute the "anomalous" suppression to the inelastic scattering of the final resonance state with co–moving secondary hadrons. How-

ever, the "comover" models predict a smooth suppression of the J/ψ and a saturation of the suppression in most central collisions that does not agree with the NA50 results.

J/ψ suppression has been recently studied by the NA60 experiment in Indium–Indium collisions [27]. The comparison between different colliding systems should allow to understand which is the variable driving the J/ψ suppression, e.g. the local energy density or the density of participants or the length L of nuclear matter crossed by the charmonium state. This information should help to disentangle the different theoretical model predicting the disappearance of the J/ψ. In Fig. 1.24 the ratio between the J/ψ and the absorption curve is shown as a function of L, N_{part}, and of the Bjorken energy density.

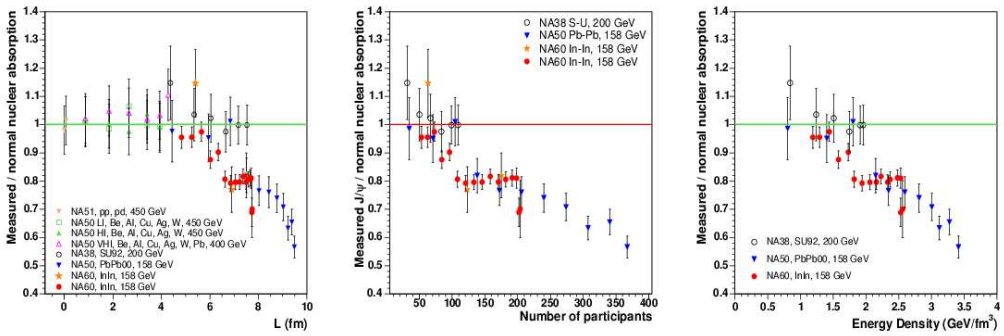

Fig. 1.24: Ratio between the J/ψ data points and the absorption curve as a function of several centrality estimators: (a) L, (b) N_{part}, (c) energy density.

The NA60 data show that the J/ψ is already suppressed in In–In collisions with a clear onset at $N_{part} \sim 90$.

The statistics accumulated at RHIC is now sufficient to draw some results on the J/ψ production: the results confirm the suppression pattern found by NA50 and NA60 experiments, as reported in Fig. 1.25.

Concerning the bottomium resonances, only at the LHC will be possible for the first time to reach energy densities (or temperatures) high enough to observe the predicted suppression: in Fig. 1.26 the Υ suppression pattern as a function of the temperature is compared with the temperature achievable at SPS, RHIC and LHC.

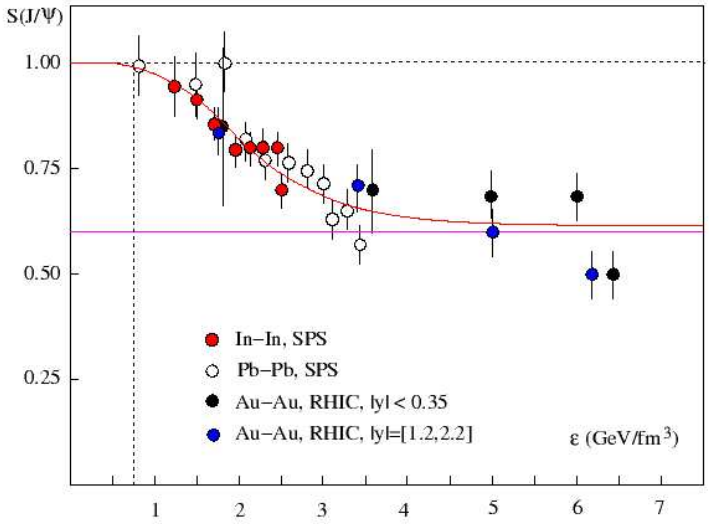

Fig. 1.25: J/ψ production as a function of the energy density: results from SPS and from RHIC.

1.6 New aspects at LHC compared to SPS and RHIC results

The observables measured by SPS experiments seem to confirm the picture given in Section 1.3 for a heavy-ion collision: the system formed in Pb–Pb central collision at 158 A GeV has a non–zero net baryon density and reaches an initial energy density of about 3.5 GeV/fm^3 and temperatures around 210-220 MeV, sufficient to have the phase transition towards the QGP according to theoretical estimates. In fact, there are indications for an initial stage of QGP (with chiral symmetry partially restored) which, after less than 1 fm/c, evolves in an hadronic stage. The last one shows collective behaviour and a large degree of thermalization; hadron yields suggest that the system is indeed thermalized already before the hadronic phase.

All these results lead, in February 2000, the CERN to announce the formation of a new state of matter: "The new state of matter found in heavy–ion collisions at the SPS features many of the characteristics of the theoretically predicted quark-gluon plasma" [28].

Preliminary results at RHIC give estimation of the same signatures observed at SPS and of new ones, in a new energy and density regime. Essentially there is the indication for a lower net baryon density of the created system which is hotter, denser, bigger and longer–lived than the one observed at SPS. Moreover, the measured particle multiplicities show the appearance

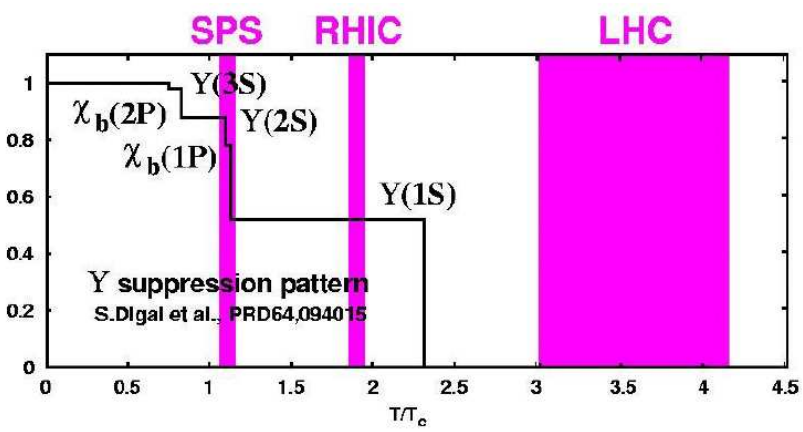

Fig. 1.26: Υ suppression pattern as a function of the temperature compared with the temperature achievable at SPS, RHIC and LHC

of low–momentum parton saturation and there is evidence for jet–quenching.

Central collisions	SPS	RHIC	LHC
$\sqrt{s}/A$ (GeV)	17	200	5500
dN_{ch}/dy	500	650	$3-8\times10^3$
ϵ (GeV/fm^3)	3.5	20	15-40
$V_{freeze-out}$ (fm^3)	10^3	7×10^3	2×10^4
τ_{QGP} (fm/c)	<1	1.5-4.0	4-10
τ_0 (fm/c)	∼1	∼0.5	<0.2

Tab. 1.3: Global observables for central collisions at SPS, at RHIC and at LHC.

At LHC we expect a jump of a factor 30 in the centre-of-mass energy with respect to the one available at RHIC. We should have a further improvement in the initial conditions: the system will be denser, hotter and at vanishing baryon density; the QGP will be formed earlier and it will remain thermalized for a longer time; the freeze–out volume will be bigger than the one observed at RHIC. In Table 1.3 [29], a comparison between the global observables measured at SPS and at RHIC and the corresponding values predicted for the LHC energies is presented.

Above all, at LHC we will study with greater precision the observables already investigated at lower energies, in addition, new observables will become accessible, due to the fact that we will enter in a qualitatively new regime.

In particular, the study of the suppression pattern will be extended to

the Υ family and a full spectra analysis of heavy–quark resonances will be feasible. About the J/ψ production at the LHC energies, some questions are yet open. Recent theoretical calculations [30, 31] predict an enhancement, rather than a suppression, due to the high number of c-$\overline{c}$ pairs expected to be produced per unit of rapidity that allows a 'statistical' J/ψ production. Another aspect to be defined is the regeneration of charmonium states via $D - \overline{D}$ annihilation in the mixed phase [32]. Different authors came to different conclusions on the importance of the yield of the secondary J/ψ with respect to the primary one, while there is a general agreement in asserting that the secondary production will be dominant for ψ'.

For the interpretation of the quarkonia data and for a deeper understanding of charm and beauty production, measurements of open charm and eventually of beauty production are of crucial importance. This will become possible at LHC.

References

[1] H.Satz, Rep. Progr. Phys. 63 (2000) 1511-1574

[2] L. D. McLerran and B. Svetitsky, Phys. Lett. 98 B (1981) 195 and Phys. Rev. D 24 (1981) 450

[3] J. Kuti, J. Polonyi and K. Szlachanyi, Phys. Lett. 98 B (1981) 199

[4] F. Karsch and E. Laermann, Phys. Rev. D 50 (1994) 6954

[5] J. Engels *et al.*, Z. Phys. C 42 (1989) 341

[6] M. Asakawa and T. Hatsuda, Nucl. Phys. A 610 (1996) 470c

[7] C.Y. Wong, *Introduction to High Energy Heavy Ion Collisions*, World Scientific, Singapore, 1994

[8] A. Coniglio and W. Klein, J. Phys. A 13 (1980) 2775

[9] J. Kertész, Physica A 161, (1989) 58

[10] H. R. Schmidt and J. Schukraft, J. Phys. G: Nucl. Part. Phys. 19 (1993) 1705-1795

[11] J. D. Bjorken, Phys. Rev. D27 (1983) 140-150

[12] M.C. Abreu *et al.* (NA50), Phys. Lett. B477 (2000) 28

[13] M. Baker *et al.* [PHOBOS Collaboration], Nucl. Phys. A 715 (2003) 65c

[14] X. Wang and M. Gyulassy, Phys. Rev. Lett. 86 (2001) 3496, [nucl-th/0008014]

[15] K. J. Eskola, K. Kajantie, P.V. Ruuskanen, K. Tuominen, Nucl. Phys. B 507 (2000) 379, [hep-ph/9909456]

[16] K. Adcox *et al.* [PHENIX collaboration], Phys. Rev. Lett. 86 (2001) 3500

[17] D. Kharzeev and M. Nardi, Nucl. Phys. B 507 (2001) 121

[18] CERES Collaboration, Nucl. Phys. A 661 (1999) 23c

[19] NA57 Collaboration, Nucl. Phys. A 681 (2001) 165

[20] D Elia [NA57 Collaboration] J. Phys. G: Nucl. Part. Phys. 31 (2004) 135

[21] T. Matsui and H. Satz, Phys. Lett. B 178 (1986) 416

[22] G.T. Bodwin, E. Braaten and G.P. Lepage, Phys. Rev. D 51 (1995) 1125

[23] E. Braaten and S. Fleming, Phys. Rev. Lett. 74 (1995) 3327

[24] NA38 Collaboration, Phys. Lett. B 220 (1989) 471

[25] S. Digal, P. Petreczky and H. Satz, hep-ph/0105234

[26] H. Satz, Phys. Rev. D 64 (2001) 094015

[27] R. Arnaldi *et al.* [NA60 collaboration], "Anomalous J/ψ suppression in In–In collisions at 158 GeV/nucleon", Quark Matter 2005 procceding, to be published

[28] CERN Press release, 10 Feb. 2000

[29] J. Schukraft, Nucl. Phys. A 698 (2002) 287c

[30] P. Braun-Munzinger and J. Stachel, Phys. Lett. B 490 (2000) 196

[31] R.L. Thews *et al.*, Phys. Rev. C 63 (2001)

[32] C.M. Ko *et al.*, Phys. Lett. B 444 (1998) 237;
P. Braun-Munzinger and K. Redlich, Eur. Phys. Jour. C 16 (2000) 519

Chapter 2

ALICE

2.1 LHC experimental conditions

ALICE (A Large Ion Collider Experiment) is a general purpose heavy–ion collision experiment designed to study the physics of strongly interacting matter and the quark gluon plasma in nucleus–nucleus collisions at the LHC.

The principal aim of ALICE, the only experiment at the LHC dedicated to the study of heavy–ion collisions, is to collect events in Pb–Pb collisions at $\sqrt{s}$=5.5 TeV per nucleon pair, to measure rare process such as jet transverse-energy spectra and to study the production pattern of the bottomium bound state. Furthermore, also intermediate–ion collisions (d–A, α–A and p–p) are foreseen to vary the energy density of the colliding system and to provide reference data for the nucleus–nucleus collisions [1]. Presently the LHC is foreseen to start operation in Summer 2007.

Whether ALICE can reach the physics goals depends not only on the detectors performances, but also on the number of events that can be collected, the number of collision systems that can be studied and on the background conditions at the LHC as explained in the following Sections.

2.1.1 Running strategy

In order to optimize the physics output, the ALICE program has been divided into two phases: an initial program based on current theoretical understanding and on the results from SPS and RHIC, and a later phase with open options whose priority will be provided by the analysis of the first LHC data. The LHC is expected to run essentially in the same yearly mode as the SPS, starting with several month of p–p running followed by several weeks of heavy–ion collisions. For rate estimates, ALICE and all LHC

experiments will use an effective time per year of 10^7 s for p–p and 10^6 s for heavy–ion operation.

The initial ALICE program, discussed and endorsed by the LHC Committee, is summarized below:

- regular p–p runs at $\sqrt{s}$=14 TeV;
- Pb–Pb physics pilot run at $\sqrt{s_{NN}}$=5.5 TeV. This run will provide information on global event properties and large cross section observables;
- 1–2 years Pb–Pb at the highest possible luminosity to get sufficient statistics for low cross section observables;
- 1 year 'p-Pb like' conditions (p–Pb, d–Pb or α–Pb) as reference data;
- 1 year Ar–Ar to study the energy density dependence.

The different options for the second phase depend on the outcome of the previous data analysis:

- dedicated p–p or 'p–p like' collisions (d–d or α–α) at $\sqrt{s_{NN}}$=5.5 TeV for a direct comparison with the Pb–Pb data;
- another intermediate–mass A–A system (N–N, O–O, Kr–Kr or Sn–Sn) to map the A–dependence;
- another 'p–A like' system (d–A or α–A);
- lower energy Pb–Pb runs;
- further high energy Pb–Pb runs to increase the statistics of rare events.

Figure 2.1 shows the approximate energy density bands covered on the basis the impact parameter values for the different colliding systems foreseen in ALICE.

2.1.2 The luminosity at LHC

The luminosity, with a strict connection with the number of collected events, is limited by the LHC machine as well as by the detector itself.

The collider luminosity is given by the number of the interactions divided by the cross section of the interaction; it depends on machine characteristics such as the ion accumulation and the injection scheme and therefore the optimization is different for different ion masses. The circulating bunches suffer losses due to electromagnetic interactions, which cross section grows with the

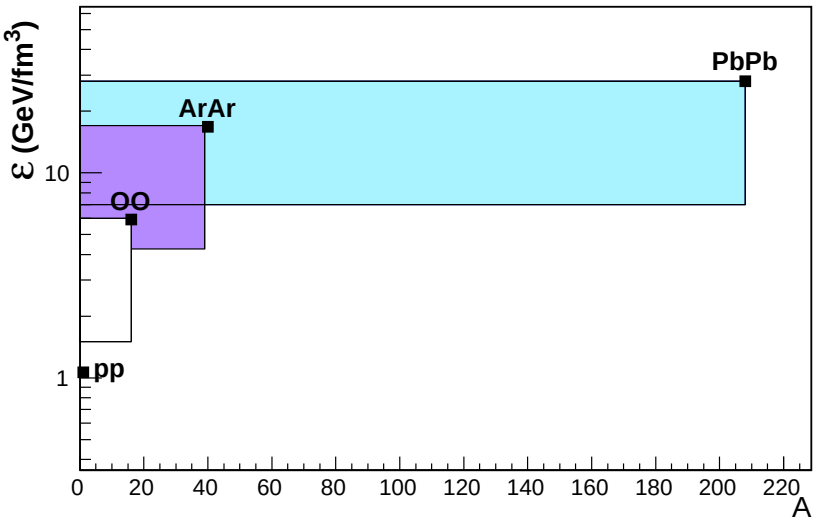

Fig. 2.1: Variation of the produced energy density with collision system. The energy density has been calculated using the Bjorken formula 1.7 with maximum charged-particle multiplicities of 6000, 1200, 230 and 6.5 for central Pb–Pb, Ar–Ar, O–O, and p–p collisions, respectively.

square of the atomic number Z: this results in a reduction of the luminosity and of the lifetime of the running beam. At LHC the maximum achievable luminosity will be 10^{27} cm^{-2}s^{-1} for the Pb–Pb collisions, 10^{30} cm^{-2}s^{-1} for Ar–Ar and 10^{34} cm^{-2}s^{-1} for p–p operations.

However, the resulting interaction rates foreseen in the last two colliding systems are too high for the operation of one of the main tracking device, the Time Projection Chamber (TPC), since the drift time of this detector is about 90 μs. As a consequence, the luminosity will be limited to 2.8×10^{27} cm^{-2}s^{-1} for Ar–Ar collisions and to 3×10^{30} cm^{-2}s^{-1} during p–p runs: in this way the pile–up in the TPC is kept at an acceptable level. In order to maximize the heavy–quarkonia meson rate in the dimuon channel, a period of high luminosity (10^{29} cm^{-2}s^{-1}) Ar–Ar runs will be dedicated to the Forward Spectrometer operating 'standalone'.

A summary of possible operations and of their conditions is listed in Table 2.1: $\mathcal{L}_{\rm low}$ indicates the highest luminosity during normal operation with working TPC, while $\mathcal{L}_{\rm high}$ is the highest luminosity for the Forward Spectrometer 'standalone' runs.

System	$\sqrt{s_{\rm NN}}_{\rm max}$ (TeV)	Δy	$\sigma_{\rm geom}$(barn)	$\mathcal{L}_{\rm low}$(cm^{-2}s^{-1})	$\mathcal{L}_{\rm high}$(cm^{-2}s^{-1})
Pb–Pb	5.5	0	7.7	1.0×10^{27}	
Ar–Ar	6.3	0	2.7	2.8×10^{27}	1.0×10^{29}
O–O	7.0	0	1.4	5.5×10^{27}	2.0×10^{29}
N–N	7.0	0	1.3	5.9×10^{27}	2.2×10^{29}
α–α	7.0	0	0.34	6.2×10^{29}	
d–d	7.0	0	0.19	1.1×10^{30}	
p–p	14.0	0	0.07	1.0×10^{29}	5.0×10^{30}
p–Pb	8.8	0.47	1.9	1.1×10^{29}	
p–Ar	9.4	0.40	0.72	3.0×10^{29}	
p–O	9.9	0.35	0.39	5.4×10^{29}	
d–Pb	6.2	0.12	2.6	8.1×10^{28}	
d–Ar	6.6	0.05	1.1	1.9×10^{29}	
d–O	7.0	0.00	0.66	3.2×10^{29}	
α–Pb	6.2	0.12	2.75	7.7×10^{28}	
α–Ar	6.6	0.05	1.22	1.7×10^{29}	
α–O	7.0	0.00	0.76	2.8×10^{29}	

Tab. 2.1: Maximum nucleon–nucleon centre-of-mass energies, rapidity shifts, geometric cross sections, and lower and upper limits on luminosities for several different symmetric and asymmetric systems.

2.1.3 Background conditions

A second important aspect to be kept into consideration is the expected background condition at LHC. As a matter of fact, the beam–induced phenomena (photo, electron and ion stimulated desorption) are potential gas sources limiting the vacuum condition at the LHC. The dynamic gas densities in the Long Straight Section (SS2) of the Insertion Region 2 (IR2, where ALICE will be installed) have been simulated for the first three years of LHC operations [2]. The resulting H_2 equivalent gas density in p–p runs amounts to $\sim 2 \times 10^{14}$ molecules/m^3, as shown in Figure 2.2.

During p–p runs, the residual gas nuclei can interact with the circulating protons and the produced secondary particles are the so–called 'machine–induced background' or beam–gas background. This background scales with the beam current, while the number of particles emitted in p–p collision at the interaction point scales with the luminosity. Therefore the machine–induced background is relatively more important when p–p runs are carried out at reduced luminosity but full intensity, as it will happen in ALICE.

Among the ALICE detectors, the beam–gas background mostly interests

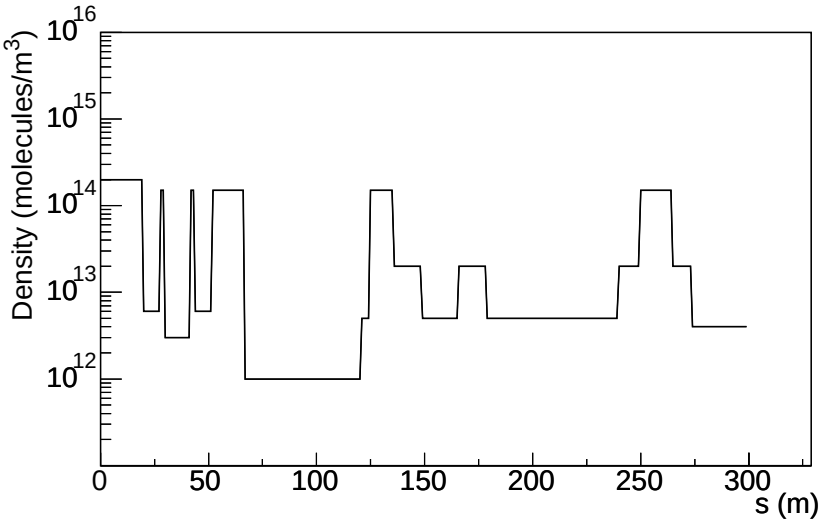

Fig. 2.2: Residual H_2-equivalent density distribution for IR2 in the first three years of LHC operation as a function of the distance from interaction point.

the Trigger detector of the Muon Spectrometer: I will discuss this argument in more details in Section 3.6.1.

2.2 The ALICE Detectors

The ALICE detectors (see Figure 2.3) have been optimized to measure and identify mid–rapidity hadrons, leptons and photons produced in the interaction, especially in heavy–ion collisions: this results in a unique design with respect to the other LHC experiments, which are optimized for p–p collisions. ALICE has been conceived to track and identify particle in a wide p_t range ($\sim$0.1–100 GeV/c), to reconstruct short–lived particles such as hyperons, D and B mesons, and to perform these tasks in an environment with large charged particle multiplicities, up to 8000 charged particle per rapidity unity at mid–rapidity. At the present moment, the theoretical predictions for multiplicity in a central Pb–Pb collision range from 2000 to 6000 charged particle per rapidity unity at mid–rapidity, while the extrapolations from RHIC provide a value of about 3500: all these values are below the one ALICE has been conceived for (8000 charged particle per rapidity unity) thus offering a safety margin larger than 2.

The detector acceptance must be sufficiently large

- to enable the event-by-event study of particle ratios, p_t spectra, and

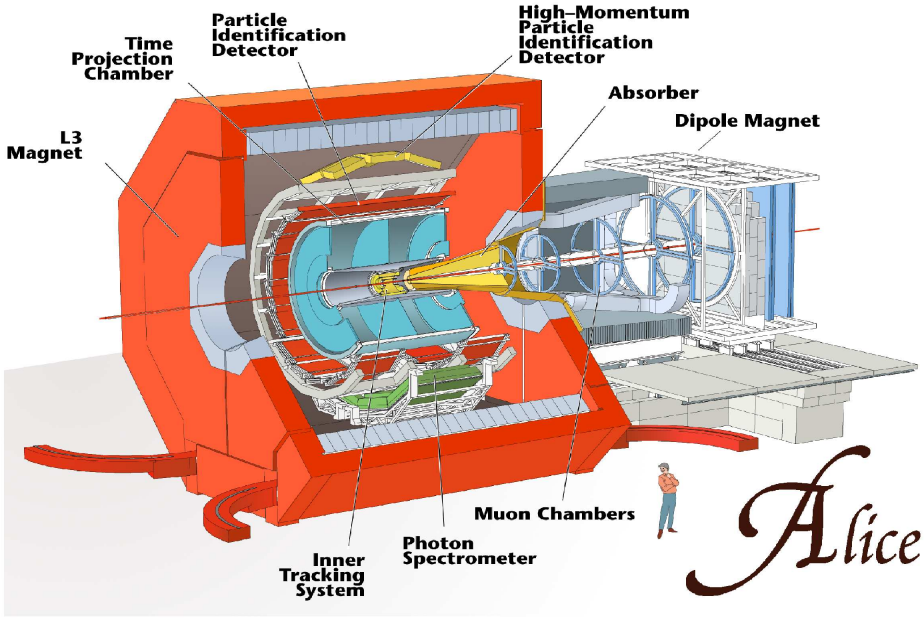

Fig. 2.3: Longitudinal view of the ALICE detector.

HBT (Hanbury, Brown and Twist) correlations;

- to detect the decay products of low transverse momentum particles (p_t<m for m>1–2 GeV);

- to collect a significant statistical sample of Υ in the dielectron channel.

The central part of the detector covers the rapidity region $|\eta|$ <0.9 and the full azimuthal angle φ, to obtain a compromise between the requirements listed above and the cost and practical implementation constrains. To gain in sensitivity on the global event structure, charged particle multiplicity will be measured in a larger rapidity domain (-3.4< η <5.1).

The detection and identification of muons are performed with the dedicated Muon Forward Spectrometer, including a large warm dipole and covering a region of large rapidities (-4.0< η <-2.4). The muon detection allow to measure the heavy–quark resonances spectrum and to identify J/ψ and ψ', Υ, Υ' and Υ'' particles via their decay in two muons.

In the following sections, a brief overview of the central barrel detectors and of the forward ones is reported. The next chapter will be dedicated to a more precise description of the Muon Forward Spectrometer.

2.2.1 The central barrel

The central barrel allows an event-by-event study, providing information on the collision topology (vertex, centrality and tracking) and measuring the production of photons and charged particles.

The sub–detectors have been chosen and designed to cope with the following constrains:

- the high particle multiplicity expected in Pb–Pb collisions;
- a track–finding efficiency of at least 90% for p_t >100 MeV/c;
- the momentum resolution, which is different for different momentum range:
  - at low momenta (<0.2 GeV/c) the resolution needs are constrained by identical particle interferometry;
  - at intermediate momenta (0.2÷2 GeV/c) a 1% resolution is required to distinguish the ω and Φ mesons to study the resonance mass and width in the dense medium;
  - at high momenta (>2 GeV/c) the resolution must allow the jet spectra measurement.

The tracking system is based on the Time Projection Chamber (TPC), the Inner Tracking System (ITS), but also the Transition Radiation Detector (TDR), can be used as a tracking detector.

All the detector of the central barrel are enclosed in the solenoid magnet constructed for the L3 experiment at LEP, with an internal length of 12 m and a radius of 5 m. A nominal field of 0.5 T has been chosen to fulfill the momentum resolution listed above and to avoid losses of the low momentum particles.

Inner Tracking System (ITS)

The ITS [5] contributes to the global tracking of ALICE by improving the momentum and the angle resolution obtained by the TPC. The task of the ITS are:

- to localize the primary vertex with a resolution better than 100 μm;
- to reconstruct the secondary vertices from decays of hyperons, D and B mesons and K^0_S;

- to track and identify particles with momentum below 100 MeV/c, detectable only by the ITS;
- to improve the momentum and angle resolution for the high-p_t particles which also traverse the TPC.

The ITS consists of six cylindrical layers of silicon detectors and covers the rapidity range of $|\eta| < 0.9$. The first layer has a more extended coverage ($|\eta| < 1.98$) to provide, together with the Forward Multiplicity Detectors (FMD), a continuous coverage in rapidity for the measurement of charged-particles multiplicity.

Because of the high particle density, up to 80 particles per cm^2, and in order to achieve the required impact parameter resolution, Silicon Pixel Detectors have been chosen for the innermost two layers (SPD), and Silicon Drift Detectors for the following two layers (SDD). The outer two layers, where the track densities are below one particle per cm^2, will be equipped with double-sided Silicon micro–Strip Detectors (SSD). The layout of the ITS and of the sub–detectors is shown in Fig. 2.4.

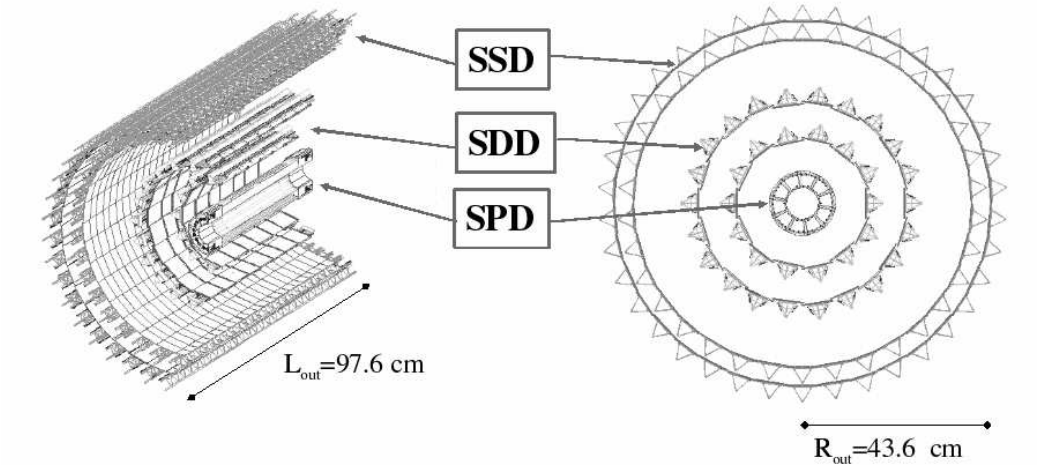

Fig. 2.4: Layout of the ITS.

Time Projection Chamber (TPC)

The TPC [6] is the main tracking detector of ALICE and also the biggest detector of the central barrel, as can be seen in Figure 2.5. It has to be remarked that the ALICE one, will be the largest TPC ever built.

The TPC, together with the ITS and the TRD, will provide:

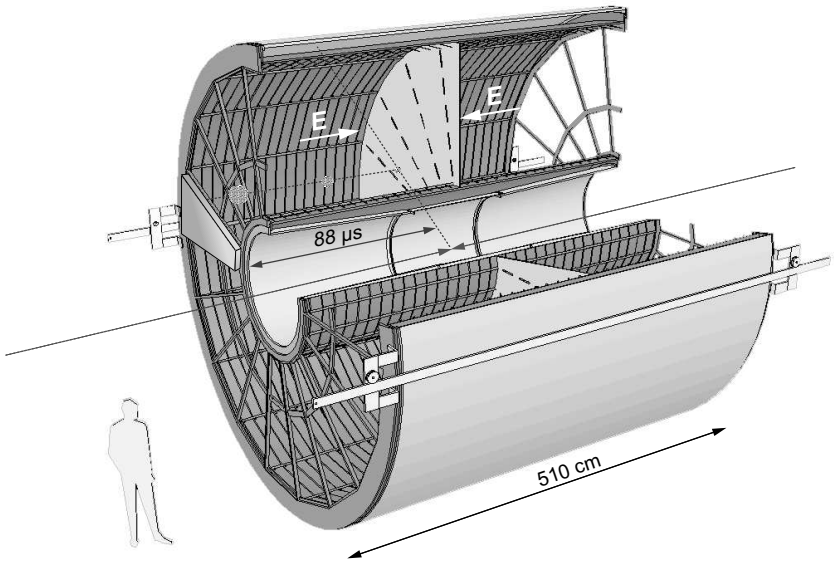

Fig. 2.5: TPC, general view. Multi–wire proportional chambers are mounted into 18 trapezoidal sectors of each end-plate.

- the track identification with two–track separation;
- the charged particle momentum measurement;
- the particle identification via dE/dx measurement of hadronic and leptonic signals for p_t <10 GeV/c.

The TPC is cylindrical in shape and has an inner radius of about 85 cm, an outer radius of about 250 cm, and an overall length along the beam direction of 500 cm. The inner radius has been fixed accordingly to the maximum acceptable hit density (0.1 hit/cm^2), while the outer radius length achieve a track extent such that the dE/dx resolution is of the order of 7%. With this value of resolution it is possible to identify electrons up to 3 GeV/c to complete the TRD electron identification.

The detector is made of a large cylindrical field cage, filled with 88 m^3 of Ne/CO_2 (90%/10%), which is needed to transport the primary electrons over a distance of up to 2.5 m on either side of the central electrode to the end-plates. Multi-wire proportional chambers with cathode pad readout are mounted into 18 trapezoidal sectors of each end-plate. The drift gas is optimised for drift speed, low diffusion, low radiation length and hence low multiple scattering, small space-charge effect, and ageing properties. The gas mixture used in the TPC imposes that the field cage operates at high voltage

gradients, of about 400 V/cm, with a high voltage of 100 kV at the central electrode which results in a maximum drift time of about 90 μs over the length of 2.5 m: this makes the TPC the slowest ALICE detector. Nevertheless, it is designed to cope with 8000 charged particle per rapidity unit, as required in the Pb–Pb collisions considering a reasonable safety margin with respect to the RHIC extrapolations (3500 charged particle per rapidity unit).

Transition Radiation Detector (TRD)

The TRD [8] has the main task of providing electron identification in the central barrel for momenta greater then 1 GeV/c, thus extending the investigation to physics accessible with electron pair and single electron spectroscopy.

The TRD will provide, along with the data from ITS and TPC, the electron identification to measure the production of light and heavy vector–meson resonances and the dilepton continuum in Pb–Pb and p–p collisions. In this way, the TRD measurements are complementary to the $\mu^+\mu^-$ ones performed by the Muon Forward Spectrometer. The electronic channel has two advantages with respect to the muonic one: the secondary vertices are known by the ITS and a correlation with other observables of the central barrel is possible. However, the low-p_t background is higher in the electron channel than in the muon one. In addition, the high-p_t cut required on each electron by the TRD trigger prevents the detection of charmonium states with $p_t \leq 5$ GeV/c.

The coverage in pseudo-rapidity matches the coverage of the other central barrel detectors ($\mid \eta \mid < 0.9$). The TRD fills the radial space between the TPC and the TOF detectors as shown in Fig. 2.6. For quality of electron identification, the TRD consists of 6 individual layers. To match the azimuthal segmentation of the TPC, the TRD is divided into 18 sectors with a further 5–fold segmentation along beam direction, z, giving a total of $18 \times 5 \times 6 = 540$ detector modules.

The working principle it is based on, is the transition X–ray (E$\sim$10 KeV) emission when a charged particle crosses the boundary between two media with different refraction indexes. Each module consists of a radiator of 4.8 cm thickness and a multi-wire proportional chamber to detect the emitted radiation. This technique ensures an electron/pion separation better then 1% for $p_t \geq 3$ GeV/c.

Although its main task is electron identification, the TRD can be used also as a tracking detector. Thanks to its excellent position resolution (600 μm in the bend direction) and to its large lever arm, it can be used in conjunction with ITS and TPC with substantial improvement of the momentum

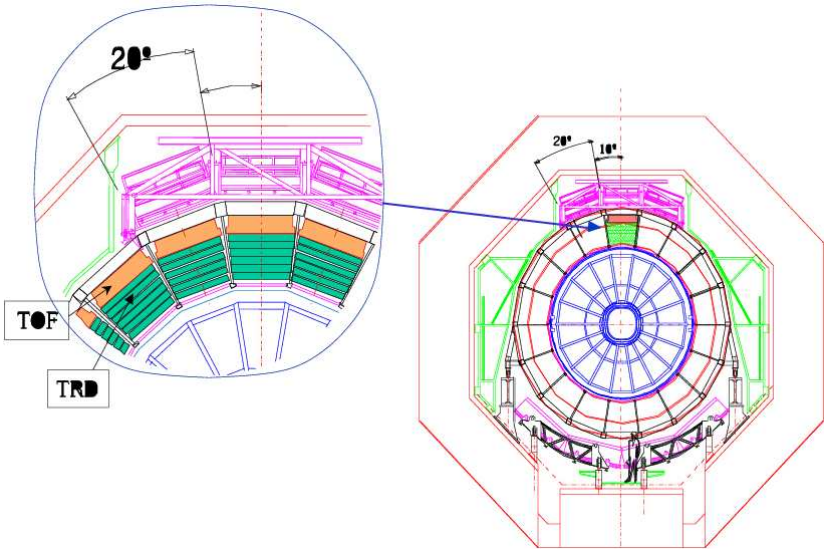

Fig. 2.6: TRD integration between TOF and TPC.

resolution at high-p_t.

Time of Flight System (TOF)

The TOF [9] is a large area array that covers the central pseudo-rapidity region ($|\eta| < 0.9$) for Particle IDentification (PID) in the intermediate momentum range (from 0.2 to 2.5 GeV/c). Since the majority of the produced charged particles is emitted in this range, the performance of such a detector is of crucial importance for the experiment. The measurement and the identification of charged particles in the intermediate momentum range will provide observables which can be used to probe the nature and the dynamical evolution of the system produced in ultra relativistic heavy-ion collisions at LHC energies.

The TOF, coupled with the ITS and TPC for track and vertex reconstruction and for dE/dx measurements in the low-momentum range (up to about 0.5 GeV/c), will provide event-by-event identification of large samples of pions, kaons, and protons. The TOF identified particles will be used to study relevant hadronic observables on a single-event basis. In addition, at the inclusive level, identified kaons will allow invariant mass studies, in particular the detection of open charm states and of the ϕ meson.

A large-coverage, powerful TOF detector, operating efficiently in extreme multiplicity conditions, should have an excellent intrinsic response: an inten-

sive R&D program has shown that the best solution for the TOF detector is the Multi-gap Resistive Plate Chamber (MRPC). Latest tests of several MRPCs show that these devices can reach an intrinsic time resolution better than about 40 ps and an efficiency close to 100%.

The detector covers a cylindrical surface with modular structure corresponding to 18 sectors in the azimuthal angle and to 5 segments along the beam axis.

High Momentum Particle Identification Detector (HMPID)

The HMPID [10] is dedicated to inclusive measurements of identified hadrons for p_t >1 GeV/c. The HMPID was designed as a single-arm array with an acceptance of 5% of the central barrel phase space. The HMPID will enhance the PID capability of the ALICE experiment by enabling identification of particles beyond the momentum interval attainable through energy loss (in ITS and TPC) and time of flight measurements in TOF. The detector was optimized to extend the useful range for π/K and K/p discrimination, on a track by track basis, up to 3 GeV/c and 5 GeV/c respectively. The particle spectra will provide information on the jet quenching, assuming that the foreseen suppression of large E_t jets leads to the suppression of high-p_t particles.

The HMPID is based on Ring Imaging Cherenkov (RICH) counters and consists of seven modules of about 1.5×1.5 m^2 each, mounted in an independent support cradle (Figure 2.7). The Cherenkov light cone is produced in the C_6F_{14} liquid radiator (β_{min}=0.77) and detected by a MWPC as shown in Figure 2.8.

PHOton Spectrometer (PHOS)

The PHOS [7] is a high resolution electromagnetic spectrometer which will detect direct photons and photons at high-p_t coming from π^0 and η decay. The main physics objectives are the following:

- testing thermal and dynamical properties of the initial phase of the collision, in particular the initial temperature and space–time dimensions of the hot zone, through measurement of direct single-photon and diphoton spectra;

- investigating jet quenching as a probe of deconfinement, through measurement of high-p_t π^0 and η decay into 2 photons;

- studying HBT correlations with neutral pions.

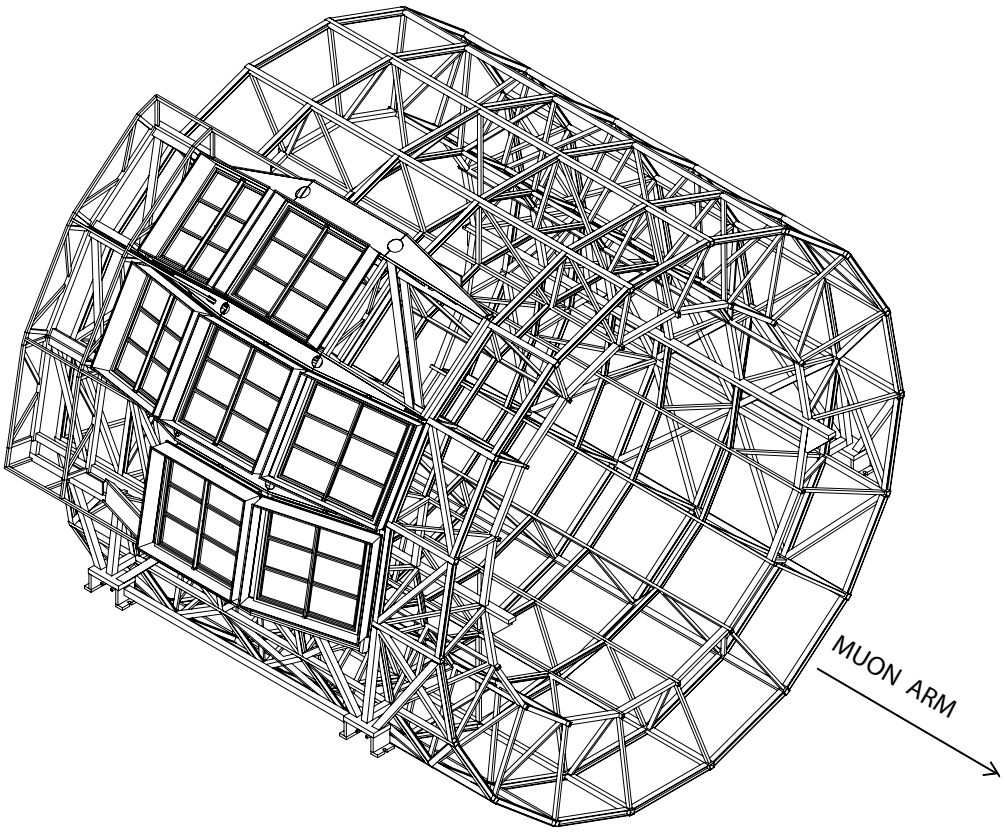

Fig. 2.7: Axonometric view of the HMPID with cradle and space frame to support the seven Ring Imaging Cherenkov (RICH) counters.

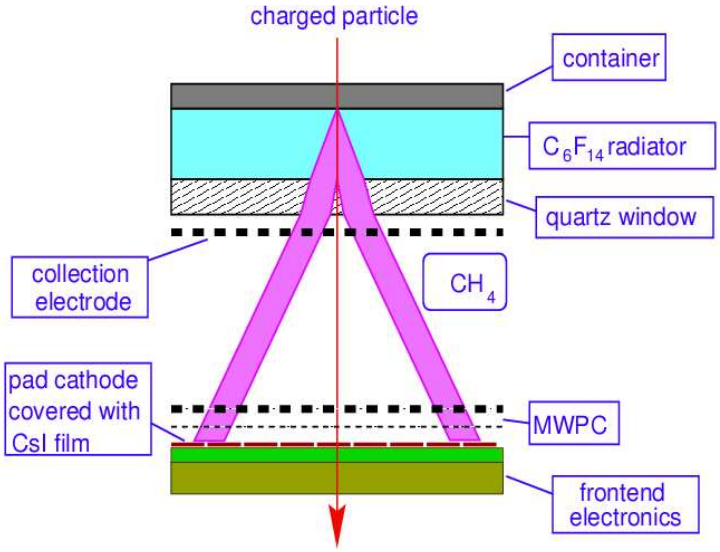

Fig. 2.8: Working principle of a RICH detector employing CsI thin films deposited onto the cathode plane of a MWPC. The Cherenkov cone refracts out of the liquid radiator of C_6F_{14} and expands in the proximity volume of CH_4 before reaching the MWPC photon detector. Electrons released by ionising particles in the proximity gap are prevented to enter the MWPC volume by a positive polarization of the collection electrode close to the radiator.

The principal requirements on PHOS include the ability to identify photons, discriminate direct photons from decay photons and perform momentum measurements over a wide dynamic range with high energy and spatial resolutions.

Since it is sensitive also to charged particles, a Charged–Particle Veto (CPV) has to be placed in front of the calorimeter.

The PHOS, made of $PbWO_4$ crystals, is positioned on the bottom of the ALICE setup, it will cover approximately a quarter of a unit in pseudo-rapidity, $-0.12 \leq \eta \leq 0.12$, and 100° in azimuthal angle.

2.2.2 The external detectors

Zero Degree Calorimeter (ZDC)

The observable most directly related to the geometry of a ion–ion collision is the number of participant nucleons, which can be estimated by measuring the energy carried in the forward direction (at zero degree relative to the beam direction) by non-interacting (spectator) nucleons. The zero degree forward energy decreases with increasing centrality. The spectator nucleons will be detected in ALICE by means of Zero Degree Calorimeters (ZDC) [11].

In the ALICE experiment, the ZDCs will be placed at 116 m from the Interaction Point (IP): at this distance, the spectator protons are spatially separated from neutrons by the magnetic elements of the LHC beam line D1 as shown in Fig. 2.9. Therefore two distinct detectors will be used: one for spectator neutrons (ZN), placed at zero degrees relative to the LHC axis, and one for spectator protons (ZP), placed externally to the outgoing beam pipe on the side where positive particles are deflected as shown in Fig. 2.9 and Fig. 2.10. It is foreseen to employ two identical sets of calorimeters on both sides of the interaction point to improve the impact parameter resolution.

The quartz fiber calorimetry technique, first developed in NA50 [12], has been adopted for the ALICE ZDC. The shower generated by incident particles in a dense absorber (the so-called "passive" material) produces Cherenkov radiation in quartz fibers ("active" material) interspersed in the absorber. This technique fulfills two fundamental requirements. Firstly, due to the small amount of space available (particularly for the neutron calorimeter), the detectors must be compact and therefore a very dense passive material must be used for the absorber to contain the shower. Secondly, the ZDC will operate in a very high radiation environment (about 10^4 Gy/day is the estimated dose for the neutron calorimeter at a luminosity of 10^{27} cm^{-2} s^{-1}): radiation hardness is guaranteed by the radiation resistance of the quartz fibers. Furthermore, the Cherenkov effect has two more advantages: it pro-

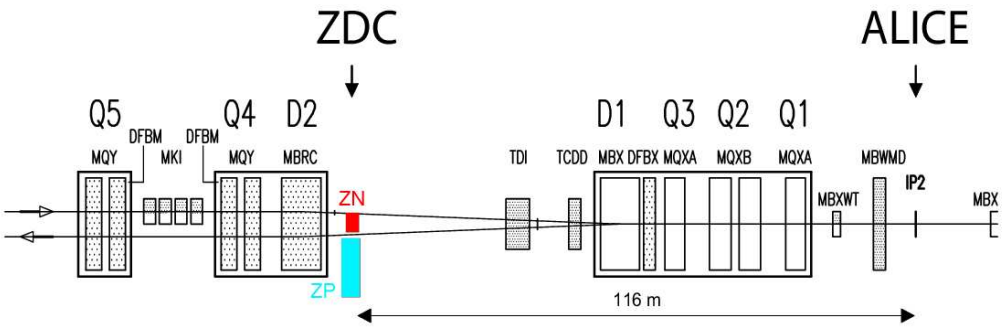

Fig. 2.9: Schematic top view of the beam line and of the ZDCs location.

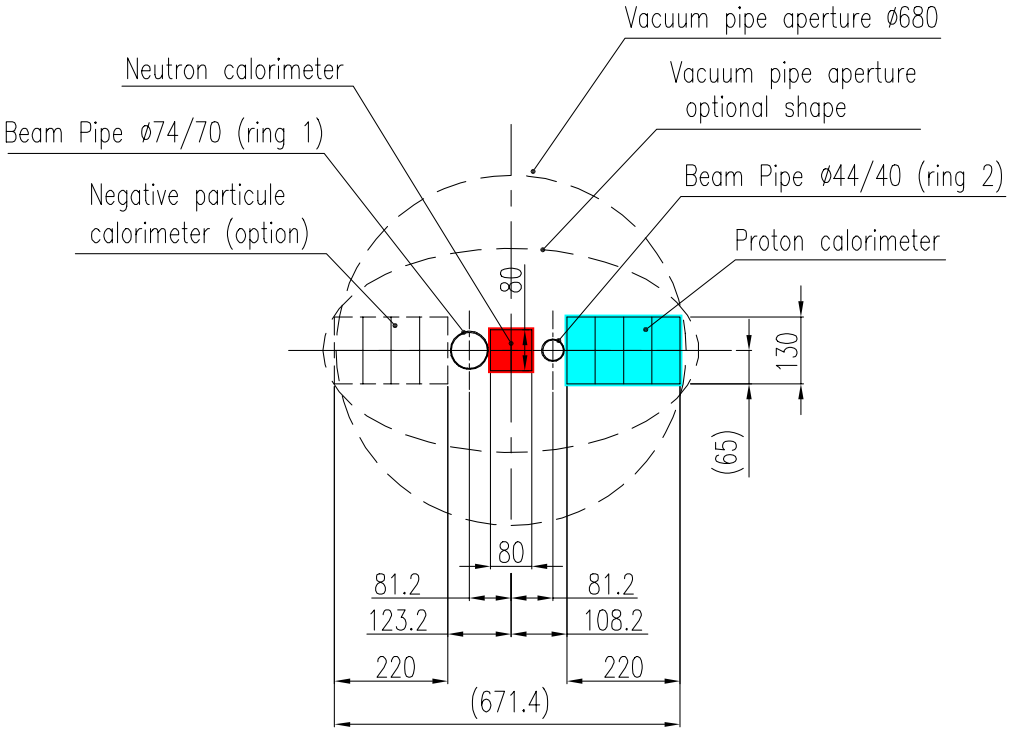

Fig. 2.10: Cross section of the beam line 116 m from the IP.

vides a very fast signal due to the intrinsic speed of the emission process and a very low sensitivity to induced radioactivation thanks to its threshold behaviour.

Table 2.2 summarizes the principal characteristics of the ZDC for protons (ZP) and for neutrons (ZN).

	ZN	ZP
Dimensions (cm^3)	$7.04 \times 7.04 \times 100$	$12 \times 22.4 \times 150$
Absorber	tungsten alloy	brass
$\rho_{absorber}$ (g cm^{-3})	17.61	8.48
Fiber core diameter (μm)	365	550
Fiber spacing (mm)	1.6	4
Filling ratio	1/22	1/65

Tab. 2.2: Dimensions and main characteristics of absorber and quartz fibers for neutron and proton calorimeters.

The ZDC project includes a forward electromagnetic calorimeter to improve the centrality trigger. It is designed to measure, event–by–event, the energy of electromagnetic particles emitted at forward rapidities, essentially photons generated from π^0 decays.

The detection technique employed for the electromagnetic calorimeter is the same as the one used for the hadronic calorimeters.

Photon Multiplicity Detector (PMD)

The PMD [13] is designed to measure the multiplicity and the spatial distribution (η–φ) of photons on an event–by–event basis in the rapidity region $2.31 < \eta < 3.5$. The PMD addresses physics issues related to event-by-event fluctuations, flow and formation of Disoriented Chiral Condensates (DCC) and provides estimates of transverse electromagnetic energy and the reaction plane on an event-by-event basis.

Measurement of photon multiplicity in the high particle density environment of ALICE requires optimization of granularity and converter thickness so that overlap of photon showers is minimum.

The PMD consists of two identical planes of gas detectors with a 3 X_0 thick lead converter in between them as shown schematically in Figure 2.11; the converter thickness is optimized such that the conversion probability of photons is high and the transverse size of the shower is small, in order to reduce occupancy. The front detector plane is used for vetoing charged-particle hits. The detector plane behind the converter is the preshower plane which registers hits from both photons and charged hadrons.

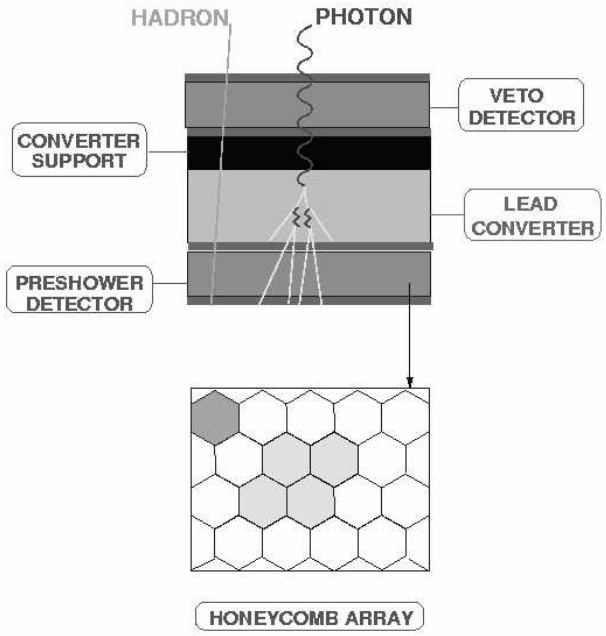

Fig. 2.11: PMD working principle.

It will be mounted on the L3 magnet door, on the opposite side with respect to the Muon Spectrometer, at 3.6 m from the interaction point (see Figure 2.12).

Forward Multiplicity Detector(FMD)

The main functionality of the FMD [4, 14] is to provide charged particle multiplicity information in the pseudo-rapidity range -3.4< η <-1.7 and 1.7< η <5.1 over the full azimuth.

The FMD will allow for the study of multiplicity fluctuations on an event-by-event basis and for flow analysis in the considered pseudo-rapidity range. Together with the pixel system of the ITS, the FMD will provide early charged particle multiplicity distributions for all collision types in the range -3.4< η <5.1.

The FMD consists of mosaics of silicon pad detectors organized in 5 rings located near to the beam pipe, on both sides of the interaction point, as shown in Figure 2.12. Overlap between the various rings and with the ITS inner pixel layer provides redundancy and important checks of analysis procedures.

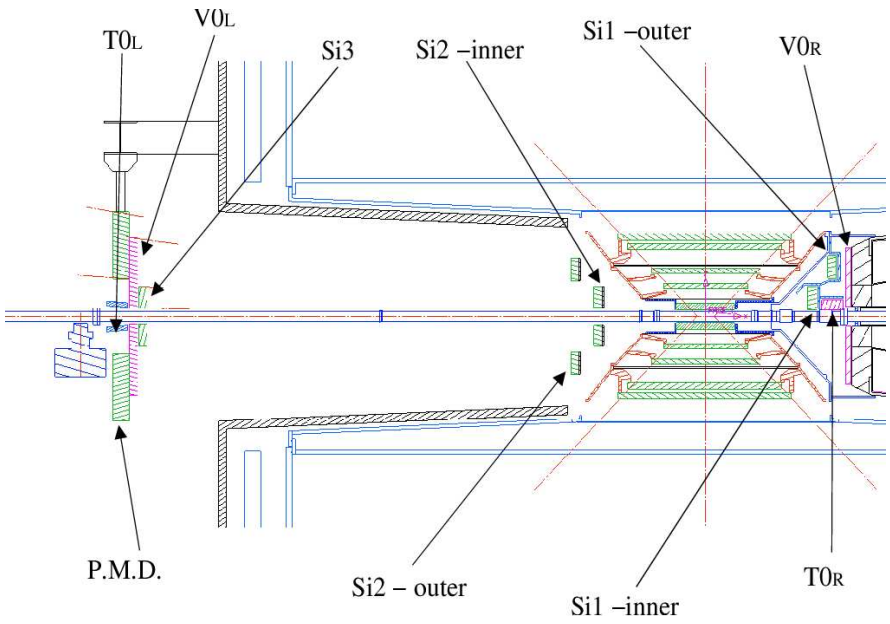

Fig. 2.12: Localization of the forward detectors: the PMD, the FMD (Si1, Si2 and Si3), the V0 and the T0.

T0

T0 detector [4, 14] is foreseen for the determination of event time. It has to perform the following functions:

- to generate a T0 signal (with 50 ps precision) for the TOF detector. This timing signal corresponds to the real time of the collision (plus a fixed time delay) and does not depend on the position of the vertex;
- to measure the vertex position (with a precision $\pm$1.5 cm) for each interaction and to provide a Level 0 trigger[1] when the position is within the preset values to discriminate against beam-gas interactions;
- to provide an early 'wake-up' signal to the TRD, prior to L0;
- to measure the particle multiplicity.

The detector consists of two arrays of Cherenkov counters with 12 counters per array: $T0_L$ (T0 Left) is placed at 350 cm from the interaction point and covers the rapidity range -5$\leq \eta \leq$-4.5, while $T0_R$ (T0 Right) is placed

[1]The ALICE trigger organized into levels, details will be given in Section 2.3

at 70 cm on the opposite side and covers the rapidity range $2.9 \leq \eta \leq 3.3$ (see Figure 2.12).

V0

To improve the ALICE Trigger System, the V0 detector [4, 14] has been proposed to identify the interaction vertex. Another important task is to reject the beam–gas background.

The V0 detector will also provide:

- a minimum bias trigger for the central barrel detectors;
- two centrality triggers in Pb–Pb collisions;
- a centrality indicator;
- a control of the luminosity;
- a validation signal for the Muon Trigger to filter the background in p–p mode [15].

The V0 is made of two scintillator hodoscopes located asymmetrically on each side of the interaction point: the $V0_R$ is fixed at the front face of the Muon Spectrometer front absorber, 90 cm from the vertex while the $V0_L$ is located on the opposite side 340 cm from the vertex as shown in Figure 2.12.

2.3 ALICE Trigger System

The challenge for the ALICE trigger [16] is to make optimum use of the component detectors, which are busy for widely different periods, and to perform trigger selections in a way which is optimised for several different running modes: ion–ion (Pb–Pb and several lighter species) and p–p, having a range of a factor 30 in counting rate.

In p–p collisions, the trigger allows the acquisition of "minimum bias" events, with the possibility to assign priority to certain category of events. To allow a single–event analysis in proton–proton, the trigger electronics has been designed to work with the 40 MHz LHC clock. In ion running mode, the trigger must select events depending on the centrality information from the ZDCs and the other forward detectors.

In addition, the Muon Trigger System will indicate the events with two unlike–sign muons assigning a special priority in case of muon p_t greater then 2.3 GeV/c to acquire events where the Υ production is more probable. The Muon Trigger System will be treated in more detail in Section 3.3.

Another feature of the ALICE environment is that the high multiplicities make events containing more than one central collision unreconstructable. For this reason, past-future protection is an important part of the ALICE trigger, thus checking for each sub–detector that no second event occurs during the readout or drift time of the device.

To perform these features, the ALICE Trigger System is organized into three levels:

1. Level 0 (L0). The first response from the trigger system has to be fast (~ 1.2 μs) in order to strobe the detectors working in track–and–hold mode (HMPID, PHOS, ITS Strip and dimuon tracking): for this reason it is placed in the underground area to reduce the cable delay.

   The L0 Trigger is based on the information from the forward detectors and the Dimuon Trigger. It must select events with vertex close to the nominal interaction point, with track number of at least 100 in the central acceptance and with a forward–backward tracks distribution compatible with a colliding beam interaction.

   The L0 rate ranges between 10^4 and few times 10^4 Hz, depending on the beam type and luminosity.

2. Level 1 (L1). The L0 signal is too fast to receive all the trigger inputs, while the L1 signal, sent at 6.5 μs, picks up all remaining fast inputs (TRD, FMD and ZDC) and reduces the rate at about 1 kHz. The L1 strobes all remaining detectors and starts the readout of the Front End Electronics (FEE).

3. Level 2 (L2). The final level of the trigger occurs about 88 μs after the interaction: this latency is essentially imposed by the drift time in the TCP to avoid pile–up. The maximum L2 rate is constrained by the Data Acquisition System (DAQ) bandwidth set at 1.25 GBytes/s.

The trigger and DAQ systems must balance the capacity to record central collisions which generate large events with the ability to acquire the largest possible fraction of rare events such as dimuon or dielectron events.

2.3.1 High–Level Trigger (HLT)

The measurements in the ALICE experiment cover basic observables such as particle production and correlations as well as probes such as open charm and beauty, quarkonia production, direct photons and jets. Most of the probes are rare signals requiring the exploitation of all the available luminosity, which makes it necessary to sift through all interactions at a rate of about

8 kHz for Pb–Pb. The first level Trigger Systems of the Muon Spectrometer and the TRD select muon and electron candidates quite efficiently, but the remaining data rate is still far higher than what can be transferred to the permanent storage system. The High–Level Trigger (HLT) system [17] rejects fake events by sharpening the momentum cut in the Muon Spectrometer, by improving the particle identification, momentum resolution and impact parameter determination for TRD electron candidates in the TPC or by filtering out low momentum tracks in the TPC. ALICE would not be able to acquire sufficient statistics for many rare probes without the HLT system.

The physics functionality of the HLT system can be summarised by the following three categories:

- Trigger: Accept or reject events based on detailed online analysis of physics observables, e.g. verify dielectron candidates after TRD L1 acceptance, sharpen dimuon transverse momentum cut or identify jets.
- Select: Select relevant parts of the event or regions of interest, e.g. remove pile-up in p–p, readout jet regions or filter out low momentum tracks.
- Compress: Reduce the amount of data required to encode the event information of the triggered and selected events as far as possible without loosing physics information.

The triggered event or selected regions of interest are finally compressed and then submitted to the event builders for permanent storage. In case of HLT reject, the event is discarded. An event is required to be triggered by L0 and accepted by both L1 and L2 in order to reach the HLT. The main difference between HLT and the lower trigger layers is the fact that there is no detector requirement imposing a maximum HLT latency, which is basically defined by trigger rate and available buffer space. Furthermore the HLT is the trigger layer allowing to combine the information of all ALICE subdetectors at one place.

References

[1] LHC Experimental Conditions, ALICE Internal Note, 2002-034

[2] I.R. Collins and O.B. Malyshev, LHC Project Note 274

[3] ALICE Collaboration, Technical Proposal, CERN/LHCC 95-71

[4] ALICE: Physics Performance Report, Volume I, J. Phys. G: Nucl. Part. Phys. 30 (2004), 1517–1763

[5] ITS Technical Design Report, CERN/LHCC 99-12

[6] TPC Technical Design Report, CERN/LHCC 2000-001

[7] PHOS Technical Design Report, CERN/LHCC 99-4

[8] A Transition Radiation Detector for Electron Identification within the ALICE Central Trigger- Addendum to the ALICE Technical Proposal, CERN/LHCC 99-13

[9] TOF Technical Design Report, CERN/LHCC 2000-12

[10] HMPID Technical Design Report, CERN/LHCC 98-19

[11] ZDC Technical Design Report, CERN/LHCC 99-5

[12] R. Arnaldi *et al.*, Nucl. Instr. and Meth. A 411 (1998) 1

[13] PMD Technical Design Report, CERN/LHCC 99-32

[14] ALICE Collaboration, Technical Design Report of the Forward detectors (2004) CERN/LHCC 2004-25

[15] B. Cheynis *et al.*, ALICE Internal Note ALICE/00-29

[16] ALICE Collaboration 2003 Technical Design Report of the Trigger, Data Acquisition, High–Level Trigger and Control System CERN/LHCC 2003-62

[17] A. Vestbo, High Level Trigger System for the LHC ALICE Experiment, ALICE-CA-2002-025

Chapter 3

The Muon Spectrometer and the Trigger System

3.1 Introduction

In year 1995, the ALICE collaboration proposed to upgrade the central detector with a Forward Muon Spectrometer.

Hard, penetrating probes, such as heavy quarkonia states, are an essential tool for probing the early and hot stage of heavy–ion collisions. At LHC energies, energy densities high enough to melt the Υ will be reached.

The complete spectrum of heavy quark vector mesons (i.e. J/ψ, ψ', Υ, Υ' and Υ''), as well as the ϕ meson, will be measured in the $\mu^+\mu^-$ decay channel by the ALICE Muon Spectrometer. The simultaneous measurement of all the quarkonia species with the same apparatus will allow a direct comparison of their production rate as a function of different parameters such as transverse momentum and collision centrality. In addition to vector mesons, also the unlike–sign dimuon continuum up to masses around 10 GeV/c^2 will be studied. Since at LHC energies, the continuum is expected to be dominated by muons from the semi-leptonic decay of open charm and open beauty, it will also be possible to study the production of open (heavy) flavours with the Muon Spectrometer.

As discussed in Chapter 2, the Muon Spectrometer will participate in the general ALICE data taking for Pb–Pb collisions at the machine–limited luminosity $\mathcal{L}$=10^{27} cm^{-2}s^{-1}. The situation is different for intermediate–mass ion collisions (e.g. Ar–Ar) where the luminosity limitations from the machine are less severe. In this case, beside a general ALICE run at low luminosity $\mathcal{L}$=10^{27} cm^{-2}s^{-1}, to match the TPC rate capability, a high luminosity one $\mathcal{L}$=10^{29} cm^{-2}s^{-1} is also foreseen, to improve the Υ statistics. For the high–

luminosity run, the Muon Spectrometer will take data together with a limited number of ALICE detectors (ZDC, ITS Pixel, PMD, T0, V0 and FMD) able to sustain the event rate. These detectors allow the determination of the collision centrality.

The main design criteria of the Spectrometer are driven by the following considerations:

- **High multitrack capability.** The tracking detectors of the Spectrometer must be able to handle the high particle multiplicity.
- **Large acceptance.** As the accuracy of dimuon measurements is statistics limited (at least for the Υ family), the Spectrometer geometrical acceptance must be as large as possible.
- **Low-p_t acceptance.** For the production of direct J/ψ, it is necessary to have a large acceptance at low-p_t since at high-p_t a large fraction of J/ψ is produced via B decay.
- **Forward region.** Muon identification in the heavy–ion environment is only feasible for muon momenta above $\sim$4 GeV/c because of the large amount of material (absorber) required to reduce the flux of hadrons. Hence, measurement of low-p_t charmonia is possible only at small angles where muons are Lorentz boosted.
- **Invariant-mass resolution.** A resolution of 70 (100) MeV/c^2 in the 3 (10) GeV/c^2 dimuon invariant–mass region is needed to resolve the J/ψ and ψ' (Υ , Υ' and Υ'') peaks.
- **Trigger.** The spectrometer has to be equipped with a selective dimuon trigger system to match the maximum trigger rate of about 1 kHz handled by the DAQ.

The Muon Spectrometer is designed, considering the criteria listed above, to detect muons in the polar angular range 2°–9°. This interval, limited at small angles by the space needed for the beam shield protecting the chambers from background, is a compromise between low-p_t acceptance and detector cost and corresponds to the pseudo-rapidity range of $-4.0 \leq \eta \leq -2.5$.

In this angular range we are still in the rapidity plateau of heavy quarkonia production; furthermore, the higher momenta hadrons (π and K) emitted at small angles have lower decay probability so that the number of muons not coming from heavy quarkonia decays is also reduced in this angular range.

Thanks to the forward geometry, heavy quarkonia detection will be extended down to p_t=0 in order to measure the production of direct J/ψ in a p_t range where the production via B decay is not relevant.

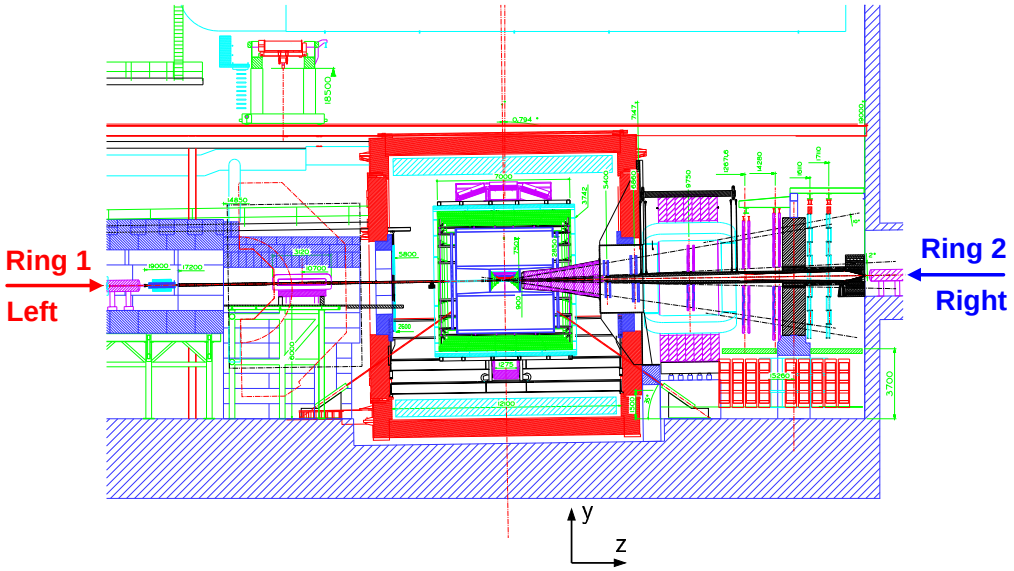

Fig. 3.1: Longitudinal section of the ALICE experimental region.

The layout of the Muon Spectrometer [1,2], as shown in Fig. 3.1 and 3.2, consists of the following components:

- a large dipole magnet placed outside the L3 magnet;
- a passive front absorber for hadrons and photons coming from the interaction vertex;
- an inner beam shield to protect the chambers from particles and secondaries produced at large rapidities.
- a high-granularity tracking system composed of 10 detection planes organized in 5 stations;
- a passive muon filter situated at about 15 m from the IP;
- four planes of trigger chambers organized in two stations.

The main parameters of the Muon Spectrometer are summarised in Table 3.1 and will be discussed in detail in Section 3.2.

The idea is to reconstruct the tracks of two unlike–sign muons measuring their momenta and the angle between the two tracks to calculate the invariant mass distribution, as can be seen in Fig. 3.3.

The required mass resolution (70 MeV/c^2 in the J/ψ mass region and 100 MeV/c^2 in the Υ mass region is essentially determined by the precision in

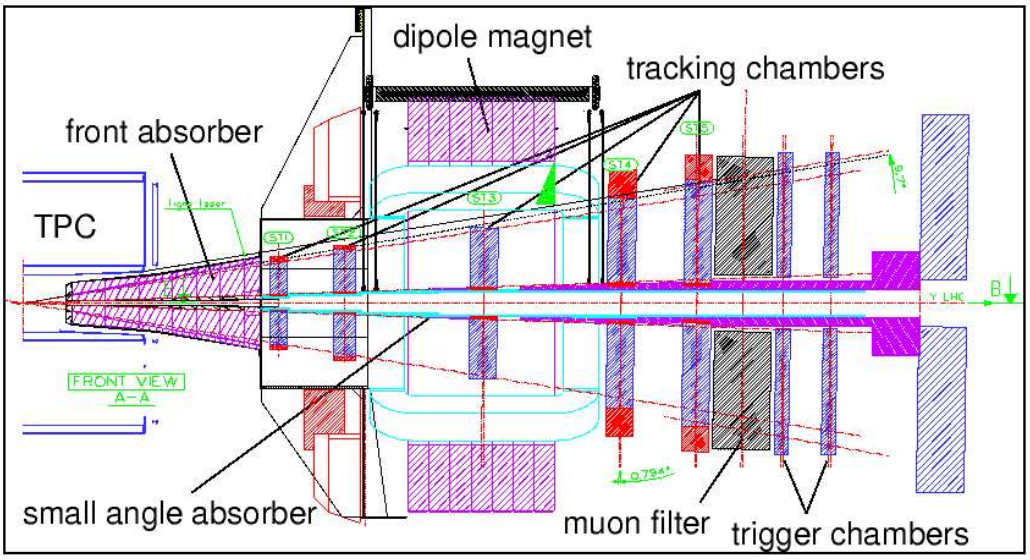

Fig. 3.2: General Layout of the ALICE Muon Spectrometer.

the measurement of the angle between the two muons and of their momenta, precision which is strictly tied to the bending strength of the spectrometer magnet as well as to the position resolution of the tracking system and to the position and composition of the front absorber. The last one has to attenuate the enormous flux of particles coming out from Pb–Pb interactions (up to 15000 particles in a forward cone of 15° for central collisions [3]) in order to allow efficient track finding and two-track resolution.

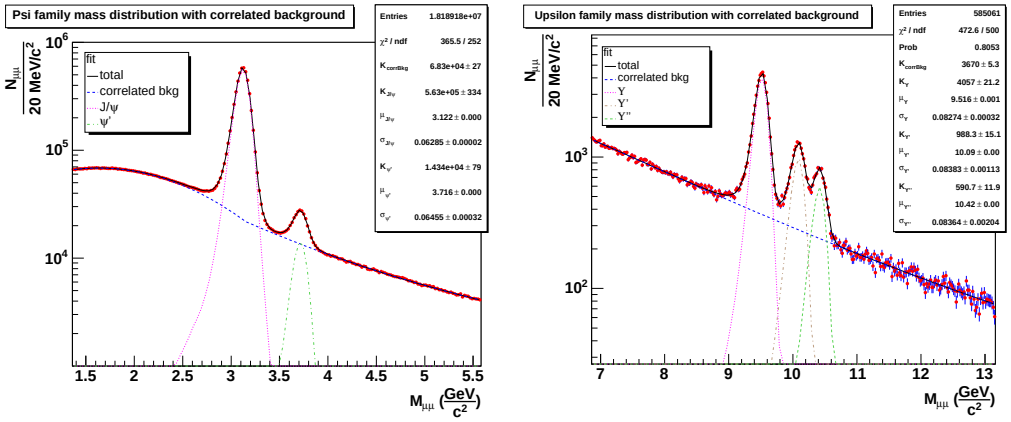

(a) J/ψ family (b) Υ family

Fig. 3.3: Mass distribution of unlike–sign dimuons by simulation. The correlated background is due to muon pairs both coming from beauty decays.

Muon detection		
Polar, azimuthal angle coverage	$2^\circ \leq \theta \leq 9^\circ$, 2π	
Minimum muon momentum	$4\,\mathrm{GeV}/c$	
Resonance detection	J/ψ	Υ
Pseudo-rapidity coverage	$-4.0 \leq \eta \leq -2.5$	$-4.0 \leq \eta \leq -2.5$
Transverse momentum range	$0 \leq p_\mathrm{t}$	$0 \leq p_\mathrm{t}$
Mass resolution	70 MeV	100 MeV
Front absorber		
Longitudinal position (from IP)	$-5030\,\mathrm{mm} \leq z \leq -900\,\mathrm{mm}$	
Total thickness (materials)	$\sim 10\lambda$ (carbon–concrete–steel)	
Dipole magnet		
Nominal magnetic field, field integral	0.7 T, 3 T m	
Free gap between poles	2.972–3.956 m	
Overall magnet length	4.97 m	
Longitudinal position (from IP)	$-z = 9.87$ m (center of the dipole yoke)	
Tracking chambers		
No. of stations, no. of planes per station	5, 2	
Longitudinal position of stations	$-z = 5\,357, 6\,860, 9\,830, 12\,920, 14\,221$ mm	
Anode–cathode gap (equal to wire pitch)	2.1 mm for st. 1; 2.5 mm for st. 2–5	
Gas mixture	80 %Ar/20 %CO_2	
Pad size st. 1 (bending plane)	$4 \times 6,\ 4 \times 12,\ 4 \times 24\,\mathrm{mm}^2$	
Pad size st. 2 (bending plane)	$5 \times 7.5,\ 5 \times 15,\ 5 \times 30\,\mathrm{mm}^2$	
Pad size st. 3, 4 and 5 (bending plane)	$5 \times 25,\ 5 \times 50,\ 5 \times 100\,\mathrm{mm}^2$	
Max. hit dens. st. 1–5 (central Pb–Pb)	$5.0, 2.1, 0.7, 0.5, 0.6 \cdot 10^{-2}\,\mathrm{hits/cm}^2$	
Spatial resolution (bending plane)	$\simeq 70\,\mu$m	
Tracking electronics		
Total no. of FEE channels	1.09×10^6	
Shaping amplifier peaking time	$1.2\,\mu$s	
Trigger chambers		
No. of stations, no. of planes per station	2, 2	
Longitudinal position of stations	$-z = 16\,120, 17\,120$ mm	
Total no. of RPCs, total active surface	72, $\sim 150\,\mathrm{m}^2$	
Gas gap	single, 2 mm	
Electrode material and resistivity	Bakelite, $\rho = 1$–$8 \times 10^9\,\Omega\,$cm	
Gas mixture	$\mathrm{Ar}/\mathrm{C_2H_2F_4}$/i-buthane/$\mathrm{SF_6}$ ratio 50.5/41.3/7.2/1	
Pitch of readout strips (bending plane)	10.6, 21.2, 42.5 mm (for trigger st. 1)	
Max. strip occupancy bend. plane	3 % in central Pb–Pb	
Max. strip occupancy non bend. plane	10 % in central Pb–Pb	
Maximum hit rate on RPCs	3 (24) Hz/cm^2 in Pb–Pb (Ar–Ar)	
Trigger electronics		
Total no. of FEE channels	2.1×10^4	
No. of local trigger cards	$234 + 2$	

Tab. 3.1: Summary of the main characteristics of the muon spectrometer

3.2 Muon Spectrometer layout

In this section functionalities and structure of spectrometer components will be examined. The Trigger System will be described in the next Section.

3.2.1 Dipole Magnet

The dipole magnet (see Fig. 3.4) will provide the bending power needed to measure the momenta of muons. It is a warm magnet 5 m long, 6.6 m wide and 8.6 m high, with a central field of 0.7 T. The field lines are oriented in the vertical direction perpendicular to the beam axis. The yoke is made of seven steel planes and the coils are of hollow aluminum for the cooling liquid.

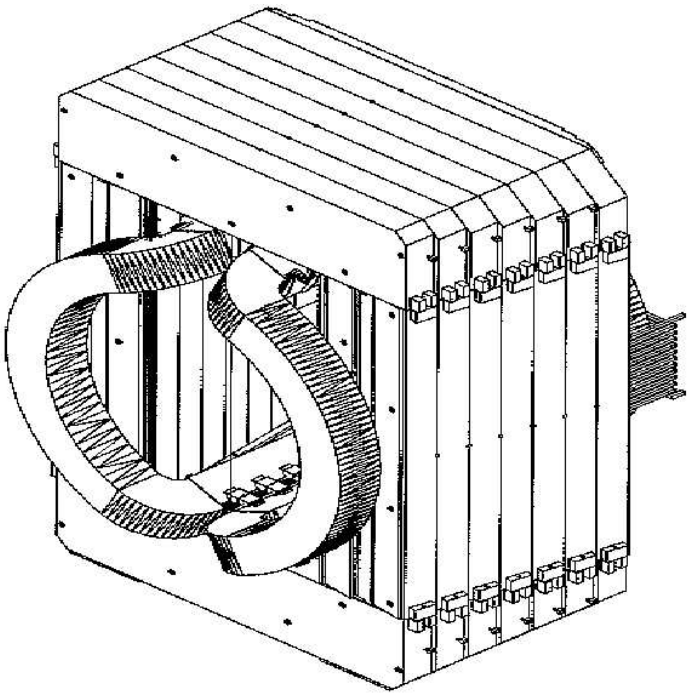

Fig. 3.4: General view of the dipole magnet.

Since the magnet location is adjacent to the large L3 solenoid, the interference between the two devices is important: to provide the data for the particle track analysis, the magnetic field of both magnets has been mapped in the entire detector space [4]. The measured field profile is reported in Fig. 3.5.

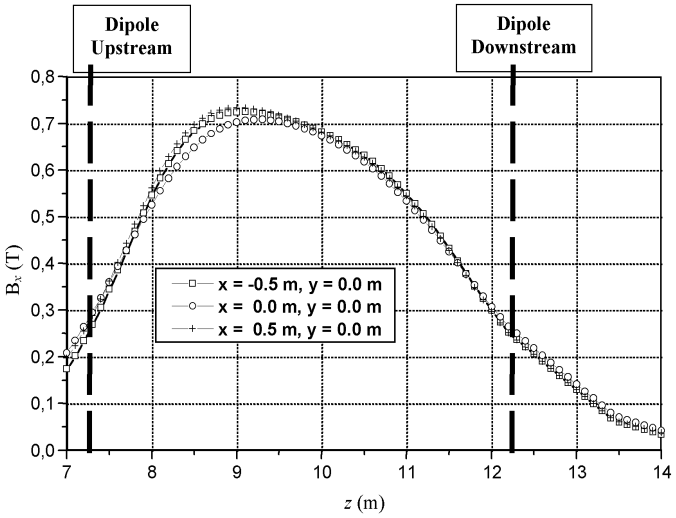

Fig. 3.5: Magnetic field profile along the beam direction for different XY position in the plane.

3.2.2 Front Absorber

The front absorber (see Fig. 3.6) is composed by a central cone 4.13 m long (corresponding to 10 interaction length) starting at 90 cm from the IP.

As said in the previous Section, the absorber has to reduce the particle flux on the tracking chambers down to 10^{-2} hits/cm^2 in central Pb-Pb collisions, which is the upper limit for track finding and two–track resolution. Moreover, this filter will allow to reduce the background due to decay muons by limiting the free path of pions and kaons.

Constituent material, radius, depth and position have been optimized in order to satisfy the above requirements, to minimize the back–scattering towards the TPC and to fulfill the mass resolution needs. In fact, due to energy loss fluctuations and multiple scattering, the presence of the absorber reduces the precision of angle and momentum measurements and the error increases with increasing absorber thickness and closeness to the IP.

The first section, 225 cm long, is made of carbon that, due to its low Z, limits the multiple scattering. The second section, far from the vertex, is made of more economic concrete. The rear section is made of 20 cm of lead interleaved with layers of borated polyethylene, which is very effective in moderating and absorbing neutrons. Due to the high Z of the rear section, which is responsible for a large amount of multiple scattering, the angle of the muon tracks will be calculated by combining the position measured with

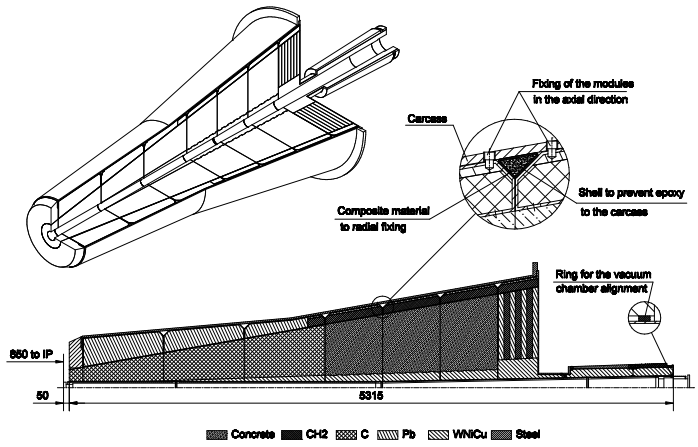

Fig. 3.6: Conceptual design of the front absorber.

the first tracking chamber and the one measured with the position of the interaction point. The last plates are made in copper instead of lead in order to reduce radiative losses of high–momenta muons, which could create electron–positron pairs into the first tracking chamber.

In addition, the front absorber is shielded outside the spectrometer acceptance (for θ >10°) with lead, tungsten and borated polyethylene to reduce particle back–scattering towards the TPC.

3.2.3 Small angle absorber

The spectrometer is shielded throughout its length by a dense absorber tube surrounding the beam pipe. It has to protect the tracking chambers from background arising from the interactions of particles emitted after collisions with the beam pipe wall.

It has an 'open' geometry with a steel outer shield 4 cm thick (see Fig. 3.7). The section nearest to the vertex is made of tungsten, while the section far from the vertex is made of lead. Geometry and materials have been chosen according to needs connected with the internal vacuum chamber.

The structure of the absorber terminates with an iron plug (1.1 m in diameter and 1 m thick), which protects the trigger stations against background particles coming from the Ring 2 side (see also Fig. 3.8 and Fig. 3.1).

3.2.4 Tracking chambers

In order to achieve the desired mass resolution of 70 (100) MeV/c^2 in the J/Ψ (Υ) mass region, the tracking detectors have to fulfill the following

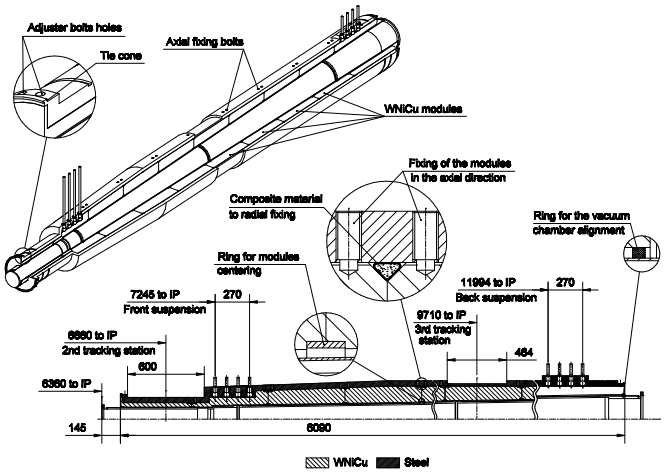

Fig. 3.7: Conceptual design of the small angle absorber.

requirements:

- a spatial resolution <100 μm in the bending plane to achieve a muon momentum resolution $\delta p/p < 1\%$;
- a resolution of about 2 mm in the non–bending plane, to reconstruct the angle of the muons and to guarantee an efficient track–finding;
- an average material thickness less than 3 X_0 to minimize multiple scattering;
- to cover a total area of about 100 m^2;
- to operate efficiently at hit densities up to 5×10^{-2} cm^{-2};
- low sensitivity to photon and neutron background;
- a detection efficiency $\geq$95%.

All these requirements can be fulfilled by the use of wire chambers with segmented cathode analogical readout: Cathode Pad Chambers (CPC) and Cathode Strip Chambers (CSC). The chambers are arranged in five stations: two are placed before, one inside and two after the dipole magnet. Each station is made of two planes of chamber. Each chamber has two cathode planes, which are both readout to provide two–dimensional hit information. The system will give redundant informations and can work even if one of the ten planes malfunctions. The stations are arranged in a projective geometry

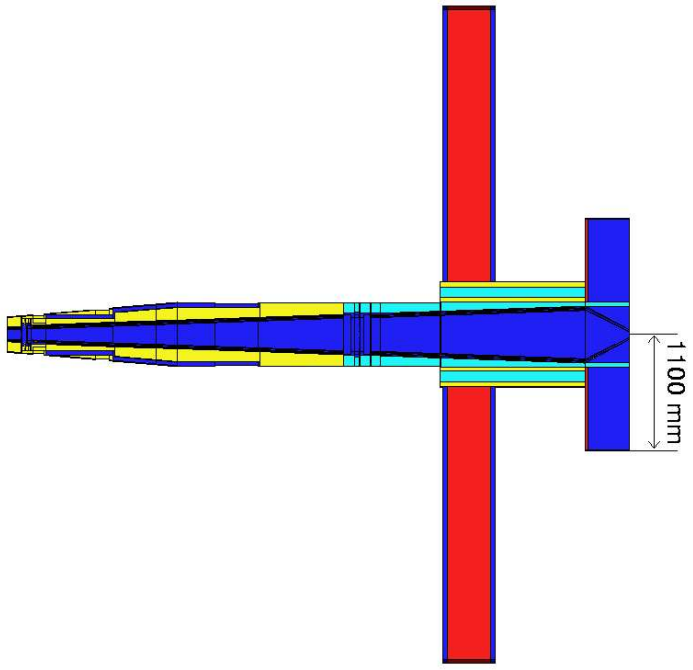

Fig. 3.8: Longitudinal section of the small angle absorber and of the muon filter (in red, described in Section 3.2.5).

with an acceptance higher than the one of the spectrometer, in order to take into account the dipole bending.

To keep the occupancy at a 5% level, a large segmentation of the readout pads is needed. For instance, pads as small as 4.2×6 mm^2 are needed for the region of the first station close to the beam pipe, where the highest multiplicity is expected. Since the hit density decreases with the distance from the beam, larger pads are used at larger radii. This enables keeping the total number of channels to about 1 million.

Multiple scattering of the muons in the chambers is minimised by using composite materials (e.g. carbon fibre). The chamber thickness corresponds to about 0.03 X_0, giving a total thickness of 3 X_0.

Because of the different size of the stations (ranging from few square meters for station 1 to more than 30 m^2 for station 5), two different designs have been adopted. The first two stations are based on a quadrant structure, with the readout electronics distributed on their surface: the layout of station 1 is reported in Fig. 3.9. Due to the tight space and to the heat dissipated by the FEE mounted on the external surface of the chambers (a total of 4 kW), a cooling system with circulating water will be implemented and air circulation will be forced by means of fans.

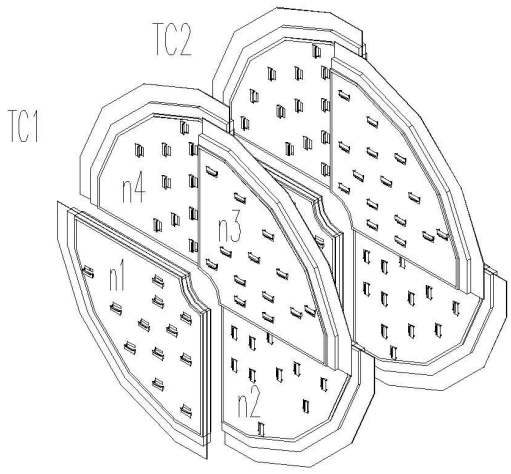

Fig. 3.9: Layout of the tracking station 1.

For the other stations, a slat architecture has been chosen, as shown in Fig. 3.10. The maximum size of the slat is 40×280 cm^2 and the electronics is implemented on the side of the slats. The slats overlap to avoid dead zones on the detector.

The FEE is made of Multi-Chip Modules (MCMs) each comprehending four 16-channel Multiplexed ANAlog Signal-processor (MANAS-16) chips, two 12-bit ADCs and a Muon-Arm Readout Chip (MARC).

Extensive tests on small–sized and full–sized tracking chamber prototypes (both for quadrant and slat architecture) have shown that these detectors achieve the required performances. In particular, spatial resolutions of the order of 70 μm have been measured.

3.2.5 Muon filter

While the front absorber and the beam shield are sufficient to protect the tracking chambers, additional protection (muon filter) is needed for the trigger chambers. For this reason, an iron wall $5.6\times5.6\times$ m^2 and 1.2 m thick (7.2 λ_{int}) is placed beyond the last tracking chamber, in front of the first trigger chamber. Front absorber and muon filter stop muons with momentum less than 4 GeV/c.

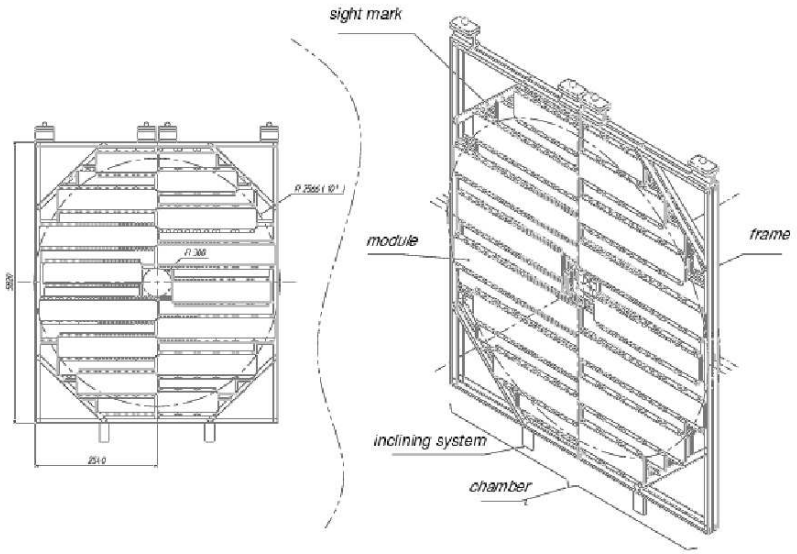

Fig. 3.10: Scheme of tracking stations 4 and 5 with detector modules and frames.

3.3 Trigger system

The trigger system will select interactions containing events with muon pairs from the decay of heavy quarkonium resonances. Moreover, muons come from several sources: decay of low mass resonances (η, ω, ρ, ϕ), decay of open charm and beauty mesons and decay of kaons and pions. At the LHC energies, the high mass dimuon continuum from the Drell–Yan process (important at SPS energies) will be drowned by the muon pairs from semi–leptonic D and B decays. In spite of the range of momenta selected by the spectrometer angular acceptance, a high number of background muons reaches the trigger stations, so that a simple trigger selection based on the presence of two muons is not sufficient.

The average number of muons in the spectrometer acceptance as a function of their transverse momentum is shown in Fig. 3.11 for a central Pb–Pb collision. As can be seen, muons from π and K decays are in the low-p_t region. To have an acquisition rate lower than 1 kHz (the maximum allowed by the DAQ bandwidth) it is necessary to reduce the probability of triggering on events where these low-p_t muons are not accompanied by the high-p_t ones emitted in the decay of heavy quarkonia (or in the semi-leptonic decay of open charm end beauty).

This is done by applying a p_t cut at the trigger level on each individual

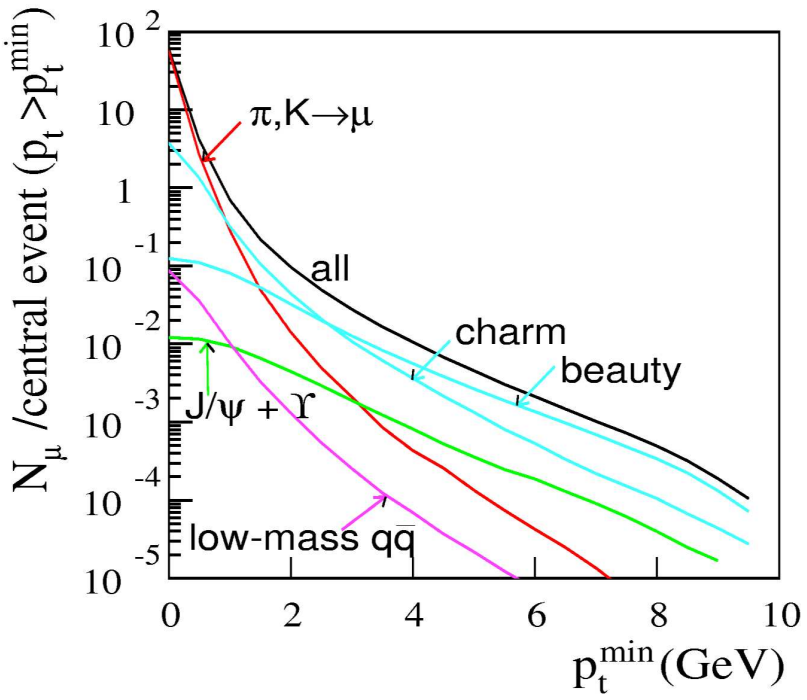

Fig. 3.11: Average number of muons per central Pb-Pb collision with $p_t \geq p_t^{min}$ as a function of p_t^{min} in the range $2.5 < \eta < 4$.

muon.

A dimuon trigger signal is issued when at least two tracks above the predefined p_t threshold are detected in one event. According to simulation results, a low-p_t cut (1 GeV/c) will be used for J/ψ and a high-p_t one (2 GeV/c) for Υ selection.

To perform the p_t selection, a position–sensitive trigger detector with spatial resolution better than 1 cm is required. This resolution is achieved by Resistive Plate Chambers (RPCs) operated in streamer mode. The details on the Trigger detector and on the operating mode will be given in Chapter 4 and Chapter 5.

The trigger system consists of four RPC planes arranged in two stations (MT1 and MT2), one meter apart from each other, placed behind the muon filter at 16 and 17 m from the IP. The total active area is about 150 m^2. Each plane of the trigger stations is made of 18 single–gap RPCs, equipped with two orthogonal strip planes (X and Y) and with a specifically designed Front End Electronic. The horizontal strips measure the bending deviation due to the dipole magnetic field, and the position in the non–bending direction is provided by the vertical strips. By convention, the X strips are horizontal

and measure the deviation along the Y axis (and vice versa for the Y strips).

The active area covered by the first station is 6.12×5.44 m^2 and for the second, arranged in a projective geometry with a ratio of 17 to 16, is 6.50×5.78 m^2. The larger dimension of the detection planes is along the vertical direction, namely in the bending plane, where the acceptance of the system extends from 2° up to 10.8°, while in the non-bending plane it ranges from 2° to 9.6°. Each detection plane is divided in two halves along the vertical direction, each made of 9 chambers (see Fig. 3.12). Dimensions and active surface for each chamber of MT1 and MT2 are listed in Table 3.2. Modules 4 and 6 have a modified shape and module 5 is smaller, in order to accommodate the beam shield. To avoid inactive zones, the RPCs are positioned on the mechanical structure on two parallel planes, to allow superposition of active and dead areas. The half–planes are hanged to a superstructure by means of rails and they can run along the X axis, to ease assembly and revision operations.

Chamber	External dimensions	Active surface
MT1, chamber 5	2230 × 720 mm^2	2210 × 680 mm^2
MT1, chamber 1÷4 and 6÷9	2740 × 720 mm^2	2720 × 680 mm^2
MT2, chamber 5	2376 × 765 mm^2	2356 × 725 mm^2
MT2, chamber 1÷4 and 6÷9	2920 × 765 mm^2	2900 × 725 mm^2

Tab. 3.2: External dimensions and active surface for the RPC modules of the trigger station.

3.4 The trigger algorithm

The principle of the transverse momentum cut on the tracks performed by the trigger is explained in Fig. 3.13. A muon created at the IP is bent by the dipole field and hits MT1 and MT2 in (X_1,Y_1) and (X_2,Y_2) respectively. If the deviation angle θ_d is smaller than 10°, it is given by:

$$\theta_d = \frac{1}{Z_F}\left(\frac{Z_1 Y_2 - Z_2 Y_1}{Z_2 - Z_1}\right), \tag{3.1}$$

where Z_1 and Z_2 are the MT1 and MT2 positions along the beam axis, and Z_F corresponds to the center of the dipole magnet and it is equal to 9750 mm; Y_1 and Y_2 are the vertical coordinates (i.e. in the bending direction) measured by the trigger stations.

If the magnetic field B is constant, for a particle with a charge q and momentum in the bending plane p_{yz}, we have:

$$p_{yz} = |\frac{qBL}{\theta_d}|, \tag{3.2}$$

where L is the length of the dipole and we assumed $p=\sqrt{p_{yz}^2 + p_x^2} \approx p_{yz}$. For small emission angles θ_e we can write:

$$p_t = psin\theta_e \approx p_{yz}\theta_e. \tag{3.3}$$

By geometrical considerations, we can evaluate θ_e as follows:

$$\theta_e = \frac{\sqrt{X_F^2 + Y_F^2}}{Z_F}, \tag{3.4}$$

with $Y_F = Y_2 - \frac{(Y_2 - Y_1)(Z_2 - Z_F)}{Z_2 - Z_1}$ and $X_F = X_1 \frac{Z_F}{Z_1}$.

By entering equations 3.1, 3.2 and 3.4 in 3.3, we find that the transverse momentum can be evaluated from the impact points in the trigger stations:

$$p_t = qBL\frac{(Z_2 - Z_1)\sqrt{(X_F^2 + Y_F^2)}}{(Z_1 Y_2 - Z_2 Y_1)} \tag{3.5}$$

To carry out the p_t cut we introduce the deviation δy_2, defined as the deviation of a track with respect to an "infinite momentum" muon which hits the MT1 station in the same point hit by the real track and MT2 station at $y_{2,\infty}$:

$$\delta y_2 = y_2 - y_{2,\infty}. \tag{3.6}$$

For each hit on the MT1 station, it is possible to evaluate the deviation δy_2 which correspond to a given p_t threshold. The calculated values are stored in Look-Up Tables (LUT) and compared with the deviation measured in the bending direction, that is measured with the horizontal strips (X).

Since deviation will increase with the emission angle, as derived from equations 3.2 and 3.3, to keep the deviation (measured in strips) constant all over the detector area the strip widths parallel to the horizontal direction (X) vary from 1 cm close to the beam pipe to 4 cm at the borders. The informations from vertical strips (Y) are used to ensure that the tracks point back to the IP. Since the required resolution on the non-bending coordinate is less stringent, for the vertical strips (Y) only 2 cm and 4 cm widths are foreseen.

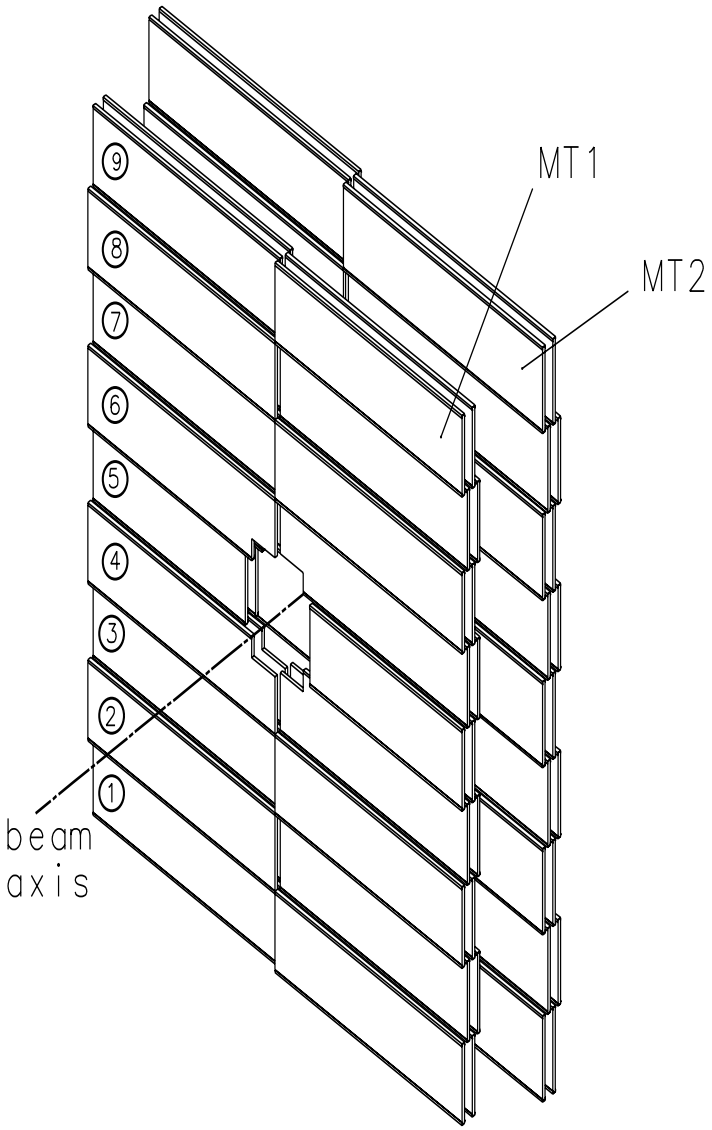

Fig. 3.12: Layout of the trigger stations.

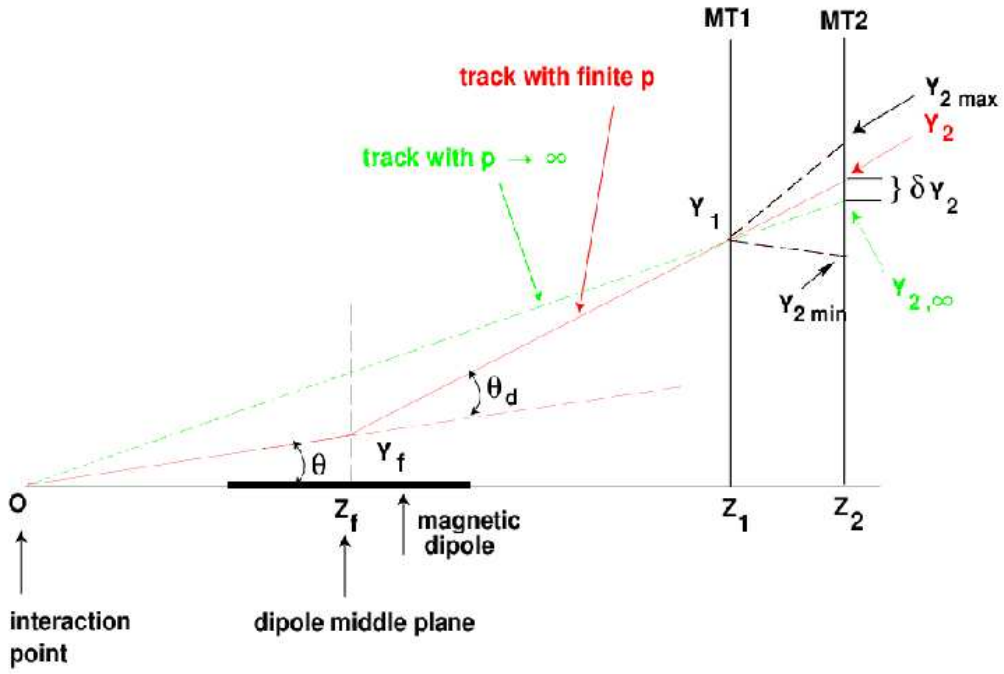

Fig. 3.13: The muon arm trigger principle: track projection on the bending plane.

3.5 The Trigger electronics

The Trigger Electronics has three main components:

- the Front End Electronics (FEE);
- the local trigger electronics;
- the regional and global trigger electronics.

The track selection is performed by the trigger electronics [5], which has to collect the information from the FEE on the RPCs in order to select unlike–sign tracks above the given p_t threshold. The general architecture of the trigger system is sketched in Fig. 3.14. The local trigger electronics (234 VME boards hosted in 16 crates placed close to the trigger stations) receives signals from the FEE to perform the trigger algorithm delivering a local L0 trigger in case of single tracks above low and high-p_t threshold. The regional and then global electronics collect the information of the various local board. A trigger is issued if at least two candidates pass the low (high) p_t threshold.

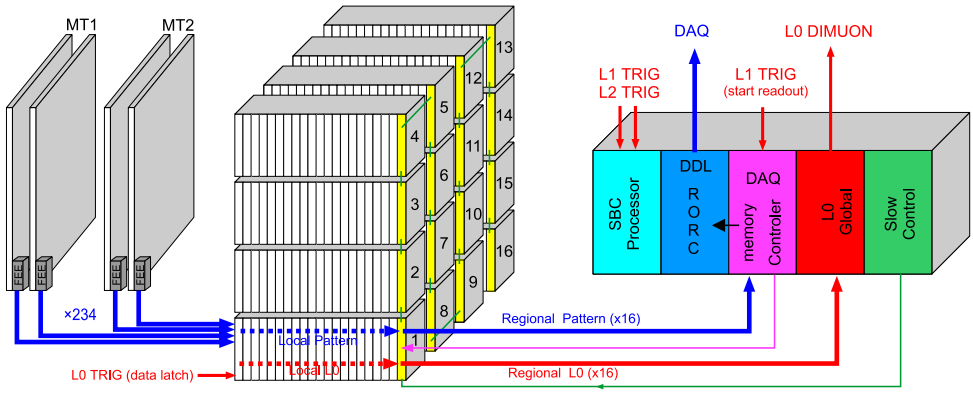

Fig. 3.14: Overview of the trigger system.

The trigger decision has to be delivered to the ALICE L0 trigger electronics in less than 800 ns after the event to strobe the signals of the muon tracking chambers. Since it is involved in the ALICE trigger decision, the trigger electronics has to work at the bunch–crossing frequency of 40 MHz foreseen for p–p collisions.

Front End Electronics (FEE)

The RPCs are equipped with a dual–threshold Front End Electronics (ADULT), designed to improve the timing properties of the detector. This

number of local trigger cards	234
decision time (fixed latency)	300 ns
working frequency	40 MHz
number of crates - 9U VME format	16

Tab. 3.3: Local trigger cards: main specifications.

technique, as it is strictly related to the RPC signal shape, will be treated in Section 5.3.1.

3.5.1 Local trigger cards

The main numbers and parameters concerning the local trigger cards are summarized in Table 3.3.

Each local trigger card receives digital signals from the FEE ('bit–pattern' sequence). It houses a pipelined memory where an exact copy of this information (the 'local pattern') is buffered and readout on occurrence of a L1 ALICE Trigger.

The L0 decision provided by the local trigger is the results of the 'trigger algorithm' which include the bit-pattern handling and the p_t cut.

The local cards are different for the bending plane with respect to the non–bending one.

Each local card L0-X, collects data from 16+16 strips for each X plane of MT1 and from the corresponding (in projective geometry with respect the IP) 32+32 strips for each X plane of MT2 (see Fig. 3.15): the X strips (horizontal) provide the deviation in the bending direction.

A multi-step processing is then performed in FPGA programmable logic for track finding and determination of the magnetic deviation in sign and amplitude:

- **Declustering**. The first step is the reconstruction of the impact coordinate from the bit-pattern. To this aim, the 16 (32) strips are divided in 31 (63) bits, to increase the position resolution (but at the expense of the doubling of data to be treated). These bits correspond to ideal strips parallel to the real ones and half in width with respect to those. The algorithm, (2N - 5) for number of adjacent strips hit N$\geq$3, is shown in Fig. 3.16 and provides the center of the cluster.

- **Mini–road and DS reduction**. Second step is shown in Fig. 3.17. A 'mini–road' $\pm$1 bit wide ($\pm$2 bit after declustering) is opened between the two planes of the same station according to a projective geometry

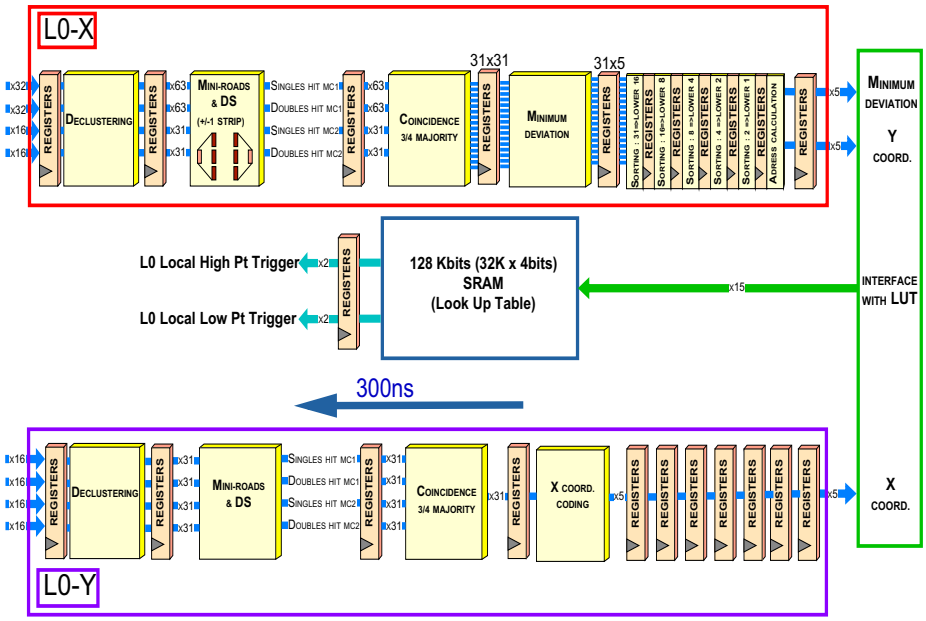

Fig. 3.15: Scheme of the locale trigger card.

cluster size	N=1	N=2	N=3	N=4	N=5
initial cluster	0 0 1 0 0	0 0 1 1 0	0 1 1 1 0	0 1 1 1 1	1 1 1 1 1
after declustering	000010000	000001000	000010000	000011100	001111100

Fig. 3.16: Declustering algorithm.

with respect to the interaction point. If the search is positive, we say that the mini-road is 'Double' (D), otherwise that it is 'Single' (S). In order to reduce the effect due to soft-background hits (see Section 3.6), a 'DS reduction' is applied: if a Double is present the Singles are eliminated. With this step, we pass from the initial 4 bit patterns (one for each detection plane) to 2 bit patterns (one for each station).

- **Road ± 8 strips with 3/4 majority**. For each Single or Double on MT1, a 'road' is opened with a fixed width of ± 8 strip (actually ± 15 bit after declustering). A valid 'road' requires the 3/4 majority condition (i.e. S–D, D–S or D–D respectively on MT1 and MT2). The full 'road' width is indicated in Fig. 3.18.

- **Minimum deviation**. The computation of the deviation is the last

bit pattern Plane 1 bit pattern Plane 2	000010000 00(1)00	000010000 00(0)00	00(0)00 000010000	010000100 000000111	100000000 000111000
"Mini-road" Singles "Mini-road" Doubles	000000000 0000D0000	0000S0000 000000000	0000S0000 000000000	0S0000000 000000D00	S00SSS000 000000000
after "DS" reduction				000000D00	S00SSS000

Fig. 3.17: 'Mini−roads' and 'DS reduction'.

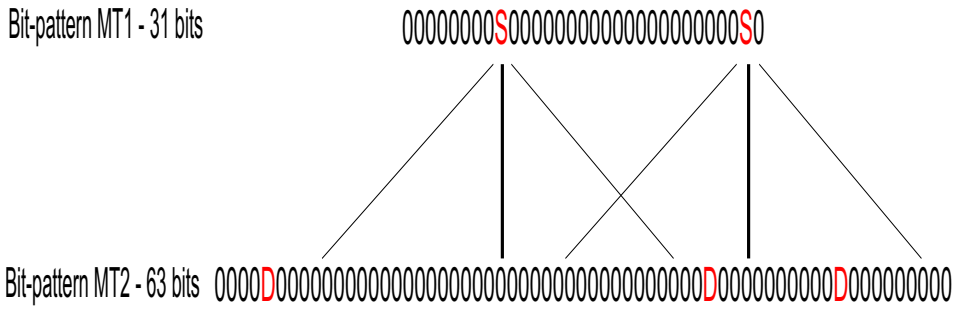

Fig. 3.18: 'Roads' for the p_t cut. The vertical bar indicates the 'zero–deviation' bit of MT2 in correspondence of the considered bit of MT1: the 'road' defined by these two bits points back to the interaction point in a straight line. The left road does not satisfy the 3/4 coincidence.

stage of the L0-X logic. In the case of multiple possibility, the track with minimum deviation is considered thus to keep the track with the higher p_t. For example, for the right road in Fig. 3.18, the track with 3 bit deviation will be considered for the 'road' on the right. The sign of the deviation is associated to the particle charge with four possibilities: +, -, 0 (empty 'road') and ± (particular case of 'zero–deviation'). The bit number (1:31) from MT1 and the minimum deviation (-15:+15) from MT2 of the valid 'road' are coded in two words (X_{pos}, X_{dev}) of 5 bits each.

In the non–bending plane, each card L0-Y collects the information from 16+16 strips for each station. It performs operations similar to those described for L0-X, but 'mini-roads' and 'roads' are narrower, ±1 bit and ±2 bits, respectively, DS reduction is not mandatory and in the case of more valid roads the choice is random. The MT1 Y position (Y_{pos} from 0 to 15) of the valid road is coded on output. An additional bit, Y_{trig}, indicates whether

or not a valid 'road' exists: finally the response of the L0-Y algorithm is a 5 bit word.

The cut on the track deviation, which principle has been described in Section 3.4, is pre-loaded in a Look-Up-Table (LUT) and performed at this level. The LUT is addressed with the 15 bits word delivered by the Local logic (X_{pos}, X_{dev}, Y_{pos} and Y_{trig}). On output, for each p_t threshold, the local decision is issued and it is coded in a 2 bit word to take into account the four possible cases: no trigger; trigger with positive deviation; trigger with negative deviation and trigger with zero ($\pm$) deviation (the case of very high momentum tracks).

3.5.2 Regional trigger cards

The goal of the regional trigger is to provide an intermediate trigger signal in order to deal with 234×4 bits coming from the local cards. The 234 local cards are distributed in 16 crates, each crate holding at most 16 local cards plus 1 regional cards that merges the information of the crate.

The words from 16 local cards are sent to a regional card and treated by eight parallel processes that are repeated in four stages, as can be seen in Fig. 3.19. Each regional card implements this scheme two times: one for the low-p_t cut and one for the high-p_t.

Two inputs	TRG_A^{in}	TRG_B^{in}	TRG^{out}	TLS^{out}	TUS^{out}	output
Nothing	00	00	00	0	0	nothing
Only 1−	01	00	01	0	0	−
Only 1+	10	00	10	0	0	+
Only 1±	11	00	11	0	0	±
2−	01	01	01	1	0	−LS
1− & 1+	01	10	11	0	1	±US
1− & 1±	01	11	11	1	1	±LS & US
2+	10	10	10	1	0	+LS
1+ & 1±	10	11	11	1	1	±LS & US
2±	11	11	11	1	1	±LS & US

Tab. 3.4: Outputs of the regional trigger card for different input combinations. Both TRG_A^{in} and TRG_B^{in} are permutable.

Fig. 3.20 shows the elementary cell of a regional card, which collects information coming from two local cards via the TRG_A and the TRG_B 2 bits inputs and establishes if there is a track and what is its deviation sign or

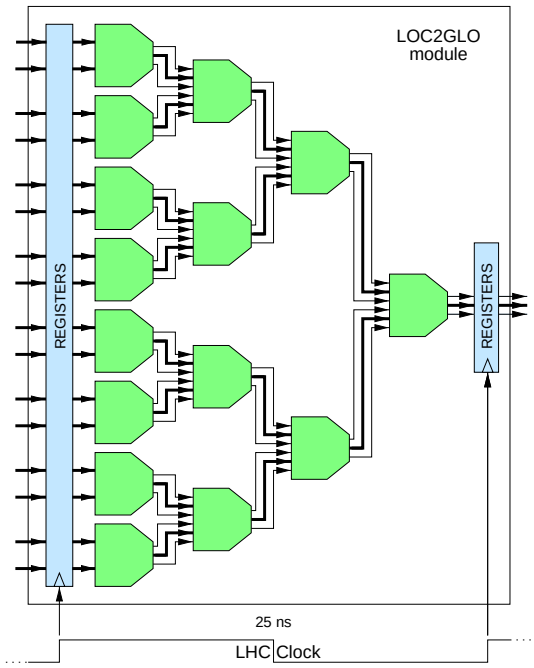

Fig. 3.19: Layout of the regional trigger card; the elementary cell is described in Fig. 3.20.

if there are 2 (or more) tracks Like-Sign (TLS) or Unlike-Sign (TUS). Outputs of an elementary cell of a regional card for different input combinations are listed in Table 3.4.

Each regional card provides a 4 bit output for each p_T threshold, therefore 2×4=8 bits are available at the output.

3.5.3 Global trigger cards

The 2×4×16=128 bits from the 16 regional cards are collected by the global card. It is similar to a regional card, with the same number of elementary cells; the difference is that TLS and TUS inputs are used already at the first stage.

The trigger signal, to be delivered to the general L0 ALICE trigger, is issued if the output from the global card indicates the presence of two opposite-sign tracks above the p_t threshold. If the high-p_t decision is non zero, a priority flag is associated to the trigger signal.

The overall timing of the trigger process is shown in Fig. 3.21: the L0 dimuon trigger is locally available in 600 ns after the bunch crossing. The

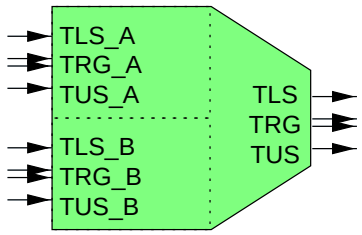

TLS = (TRG_A [0] . TRG_B [0]) + (TRG_A [1] . TRG_B [1]) + TLS_A + TLS_B
TRG [0] = TRG_A [0] + TRG_B [0]
TRG [1] = TRG_A [1] + TRG_B [1]
TUS = (TRG_A [0] . TRG_B [1]) + (TRG_A [1] . TRG_B [0]) + TUS_A + TUS_B

Fig. 3.20: Elementary cell of the regional trigger card and the associated logical equation.

time corresponding to the transfer to the ALICE L0 trigger module must be added.

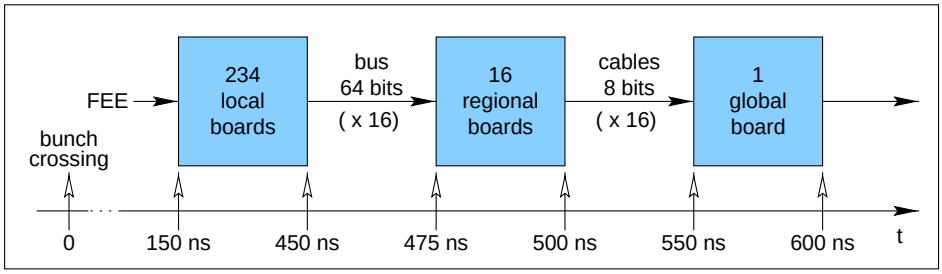

Fig. 3.21: Timing of the dimuon trigger process.

3.6 Simulations for muon trigger environment

Illumination of trigger chambers, trigger rates and trigger efficiency have been estimated by means of simulations. The baseline of the simulations is the HIJING program, in one case parametrized with jet quenching and nuclear shadowing (the so-called 'standard' conditions), in another case without these effects. Under 'standard' conditions 5800 particles per unit of rapidity at zero rapidity are generated in Pb-Pb collisions, against 8000 particles without jet quenching and shadowing, so that we refer to this last case as 'Hijing 8000' .

Muons pairs from J/Ψ and Υ resonance decays, single muons from π and K decays, single muons from charm decays and soft-background (mainly electrons leaking out of the absorbers), are taken into account as contributions to signal and background. Single muons from beauty decays do not contribute significantly and are neglected. Soft-background creates random hits that are not correlated between the different trigger planes, so that it essentially creates ambiguities in the trigger patterns but, in any case, the trigger probability increases smoothly with the number of soft-background hits. Moreover, an important point for the trigger rates is that soft-background has a widely spread time structure and a large part of the hits (about 2/3) are rejected by the time gate of 20 ns on the trigger electronics.

'Standard' and 'Hijing 8000' simulation conditions for background events on the trigger are summarized in Table 3.5. The number of muons from π and K decays as well as soft-background predicted by 'Hijing 8000' are a factor 2 higher compared to the 'standard' simulation.

	Muons from π and K decays	Muons from charm decays	Soft-background per plane
'Standard' conditions Pb-Pb central	8.5	1.5	10×1.5=15
'Hijing 8000' conditions Pb-Pb central	17	1.5	30

Tab. 3.5: 'Standard' and 'Hijing 8000' simulation conditions for background events on the trigger for central Pb-Pb collisions.

3.6.1 RPC illumination

Results from simulations can be used to compute the hit rates (or illumination) for the trigger chambers. The hit density per central Pb-Pb collision predicted by 'Hijing 8000' is plotted as a function of the distance from the beam axis in Fig. 3.22 for MT1 (top) and for MT2 (bottom). The hit densities decrease by about one order of magnitude with increasing distance from the beam. As can be seen, in MT1 or MT2 for central Pb-Pb collisions the maximum hit density is 2×10^{-3} hit/cm^2.

For peripheral Pb–Pb collisions, it is assumed that the hit density distribution is the same as in a central Pb-Pb collision and that only the total number of hits changes with the impact parameter b. For a given b the number of hits has been computed by assuming that it is proportional to the

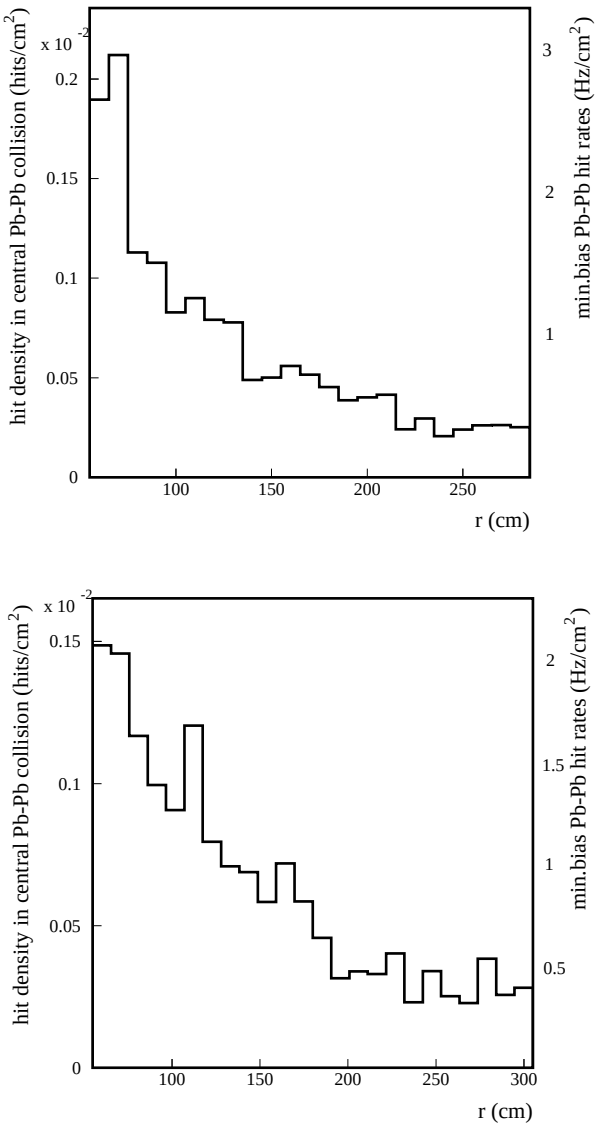

Fig. 3.22: Illumination of station MT1 (top) and MT2 (bottom). Left vertical scale: hit density distribution per central Pb-Pb collision. Right vertical scale: hit rate distribution for minimum bias Pb-Pb collisions.

energy $E_s(b)$ emitted in the angular acceptance of the spectrometer ($E_s(b)$ obtained with Hijing) [2]:

$$N_{hits}(b) = N_{hits}(b=0) \times \frac{E_s(b)}{E_s(b=0)} \tag{3.7}$$

The hit rate distribution obtained are shown in Fig. 3.22 (right vertical scale). As can be seen, the maximum hit rate is about 3 Hz/cm^2 for station MT1. The same method has been used for evaluating the hit rates in Ar–Ar.

In Table 3.6 are listed the maximum hit rates on MT1 for Pb–Pb and for Ar–Ar at nominal luminosity. Rates for MT2 are almost identical.

	Luminosity ($cm^{-2}s^{-1}$)	Max. rate (Hz/cm^2)
Pb-Pb	10^{27}	3
Ar-Ar	10^{29}	24

Tab. 3.6: Maximum hit rates on MT1 for different colliding systems at nominal luminosity. These value include a safety factor of 2.

According to recent simulations [6], the expected hit rate distribution in p–p has a shape similar to the one reported in Fig. 3.22 for Pb–Pb collisions. The maximum expected rate is about 2 Hz/cm^2 (at luminosity 5×10^{30} cm^{-2}s^{-1} and considering a safety factor of 2).

Furthermore, in the particular case of p–p collisions, the hit rate on the RPCs will be enhanced by beam–gas interactions as explained in Section 2.1.3. Simulations have been undertaken to evaluate the fluxes of the background charged particles on the trigger chambers [7].

The simulation is of major importance for the evaluation of the requirement for the lifetime of the detector, as explained in Section 5.1.1.

According to the simulation, the number of beam–gas interactions per second and per meter, and therefore the charged particle flux on the trigger chambers, is proportional to the H_2–equivalent residual gas density. In particular, this simulation has been done with the H_2–equivalent residual gas density shown in Fig. 2.2 and described in Section 2.1.3, this density refers to the third year scenario [8]; in this case the maximum resulting H_2–equivalent gas density amounts to $\sim2\times10^{14}$ molecules/m^3.

The total charged particle flux on MT1 is presented in Fig. 3.23, it includes the sum of the contributions from the two circulating beams and from all charged particle species (muons, hadrons and electrons). Similar results have been found for the second trigger station. The two–dimensional plot does not indicates an azimuthal symmetry: the charged particle rate on MT1

shows in fact a high rate area located at $|\ y\ | \leq 0.5$ m and $1 \leq x \leq 2$ m, where fluxes close to 50 Hz/cm^2 are reached. Elsewhere, the particle flux does not exceed 10 Hz/cm^2.

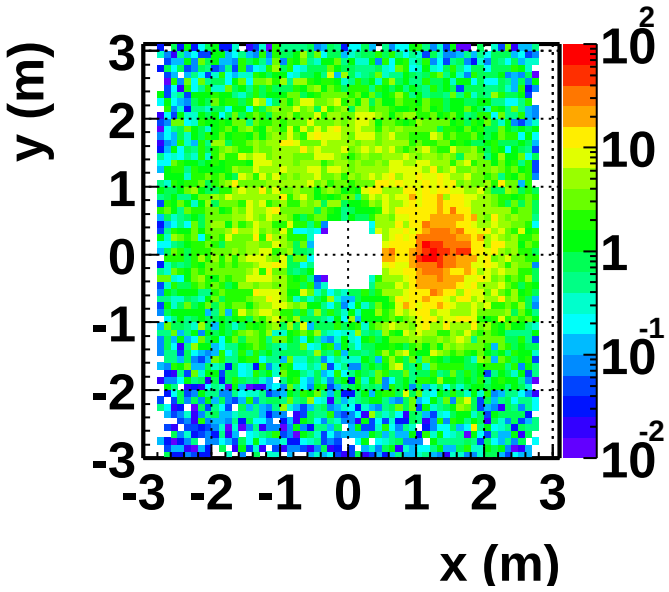

Fig. 3.23: Total charged particle flux on MT1 for p-p data taking.

A separated analysis on each contribution indicates that the high rate area is due to electrons from showers originated by hadrons from Ring 2 with energies greater than 100 GeV surviving to the beam shield iron plug.

In a more recent and accurate calculation [9], the residual gas densities have been estimated using the VAcuum Stability COde (VASCO) for two different scenarios: the machine start–up and after machine conditioning. Machine conditioning using electron scrubbing is expected to lower the secondary electron emission avoiding electron multiplication. The residual gas mean densities are estimated to be a few 10^{14} molecules/m^3 at machine start–up and about 30 times lower after machine conditioning (6.5×10^{12} molecules/m^3). This last value is about a factor 5 lower that the one referring to the third year scenario used for the simulation of the charged particle background due to beam–gas interaction.

In conclusion, in order to deal with a more realistic value of the background contribution, the results of the simulation of the beam–gas background must be rescaled by a factor 5, obtaining:

- $\sim$10 Hz/cm^2 on a limited area ($|\ y\ | \leq 0.5$ m and $1 \leq x \leq 2$ m);

- $\sim$2 Hz/cm^2 elsewhere.

These value must be added to the number of particles emitted in the collision at the interaction point (2 Hz/cm^2).

3.6.2 Trigger rates

The mean luminosity and the collision frequency (f^{coll}), considered for the calculation of the trigger rates, are reported in Table 3.7 for each colliding system.

	Pb–Pb	Ar–Ar	p–p
$\mathcal{L}$ (cm^{-2}s^{-1})	5×10^{26}	5×10^{28}	3×10^{30}
f^{coll} (Hz)	4000	1.5×10^{5}	2×10^{5}

Tab. 3.7: Mean luminosity and corresponding number of inelastic collisions per second considered for the evaluation of the trigger rates.

The trigger rates, presented in Table 3.8, are given for the low and high-p_t cut ($F_{\mu\mu}^{Lpt}$ and $F_{\mu\mu}^{Hpt}$), as well as without cut ($F_{\mu\mu}^{Apt}$) corresponding to a minimum accessible p_t ($\sim$0.5 GeV/c).

	$F_{\mu\mu}^{Apt}$ (Hz)	$F_{\mu\mu}^{Lpt}$ (Hz)	$F_{\mu\mu}^{Hpt}$ (Hz)
Pb–Pb collisions	930	330	65
Ar–Ar collisions	4500	630	73
p–p collisions	30$\pm$7	10$\pm$4	5$\pm$3

Tab. 3.8: Trigger rates for Pb–Pb, Ar–Ar and p–pp minimum bias collisions.

In all cases, the rates match the interaction rate of 1 kHz allowed by DAQ bandwidth with a safety margin.

For the trigger rates, the p–p mode needs a special treatment due to the beam-gas background, which give dimuon-like triggers. In order to reject these events, the V0 detector has been proposed to recognize the background-induced triggers allowing their elimination [10].

3.6.3 Trigger efficiency

A preliminary important remark, concerning the trigger efficiency and the choice of the p_t thresholds, is that the best compromise between background

rejection and signal detection efficiency should be found. Furthermore the threshold values must guarantee a trigger rate below 1 kHz, that is the maximum rate allowed by the DAQ bandwidth.

The background rejection efficiency (for single muons) for low and high-p_t cut are listed in Table 3.9. The rejection efficiency increases obviously as the cut on p_t increases.

	(π, K)	charm	beauty
1-ϵ_{trig}^{Apt}	55%	32%	11%
1-ϵ_{trig}^{Lpt}	87%	73%	30%
1-ϵ_{trig}^{Hpt}	96%	92%	64%

Tab. 3.9: Background rejection efficiency for muons from (π, K), charm and beauty decays.

In Table 3.10 are listed the efficiency on J/Ψ and Υ (for muon pair) for low and high-p_t cut.

	J/ψ	Υ
ϵ_{trig}^{Apt}	90%	97%
ϵ_{trig}^{Lpt}	71%	97%
ϵ_{trig}^{Hpt}	22%	88%

Tab. 3.10: Detection efficiency for J/Ψ and Υ decays in muon pairs.

In Fig. 3.24, the trigger efficiency for signal detection (i.e. J/ψ and Υ) is plotted as a function of transverse momentum and of resonances rapidity. While the efficiency for the Υ is rather flat, for the J/ψ it is more disuniform, due to kinematics of the decay of this resonance.

3.7 Physics performance for p–p collisions at 14 TeV

Recent works have been carried out to study, through simulations, the physics performance of the ALICE Muon Spectrometer in the detection of heavy quarkonia produced in p–p collisions at 14 TeV, and of exploring possible contributions to our present understanding of physics [11].

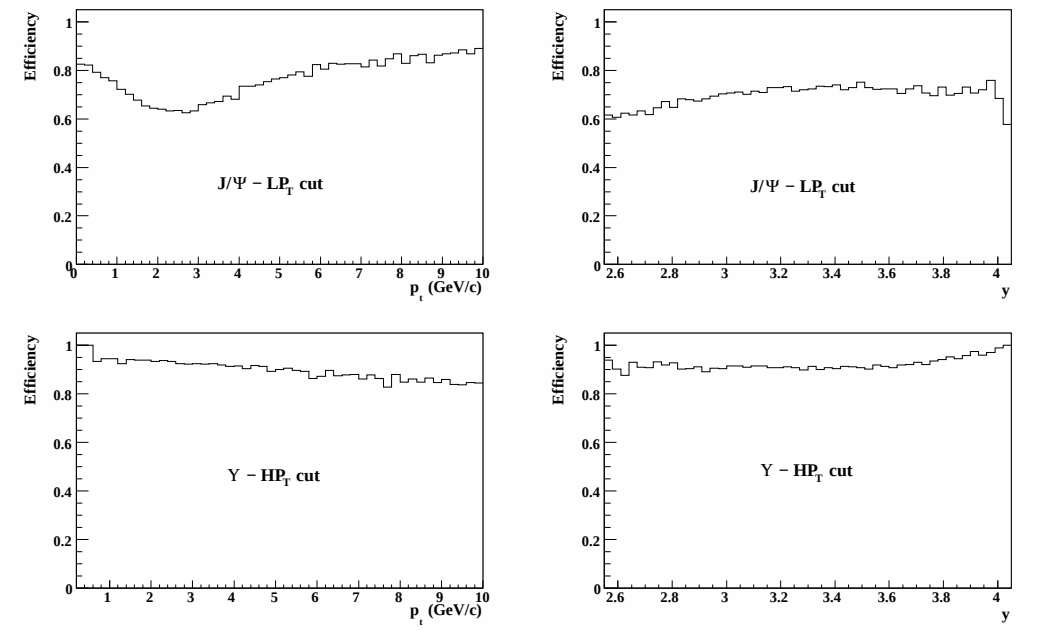

Fig. 3.24: Trigger efficiency versus transverse momentum p_t (left) and rapidity Y (right) and of J/ψ (top) and Υ (bottom). For the J/ψ (Υ) the low–p_t (high–p_t) cut has been applied.

Yields for charmonium and bottomonium states expected in 10^7 s of collected data with foreseen luminosity for p–p collisions at 14 TeV have been evaluated.

The analysis was performed with the aid of the fast simulation, which enables processing of the expected high statistics. The input parameterizations of quarkonia rapidity (y) and transverse momentum (p_t) distributions were provided, respectively, by Color Evaporation Model and by recent results from CDF data, opportunely scaled to LHC centre-of-mass energies.

The simulation takes into account the correlated background, constituted by muons coming from heavy flavoured hadron decays, but they do not yet include the combinatorial background of muons from pions and kaons decay. Though its contribution is expected to be only a fraction of the correlated one, the combinatorial background has to be added in the near future.

Simulation results end in very high statistics for J/ψ, and high statistics for ψ' and bottomonium states, thus allowing an accurate analysis of quarkonia in different p_t and y bins, showing that p_t and y distributions can be precisely measured.

The distributions were corrected for the Muon Spectrometer acceptance and divided by the integrated luminosity in order to obtain the J/ψ and Υ differential cross section in the interval $2.5 < y < 4.0$ (the detector acceptance).

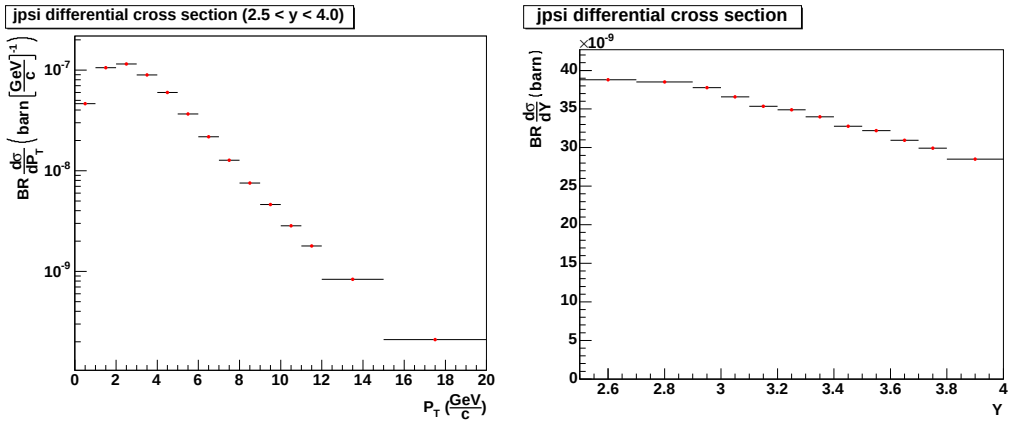

(a) p_t (b) y

Fig. 3.25: p_t and y differential cross section for J/ψ, obtained simulating 10^7 s of p–p data taking after background subtraction. p_t cross section is integrated in the detector rapidity coverage ($2.5 < y < 4.0$).

The obtained p_t differential cross section for J/ψ and Υ can be used to provide very useful information on the quarkonia production mechanism. This topic has already been analyzed by CDF data, but the higher centre-of-mass energy and, most importantly, the possibility of studying quarkonia down to p_t=0 will allow ALICE to contribute significantly to open questions concerning perturbative QCD in the low-p_t region.

Furthermore, it was for the first time noted that the y distributions of J/ψ in rapidity region covered by the ALICE Muon Spectrometer could provide important information on gluon distribution functions at low value of the Bjorken variable x. At present the available data cover an x region down to 10^{-5} for energies on the order of charmonium state mass, and even higher x values for the energy scale of bottomonium. For lower x values, extrapolation are used for gluon distributions.

The performed calculations show that, owing to the high rapidity range covered by the ALICE Muon Spectrometer, the shape of the J/ψ rapidity differential cross section is sensitive to gluon distribution functions at low-x. In addition, the comparison with simulations suggests that the measured y distributions can, in principle, be used to constrain the gluon PDFs in the x range of sensitivity.

References

[1] Forward Dimuon Spectrometer Technical Design Report, CERN/LHCC 99-22

[2] Addendum to the Forward Dimuon Spectrometer Technical Design Report, CERN/LHCC 2000-046

[3] The Forward Dimuon Spectrometer: Addendum to the ALICE Technical Proposal, CERN/LHCC 96-32 (1996)

[4] D. Swododa, C. de Almeida, A. Meynet, H. Taureg, A. Tournaire, ALICE Internal Note ALICE-INT-2005-023

[5] R. Arnaldi *et al.*, Nucl. Instr. and Meth. A 456 (2000) 126-131

[6] F. Yermia, Ph.D Thesis, Università degli Studi di Torino, February 2005.

[7] R. Guernane, A. Morsch and E. Vercellin, ALICE Internal Note ALICE-INT-2003-41

[8] L.R. Collins and O.B. Malyshev, LCH Project Note 274

[9] A. Rossi and N.Hilleret, LHC Project Report 674 (2003)

[10] B. Cheynis *et al.*, ALICE Internal Note ALICE/00-29

[11] D. Stocco, Graduation Thesis, Università degli Studi di Torino (2005) *http://www.to.infn.it/∼stocco/work/specThesis/tesi.pdf*

Chapter 4

Resistive Plate Chambers

The Resistive Plate Chambers (RPCs) are gaseous detector designed to measure the time and the position of charged particles crossing its active area, that is the gas volume.

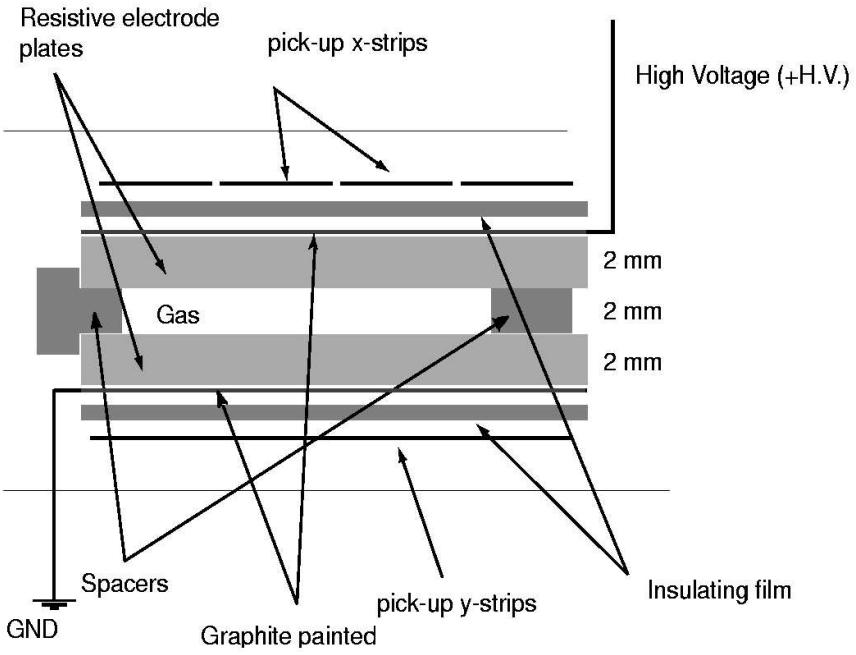

Fig. 4.1: Structure of a single-gap Resistive Plate Chamber.

The typical structure of a single–gap RPC is presented in Fig. 4.1: the 2 mm thick gas gap (the active volume) is enclosed between two parallel bakelite plates (2 mm thick) treated with linseed oil to smooth the surface. The electrodes are separated by a frame and by spacers of insulating material;

the spacers, 10 mm diameter cylinders with a 2 mm height, are placed on a 10×10 cm^2 grid. The external side of the electrodes are covered with a thin graphite layer to ensure a uniform electric field all over the active volume; a foil of insulating material (PET) is glued on the conductive layer. One electrode is connected to the HV and the other one to the ground. The signal produced in the gap by a charged particle is picked–up by two orthogonal strip planes placed on the external side of the electrodes. Two external stiffener planes ensure the rigidity of the complex.

4.1 Historical development

At the end of the Forties, the development of the spark counter lead to the introduction of the Parallel Plate Counter (PPC) [1]: two metallic parallel electrodes, fed with constant voltage, enclose a gas volume. Since the electrodes resistivity is low, the spark induced by the crossing particle will be distributed on the whole surface of the detector, thus loosing the position information. To overcome this problem several attempt employing glass electrodes have been made [2, 3] and at the beginning of the Eighties, Yu. N. Pestov of the Nuclear Physics Institute of Nvosibirsk finally presents a new detector denominated "spark counter with a localized discharge" [4]. Two glass electrodes enclose a gas layer 0.1 mm thick kept at a pressure of 12 atm, the anode is made of conductive glass (ρ=10^9–10^{10} Ωcm) while the cathode is made of ordinary glass (ρ=10^{12}–10^{13} Ωcm). The prototype area is 30×30 cm^2 and the gas mixture is composed of Argon (85.6%), isobutane (10%), butadiene (2.5%) and ethylene (1.9%). The working tension is 3.75 kV. Pick-up strips are placed on the anode side and are read on both ends: the impact coordinate in the direction parallel to the strips is calculated from the relative delay of the two signals. The spatial resolution in this direction is of 0.2 mm. The pulse amplitude is large (up to several volts) and the time resolution is extremely good (30 ps). Currently, this detector is developed for time of flight measurements.

These good performances in space and time resolution need high precision in the realization of the detector: the inner surface of the electrodes must in fact be absolutely free from imperfection. A further complication is the high pressure needed to work. These considerations limit their manufacturing as large area detectors.

To reduce cost and technical difficulties, R. Santonico (Rome University) proposes in 1981 a simplified version of the Pestov counter: the Resistive Plate Chambers (RPC) [5]. The gas is kept at atmospheric pressure, the gap width is increased at 1.5 mm and the electrodes are made of 2 mm bakelite, a

plastic laminate produced with high pressure manufacturing processes (HPL) that can be easily made in large area format; the bakelite production has been carried out by the Gruppo Frati S.p.A. (Pavia). Bakelite resistivity is of the order of 10^{11} Ω cm. The electrode surface facing the gas is cleaned and treated with linseed oil, in order to reduce the noise due to imperfections and scratches. The first RPC prototype (85×13 cm^2), tested with cosmic rays (flux$<$0.1 Hz/cm^2), shows high efficiency (up to 97%) at HV=10000 V. The average amplitude of the pulses is 200–400 mV, with a rise time of a few nanoseconds, the signal occurs few nanoseconds after the physic event and the FWHM of the time distribution is 1.2 ns.

In 1988 an upgraded version of the detector [6] is presented. Its size is larger than the one of the first prototype and small PVC spacers are therefore introduced between the electrodes, to keep them at constant distance all over the gas gap. On the area occupied by the spacers the detector is obviously inefficient (geometrical inefficiency). Also in this case, the RPC demonstrates its validity for detection of cosmic–like particle fluxes and a test made with a 5 GeV pion focused beam from the PS at CERN [7] shows that the detector reaches an efficiency of 90% up to local particle fluxes of about 60 Hz/cm^2. Concerning the time resolution, it degrades with the increasing rate, reaching a value of 4 ns for rates of 100 Hz/cm^2.

The same prototype is employed in a test [8] with an adjustable flux of gamma rays which invests all the sensitive area of the detector. In these conditions, when the γ–ray flux induces a counting rate of 15 Hz/cm^2 on the RPC, the efficiency for cosmic rays detection is below 80%.

Tests made on different prototypes [9], confirm this circumstance that can be explained by the lateral diffusion of the electric charge delivered on the electrodes by the sparks: if the beam is focused, the charges spread all over the electrode surface, resulting in a speed-up of the tension recovery.

At this level of the RPC development, the maximum rate capability of the fully exposed detector is below 10 Hz/cm^2. However, it is simple to build and operate, it is suitable to cover large detection areas, it has a quite low cost, good time resolution and a low sensitivity to photons and neutrons [10].

In 1994 the L3 experiment at the CERN–LEP was upgraded installing a forwad–backward muon spectrometer with a muon trigger including two RPCs layers. The chambers have been operational from 1994 till the end of the LEP running (2000): after 7 years of running, the RPCs still show efficiency higher than 90% [11].

This encouraging results and the detector features make the RPC a candidate to give the dimuon trigger in the forthcoming experiments at the Large Hadron Collider at CERN. The limited rate capability, which is too low for the predicted counting rates, will be improved by examining different gas

mixtures and operating modes and by testing the effect of a reduced resistivity of the electrodes. Details on that will be given in Section 4.3, after the description of the signal formation process on the RPC.

4.2 Signal formation process and gas mixture

The RPC signal formation process is the typical one of gaseous detectors [12]. When a charged particle passes through the gas volume, it interacts with the gas molecules: if they receive an energy high enough to be ionized, electron–ion pairs are created.

Due to the electric field applied between the electrodes, electrons migrates toward the anode and acquire the energy:

$$U = e \cdot E \cdot l, \tag{4.1}$$

where eE is the electric force and l the path of the charge between two collisions in the electric field direction.

If electrons have an energy greater than the ionization energy of the gas for $l < \lambda$ (with λ mean free path), collisions with gas molecules can determine their ionization and the creation of new electron-ion pairs, starting a multiplication process that can produce an "avalanche". According to the Townsend mechanism [13], if the electric field is constant, the multiplication increases exponentially and the number $n(x)$ of electrons that reaches the anode will be

$$n(x) = n_0 e^{\alpha x} \tag{4.2}$$

where n_0 is the number of primary electrons, x the distance between the origin of the primary electrons and the anode and α is the first Townsend coefficient. The coefficient α depends on the gas used and on the E/p ratio between the electric field and the gas pressure. From equations 4.1 and 4.2, we can deduce that the multiplication process can be favored increasing the electric field, decreasing the gas density (that means increasing the mean free path) and using monoatomic gases in the mixture, such as noble gas, because they have an α value greater than the one of multiatomic gases. This can be explained by the fact that if the gas is multiatomic the energy transmitted to the molecule can also be dissipated through other channels (dissociation, excitation of vibrational or rotational states) without formation of ions. One of the widely used noble gas is Argon, with a ionization energy of I=15.8 eV.

Due to the small thermal and drift speeds, ions stay near the point where they have been produced; since both speeds are higher for the electrons, they drift along the electric field lines and spread also along the other directions.

Therefore the avalanche assumes the shape of a drop, with the electrons concentrated in the region with the largest radius as shown in Fig. 4.2 a.

The multiplication process follows equation 4.2 only if the field generated into the drop by the charge separation, E_{CE}, is small with respect to the external electric field, E_0 (see Fig. 4.3). This condition is satisfied when the multiplication factor M, defined as $M=n/n_0$, is lower than 10^6, while for higher values of M the avalanche grows so that the applied electric field is no longer homogeneous; when E_{CE} becomes equal to E_0 electrons and ions recombine with emission of ionizing photons (Fig. 4.2 b). At the extremities of the drop, where the field is higher, these photons start secondary avalanches that trigger a discharge between the electrodes, called "streamer" (Fig. 4.2 c). We can define a discharge as the continuous current flowing from an electrode to the other.

The threshold for the degeneration of the avalanche in streamer is the Raether condition [14]:

$$M \simeq 10^8 \;\Rightarrow\; \alpha x_c \simeq 20, \tag{4.3}$$

where x_c is the length of the critical drift path. In a RPC the maximum possible value of x_c is given by the gap length: this means that to work in streamer mode with a 2 mm gap, the first Townsend coefficient has to be of the order of 10 mm^{-1}.

If the electric field or the drift path are slightly smaller than the one required to fulfill the Raether condition, the spark may occur, but with a delay. This happens when electrons are extracted from the cathode by ultraviolet rays (generated from electron-ion recombination and from ion dis–excitation) or by positive ions approaching the electrode.

The ultraviolet photons can initiate secondary avalanches also in zones of the detector near to the passage of the particles, thus increasing the noise as well as the cluster size, that is the number of contiguous strips fired by the crossing particle.

To reduce these effects, polyatomic molecules, such as isobutane, are added to the gas mixture for two reasons: first, they can absorb ultraviolet rays and dissipate their energy in mechanic channels; second, if their ionization potential is lower than the one of the noble gas, they can receive the charge of positive ions and neutralize it at the cathode without extracting electrons. In this way the discharge is "quenched".

Ultraviolet rays are also absorbed by the linseed oil layer which is on the gas side of the RPC electrodes.

The reduction of secondary processes is also favored by the addition of electronegative gases, such as freon or SF_6. In fact, a free electron can be

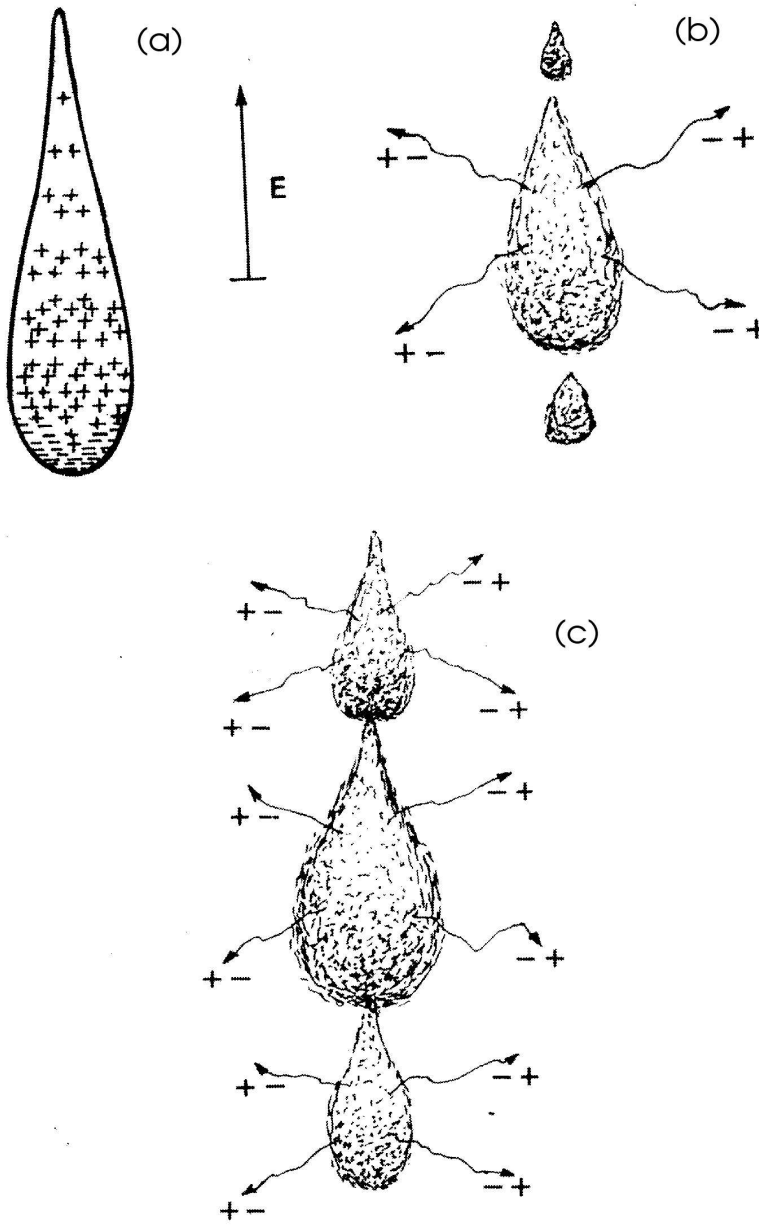

Fig. 4.2: Shape of the avalanche (a) and evolution of the avalanche to the streamer (b, c).

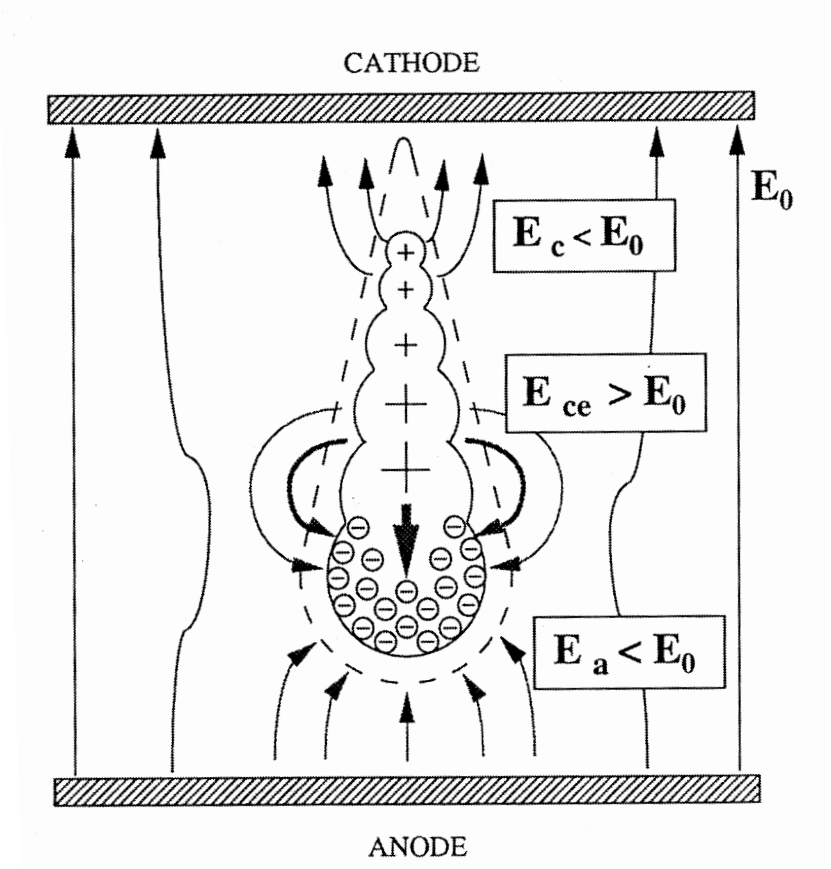

Fig. 4.3: Electric field in presence of a big avalanche. E_0 is the field applied to the electrodes; E_a is the charge field; E_c is the avalanche–cathode field.

captured by a molecule of these gases giving birth to a negative ion that can be neutralized interacting with an ion of opposite sign. The result of the process is the loss of an electron-ion pair but also a reduction of the lateral extension of the spark. Recombination of negative ions with positive ions can occur without emission of ultraviolet photons because the disexcitation can be achieved through mechanic channels. Moreover, negative ions have a much smaller drift velocity and therefore do not contribute to the fast signal, as is explained further on. In particular, SF_6 quenches the spark thanks to its electron affinity value of 1.05 ± 0.10 eV, but above all thanks to its electron attachment cross section that is a strongly decreasing function of the electric field [15]. Therefore, when the space charge field reduces the applied one, the attachment becomes very effective and negative ions are created.

The charge released by the spark neutralizes the voltage applied on the electrodes to a limited extent of a small area (about 0.1 cm^2), because of the high resistivity of the electrodes. The recovery time of the charge and consequently of the working potential, depends also on the resistivity.

In RPCs the ion drift does not induce useful signals, because it is distributed over a time interval much longer with respect to the electron–induced pulses. Only the electrons contribute to the signal picked up by the readout strips, and it is possible to show that the charge induced on the strips is only a fraction of the total charge dissipated in the gas [16].

Depending on the gas mixture components and their percentage and on the voltage applied to the electrodes, the RPCs can be operated in avalanche or streamer mode; details will be given in next Section.

4.3 Operating modes

Historically, the first operating method of the RPCs was the streamer mode. With a gas mixture made up of 70% Argon, 30% isobutane and a small amount of freon, the electric signals induced on the pick–up strips are quite large, up to 400 mV, so that they can be discriminated from the underlying noise without any previous amplification. This represents an advantage in terms of reliability, simplicity and cost. The cluster size is quite small, as well as the intrinsic noise (the so–called "single rate", typically 0.1 Hz/cm^2). At low operating voltages, close to the efficiency plateau knee, the time distribution shows a double-peak feature due to streamers delayed with respect to the avalanche induced by the primary electrons. An improvement of the time resolution can be reached at a quite high running voltage, which nevertheless causes a worsening of cluster size and single rate and an increase of the currents drawn by the detector. The main drawback of the streamer

mode is the rate capability, which is limited by the large amount of charge deposited on the electrodes by the sparks: the electric field is neutralized in the zone interested by the passage of a particle and another particle crossing the chamber in the same zone during the recovery time (imposed by the electrode resistivity) is not detected.

In fact, taking into account the typical parameters of RPCs working in streamer mode:

- Δq= 500 pC the streamer charge;
- A=0.1 cm^2 the streamer area;
- d=2 mm the gas gap,

the capacitance of the gap zone interested by the streamer is given by:

$$c = \epsilon_0 \frac{A}{d} = 8.85 \times 10^{-2} \frac{F}{m} \frac{10^{-5} m^{-2}}{2 \times 10^{-3} m} \simeq 4.5 \times 10^{-14} F. \tag{4.4}$$

Therefore, the drop of the voltage in this zone is:

$$\Delta V = \frac{\Delta q}{c} = \frac{500\ pC}{4.5 \times 10^{-14} F} \simeq 10\ kV. \tag{4.5}$$

The obtained value is comparable with the applied voltage between the electrodes at the efficiency plateau ($\sim$ 9000 V), and this means that the HV is locally neutralized after the streamer.

The problem can be faced from two sides:

- lowering the resistivity of the electrodes, to speed up the recovery time,
- lowering the charge deposited at each event, in order to reduce the voltage drop between the electrodes.

The first approach is abandoned when, in 1993, Santonico *et al.* [17] point out the disadvantages of low–resistivity electrodes: high amount of power dissipated in the gas and noise rate. In 1997, the ALICE dimuon trigger collaboration starts to investigate this possibility again and chooses the streamer mode for the trigger chambers with the characteristic that will be discussed in detail in the next Chapter.

The second approach persuades several researchers belonging to the ATLAS and CMS collaborations [17, 18] to find a gas mixture that prevents the formation of streamers. The particle passage is detected only by means of the fast and small signal induced by the primary electrons [18] (10–15 mV of amplitude, released charge of the order of dozens of pC). These studies

lead to the proposition of the avalanche mode operation, which uses gas mixtures with high percentages of freon and small percentages of SF_6, in order to increase the voltage threshold after which the multiplication degenerate in streamer reducing the probability to have a discharge. The result is an improvement of the rate capability and of the time resolution with respect to the streamer mode because, respectively, the recovery time of the working voltage is shortened due to the small charge of the signal and the initial avalanche is always in time with the passage of the ionizing particle.

However, in avalanche mode single rate and cluster size are larger than in streamer mode. In fact, according to equation 4.2, the number of electrons that reach the anode in RPCs working in pure avalanche mode depends strongly on the position of the primary electron with respect to the anode. This means that the charge distribution spectrum is not a narrow peak so that the discrimination thresholds must be set at low values resulting in high values of noise rate and cluster size.

As shown, the knowledge of the signal charge spectrum is fundamental to choose the discrimination threshold. Crotty *et al.* [19] found that it depends on the applied voltage: for low voltages (under the knee of the efficiency plateau) it has an exponential shape, which becomes similar to the Landau distribution in the first 400 V of the efficiency plateau; increasing the voltage the distribution approaches a Gaussian shape, with the increase of the percentage of signals that degenerate in streamer.

Moreover, signal pre–amplification is mandatory, together with an effective screening of external electromagnetic interferences.

The avalanche operation mode has been chosen by the ATLAS and CMS collaborations for the RPCs of the muon trigger [20]: their chambers, with a gas mixture composed by tetrafluorethane (94.7%), isobutane (5%) and sulfur-hexafluoride (0.3%), can reach a time resolution of 1.5 ns and an efficiency of 99% for incident fluxes up to 500 Hz/cm^2.

4.4 Equivalent circuit of a RPC

The resistivity of the electrodes of a RPC is an important parameter because it influences the recovery time of the tension after the passage of a particle, namely it imposes a limit on the rate capability.

Knowledge of the electric scheme of a RPC can suggest indirect methods to get information about the electrode resistivity.

As shown in Fig. 4.4, R_s and R_c are respectively the surface resistivity of bakelite and of the graphite layer, C_g is the capacity of the gas gap, R_b and C_b are respectively the resistance and the capacity of the electrodes. The coaxial

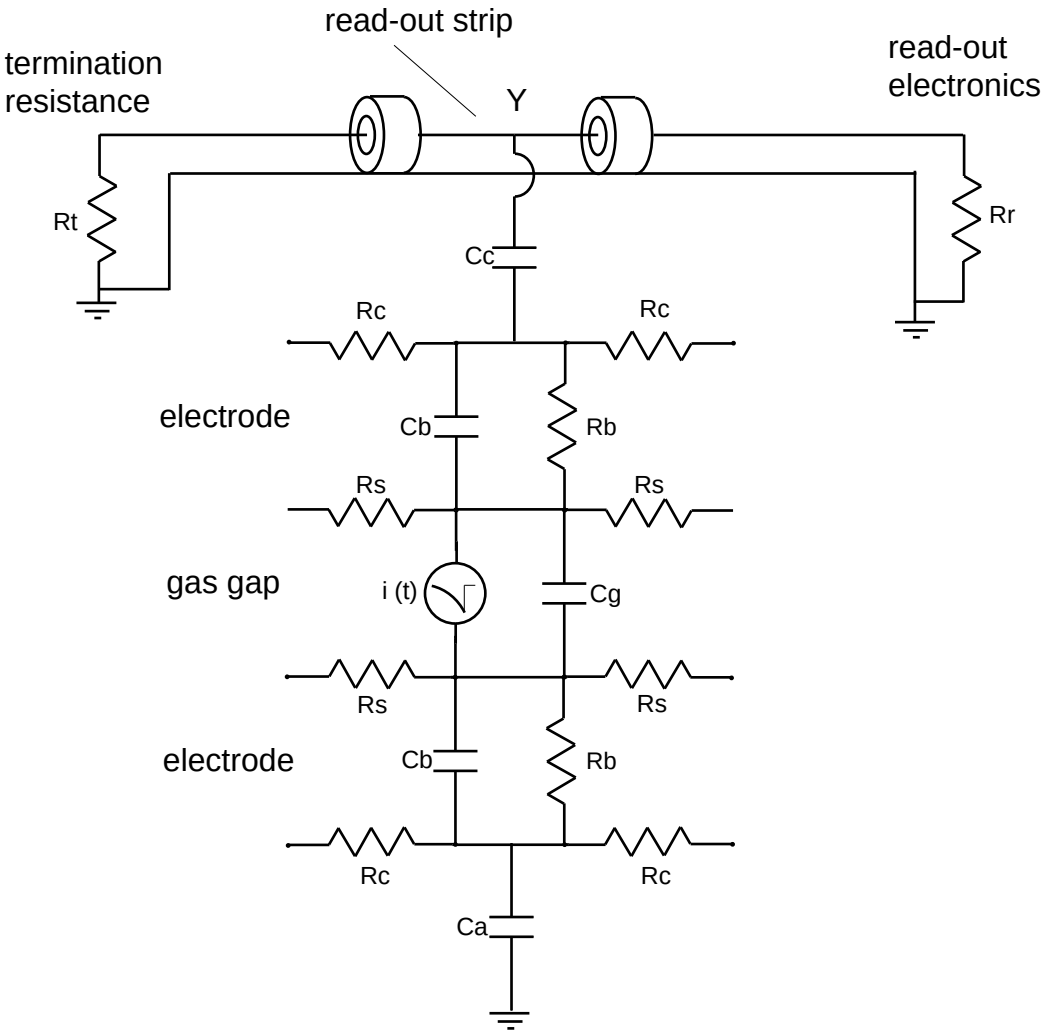

Fig. 4.4: Electric scheme of a RPC.

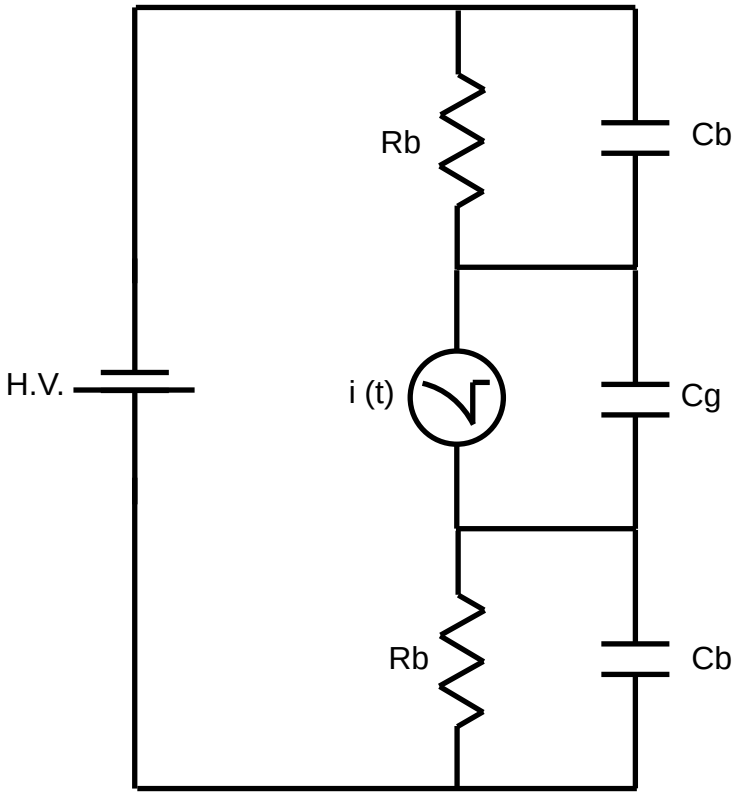

Fig. 4.5: Reduced scheme of a RPC.

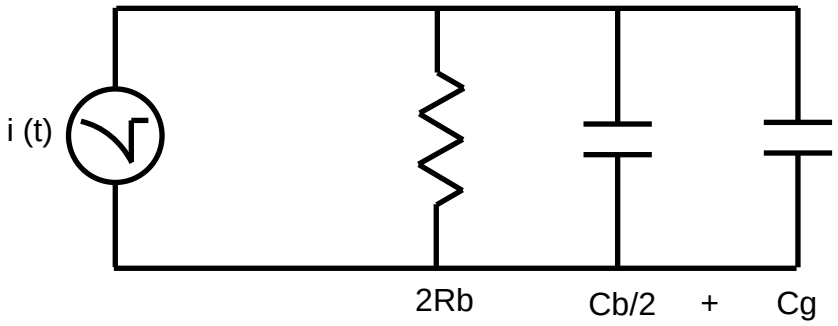

Fig. 4.6: Equivalent circuit used to calculate the recovery time of a RPC.

cable represents the readout strip, R_r is the readout impedance (typically 50 Ω) and R_t=R_r is the termination resistance which is connected at the other end of the strip to avoid signal reflection. Since the signal formation time is much shorter of any time constant in the model, we can safely neglect the contributions of adjacent areas considering R_c, R_s, C_c and C_a infinite, so that the scheme can be reduced to the one illustrated in Fig. 4.5.

If g is the thickness of the gas gap, d the thickness of the electrodes, ρ its resistivity, ϵ_r its dielectric constant and $\epsilon_0 = 8.85 \times 10^{-12}$ F/m the dielectric constant of free space, capacities and resistances in the circuit can be evaluated as follows:

$$C_g = \frac{A}{g}\,\epsilon_0, \tag{4.6}$$

$$C_b = \frac{A}{d}\epsilon_0\epsilon_r, \tag{4.7}$$

$$R_b = \rho\frac{d}{A}. \tag{4.8}$$

The typical value of ϵ_r for the bakelite is between 5 and 10, which also corresponds to the ratio between C_b and C_g, since $g = d$.

After applying high voltage, the internal surface of the electrodes will be charged by current flow through them, so that, in a static situation, all the voltage is applied to the gas gap. The streamer can be described as a current generator that discharges the C_g capacitor and the voltage is transferred to the C_b capacitors. To calculate the time of the signal formation (or of the time recovering) we can concentrate on the last phase by referring to the equivalent circuit of Fig. 4.6:

$$\tau = R \times C = 2R_b \times (C_b/2 + C_g), \tag{4.9}$$

which, from equations 4.6, 4.7 and 4.8, with $g = d$, can be written:

$$\tau = \epsilon_r\epsilon_0\rho(1 + 2/\epsilon_r). \tag{4.10}$$

This means that the constant time of the circuit depends on the resistivity and on the dielectric constant of the material, and not on the area A. If ρ=10^{11} Ω·cm and ϵ_r=5, the constant time is of the order of 10 ms.

From Fig. 4.5 it is also possible to calculate the effective voltage V_g applied to the gas gap, from which depend the ionization and multiplication processes after the passage of a charged particle through the gas gap. Considering a macroscopic continuous current, the capacitors can be neglected and V_g can be expressed as follows:

$$V_g = V_0 - 2R_b i \tag{4.11}$$

where V_0 is the potential applied to the electrodes and i is the current flowing through the chamber. This equation provides an interpretation for the decrease of the efficiency with high counting rate: the current i is proportional to the counting rate so that for high values of the last one, V_g may fall under the required values for a good efficiency. On the other side, increasing the operating voltage is only of limited utility, because it causes as well a further increase of the current.

In conclusion, the electric scheme of Fig. 4.5 suggests that the recovering time of the voltage applied to the gas gap after a streamer depends on the electrode resistivity and that its value can be calculated by the displacement of the efficiency curve measured for high counting rate, with respect to the curve obtained for nearly null counting rate.

4.5 Environmental conditions

In order to be able to perform comparisons between data taken in different environmental conditions, temperature and pressure have to be monitored, because of their influence on gas density and consequently on the first Townsend coefficient as described in Section 4.2.

The influence of temperature and pressure on the gas density can be deduced from the equation of state:

$$\text{density} \propto \frac{nR}{V} = \frac{p}{T}. \tag{4.12}$$

The increase of the gas density (with increasing pressure or decreasing temperature) determines a shortening of the electron mean free path, namely a decrease of the gas gain, while the decrease of the gas density (with decreasing pressure or increasing temperature) induces an increase of the avalanche gain.

This implies that, for small changes of pressure and temperature, the voltage applied to the RPC electrodes, V_a, must be scaled to a given standard pressure p_0 and temperature T_0, according to the relationship [21, 22]:

$$V = V_a \frac{p_0}{p} \frac{T}{T_0}. \tag{4.13}$$

where the temperature must be expressed in Kelvin and the pressure in mbar. All the results presented in this thesis are rescaled using this formula with T_0=293.15 K (20°C) and p_0=970 mbar. For large changes of pressure and temperature the linear scaling of the voltage with the gas density is no longer true and more complex relationships have to be taken into account [23].

Moreover, the knowledge of temperature and of relative humidity is important because they influence the electrodes resistivity, thus affecting the rate capability of the detector [24]. Details about that will be given in Section A.

4.6 Linseed oil treatment

Linseed oil is a drying oil which contains mainly linolenic acid (50-65%), oleic acid (16-26%) and linoleic acid(14-24%). It readily absorbs oxygen from the air and polymerizes thus producing a hard, insoluble film when it dries. The drying property is due to the unsaturated bonds in the linoleic and linolenic groups. Linseed oil, largely used for paints and varnishes, has a resistivity of about 10^{11}–10^{12} Ω·cm.

At the end of the assembling process, the gas gap of the RPC is filled with boiled linseed oil diluted with n-penthane or epthane; then it is slowly drained away leaving a thin layer of oil on the inner side of the electrodes. The polymerization process, which results in the hardening of the oil layer, is speed up by forcing air circulation inside the gas gap from the gas inlets. Different dilution grades give different thicknesses of the final layer. At first, the oil was only slightly diluted (70% oil and 30% n-penthane) and the oiling procedure was repeated twice, with a resulting thickness of about 30–40 μm. Problems experienced by the RPCs produced for the BaBar experiment (see next section), have driven the choice to use a more diluted linseed oil (typically 30% oil and 70% n-penthane) and now oiling is usually performed only one time. The resulting layer is much thinner, of the order of 5-10 μm.

As explained in previous Section 4.2, the linseed oil layer hides the imperfections (such as scratches) of the electrode surface, so reducing the intrinsic noise of the detector, moreover it acts as a quencher by absorbing UV photons. Test carried out on RPC prototypes have demonstrated that the linseed oil layer does not affect the RPC efficiency [25].

4.7 The BaBar case

The BaBar experiment at SLAC [26] uses a detector composed of 774 RPC modules operated in streamer mode, for both muon identification and K_L detection. The total area of the RPCs is about 2000 m^2; the resistivity of the bakelite electrodes is 10^{11}–10^{12} Ω·cm; the gas mixture used was initially $Ar/C_2H_2F_4/C_4H_{10}$ with the respective percentages 48/48/4, later changed with the ones currently used: 59/37/4. The modules operate at cosmic–like

counting rate, with the exception of some of them that have to tolerate up to 5 Hz/cm^2.

The chambers were tested in Italy before having been used at SLAC and showed good performances: the average dark current was less than 10 μA/m^2, single rate was about 1 kHz/m^2 and the efficiency was higher than 95%. Installation started in May 1998, data taking at the end of that year.

Since the beginning of the operation, RPCs have suffered persistent efficiency decrease and dark current increase. Dark current problems were blamed to the rise of the temperature in the chamber zone that during Summer 1999 reached 33°C. In October 1999, a cooling system was installed in order to stabilize the temperature at 19–21°C, nevertheless the chambers did not recover the initial values of efficiency and dark current.

Several chambers were opened to check the inner surface conditions of the electrodes [27]:

- uncured linseed oil droplets had formed, some bridging the gap and forming electric–short spots;
- uncured linseed oil was accumulated around the spacers and the frame edges;
- chemical analysis discovered the presence of phthalates, which were not existing in original oil and which might prevent the linseed oil polymerization.

The first two points indicate that the oil coating was not completely cured.

In conclusion, the high temperatures reached and the presence of contaminating substances can explain the formation of the linseed oil 'stalagmites' that, in turn, can be the origin of the dark current and efficiency problems, as described in reference [27].

Tests have been carried out to look into the temperature effect: after raising the temperature to 36°C for 10 days, and then returning to room temperature, the dark current increases by a factor 5–9 and the efficiency drops by 9–17%. Another test show that even a moderate temperature rise to 28°C results in unrecoverable damage.

Concluding, the BaBar experience has suggested to rise the linseed oil dilution and to reduce the oil layer thickness, in order to ensure the proper polymerization. Moreover, it indicates that the detector temperature and the purity of the gas mixture must be kept under control.

In 2002 the BaBar collaboration installed over 200 2^{nd} generation RPCs in the forward endcap, while over 400 RPCs belonging to the original production

continued to operate in the barrel and in the backward endcap. At low rate, RPCs operated in streamer mode have proved to be reliable and efficient. During the data taking, good gas flow is found to be crucial, furthermore humidified gas is clearly necessary for long term operation.

Nevertheless, signs of ageing and efficiency loss are seen in the chamber exposed to higher rate (near to the beam line) while they are still efficient for the cosmic ray detection: this loss of rate capability can be probably ascribed to the high resistivity of the bakelite plates (10^{11}–10^{12} Ω·cm). Furthermore, a correlation between increased dark current, background rate and position in the gas flow string was found: this suggests that the downstream RPCs have been exposed to contamination in the gas produced in the first upstream RPC.

References

[1] J. Warren Keuffel, Review of Scientific Instruments, vol.20, N.3 (1949) 202

[2] V. V. Parkhomchuck, Yu.N. Pestov e N. V. Petrovikh, Nucl. Instr. and Meth. 93 (1971) 269

[3] Yu.N. Pestov e G.V. Fedotovich, Preprint IYAF 77-78, Slac Translation 184 (1978)

[4] Yu.N. Pestov, Nucl. Instr. and Meth. 196 (1982) 45

[5] R. Santonico and R. Cardarelli, Nucl. Instr. and Meth. 187 (1981) 377-380

[6] R. Santonico and R. Cardarelli, Nucl. Instr. and Meth. A 263 (1988) 20-25

[7] M. Bertino *et al.*, Nucl. Instr. and Meth. A 283 (1989) 654-657

[8] M. Iori and F. Massa, Nucl. Instr. and Meth. A 306 (1991) 159-168

[9] I. Crotty *et al.*, Nucl. Instr. and Meth. A 329 (1993) 133-139

[10] Y.H. Chang *et al.*, Nucl. Instr. and Meth. A 349 (1994) 47-55

[11] M. Alviggi *et al.*, Nucl. Instr. and Meth. A 508 (2003) 159-165

[12] E. Chiavassa, L. Ramello, E. Vercellin, *Rivelatori di particelle*, Torino 1991

[13] J.S. Townsend, *Electrons in gases*, Hutchinson, London (1947)

[14] H. Raether, *Electrons Avalanche and breakdown in Gases*, Butterworths, London (1964)

[15] P. Camarri *et al.*, Nucl. Instr. and Meth. A 414 (1998) 317-324

[16] M.Abbrescia *et al.*, Nucl. Instr. and Meth. A 398 (1997) 173-179

[17] R. Cardarelli *et al.*, Nucl. Instr. and Meth. A 333 (1993) 399-403

[18] I. Crotty *et al.*, Nucl. Instr. and Meth. A 337 (1994) 370

[19] E. Cerron Zeballos *et al.*, Nucl. Instr. and Meth. A 396 (1997) 93-102

[20] A. Di Ciaccio, Nucl. Instr. and Meth. A 384 (1996) 222-224

[21] P. Camarri *et al.*, Nucl. Instr. and Meth. A 409 (1998) 646-649

[22] M.Abbrescia *et al.*, Nucl. Instr. and Meth. A 359 (1995) 603-609

[23] R. Santonico, Nucl. Instr. and Meth. A 456 (2000) 1-5

[24] R. Arnaldi *et al.*, Nucl. Instr. and Meth. A 456 (2000) 140-142

[25] M. Abbrescia *et al.*, INFN/TC-96/14, (1996)

[26] BaBar - Technical Design Report, SLAC-R-95-457 (1995)

[27] Anulli *et al.*, Nucl. Instr. and Meth. A 508 (2003) 128-132

Chapter 5

Resistive Plate Chambers for the ALICE Muon Spectrometer

5.1 Detector characteristics

The choice of the trigger detectors for the Muon Spectrometer was driven by selectivity, rate capability, time and spatial resolution constraints and by the need to cover a large detection area. The requirements to be fulfilled are the following:

- muon detection efficiency $\geq$95%;
- spatial resolution not worse than 1 cm, necessary to perform the p_t cut;
- time resolution of 1-2 ns, to allow the identification of the bunch crossing;
- rate capability of the order of 100 Hz/cm^2, including a large safety factor (the maximum expected value is about 24 Hz/cm^2 for Ar–Ar at a luminosity of 10^{29} cm^{-2}s^{-1}, as shown in Section 3.6);
- readout granularity to cope with the expected hit density (2×10^{-3} hits/cm^2 in a central Pb–Pb collision);
- low sensitivity to γ and neutron background.

Resistive Plate Chambers offer different advantages with respect to competing detectors: a scintillator array would be too expensive and limited streamer tubes do not satisfy the required time resolution because the signal is spread over about 70 ns.

Collision system	Luminosity ($cm^{-2}s^{-1}$)	Months	Max hit rate (Hz/cm^2)	Integrated hits ($10^6/cm^2$)
Pb-Pb	10^{27}	6	3	18
Ar-Ar	0.6×10^{29}	2	24	48
d-Pb	1.1×10^{29}	2	15	30

Tab. 5.1: Heavy–ion program for the first ten years at LHC in the possible scenario described in Section 2.1.1. One month corresponds to 10^6 s of effective data taking and the maximum hit rate values already include a safety factor of 2.

Taking into account the requirements and the consideration listed above, the trigger detector for the Muon Forward Spectrometer of the ALICE experiment is single gap RPCs with low–resistivity bakelite electrodes (1–8×10^9 Ω·cm): the general structure of this detector has been described in Chapter 4 and shown in Fig. 4.1.

It must be remarked that the ALICE experiment will collect data for different colliding system resulting in a wide range of working conditions, that is to say that the requirements for the RPCs can vary from p–p collisions with respect to the heavy–ion ones.

In the following paragraphs are carefully illustrated the requirement differences for p–p and heavy–ion collisions concerning the ageing and the position resolution.

5.1.1 Ageing requirements

Since the ageing of the detector is strongly dependent on the integrated hits (i.e. the integrated current), we can assume that the lifetime requirement for our detector has to be of the order of 100 $Mhit/cm^2$ for the whole heavy–ion program (see Table 5.1 for the program of the first ten years considering one month/year of data taking). The obtained value has been calculated considering the rate value expected in the central part of the trigger system where the maximum irradiation is foreseen as pointed out in Section 3.6. In the external area of the Trigger planes, where a lower rate is expected, the lifetime required for the detector is about 25 $Mhit/cm^2$ for ten years of heavy–ion data taking. Furthermore, all these values already include a safety factor of 2.

Concerning the p–p program, present simulations [1] estimate a mean rate of 2 Hz/cm^2 on the whole surface with one high rate area of about 10 Hz/cm^2

due to the interaction of beam particles with the residual gas of the beam pipe (machine–induced background): the high rate area will interest 1 or 2 RPCs per plane. Even if these expected rates are not high, the 10^7 s/year p–p data taking (corresponding to about 8 month/year) leads to a lifetime requirement of about 100 Mhit/cm^2 per year for the RPCs covered by the high rate area and of about 20 Mhit/cm^2 per year for the other RPCs: this means that the total amount of integrated hits is, for the most irradiated RPCs, one order of magnitude higher than for the heavy–ion program and, for the other RPCs, a factor 2 greater with respect to the heavy–ion data taking.

5.1.2 Position resolution requirements

One of the aim of the Trigger System is to reject events due to background muons from pion or kaon decays with a cut on the muon transverse momentum p_t as described in Section 3.3. The p_t selection is implemented on the basis of the particle deviation: this information is provided by the two stations of the Trigger System and its accuracy is related to the position resolution of the RPCs.

In particular, the requirement on the cluster size and on the position resolution for the heavy–ion data taking is stringent, in order to minimize the occupancy of the readout strips and to preserve the selectivity of the trigger as discussed in Section 3.4.

Since the expected trigger rate is lower in p–p collisions with respect to the one in the heavy–ion program, the requirements on p_t cut, i.e. on the space resolution, are less stringent. Furthermore it is possible to accept larger cluster size for the p–p data taking, since the maximum occupancy is smaller.

5.2 Detector description

The two station of the Trigger System are made of 72 RPCs: the precise values of the external dimensions and of the active surface of these chambers are listed in Table 3.2 of Chapter 3.

The chambers are readout on both sides by means of two planes of orthogonal strips oriented along the horizontal (X) and vertical (Y) directions (perpendicular to the beam axis) and arranged in projective geometry. Width and length of the strips vary with the distance from the beam axis to keep the occupancy constant, because the background flux is higher in the zone close to the beam (see Section 3.6). Their widths are also conditioned by the position resolution needed for the p_t cut, as explained in detail in para-

graph 3.4. In Table 5.2 are reported the number of strips for each width, both in X and Y direction, while the strip length varies from 170 to 730 mm.

	strip X (horizontal)			strip Y (vertical)	
width (mm) MT1/MT2	10.6-11.3	21.2-22.6	42.4-45.2	21.2-22.6	42.4-45.2
nb. of strips	3840	8448	2688	3008	3008
total	14 976			6016	

Tab. 5.2: Number of strips for each width in X and Y direction.

Maps of the disposition of the strips on one quarter of the first plane of the first Trigger Station (MT11) are shown in Fig. 5.1 and Fig. 5.2: each row (L5–L9) correspond to one RPC.

All strip planes have been produced at the I.N.F.N. Technological Laboratory of Turin: in Fig. 5.3 is shown the engraving process of the copper foil coupled with a mylar sheet. In Fig. 5.4 is presented one of the completed strip planes: two foils of engraved copper, one with the strips and one for the ground connection, are glued on both sides of a 3 mm styrofoam sheet.

The stiffener planes, that lodge the gas gap and the reading planes, are made up of nomex (8.8 mm thick) enclosed between two 0.6 mm aluminum sheets. The strips planes and the stiffener ones are coupled by means of the connectors that, passing through the stiffener plane, bring the signal from the strips to the Front End Electronics as sketched in Fig. 5.5.

Strip planes, drilling of stiffener planes, mounting of FEE connectors and mechanical support have been realized in the I.N.F.N. Technological Laboratory, as well as the final assembly.

5.3 Performance of low-resistivity RPCs operating in streamer mode

ALICE is the only experiment at LHC dedicated to the study of the heavy–ion collisions, so that the RPCs have been optimized to cope with the constrain given by physic studied in such collisions.

The maximum expected rate on the trigger planes will be of the order of 25 Hz/cm^2 (in Ar–Ar collisions) and can be tolerated in streamer mode; in addition, the high signal to background ratio of a streamer gas mixture allow to achieve a cluster size value lower than the one obtained working in avalanche mode, thus providing a high trigger selectivity (see Section 3.4).

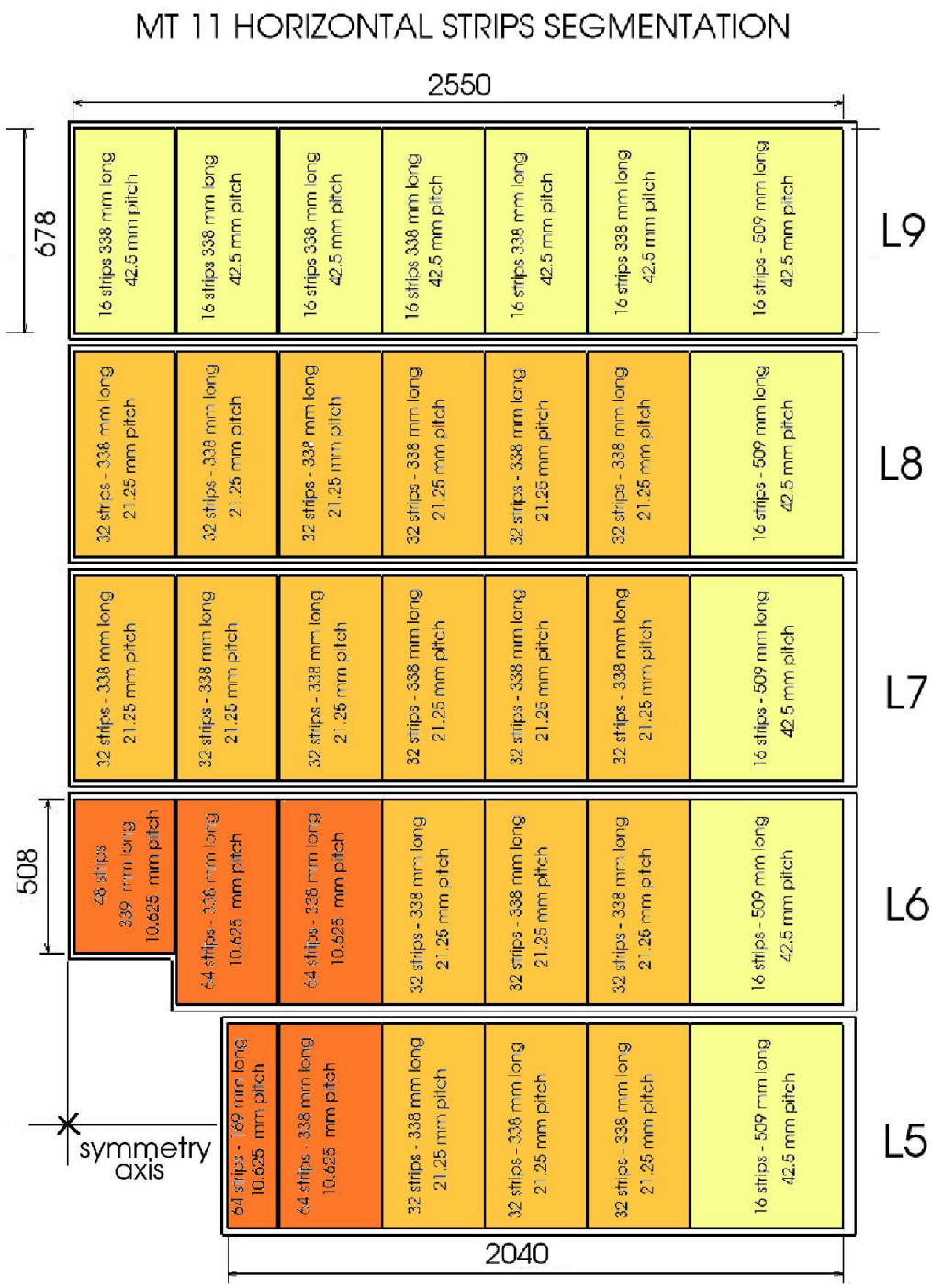

Fig. 5.1: Map of the X strips for one quarter of the trigger plane MT11. The color indicates different strip pitches while the number of strips and their length are displayed on the figure. The other quarters of the Trigger Plane are built symmetric with respect to the symmetry axis shown in Figure.

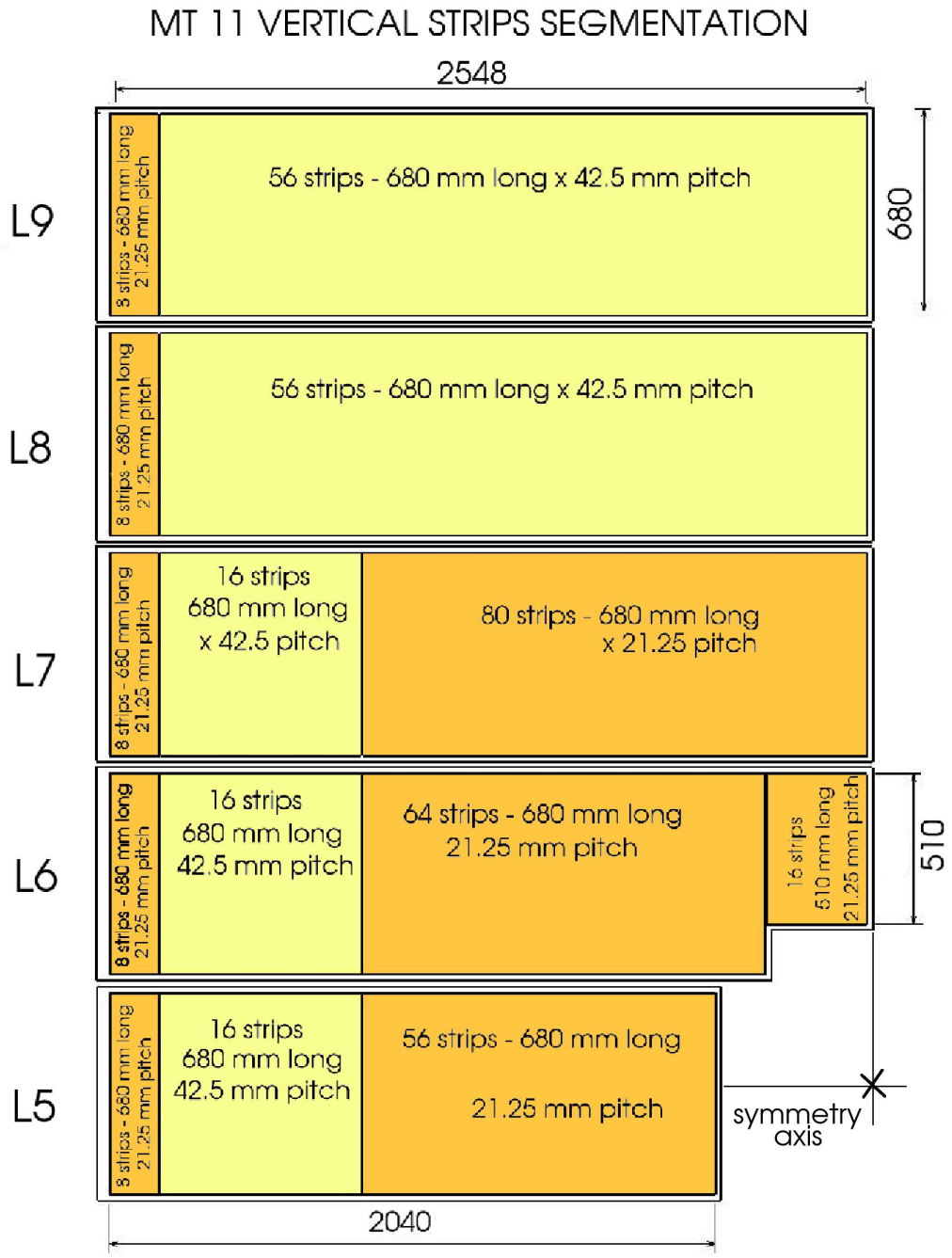

Fig. 5.2: Map of the Y strips for one quarter of the trigger plane MT11. The color indicates different strip pitches while the number of strips and their length are displayed on the figure. The other quarters of the Trigger Plane are built symmetric with respect to the symmetry axis shown in Figure.

Fig. 5.3: Engraving process of the strip planes produced at the Technological Laboratory of Turin.

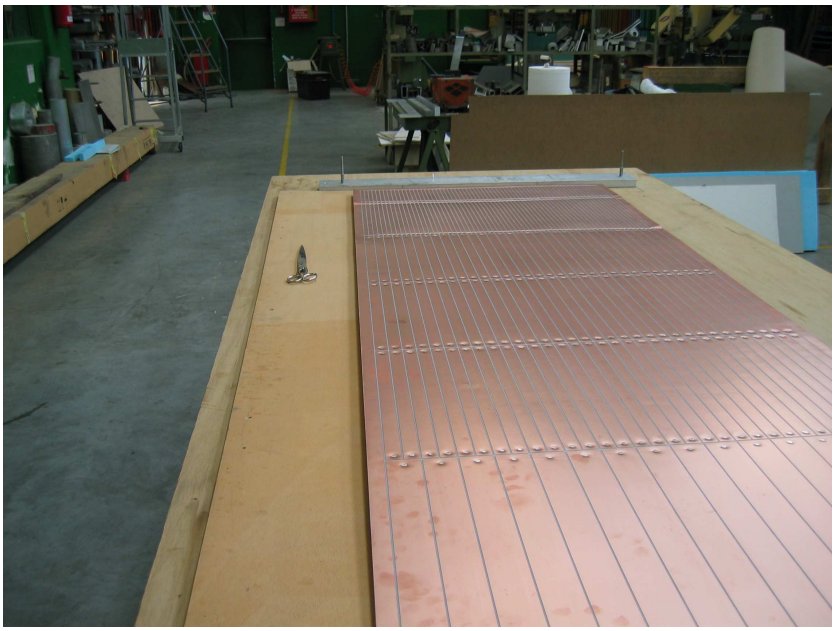

Fig. 5.4: Strip plane produced at the Technological Laboratory of Turin. In this picture the strip plane is already coupled with the stiffener planes by means of the signal connectors.

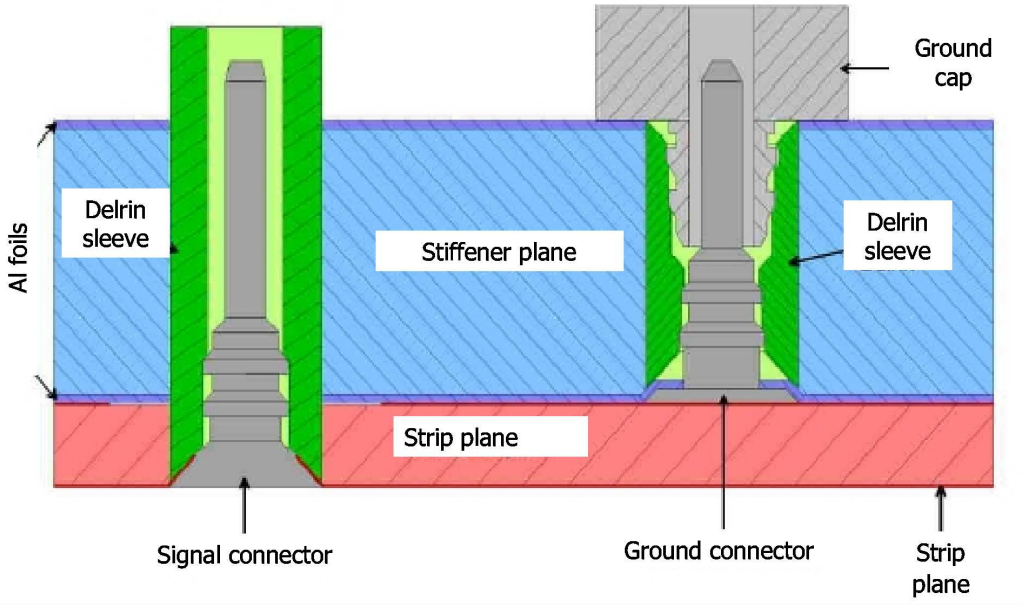

Fig. 5.5: Mechanical scheme of the connector mounting.

These circumstances have persuaded the Trigger collaboration to focus the efforts to the optimization of the RPCs operated in streamer mode.

Tests on small RPC prototypes (50×50 cm^2) have demonstrated that low–resistivity RPCs working in streamer mode with a gas mixture composed of 49% Ar, 40% $C_2H_2F_4$, 7% C_4H_{10} and 4% SF_6 can provide the performance reported in Table 5.3 and described in details in reference [2, 6, 7].

Rate capability (uniform illumination)	$\simeq$300 Hz/cm^2
Time resolution RMS (ADULT)	$\leq$2 ns
Cluster size (strip) for 2 cm strips	1.12
Cluster size (strip) for 1 cm strips	1.5
Position resolution with 1 cm strips	$\leq$2.5 mm
Dark current (current drawn in the absence of irradiation)	1-2 μA
Single rate	$\sim$0.1 Hz/cm^2

Tab. 5.3: Summary of the performances of a 50×50 cm^2 low-resistivity RPC

Values of Table 5.3 fulfill, with large safety margins, all the requirements for the ALICE Muon Trigger reported at the beginning of this Chapter in Section 5.1.

In particular the time resolution has been achieved with a technique especially developed by the Trigger Collaboration and described in the next paragraph.

5.3.1 Time resolution and ADULT: A DUaL-Threshold discrimination technique

To get the RPC signal in a 25 ns wide gate, given by the LHC clock, it is required an intrinsic time resolution of 1–2 ns, since the other variables, like delay adjustment and cable length, produce a relevant spread in the time distribution of the signals.

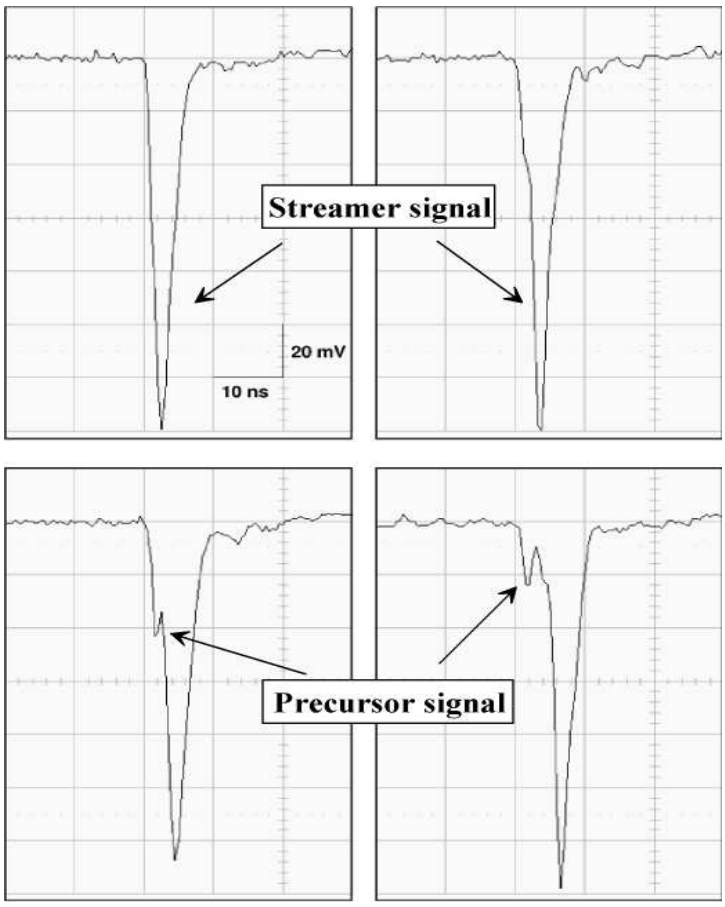

Fig. 5.6: Typical pulses picked–up on a RPC operated in streamer mode, with a digital oscilloscope (1 GHz bandwidth) via a short BNC cable (50 Ω impedance).

The typical shape of RPC pulses in streamer mode, picked-up with an

oscilloscope and shown in Fig. 5.6, has the following features:

- a first signal, called precursor (Fig. 5.6, bottom), with typical amplitude of 20-50 mV, rise time of 2 ns and width of 5 ns, which is fixed in time relatively to the particle passage through the chamber;
- a second signal, due to the streamer, which may be delayed from the precursor by a time (typically of the order of several nanosecond) whose mean value depends on the applied voltage on the RPC and which shows non negligible event-by-event time jitter.

Only at high working voltages it is possible to reduce the jitter of the streamer and to obtain a good time resolution, but this operation has the drawback of the degradation of the cluster size. Otherwise we should lower the discrimination thresholds so to detect the precursor signal, but this would increase the single rate as well as the cluster size.

To improve the time resolution, the Trigger Collaboration has studied a new-concept discrimination: ADULT (A DUaL Threshold discrimination technique) [2, 3] based on the shape of the streamer signal.

Two single threshold discriminators per channel are used:

- a low threshold (10 mV) to detect the avalanche precursor;
- a high threshold (typically 80 mV) to confirm the streamer signal formation.

The two out–coming signals, with the low threshold one delayed by 15 ns, are sent to a coincidence. In this way, the time reference is given by the avalanche precursor and efficiency, cluster size and single rate depend on the streamer signal which is well above the noise. A comparison of time distributions obtained by means of the ADULT technique with respect to the results given by single–threshold discriminators in the same operating conditions is shown in Fig. 5.7: with ADULT we obtain a very narrow peak ($\sigma \leq 1$ ns) already for high voltages corresponding to the efficiency plateau knee, preserving in this way a low cluster size.

The RMS of the time distribution, in a 25 ns gate, are summarized in Fig. 5.8, with ADULT and with a single–threshold discriminator: a time resolution of about 1.5 ns is obtained with ADULT quite independently from the operating voltage [4].

The ADULT technique is implemented in the ALICE trigger front-end chip integrated on the Front End Board (Fig. 5.9): a scheme of one ADULT channel is shown in Fig. 5.10. The chip is built in AMS BiCMOS 0.8 μm technology and, in addition to the ADULT stage, it includes a "one–shot" system,

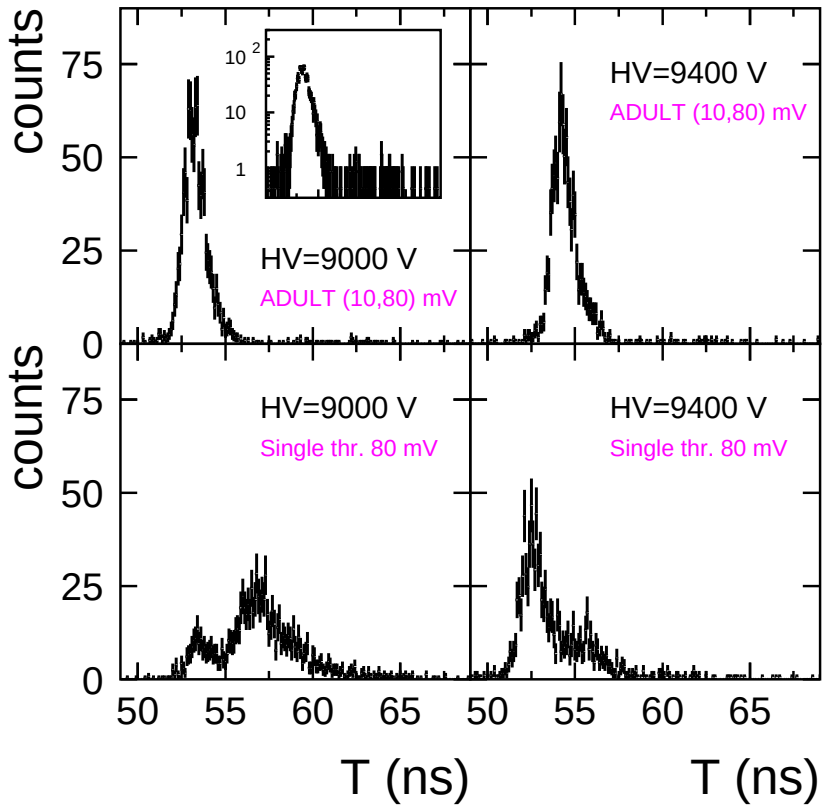

Fig. 5.7: Top: time distributions obtained with ADULT (low threshold at 10 mV and high threshold at 80 mV); the left plot is also shown in logarithmic vertical scale. Bottom: time distributions obtained in the same operating conditions with single threshold discriminators (threshold=80 mV). The plateau knee is at 8800 V.

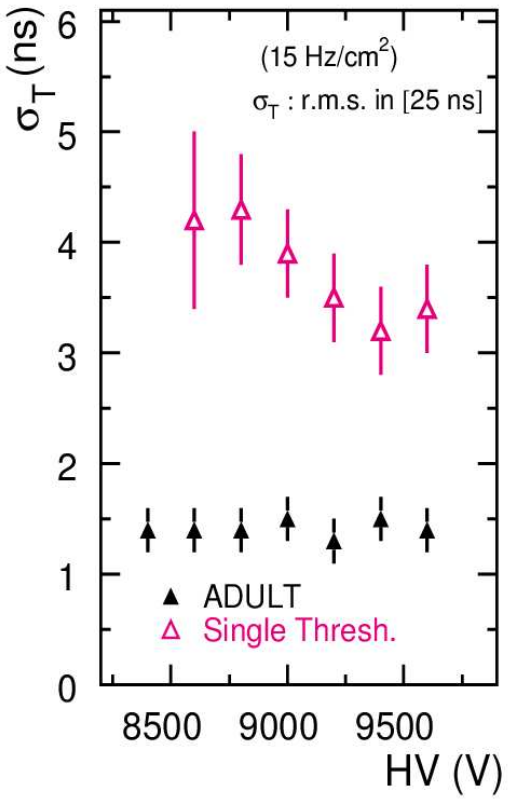

Fig. 5.8: Time resolution, as a function of the applied voltage, in a 25 ns gate, with ADULT and with a single–threshold discriminator.

which prevents re–triggering within 100 ns, and a remotely–controlled delay (up to 50 ns) to synchronize the outputs of the 21,000 channels of the trigger detector. The output signals from the front–end have a width of 20 ns to be associated to a well defined bunch crossing at LHC.

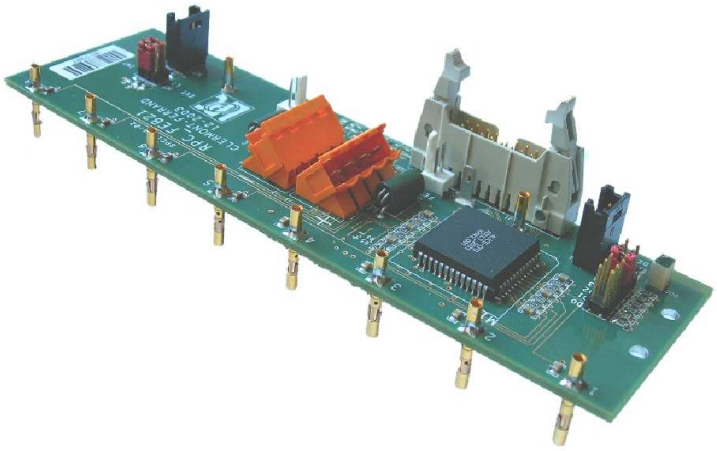

Fig. 5.9: Front End Board for 2 cm pitch wide strips.

The threshold values are fixed by default at 10 and 80 mV; it is nevertheless possible to access them by means of an external control. An adjustable delay is foreseen to compensate for the different signal cable length.

Test have been performed to check the radiation hardness in condition close, or worse, than the expected one in the ALICE working environment and no problem has been observed [5]. Production and test of all FEE cards are presently completed.

5.3.2 Results of ageing tests on small RPC prototypes

To simulate the effect of years of operation in the ALICE environment, several 50×50 cm^2 prototypes have been exposed to the γ flux from the ^{137}Cs source of the Gamma Irradiation Facility at CERN.

Four small prototypes have been tested since June 2001 with:

- different construction characteristics such as the number of linseed oil layers (single, double and triple);
- different operating conditions:
  - gas mixture humidity;

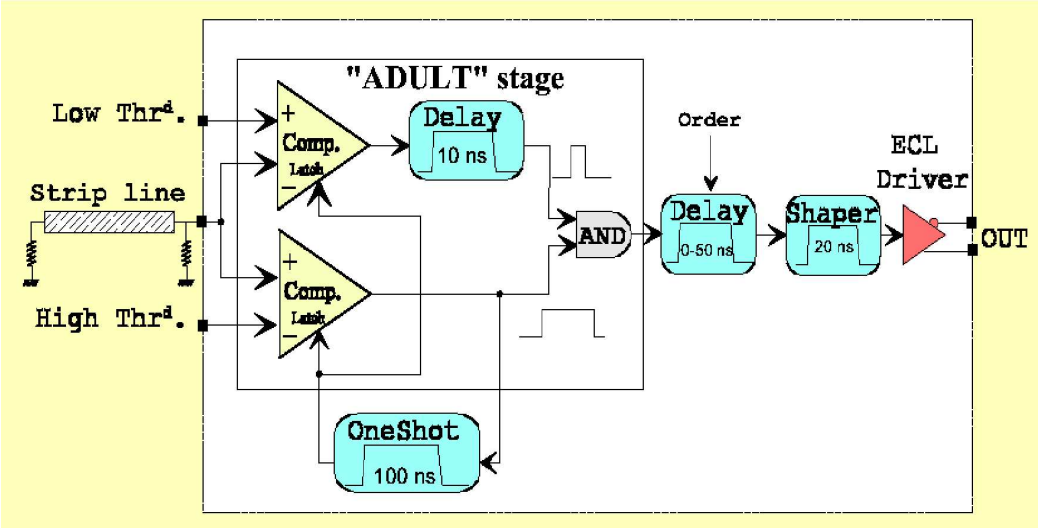

Fig. 5.10: Block diagram of a single channel of the ADULT chip

– percentage of SF_6 (1 and 4%).

Despite an observed dark current increase, the efficiency for cosmic rays was stable for a period equivalent to 10 years of heavy-ion data taking for all tested RPCs.

Nevertheless, the results of this test indicate that with a double layer of linseed oil we obtain a noticeable improvement in matter of ageing: the increase of the current and of the rate without irradiation persists but it is slower than the single-oiled chamber one; moreover, the maximum value reached at the end of the ageing is lower for chambers flushed with the streamer mixture with 1% of SF_6 with respect to the one with 4% of SF_6 [8,9].

On the basis of these considerations the SF_6 percentage has been lowered to 1% and the streamer gas mixture for ALICE will therefore be: 50.5% Ar, 41.3% $C_2H_2F_4$, 7.2% C_4H_{10} and 1% SF_6. Furthermore, since no relevant improvement for the triple linseed oil layers were found, all produced RPCs have a double layer of linseed oil.

5.4 Preliminary test with a highly–saturated avalanche gas mixture

As described in Section 5.1, the severe requirement on position resolution for the heavy–ion program is accompanied by a lower integrated rate, while the p–p operations have less stringent requirements on p_t selection and on the

position resolution but an harsh requirement on the detector lifetime hardly achievable operating the RPCs with streamer gas mixture.

According to the specific aspects of p–p data taking for ALICE and in particular to the ageing requirements, an operation mode referred as highly–saturated avalanche was investigated. As a matter of fact, the R&D carried out by ATLAS and CMS demonstrated that operation in avalanche mode results in a higher detector lifetime (up to 200 mC/cm^2) compared to streamer [10–12].

The main goal of this research was actually to investigate if it is possible to work in highly–saturated avalanche mode with our dual-threshold Front End Electronics (ADULT) specially developed to improve the timing performance in streamer mode. Indeed, this electronics does not include an amplification stage, but a minimum threshold value of 10 mV is achievable by means of and external control.

Among several highly quenched mixtures studied with cosmic rays in the Clermont–Ferrand Laboratory with a 50×50 cm^2 RPC, a mixture composed of 88% $C_2H_2F_4$, 10% C_4H_{10} and 2% SF_6 has been finally selected [13]. A detailed study to get running performances in such conditions and in conjunction with our FEE has been undertaken. In particular, the functioning plateau width, which should not be less than 400 V, has been investigated.

The FEE thresholds has been set at 10 mV for the efficiency measurement; the shape of each signal is sampled each nanosecond to study amplitude, timing and released charge. The analysis of the signal provide the streamer contamination which can be correlated to the efficiency as shown in Fig. 5.11: considering the voltages providing efficiency higher than 90% and streamer contamination lower than 20%, a 600 V plateau width (marked by the two dotted vertical lines in Fig. 5.11) is achieved.

This test therefore demonstrated that it is possible to work in highly–saturated avalanche mode with our FEE obtaining a plateau width of 600 V and working point of about 11000 V.

In conclusion, to fulfill the scenarios of the different colliding systems, and having the possibility to use the same FE electronics both in streamer and in highly–saturated avalanche mode, we have performed ageing and beam tests with different gas mixtures:

- a quenched streamer mixture (50.5% Ar, 41.3% $C_2H_2F_4$, 7.2% C_4H_{10} and 1% SF_6, RH=50%) with excellent position resolution (2.5 mm for 1 cm wide strips) and low cluster size (1.5 for 1 cm wide strips), gas mixture appropriate to the heavy-ion operations [6];

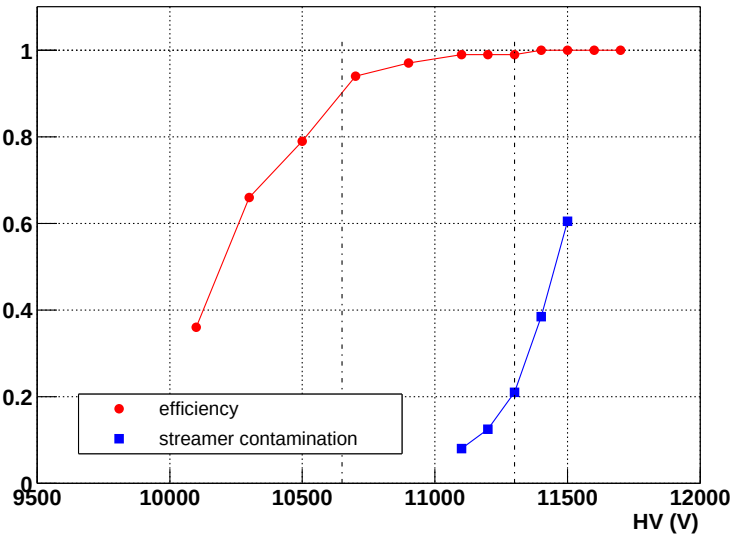

Fig. 5.11: Efficiency plateau and streamer contamination as a function of the applied voltage. The two dotted vertical lines refer to efficiency higher than 90% and streamer contamination lower than 20%.

- a highly–saturated avalanche mixture (~90% $C_2H_2F_4$, 10% C_4H_{10} and different percentages of SF_6, RH=50%) with better ageing properties but with larger cluster size, this gas mixture is suitable for the p–p program.

The drawback of the highly–saturated avalanche running mode, called hereafter maxi–avalanche mode, is that it is mandatory to use the external control of the Front End Electronic cards to set the threshold: this implies a more complicated setup for the final installation of the Trigger System.

All tests presented in this thesis have been performed with RPCs fully equipped with Front End Electronic cards with the ADULT chip. The thresholds are set at:

- 10 mV/80 mV for the streamer mode;

- 10 mV/10 mV for the maxi-avalanche mode (as the two thresholds are set at the same value, the ADULT chip works as a standard single threshold discriminator).

5.5 Test Bench for final RPCs validation

In summary, as far as concern the gas gap, the strip and the stiffener planes and the front-end electronics, we can consider ended our R&D and the production has started at the beginning of the year 2004.

A total amount of 120 gas gap have been produced at the General Tecnica: among these, 72 gaps will be employed in the two station of the ALICE Trigger System as described in Section 3.3; the remaining ones will be used as spares.

In order to select the best possible detectors and to build a reserve of spares, we are testing all the produced gaps: gas tightness and spacer gluing were tested at INFN–LNGS with the "push test" [14], while the Technological Laboratory of Turin houses the test bench station to validate the assembled RPCs performing test with cosmic rays.

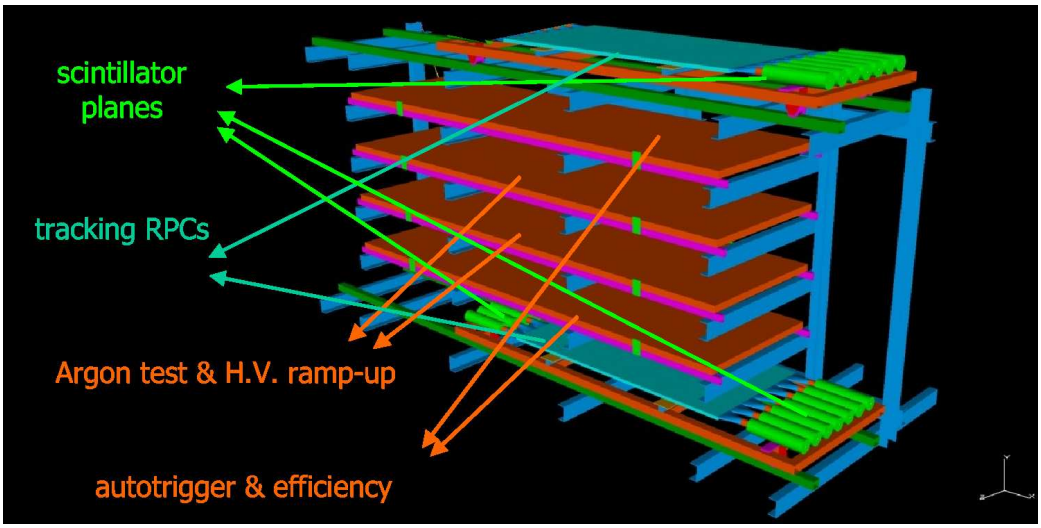

Fig. 5.12: Picture of the test bench station for the validation of the produced RPCs (Technological Laboratory of Turin).

The test station is shown in Fig. 5.12 and consists of:

- 3 plane of plastic scintillators (9 per plane);
- 2 RPCs for tracking the cosmic rays at a distance of about 180 cm;
- 4 slot to house the RPCs under test (at a distance of 30–35 cm the one from the other):
  - the 2 central ones are used for the Argon test and the high voltage ramp–up;

– the top and bottom positions, characterized by a more uniform acceptance of the cosmic ray trigger, are employed for efficiency measurement and the complete test of the chambers.

The cosmic ray trigger is provided by the coincidence of the 3 scintillator planes together with the 2 tracking RPCs, it covers a total area of about 90×150 cm^2: we therefore test two half–chamber at the time.

All tested RPCs are equipped with the final FEE with the ADULT chip. The tests are made with the ALICE streamer gas mixture (50.5% Argon, 41.2% $C_2H_2F_4$, 7.3% C_4H_{10} and 1% SF_6, RH=50%) and include:

1. the electrodes resistivity measurement flowing the RPCs with pure Argon. When the HV applied to the gas gaps reaches a value of ∼2000V, Argon starts to conduce electrons. The UV rays, emitted in Ar^+–e^- recombinations in the gas or at the cathode, are not stopped by any quencher and induce emission of electrons from nearby Ar atoms; the Ar therefore becomes a conductive plasma which short-circuits the electrodes. The measure of the current–voltage relation above the critical HV value allows to determine the ohmic resistance of the bakelite electrodes, and thus their resistivity.

2. Rate and distribution of single counts hits measurement with the "autotrigger" (self–triggering) method. In this case the trigger is provided by the coincidence of the logic OR of the two strip planes. The measurement is repeated over a wide high voltage range (7100÷8300 V).

3. Mapping of the efficiency as a function of the applied voltage with coarse resolution (20×20 cm^2 cells obtained with the tracking). The efficiency plateaux are fitted and the following parameters are extracted:

   - maximum efficiency values;
   - voltage giving an efficiency of 50% and of 90%;
   - slope of the curve in the linear region.

4. High resolution (2×2 cm^2 cells) mapping of the RPC efficiency for two HV setting close to the working point.

The test provides a complete characterization of the detector (efficiency, cluster size, absorbed current, single counts rate ...). Test results are organized in a database, all gaps will have an "identity card" where all the collected information will be stored: resistivity of the bakelite, ohmic resistance, ramp-up history, map and intensity of dark hits, dark current, efficiency curves and maps. This allows for an accurate choice of their final destination (accepted, spare or rejected).

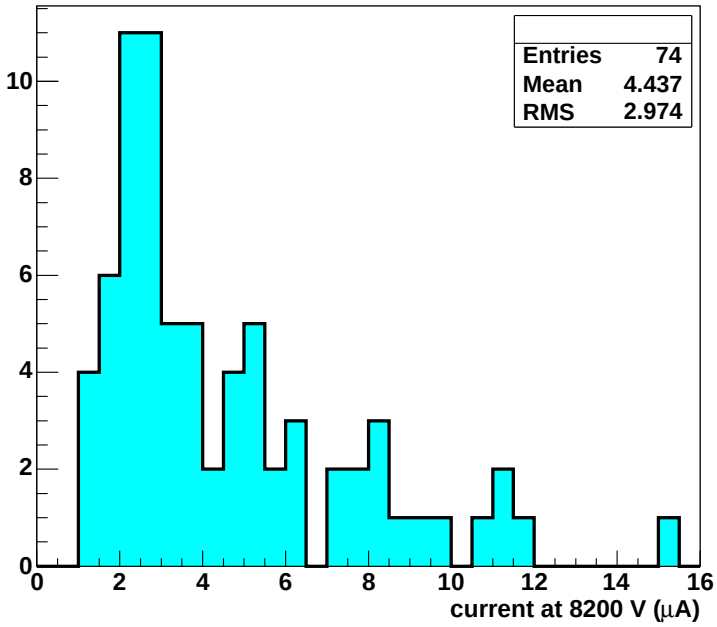

Fig. 5.13: Distribution of dark current at 8200 V for 74 tested RPCs.

After the test, RPCs are rejected in case of:

- noisy spots hotter than 50 Hz/cm^2;
- dark current >8 μA or leakage current >0.5 μA at 5000 V.

The chambers will be accepted only if they show:

- good efficiency uniformity, i.e. all the HVs corresponding to 50% efficiency measured on the 20×20 cm^2 cells must stay in a 300 V range;
- high efficiency, greater than 90% in all the 2×2 cm^2 cells of the active area (spacers excluded).

In Fig. 5.13 the dark current for the tested RPCs are shown; up to the end of 2005, 74 chambers have been tested:

- 12 gaps show high current and high noise rates;,
- on 1 gap, an efficiency hole (6×6 cm^2) has been found, but no gaps have been discarded because of efficiency disuniformity.

A total of 61 gaps have been accepted and are ready for installation in the ALICE cavern foreseen for March 2006. The test is still in progress.

References

[1] R. Guernane, A. Morsch and E. Vercellin, ALICE Internal Note ALICE-INT-2003-41

[2] R. Arnaldi *et al.*, Nucl. Instr. and Meth. A 457 (2001) 117–125

[3] F. Jouve, Ph. Rosnet, L. Royer *et al.*, Production Readiness Review, ALICE-EN-2003-020

[4] P. Dupieux, Nucl. Instr. and Meth. A 508 (2003) 185-188

[5] Ph. Rosnet and L. Royer, arXiv:hep–ph/0501045 v1

[6] R. Arnaldi *et al.*, Nucl. Instr. and Meth.. A 451 (2000) 462–473

[7] R. Arnaldi *et al.*, Nucl. Instr. and Meth.. A 490 (2002) 51–57

[8] R. Arnaldi *et al.*, Nucl. Instr. and Meth.. A 533 (2004) 112-115

[9] G. Travaglia, Ph.D Thesis, Università degli Studi di Torino e Università degli Studi di Messina, February 2004
http://www.to.infn.it/pinot/documents/PHDtheses.html

[10] G. Aielli *et al.*, Nucl. Instr. and Meth.. A 478 (2002) 271-276

[11] G. Aielli *et al.*, Nucl. Instr. and Meth.. A 533 (2004) 98-101

[12] M. Abbrescia *et al.*, Nucl. Instr. and Meth.. A 533 (2004) 102-106

[13] F. Yermia, Ph.D Thesis, Università degli Studi di Torino, February 2005
http://www.to.infn.it/pinot/documents/PHDtheses.html

[14] A. Bergnoli *et al.*, Nucl. Instr. and Meth.. A 533 (2004) 203-207

Chapter 6

Beam tests

6.1 Introduction

In the previous Chapter I have described the performances of small RPC prototypes (50×50 cm^2): these studies demonstrated that the requirements for the ALICE Trigger System are fulfilled. However, as the dimensions of the RPCs employed in ALICE are about 70×280 cm^2, we need a validation of the obtained results for full–size RPCs. Furthermore, the big size of the ALICE chambers points out the problem of the uniformity of the performances on the whole active surface; the main causes of dis–uniformity can be related to:

- difference in the gas gap width, either for construction reason or for stress induced by the external mechanics;
- bad graphite layer quality;
- problems with the strip planes.

This Chapter is devoted to the description of beam tests on a pre–production RPC and on three chambers belonging to the final production. These tests have been carried out with the streamer gas mixture (50.5% Ar, 41.3% $C_2H_2F_4$, 7.2% C_4H_{10}, 1% SF_6, RH=50%) and with the highly–saturated avalanche mixture (88% $C_2H_2F_4$, 10% C_4H_{10}, 2% SF_6, RH=50%).

The goal of the beam tests, performed with μ beam from CERN–SPS (X5) and γ irradiation at the Gamma Irradiation Facility (GIF) [2], is the study of the uniformity of full size RPCs with respect to the plateau position and to the rate capability.

6.2 Preliminary test with cosmic rays

Previous tests have highlighted that a possible cause of dis–uniformity is the curvature of the stiffener planes which can press the gas gap producing a difference on the plateau position in different zones of the chamber. As a matter of fact, the initial project of the external mechanics foresaw curved stiffener planes: in particular the gap is mainly squeezed in the central region parallel to the long side of the RPC: measuring the efficiency plateau position we get a difference between the central position and the lateral ones of about 800 V [1].

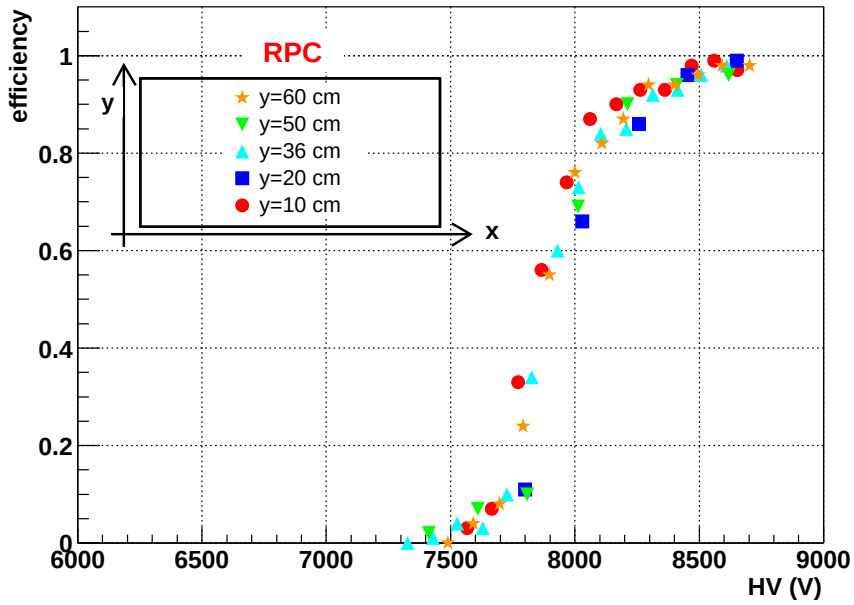

Fig. 6.1: Efficiency plateaux measured at fixed X and for different value of Y: 10, 20, 36, 50 and 60 cm; the position of the tested areas are reported in the sketch inside the plot. The RPC is closed with flat stiffener planes.

In Spring 2003 we have tested a pre–production RPC (72×210 cm^2) with cosmic rays in the laboratory of Turin. The chamber is closed with flat stiffener planes, as it was not possible to produce planes with a controlled curvature to reduce the effect of the pressure on the gas gap. The trigger is provided by the coincidence of three scintillators covering about 10×10 cm^2. The efficiency plateaux have been measured at fixed X and for five different value of Y: 10, 20, 36, 50 and 60 cm (the X and Y axis are reported in

Fig. 6.1). The results are plotted in Fig. 6.1: no dis–uniformity can be noticed and therefore flat stiffener planes will be used for final RPCs.

6.3 Setup description

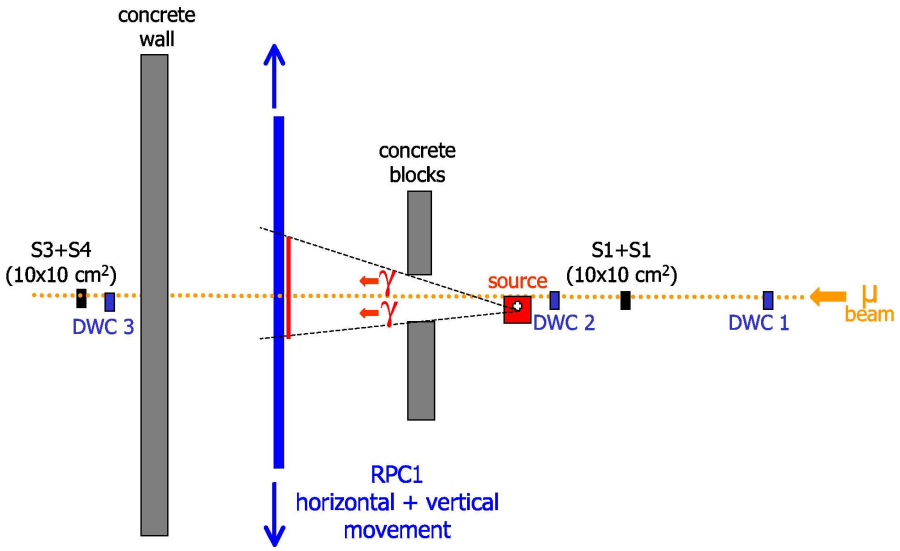

Fig. 6.2: Experimental setup for the beam test, not in scale (top view).

The experimental setup, the same for all performed tests, is sketched in Fig. 6.2 and includes:

- the RPC under test, fully equipped with Front End Electronic cards (FEE with the ADULT chip) and two orthogonal strip planes segmented as foreseen in ALICE. The mechanical support of the chamber allows to move the RPC with respect to the beam, both horizontally and vertically, to measure the efficiency plateau in different areas of the chamber itself.

- The trigger is given by 2 pairs of scintillators which cover a total area of 10×10 cm^2 (S1 and S2 placed before the γ source, S3 and S4 behind the back concrete wall).

- The ^{137}Cs γ source of the GIF[1].

[1]More details about the Gamma Irradiation Facility are reported in Section 7.2

- Three Delay Wire Chambers (DWC1, DWC2 and DWC3) to track the beam muons.

To lower the total current on the RPC, two concrete blocks shield the chamber from the γ–rays from the ^{137}Cs source: in this way only a part of the RPC is under irradiation, condition similar to the one that will occur in ALICE, where a not uniform irradiation is expected.

To check the homogeneity of the RPC we measure the efficiency plateau in different zones of the chamber, both with and without γ induced rate, varying the γ flux with the GIF absorbers.

The data acquisition has been realized with the DATE system (Data Acquisition and Test Environment), the software framework developed at CERN for the ALICE DAQ system. The signals discriminated by the FEE are sent to an LVDS to ECL converter and through a programmable delay to pattern units (Coincidence Register with a 100 ns gate) and to scalers for efficiency and counting rate monitoring; some of these signals were also sent to TDCs for timing analysis. Furthermore, the LVDS to ECL converter provides the logic OR of the 16 inputs, also sent to scalers. The block scheme of the electronics is presented in Fig. 6.3, while in Fig. 6.4 is shown how the muon beam trigger, given by the coincidence of the scintillator hodoscope with the burst, is distributed to the CAMAC modules (TDC, Coincidence Register and Status A for the interrupt handling).

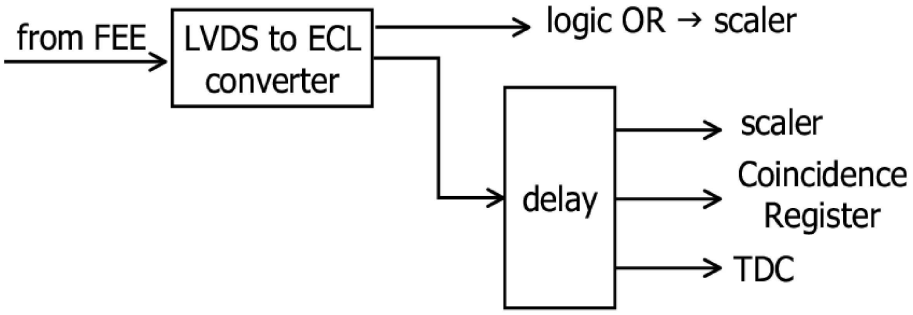

Fig. 6.3: Block scheme of the electronics for the RPC signals.

6.4 Data analysis

The efficiency of the chamber is calculated using the Coincidence Register information. For each tested position we define, with a preliminary analysis,

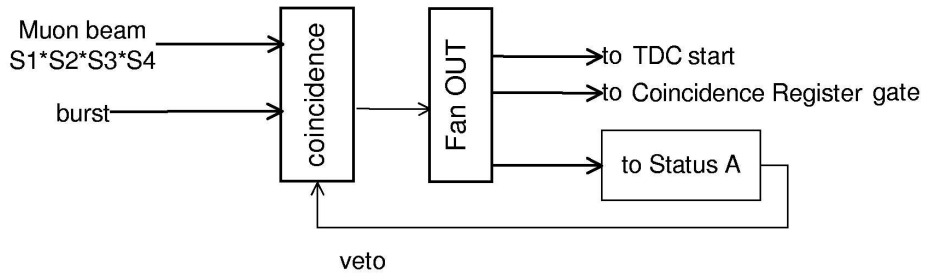

Fig. 6.4: Block scheme of the trigger distribution for the beam test.

the range of X and Y strips covered by the trigger: the RPC is considered efficient if there is one or more hits on these strips in the analyzed event.

We thus calculated the efficiency of the plane X, of the plane Y and of the coincidence of the two planes.

The obtained efficiency plateaux are fitted with the integral of a Gaussian with variable sigma:

$$efficiency(HV) = \int_0^{HV_{max}} exp(\frac{1}{2}\frac{(HV - par[1])^2}{\sigma^2(HV)})dHV \qquad (6.1)$$

with σ defined as:

$$\sigma(HV) = par[2] + par[3]\frac{HV - par[1]}{par[2]} \qquad (6.2)$$

The fit parameters allow us to obtain:

- A, the maximum efficiency of the plateau;
- B, the slope of the plateau in the linear region;
- V_0, the high voltage giving the 50% of the maximum efficiency A;
- ΔV, the high voltage interval between 10 and 90% of the maximum efficiency A.

Once these parameters are obtained it is possible to get the efficiency of the chamber at a given voltage or the high voltage that gives a fixed efficiency; considering all the values obtained in the different tested positions, it is possible to get the distribution of a particular parameter over the whole surface of the RPC under test.

The DWC information is used to track the muons and to check the shape and the intensity of the beam projection on the RPC.

6.5 Test of a pre–production RPC

In September 2003, we have tested a pre–production RPC (RPC1) with μ beam from CERN–SPS (X5) and γ irradiation at GIF, both in streamer and in maxi–avalanche mode.

RPC1 was fully equipped with strip planes segmented as foreseen for the central chamber of the first trigger plane MT1 (i.e. 1, 2 and 4 cm wide strips, as described in detail in Section 5.2, Fig. 5.1 and Fig. 5.2). In Fig. 6.5 is shown a sketch of RPC1 concerning the spatial coordinates, the strip numbering and the position of the gas inlets and outlets.

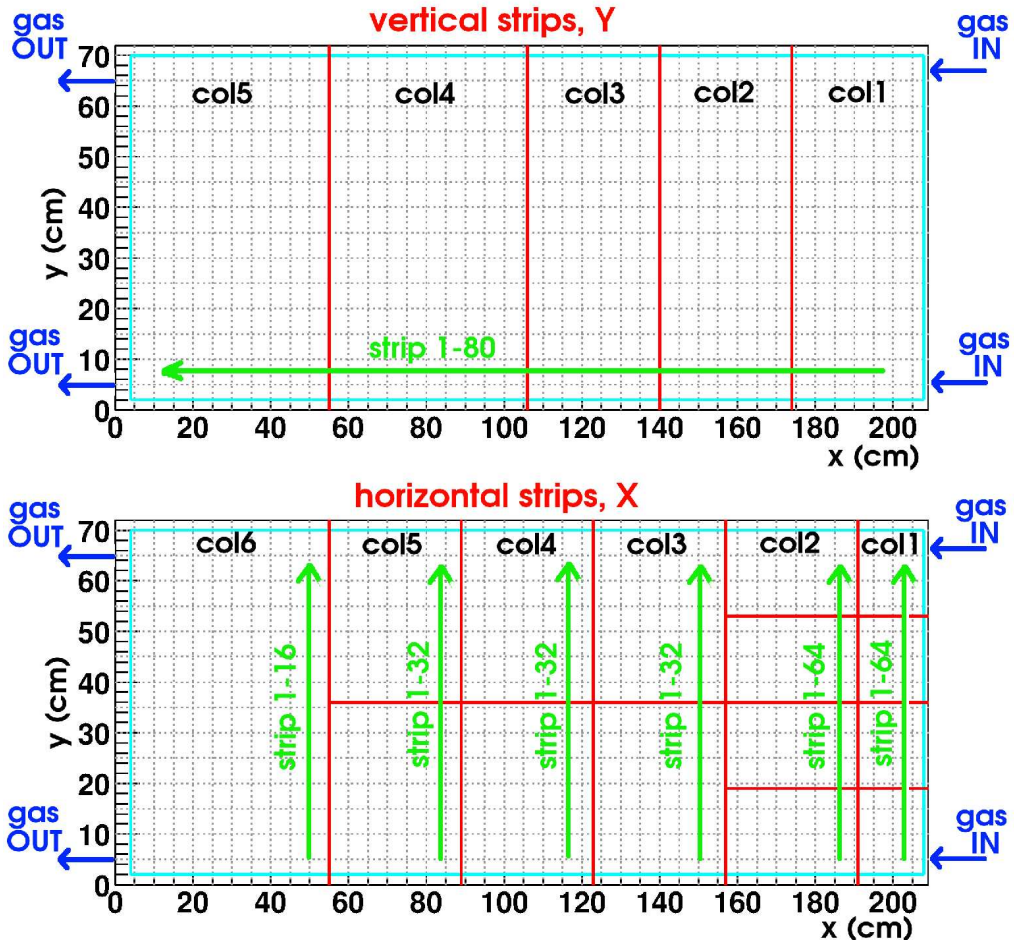

Fig. 6.5: Sketch of RPC1 (210×72 cm^2): spatial coordinates, strip numbering,inlets and outlets of the gas. The chamber is virtually divided into column (col1, col2 ...) identified by the strip segmentation.

The beam intensity varied from ∼400 to ∼10000 muons/burst, giving different rates and different μ distribution on the chamber: for the most part of the test the μ mean rate on RPC1 was ∼17 Hz/cm^2, reaching 35–40 Hz/cm^2 in the central part of the beam spot (see Fig. 6.6). It must be pointed out that we do not had the control of the beam intensity as well as of its focusing, since we worked in parasitic mode.

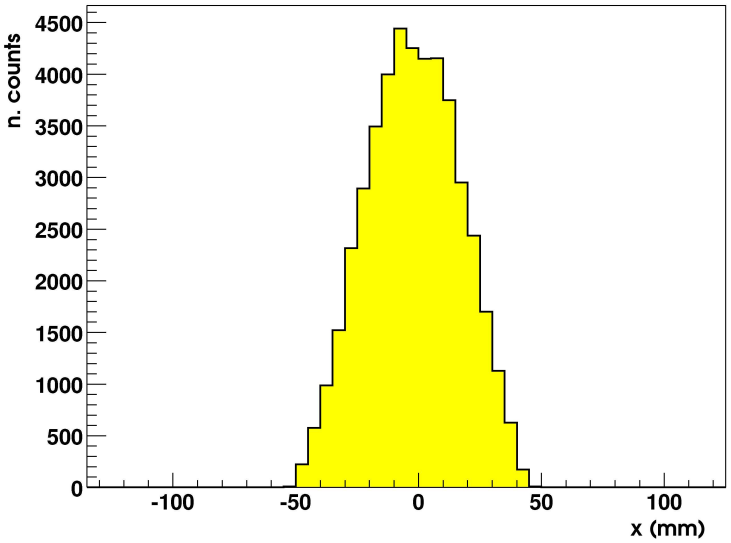

Fig. 6.6: Beam pattern on the 10×10 cm^2 DWC; the histogram refers to the X coordinate of the second DWC, the profiles of the Y coordinate and of the first DWC are similar.

Only 80 cm in the horizontal direction of the chamber were under γ irradiation while the rest of the surface was shielded by the two concrete blocks, as said in Section 6.3 and shown in Fig. 6.7; in the same picture is plotted the beam profile on the two strip planes of RPC1 reconstructed with the Coincidence Register information.

We measured the efficiency plateau of RPC1 in different zones of the chamber sampling the whole active surface, both with and without γ induced irradiation to evaluate the plateau position at different rates. The γ flux has been varied by mean of the GIF absorbers to get a counting rate of ∼40 Hz/cm^2 (ABS=50) or ∼80 Hz/cm^2 (ABS=20).

The gas flow was 60 cc/min (corresponding to 1.2 vol/h); the 2 gas inlet are at coordinates (x=210 cm, y=0 cm) and (x=210 cm, y=72 cm) and the 2 gas outlet at (x=0 cm, y=0 cm) and (x=0 cm, y=72 cm), as shown in Fig. 6.5.

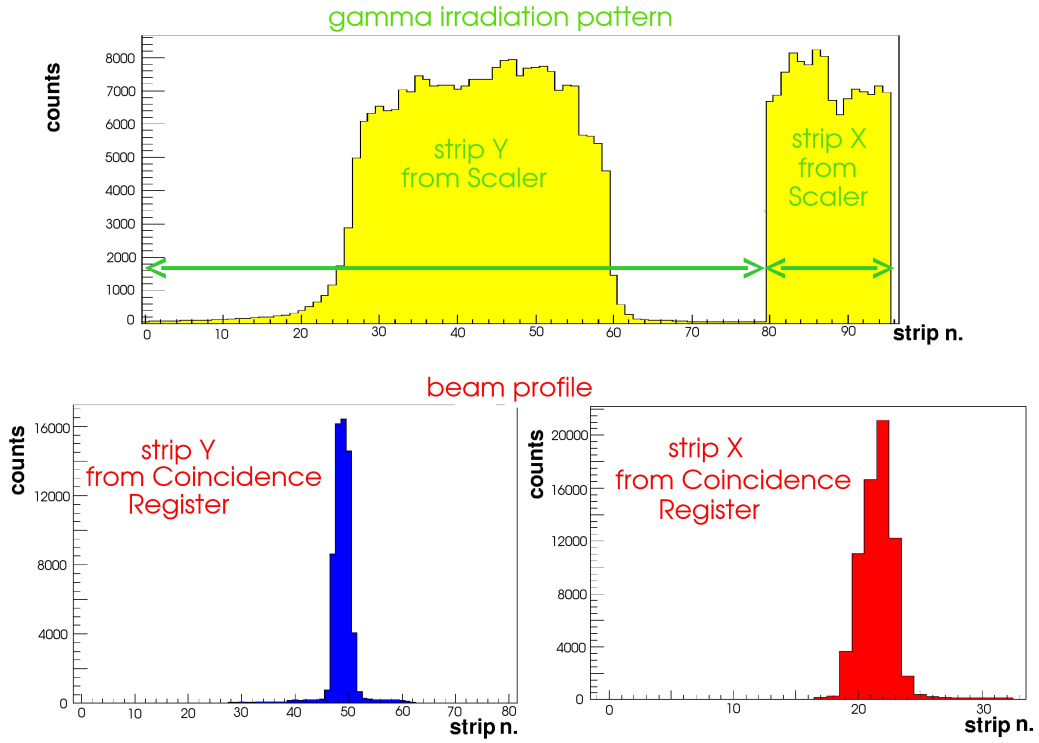

Fig. 6.7: γ irradiation pattern on RPC1 (top) and the beam profile on RPC1 plane Y (bottom, left) and on RPC1 plane X (bottom, right). In this case, the strip width is 2 cm for both readout planes.

The test has been carried out with two gas mixture:

- a quenched streamer mixture (50.5% Ar, 41.3% $C_2H_2F_4$, 7.2% C_4H_{10}, 1% SF_6) with the ADULT thresholds set at 10 mV and 80 mV;
- a highly–saturated avalanche mixture (maxi–avalanche, 88% $C_2H_2F_4$, 10% C_4H_{10}, 2% SF_6) employing the external ADULT thresholds set at 10 mV.

The total duration of the data taking has been divided in three periods:

- during the first 5 days the RPC has been flushed with the streamer gas mixture without humidification;
- the following 3 days were devoted to the study of the new maxi–avalanche gas mixture, in this case water was added to the gas mixture to get a relative humidity of about 50%;
- during the last 2 day the chamber has been newly operated in streamer mode, this time with a wet gas mixture (RH=50%).

6.5.1 RPC1: streamer gas mixture results

The efficiency of the chamber has been calculated with 2 methods:

- using the Coincidence Register information. RPC1 is considered efficient if there are one or more hits on the range of strips X and Y covered by the trigger.
- tracking the muons with the first two DWCs. RPC1 is considered efficient if the position of the hit, reconstructed with the Coincidence Register information, and the projection of the track identified by the DWCs correspond within a tolerance of 30 mm; this tolerance has been chosen considering the error due to the tracking ($\sim$15 mm, mainly due to the 6 m distance between the DWCs and RPC1) and the RPC strip width (1, 2 and 4 cm). For this kind of analysis, we also search for differences between the efficiency plateau position with respect to the incident rate. In Fig 6.6 is reported the beam profile, in the central part the rate is higher with respect to the rate in the external area. The area identified by the trigger is thus virtually divided in two zone:
  - the "core" with a 20 mm radius with rate up to 35–40 Hz/cm^2;
  - the "outer circle", that is the external area with rate of 10–15 Hz/cm^2.

The tracking therefore allow the evaluation of the efficiency on the whole area covered by the trigger, or in the "core" and in the "outer circle" areas.

As an example, it is reported in Fig. 6.8 the efficiency plateaux for a central position: no significant differences are observed both with respect to the employed method and with respect to the incident rate, as the position for the plateau of the "core" is the same as for the "outer circle".

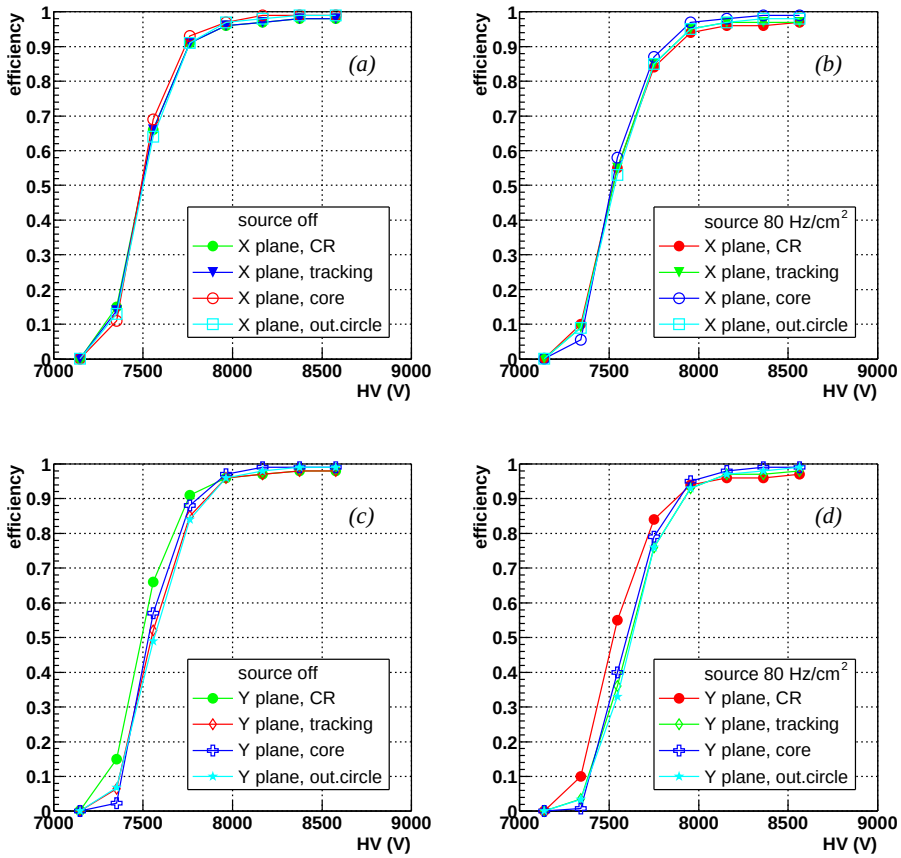

Fig. 6.8: Efficiency plateau for a central position (dry streamer gas mixture): (a) X plane with source off; (b) X plane with ∼80 Hz/cm^2 γ induced rate; (c) Y plane with source off; (d) Y plane with ∼80 Hz/cm^2 γ induced rate. Different markers refer to different analysis methods.

The results of the efficiency mapping are shown in Fig. 6.9 and 6.10, where are presented, for the different tested positions, the values of the effective

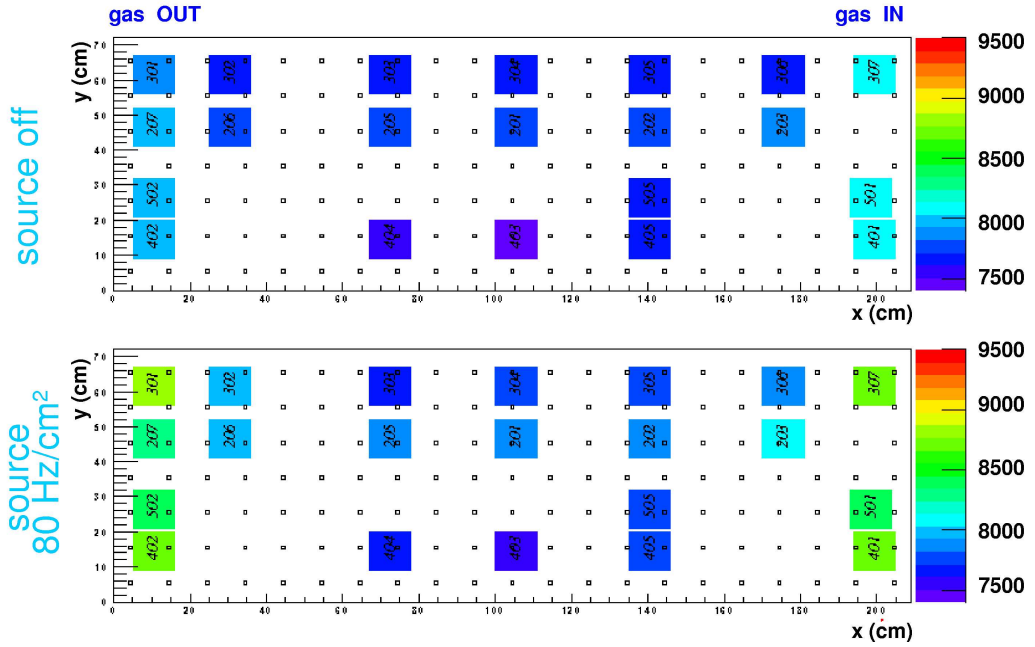

Fig. 6.9: RPC1 high voltage map (dry streamer gas mixture): for each tested position (displayed with a colored square at the given X and Y chamber coordinates) the value of the effective voltage that gives an efficiency of 90%, without γ induced rate (top) or with $\sim$80 Hz/cm^2 γ induced rate (bottom), is represented; the white squares correspond to the spacers.

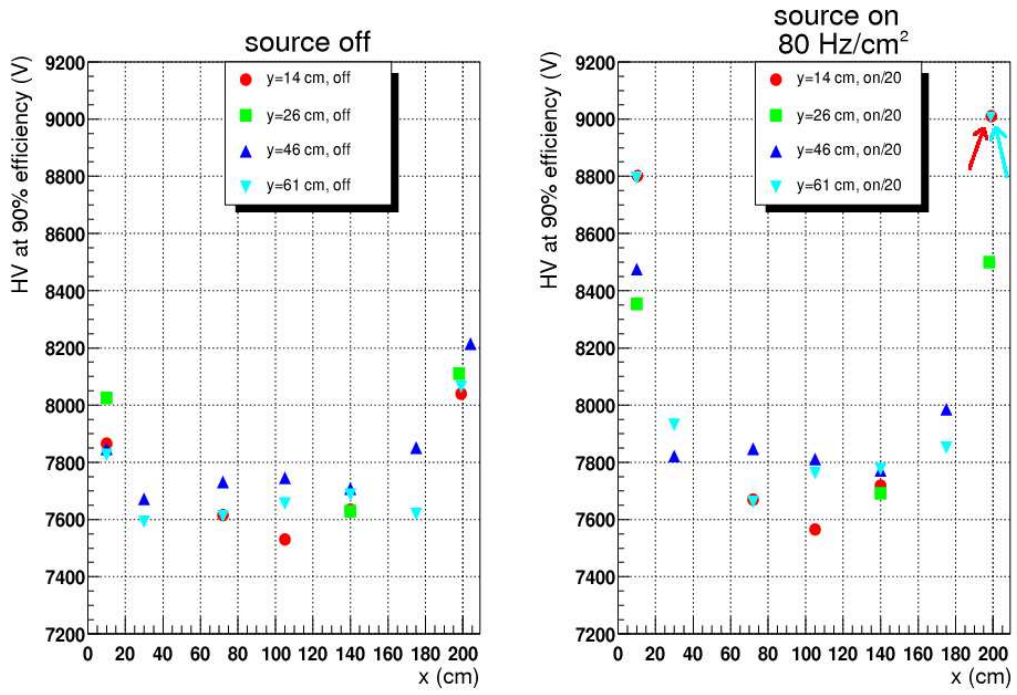

Fig. 6.10: RPC1 (dry streamer gas mixture): values of high voltages at 90% efficiency as a function of the X coordinate at a given Y coordinate , without γ induced rate (left) and with $\sim$80 Hz/cm^2 γ induced rate (right). The two arrow in the right plot indicate that at x=200 cm the efficiency plateau is not even reached, it is therefore impossible to evaluate the high voltages at 90% efficiency.

voltage that give an efficiency of 90% both with the source off and on. RPC1 shows a uniform behaviour (with the plateau at HV=8000 V) on the whole surface except for the region close to the gas inlets and outlets: without gamma irradiation the voltage values are highest for the extreme positions at x=10 cm and especially at x=200 cm, where the efficiency plateau is not even reached; moreover, for this positions, when the source is on, the plateau HV value undergoes a remarkable increase (up to 1000 V), that is to say that the efficiency decreases with the rate.

The effect can be ascribed to the fact that, during this test and the preliminary one with cosmic rays in Turin, RPC1 was flushed with dry mixture during about one month: this can potentially results in a local increase of the bakelite resistivity and thus in a worsening of the rate capability especially in the areas near to the gas inlets/outlets where the gas flow effect is bigger.

To investigate if the above interpretation is correct, in the second part of the test, RPC1 has been flushed with wet gas mixture[2] (RH=50%); actually, if the observed effect is due to the dry gas mixture, the uniformity of the rate capability is expected to be, at least partially, restored.

In this condition we repeated the efficiency mapping. The values of the effective voltage that give an efficiency of 90% without gamma irradiation and with the source on (40 and 80 Hz/cm^2 of induced gamma rate) are shown in Fig. 6.11, due to the short duration of this phase of the test, only a few measurements could have been done.

The difference of the voltage at 90% efficiency measured in the lateral positions (x=10 cm and x=200 cm) with the source on with respect to the ones measured with the source off is smaller (600 V) than when we flowed the chamber with the dry mixture (>1000 V). This means that flowing with a wet mixture allows a quick decrease of the resistivity with a partial recovery of the rate capability: now the efficiency plateau is reached, even if at different voltages, in every tested position, also at x=200 cm. Unfortunately, since only 10 days of data taking were available, it was not possible to wait enough time to see a total recovery of the rate capability.

Furthermore, to corroborate our hypothesis, we tested a new pre–production chamber (RPC2, with the same characteristics of RPC1) in Turin's laboratory: we checked the uniformity over the whole surface with respect to the plateau position for the detection of cosmic rays. This RPC has been flushed with a wet gas mixture from the beginning. The obtained results are shown in Fig. 6.12: the mean voltage that gives a 90% efficiency is (8239±84) V and there are no relevant disuniformity whereas on RPC1 a difference was soon observed.

[2]The gas mixture is the same as before, with a flow of 60 cc/min.

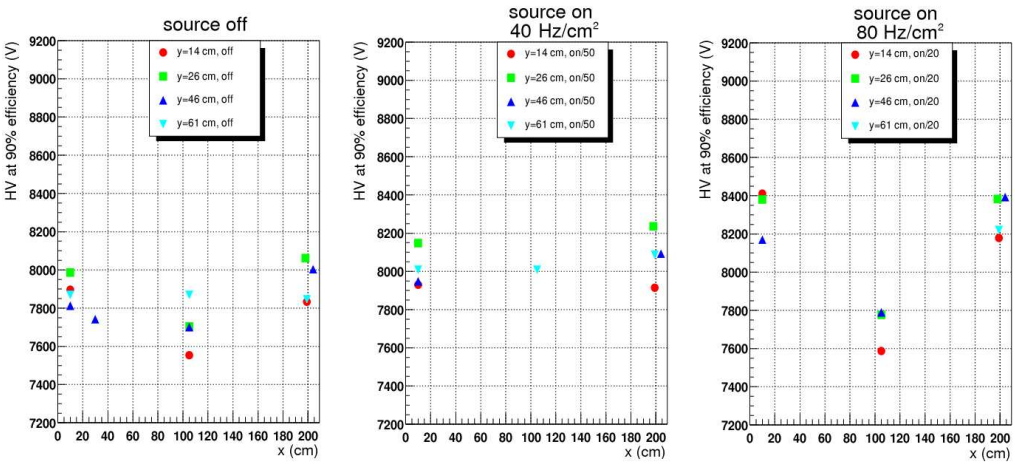

Fig. 6.11: RPC1 (wet streamer gas mixture): values of high voltages at 90% efficiency as a function of the X coordinate at a given Y coordinate , without γ induced rate (left), with $\sim$40 Hz/cm^2 γ induced rate (center) and with $\sim$80 Hz/cm^2 γ induced rate (right).

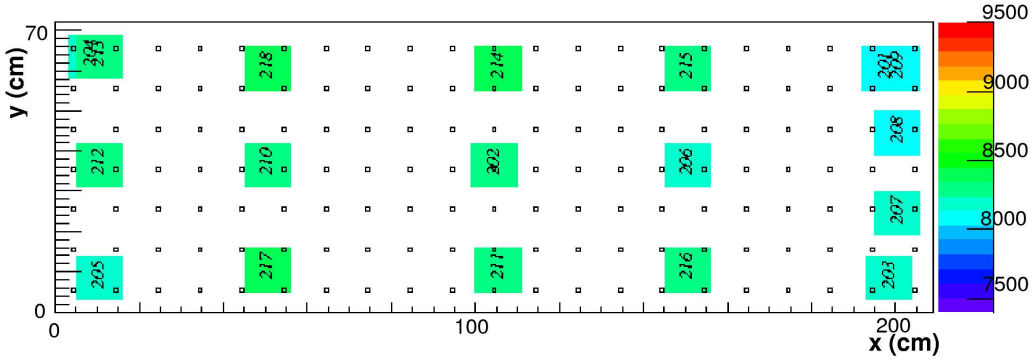

Fig. 6.12: RPC2 high voltage map (wet streamer gas mixture): for each tested position (displayed with a colored square at the given X and Y chamber coordinates) the value of the effective voltage that gives an efficiency of 90% for the detection of cosmic rays is represented; the white squares correspond to the spacers.

6.5.2 RPC1: highly–saturated avalanche gas mixture results

RPC1 has also been tested with a wet highly–saturated avalanche gas mixture (88% $C_2H_2F_4$, 10% C_4H_{10}, 2% SF_6, RH=50%).

The beam test with this gas mixture was devoted to the study of the performance of the RPC in this working condition, as well as to investigate the uniformity over the RPC active area. To this aim, we repeated the efficiency measurement in different zones of the chamber mapping the active surface, both with and without γ induced rate. The analysis of these data has been performed with the same methods used for the data obtained with the streamer gas mixture.

As an example, is reported in Fig. 6.13 the efficiency plateau for a central position. As well as with the streamer gas mixture, no significant differences, both with respect to the employed method and with respect to the beam incident rate, have been pointed out. The efficiency plateau is at 11000 V.

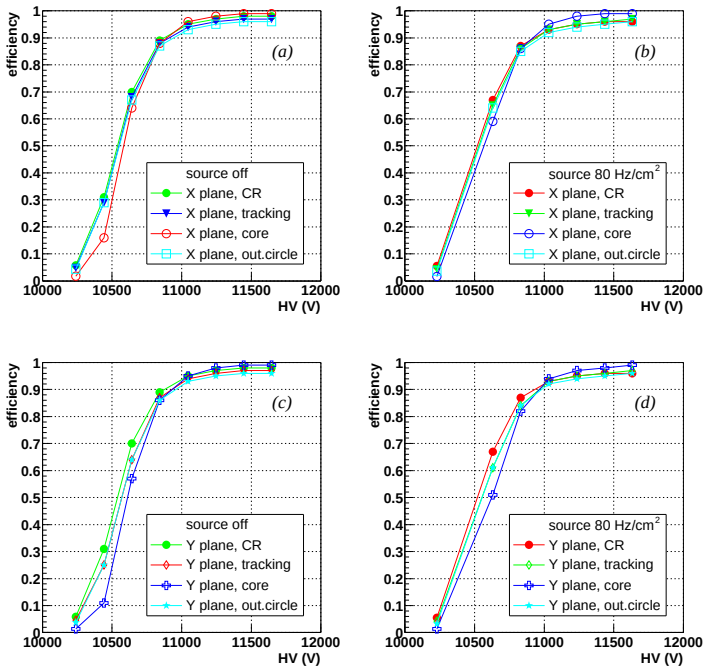

Fig. 6.13: Efficiency plateau for a central position (wet maxi–avalanche gas mixture): (a) X plane with source off; (b) X plane with ∼80 Hz/cm^2 γ induced rate; (c) Y plane with source off; (d) Y plane with ∼80 Hz/cm^2 γ induced rate. Different markers refer to different analysis methods.

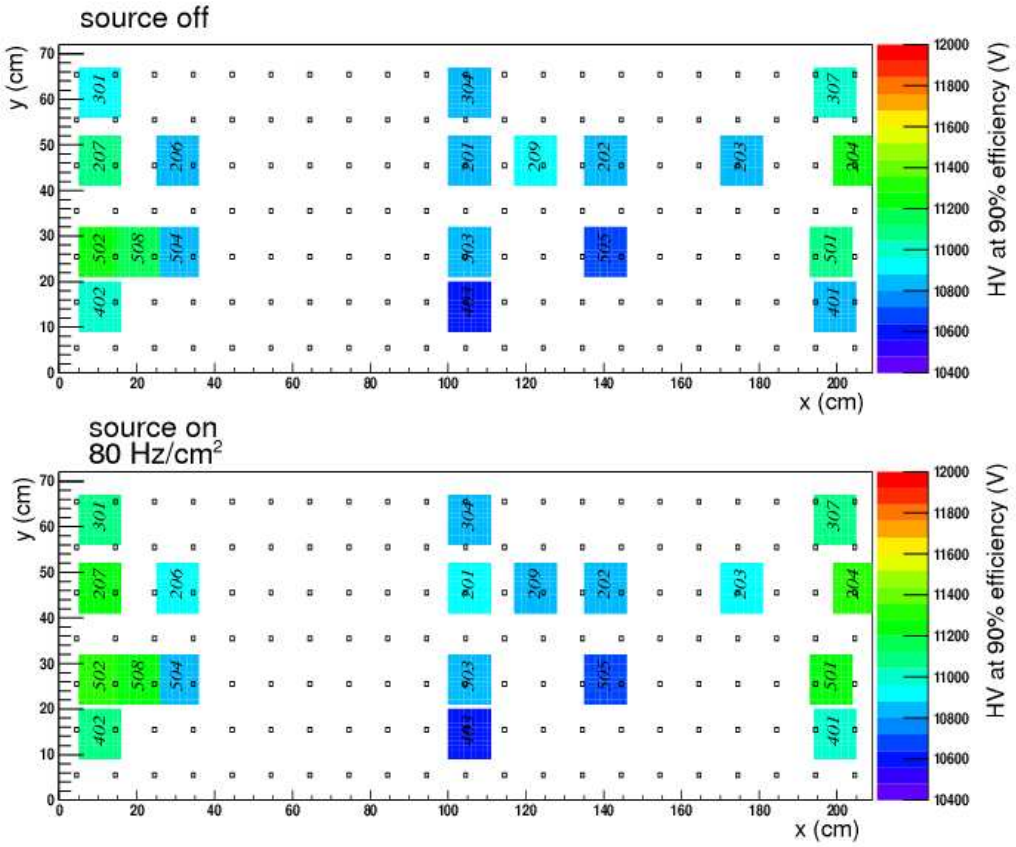

Fig. 6.14: RPC1 high voltage map (wet maxi–avalanche gas mixture): for each tested position (displayed with a colored square at the given X and Y chamber coordinates) the value of the effective voltage that gives an efficiency of 90%, without γ induced rate (top) or with $\sim$80 Hz/cm^2 γ induced rate (bottom), is represented; the white squares correspond to the spacers.

The results of the efficiency mapping are shown in Fig. 6.14 and Fig. 6.15, where are presented, for the different tested positions, the values of the effective voltage that give an efficiency of 90% both with the source off and on. RPC1 shows therefore a uniform behavior on the whole surface except for the region close to the gas inlets and outlets but the disuniformity pointed out during the dry streamer gas mixture operations is less relevant with the maxi–avalanche gas mixture.

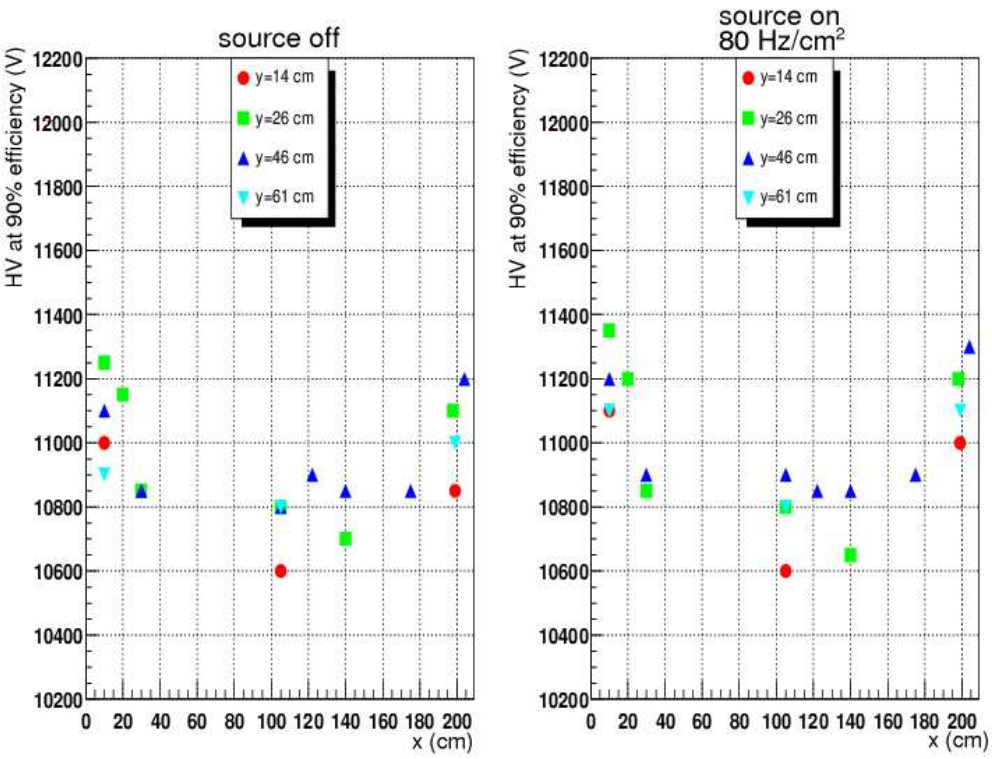

Fig. 6.15: RPC1 (wet maxi–avalanche gas mixture): values of high voltages 90% efficiency as a function of the X coordinate at a given Y coordinate, without γ induced rate (left) and with $\sim$80 Hz/cm^2 γ induced rate (right).

6.5.3 Comparison of the performance in streamer and in highly–saturated avalanche mode

As already mentioned the goal of the beam test was to check the uniformity of the RPC on the whole active area and to compare the performance of the chamber in maxi–avalanche and in streamer mode, with a special attention to time resolution and cluster size.

The performance of the chamber concerning the time resolution as a function of the applied voltage is shown in Fig 6.16: the results refer to a position covered by 2 cm wide strips. These results, together with the ones for the 1 and 4 cm wide strips are summarized in Table 6.1: altogether, no significant differences can be observed with respect to the strip width and also in comparison with the results obtained with the streamer gas mixture reported in Section 5.3, since a time resolution of about 1 ns is obtained in every performed measurement.

strip	source off		source on (80 Hz/cm^2)	
width	sigma (ns)	RMS (ns)	sigma (ns)	RMS (ns)
1 cm	1	1.1	1	1
2 cm	0.9	1	0.9	0.9
4 cm	1	1.1	1	1.1

Tab. 6.1: Time resolution at working point (HV=11000 V) for different strip width in absence of irradiation and with 80 Hz/cm^2 of γ induced rate (wet maxi–avalanche gas mixture). The efficiency knee is at 10800 V.

With the information provided by the Coincidence Register it is possible to calculate the cluster size. Also for this parameter, the analysis has been done for the three different strip width (1, 2 and 4 cm). Fig. 6.17, 6.18 and 6.19 show the trend of the mean cluster size as a function of the applied voltage shifted by the knee voltage: this means that the zero corresponds to the knee of the efficiency plateau. In the same Figures are plotted the curves obtained with the streamer gas mixture: the shift of the knee voltage to zero allow an easy comparison of the two set of data.

For the 2 and 4 cm wide strips, the cluster size values are similar, while for the 1 cm wide strips an increase for the maxi–avalanche with respect to the streamer gas mixture can be noticed. All the obtained results are reported in Table 6.2.

The obtained results show that it is possible to work in maxi–avalanche mode in stable conditions, with a similar timing and cluster size performance

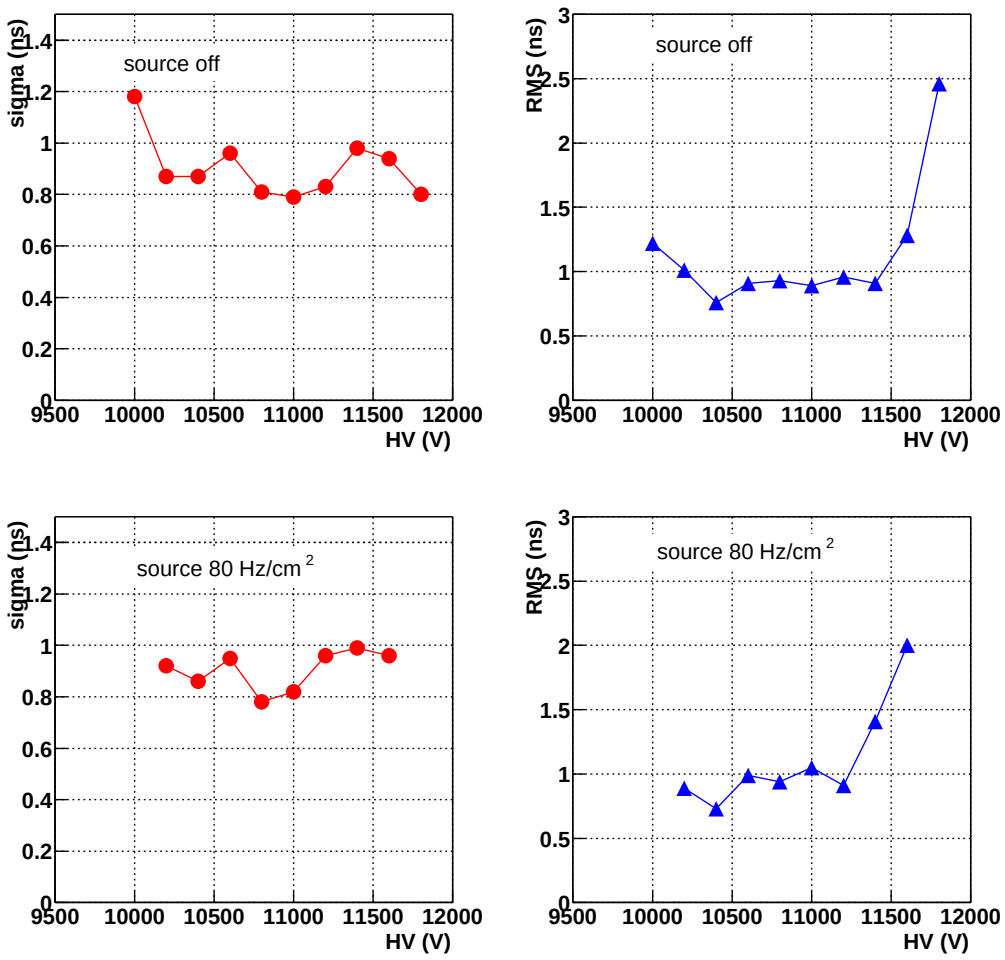

Fig. 6.16: Time resolution as a function of the applied voltage for 2 cm wide strips in absence of irradiation (top) and with 80 Hz/cm^2 of γ induced rate (bottom) for the wet maxi–avalanche gas mixture.

strip width	source off		source on (80 Hz/cm^2)	
	streamer	maxi–avalanche	streamer	maxi–avalanche
1 cm	1.5	1.8	1.45	1.7
2 cm	1.1	1.26	1.33	1.41
4 cm	1.33	1.33	1.12	1.18

Tab. 6.2: Cluster size values (high voltages 400 V above the efficiency knee) for different strip width in absence of irradiation and with 80 Hz/cm^2 of γ induced rate.

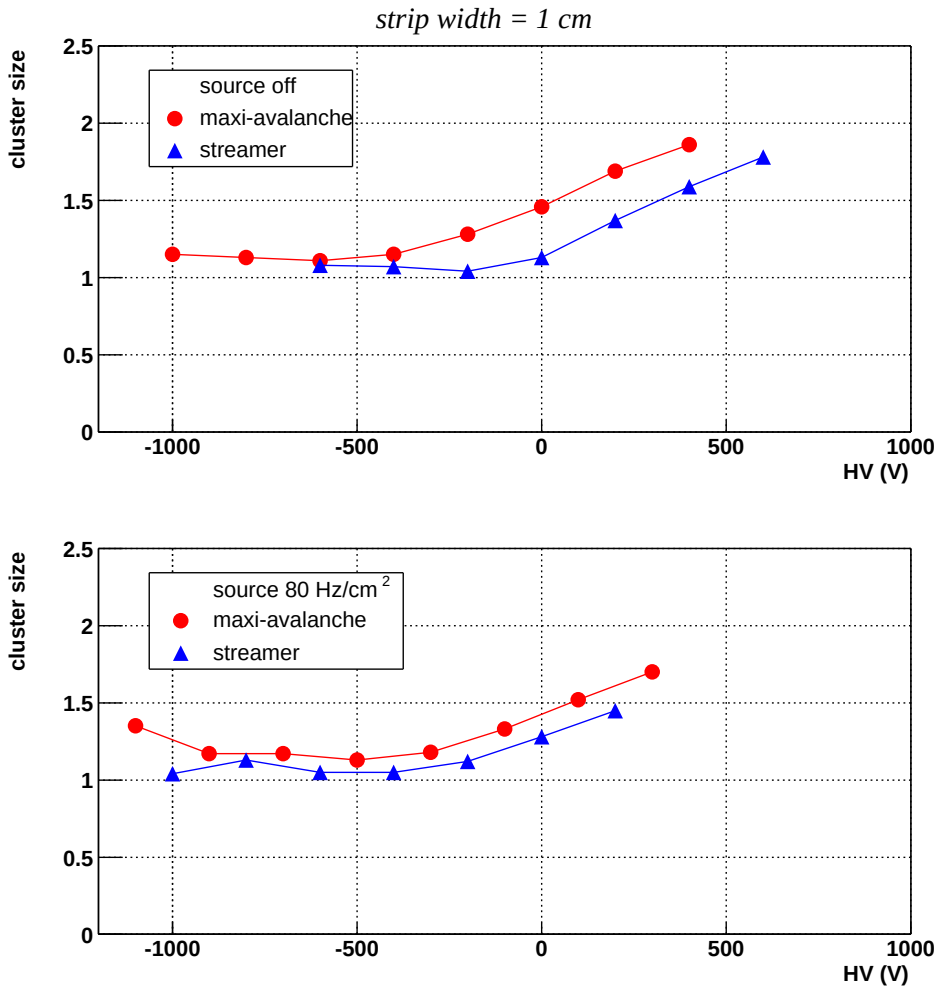

Fig. 6.17: Cluster size as a function of the applied voltage for 1 cm wide strips in absence of irradiation (top) and with 80 Hz/cm^2 of γ induced rate (bottom) for the wet maxi–avalanche gas mixture. The indicated voltage is shifted by the knee voltage (i.e. zero corresponds to the knee of the plateau).

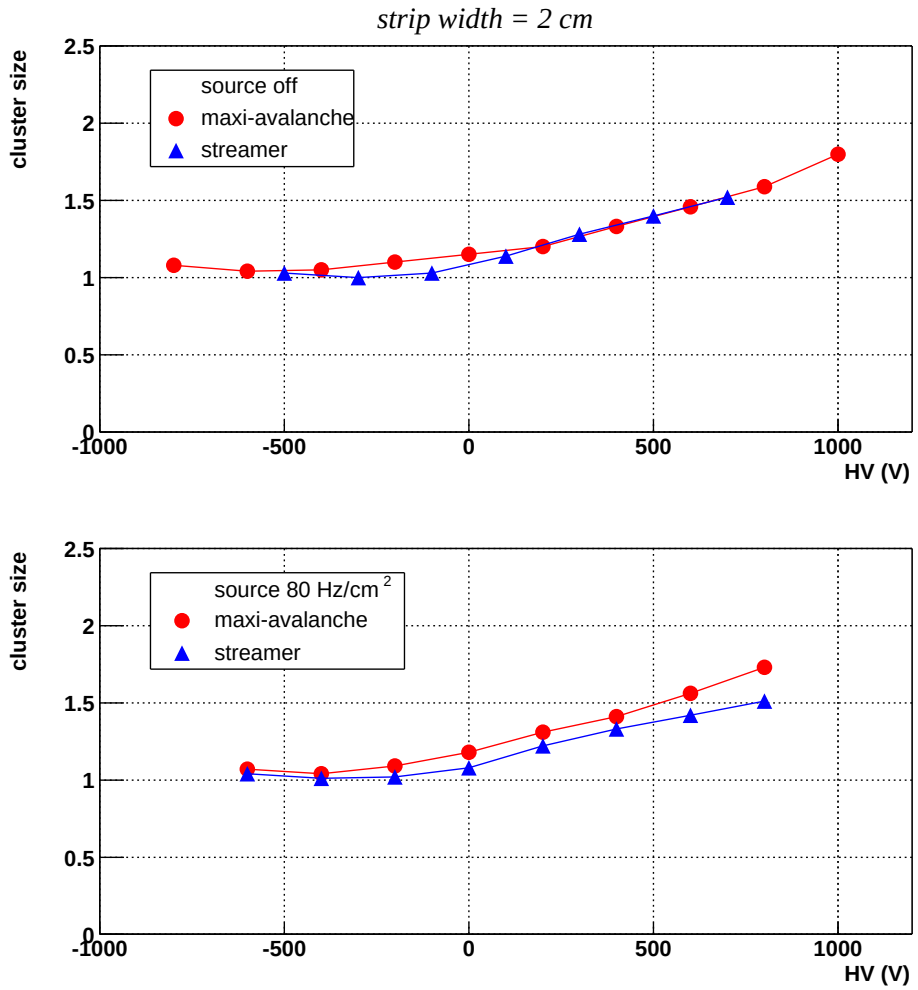

Fig. 6.18: Cluster size as a function of the applied voltage for 2 cm wide strips in absence of irradiation (top) and with 80 Hz/cm^2 of γ induced rate (bottom) for the wet maxi–avalanche gas mixture. The indicated voltage is shifted by the knee voltage (i.e. zero corresponds to the knee of the plateau).

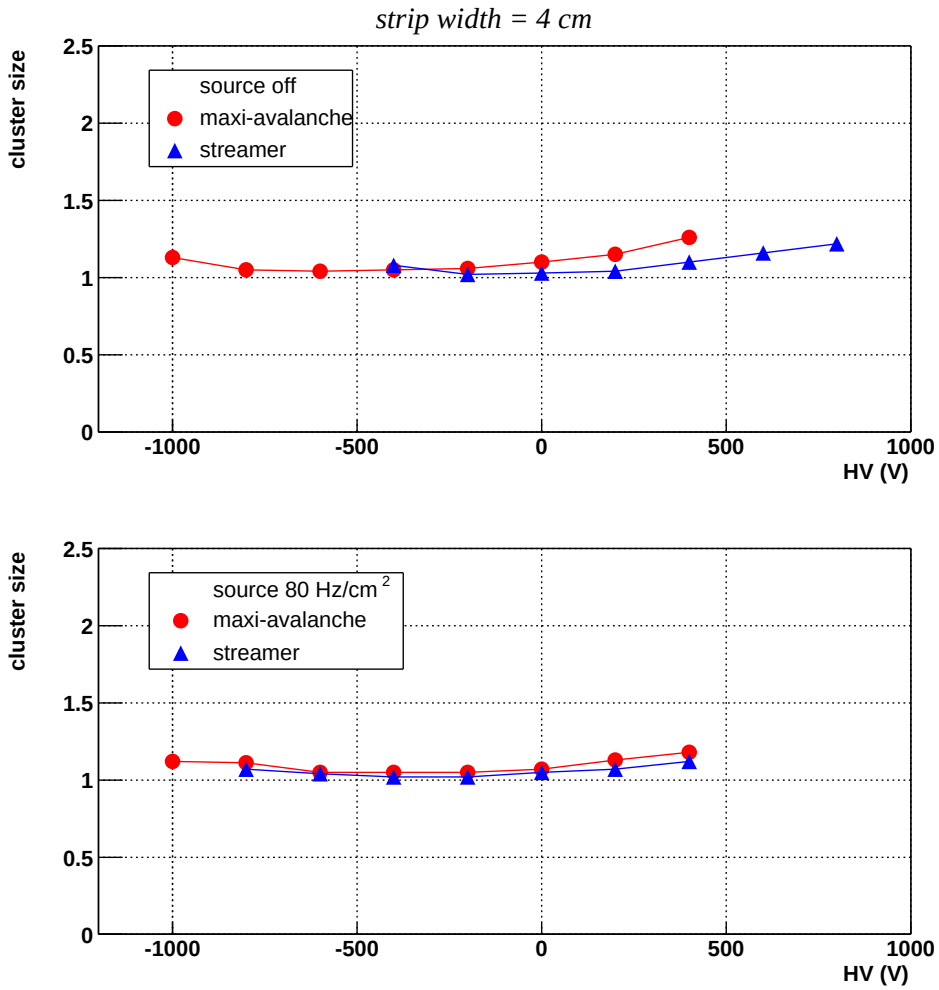

Fig. 6.19: Cluster size as a function of the applied voltage for 4 cm wide strips in absence of irradiation (top) and with 80 Hz/cm^2 of γ induced rate (bottom) for the wet maxi–avalanche gas mixture. The indicated voltage is shifted by the knee voltage (i.e. zero corresponds to the knee of the plateau).

as in streamer mode; moreover, the dark current and dark rate are low (1 μA, 0.1 Hz/cm^2).

Furthermore, during the test, the chemical analysis of the exhaust gas has been performed both in streamer and in maxi–avalanche mode operations; the results are reported in Table 6.3: it can be noticed that the current of the RPC in maxi–avalanche is about three times lower that the current drawn by the chamber working in streamer mode in the same irradiation conditions.

	maxi–avalanche	streamer
HV_{eff}	11240 V	8260 V
mean rate	91 Hz/cm^2	85 Hz/cm^2
mean current	86 μA	274 μA
HF	0 mg/l	0.03 mg/l
total impurities	0.091%	0.594%

Tab. 6.3: HF and impurity content in samples of exhaust gas for RPC1 working in streamer and in maxi–avalanche mode.

In comparison with the streamer mode, the maxi–avalanche mode provides a lower percentage of impurities and a spectacular decrease of HF, one of the most aggressive and dangerous acid for the bakelite surface: this is a promising message in view of the ageing test.

6.5.4 Conclusions and remarks

On the basis of the results obtained with the test of the pre–production RPC1 we can conclude that:

- the observed disuniformity in the efficiency plateau position was mainly due to the use of a dry gas mixture and can be solved by flushing the chamber with a wet gas mixture;
- the performance in term of efficiency, cluster size and time resolution with the streamer gas mixture are in agreement with the one obtained with small prototypes and reported in Section 5.3;
- it is possible to work in maxi–avalanche mode with the same FEE used for the streamer mode simply by lowering the threshold to the value of 10 mV by mean of the external control;
- good performance with the maxi–avalanche gas mixture have been achieved with a promising message in view of ageing test from the exhaust gas analysis.

6.6 Test of three chambers of the final production

In June 2004, we have tested three gas gaps belonging to the first set of 35 RPCs produced for the Muon Spectrometer (I.D. numbers 14, 16, 18, hereafter RPC14, RPC16 and RPC18) with μ beam from CERN–SPS (X5) and γ irradiation at GIF. The experimental setup is the same already described at the beginning of the Chapter.

The chambers are equipped with:

- 64 vertical strips (56 strips 680×42.5 mm^2 and 8 strips 680×21.25 mm^2);
- 112 horizontal strips (6 "columns" of 16 strips 338×42.5 mm^2 and 1 "column" of 16 strips 509×42.5 mm^2).

as shown in Fig. 6.20: this strip plane segmentation corresponds to the one foreseen for the chamber number 1 or number 9 of the first trigger plane MT11 (see Fig. 5.1 and Fig. 5.2).

The two concrete blocks shield the chamber from the γ–rays leaving under irradiation ∼120 cm in the horizontal direction, as shown in Fig. 6.21; in the same picture there is the beam profile and its position with respect to the irradiated area. The pattern disuniformity is due to some detectors, and their mechanical support, put between the γ source and our RPC. The first chamber, RPC14, has been tested in these conditions, while for RPC16 and RPC18 a further lead shield has been put on the right concrete block (γ source on the back, see Fig. 6.2) to obtain a more uniform irradiation on the RPC under test and to shield the peak; the new pattern of the irradiation is shown in Fig. 6.22

Furthermore, RPC14 has been tested with the 25 ns bunched beam (total cycle 12.0 s and flat top 2.2 s, see also Fig.6.23) during the LHC cycle study. Concerning RPC16 and RPC18, the beam was not bunched each 25 ns and it had the usual total cycle of 16.8 s with 4.8 s flat top.

The beam intensity, not under our control, varied between ∼400 and ∼10000 muons/burst, giving different rates (1÷45 Hz/cm^2) and different μ distributions on the chamber:

- low beam intensity (≤5000 muons/burst) corresponds to a uniform distribution on the 10×10 cm^2 DWC (see fig. 6.24, top);
- high beam intensity (≥6000 muons/burst) corresponds to muons distributed with a sharp peak (FWHM ∼40 mm) on the 10×10 cm^2 DWC (see fig. 6.24, bottom);

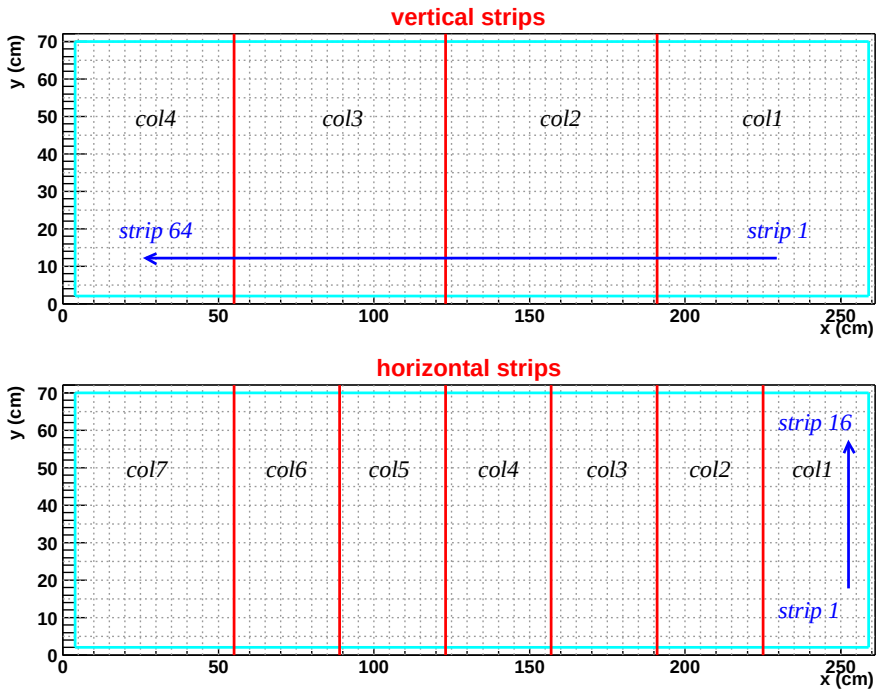

Fig. 6.20: Sketch of the tested RPCs: spatial coordinates and strip numbering. The chamber is virtually divided into column (col1, col2 ...) identified by the strip segmentation.

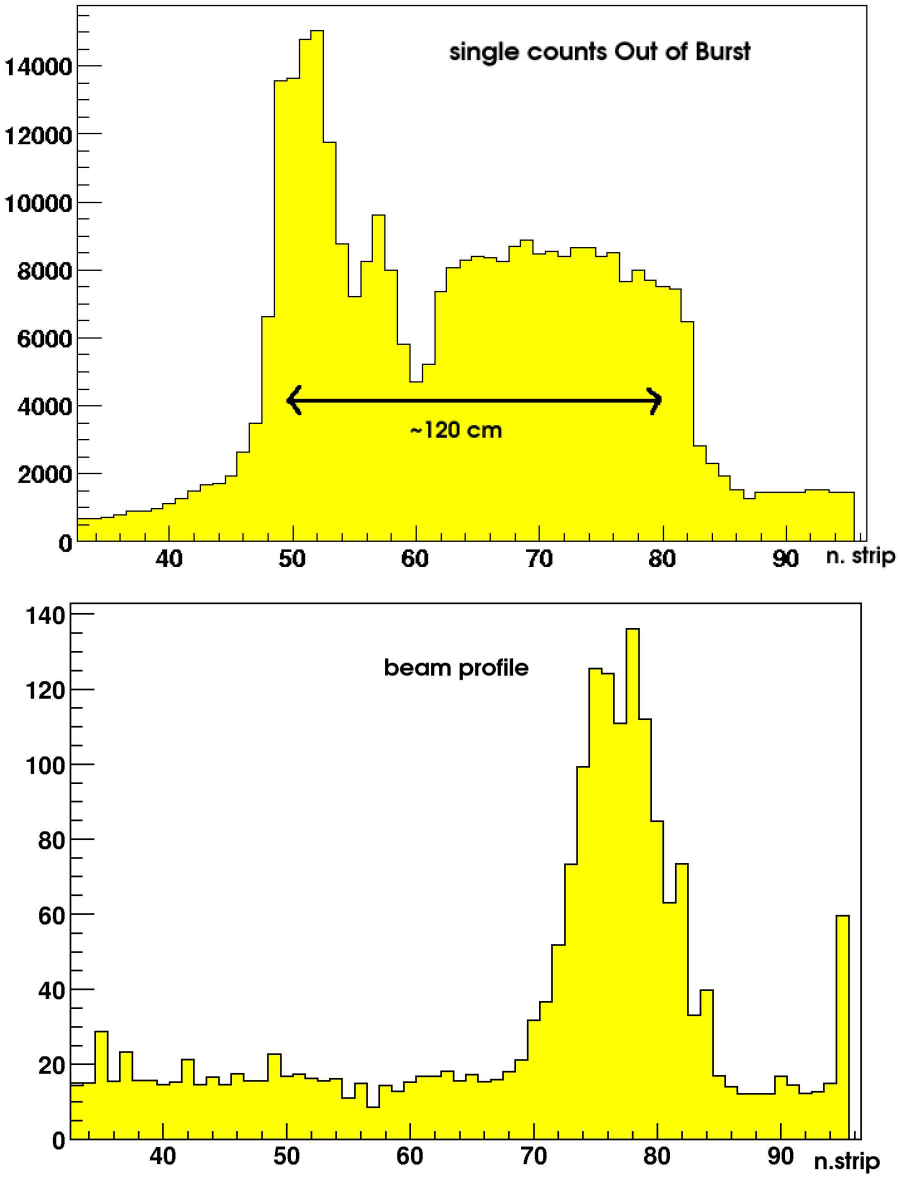

Fig. 6.21: γ irradiation pattern on the RPC14 (top) and the beam profile position with respect to the irradiated area (bottom) given by the single counts of the 64 Y strips.

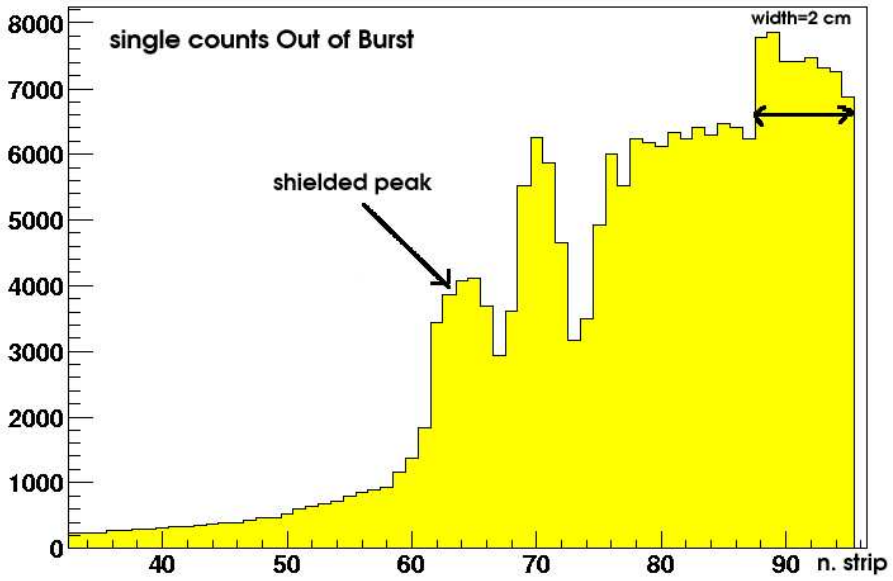

Fig. 6.22: γ irradiation pattern on the RPC16 and RPC18: 64 strips Y single counts.

All RPCs were flushed with the streamer mixture (50.5% Ar, 41.3% $C_2H_2F_4$, 7.2% C_4H_{10}, 1% SF_6, RH=50%) at 100 cc/min (corresponding to 1.6 vol/h); the 2 gas inlet are at coordinates (x=0 cm, y=0 cm) and (x=0 cm, y=72 cm) and the 2 gas outlet at (x=261 cm, y=0 cm) and (x=261 cm, y=72 cm).

To check the homogeneity of the RPC we measured the efficiency plateau in different zones of the chamber, both with and without γ induced rate. The γ flux could be varied by mean of the GIF absorber to get a counting rate of $\sim$40 Hz/cm^2 (ABS=5) or $\sim$85 Hz/cm^2 (ABS=2).

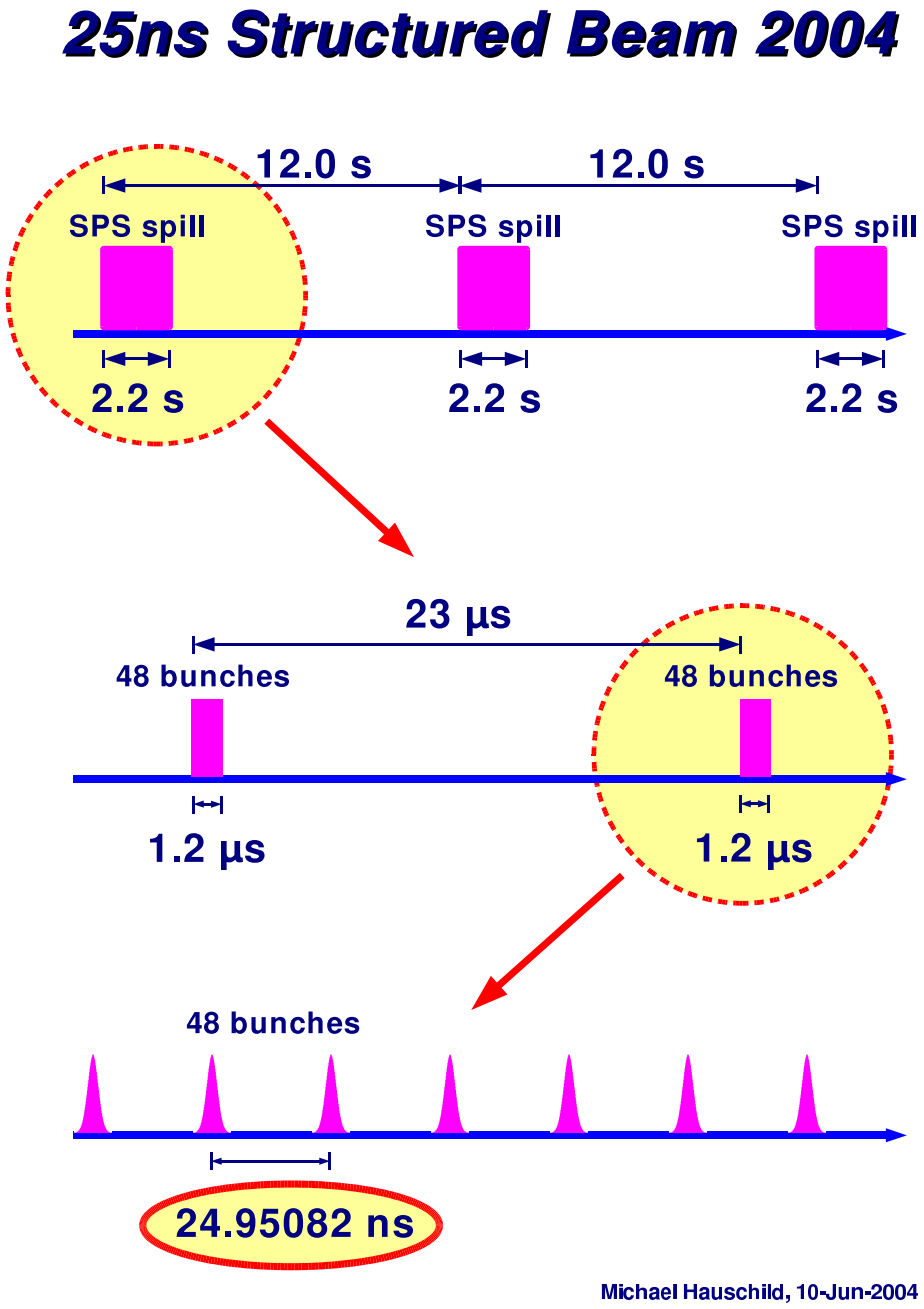

Fig. 6.23: Details of the structure of the 25 ns bunched beam for LHC.

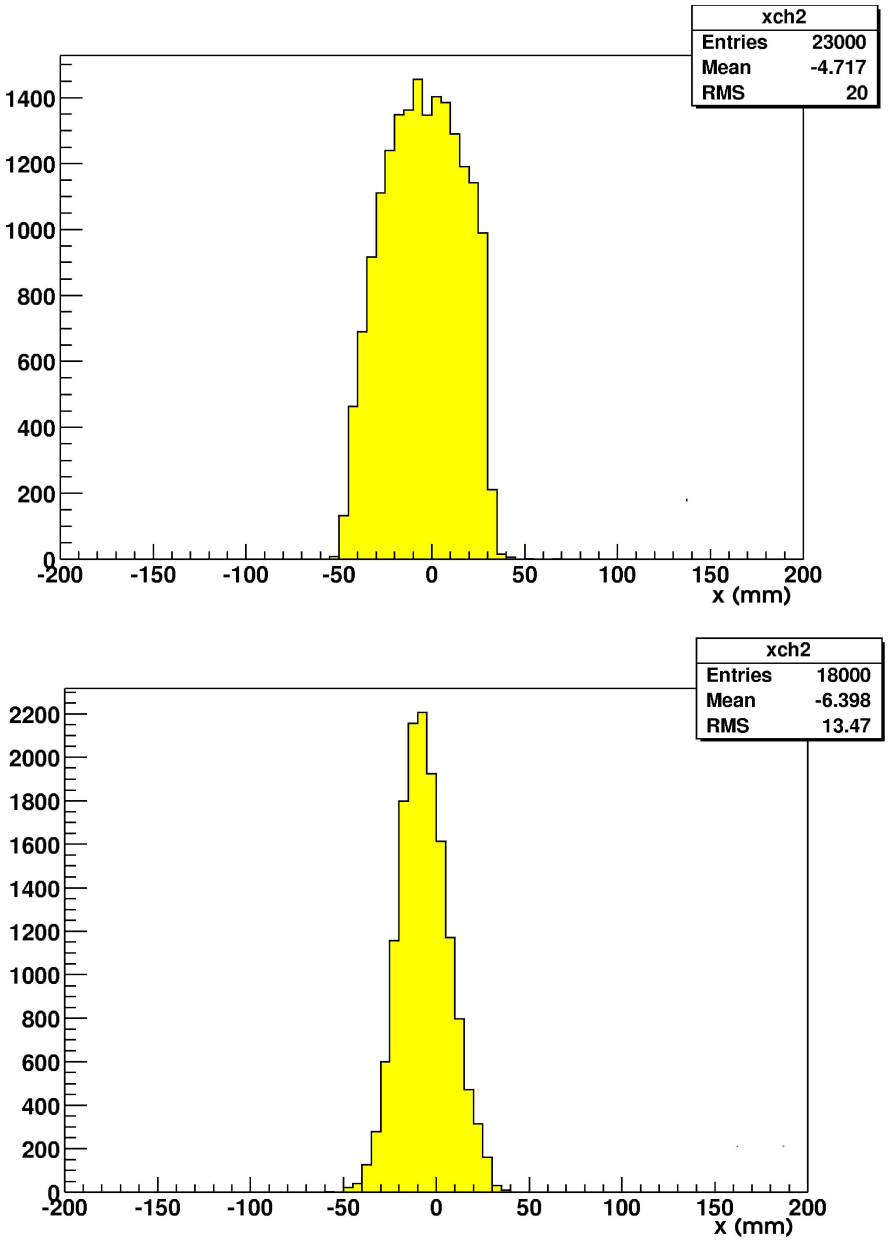

Fig. 6.24: Beam pattern on the 10×10 cm^2 DWC with low beam intensity (top) and with high beam intensity (bottom). Both histograms refer to the X coordinate of the second DWC, the profiles of the Y coordinate and of the first DWC are similar to these ones.

6.6.1 RPC14: results

The problems observed with the pre–production RPC tested in September 2003 (RPC1) have been totally solved flushing the RPCs with a humid gas mixture; RPC14 shows a good uniformity:

- in all positions (including the corners) the plateaux reaches ∼98–99% of efficiency, both with and without γ irradiation;
- the efficiency values over the whole active area are shown in Fig. 6.25 in a map and in Fig. 6.26 with their distribution, the mean efficiency at HV=8150 V (defined as working value) is 0.984±0.006 in absence of γ induced rate and 0.978±0.006 at 40 Hz/cm^2;
- the mean voltage that gives a 90% efficiency is (7645±75) V at source off and (7705±77) V at source on, map and distribution are plotted in Fig. 6.27 and Fig. 6.28;
- the rate capability is good on the whole surface of the RPC, including the borders. As an example the efficiency plateaux of one corner with the source off and in two irradiation condition (40 and 85 Hz/cm^2) is plotted in Fig.6.29;
- at working point (HV=8150 V) the dark rate is low (0.1–0.2 Hz/cm^2) as well as the dark current (2–2.5 μA).

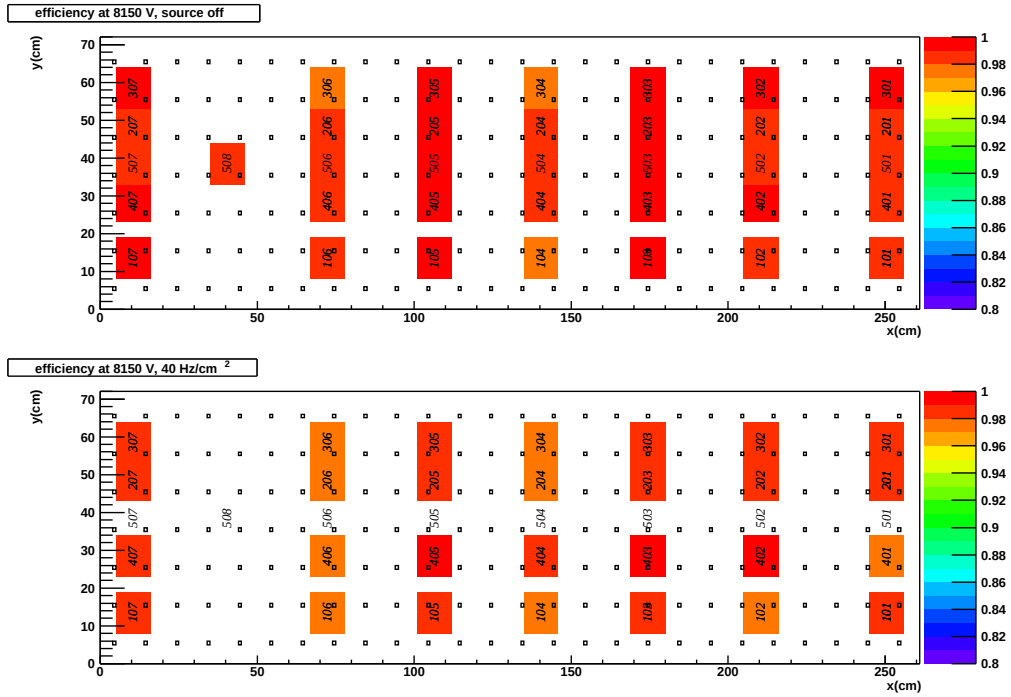

Fig. 6.25: RPC14 efficiency map: for each tested position (displayed with a colored square at the given X and Y chamber coordinates) the efficiency of the RPC at working point (HV=8150 V), without γ induced rate (top) or with $\sim$40 Hz/cm^2 γ induced rate (bottom), is represented.

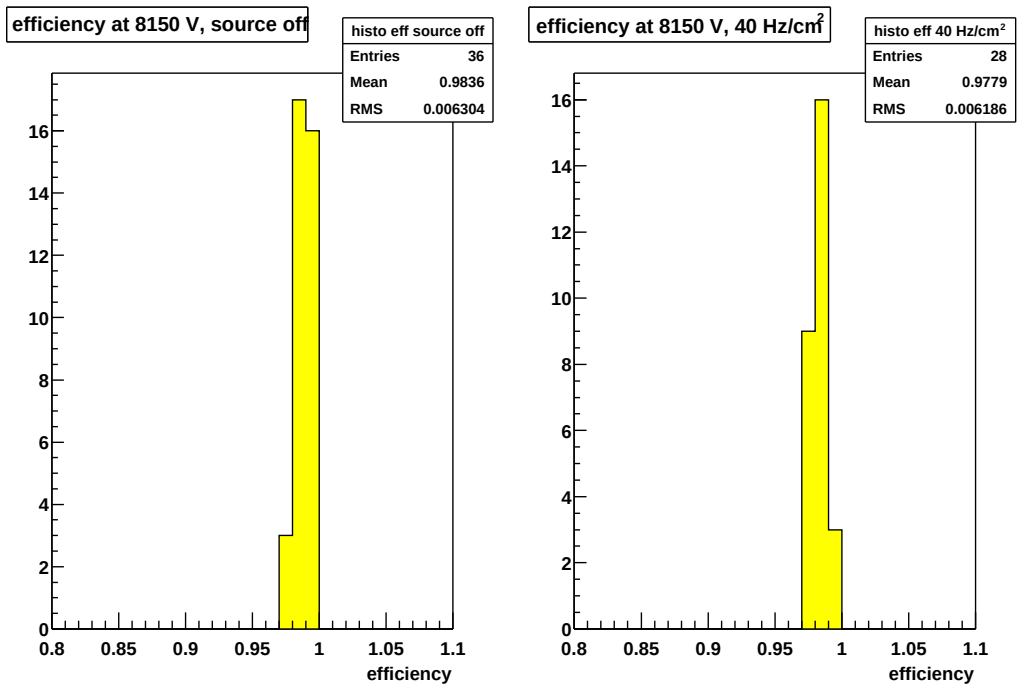

Fig. 6.26: RPC14 efficiency distribution at working point (HV=8150 V), without γ induced rate (top) and with $\sim$40 Hz/cm^2 γ induced rate (bottom).

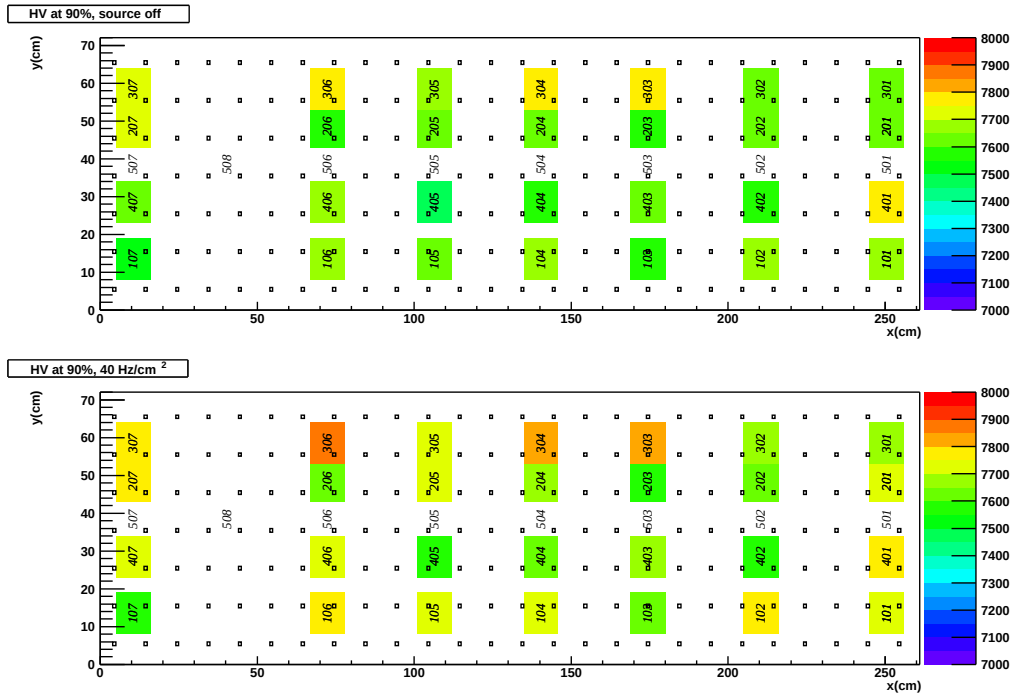

Fig. 6.27: RPC14 high voltages map: for each tested position (displayed with a colored square at the given X and Y chamber coordinates) the value of the effective voltage that gives an efficiency of 90%, without γ induced rate (top) or with $\sim$40 Hz/cm^2 γ induced rate (bottom), is represented; the white squares correspond to the spacers.

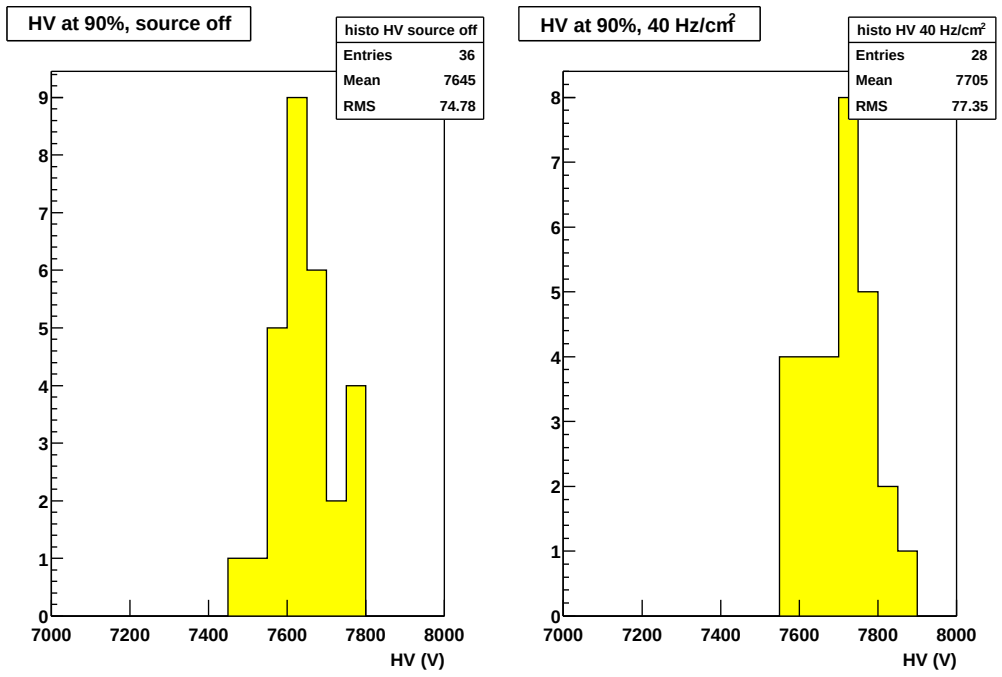

Fig. 6.28: RPC14 high voltages at 90% efficiency distribution, without γ induced rate (top) or with $\sim$40 Hz/cm^2 γ induced rate (bottom).

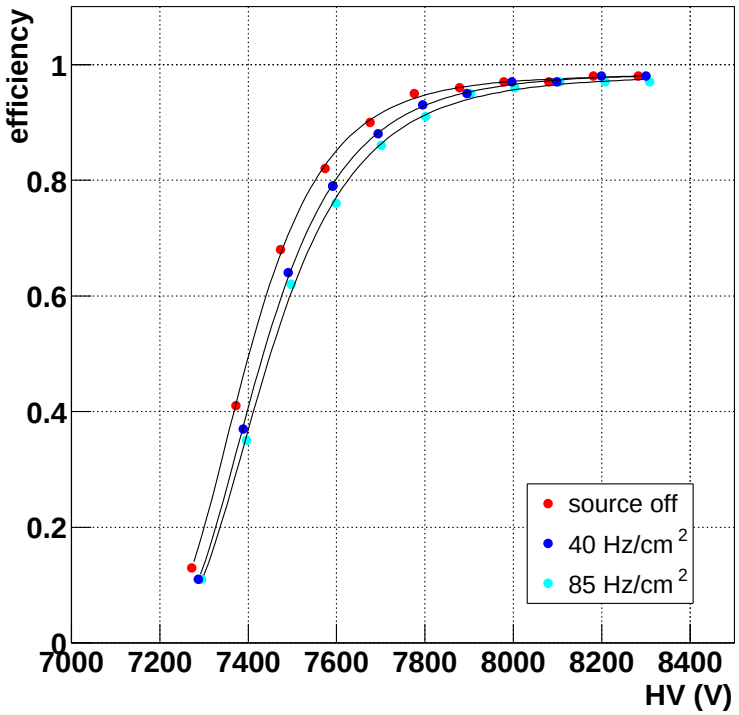

Fig. 6.29: RPC14 efficiency plateaux without γ induced rate (red), with $\sim$40 Hz/cm^2 of γ induced rate (blue) and with $\sim$85 Hz/cm^2 of γ induced rate (azure).

6.6.2 RPC16 and RPC18: results

Also RPC16 and RPC18 show a good and uniform behaviour reaching ∼98–99% of efficiency for all positions with a satisfactorily rate capability. The detailed plots of the efficiency plateaux, the map and distribution of the efficiency at HV=8150 V and of the voltage giving 90% efficiency are reported in Appendix B.

The efficiency distribution as a function of the applied voltages, obtained as a result of this beam test, have been used to calculate with a simple simulation the efficiency of the Trigger System, that is of four RPCs planes. The results of this simulation are reported in Appendix C.

6.6.3 Conclusions

In Table 6.4 are summarized the mean value of the voltage that gives an efficiency of 90% (HV at 90%) and of the efficiency at HV=8150 V (eff. at 8150 V) of the three RPCs that we have tested; both values are reported with with source off and source on (40 Hz/cm^2).

RPC no.	HV at 90%(V) source off	HV at 90 (V) 40 Hz/cm^2	eff. at 8150 V source off	eff. at 8150 V 40 Hz/cm^2
14	7645±75	7705±77	0.984±0.006	0.978±0.006
18	7629±35	7682±55	0.982±0.007	0.977±0.007
16	7604±56	7656±60	0.982±0.006	0.979±0.006

Tab. 6.4: Summarizing table of the 3 tested RPCs.

The "working voltage" is chosen at 8150 V for the three RPCs: the efficiency behaviour is practically the same for all tested RPCs both in absence of irradiation and with 40 Hz/cm^2 of induced γ rate; the difference between the HV at 90% at source off and with γ irradiation of 40 Hz/cm^2 (50–60 V) is due to the voltage drop produced by the current through the bakelite as explained in Section 4.4.

The test show that each RPCs has a uniform behaviour over the whole active area and that this behaviour is quite the same for the three chambers of the final production.

References

[1] G. Travaglia, Ph.D Thesis, Università degli Studi di Torino e Università degli Studi di Messina, February 2004
http://www.to.infn.it/pinot/documents/PHDtheses.html

[2] S. Agosteo *et al.*, Nucl. Instr. and Meth. A 452 (2000) 94-104
http://pcessgif04.cern.ch/

Chapter 7

Ageing tests

7.1 The ageing problem

The R&D of the last years has also been carried out to understand the ageing problems focusing on the effects due to protracted flowing the RPCs with dry gas mixture and to long term operation of the detector in condition of high counting rates.

These operating conditions can result in a worsening of the RPC performances, as an increase of the dark current and of the dark rate (i.e. current and rate in absence of irradiation) and a possible decrease of the efficiency.

It has been proved that the dry gas mixture increases the bakelite resistivity while the wet gas mixture turns out to be effective in preserving the initial resistivity [1]. The effect of the humidity on the bakelite resistivity, together with the dependence on temperature, has been widely investigated with several bakelite measurement in controlled environmental conditions; the results of this study are reported in Appendix A.

Furthermore, the protracted operation at high rates also results in a bakelite resistivity increase due to the nature of the conduction mechanism. To prevent this effect, and to preserve the rate capability performances, the RPCs for the ALICE Muon Forward Spectrometer are made up of low-resistivity ($\rho \sim 1$–8×10^9 Ω·cm) bakelite electrodes [2].

Another effect of long–term operation is a surface damaging due to the production of pollutants, and particularly of HF, in avalanche and especially in streamer discharges; this effect results in a dark current and dark rate increase. To protect the inner surface of the RPCs, two linseed oil layers, instead of the usual single oil layer, are deposed on it for the RPCs of the ALICE production: the improvement on the lifetime of the detector due to the second layer of linseed oil has been demonstrated in previous ageing tests

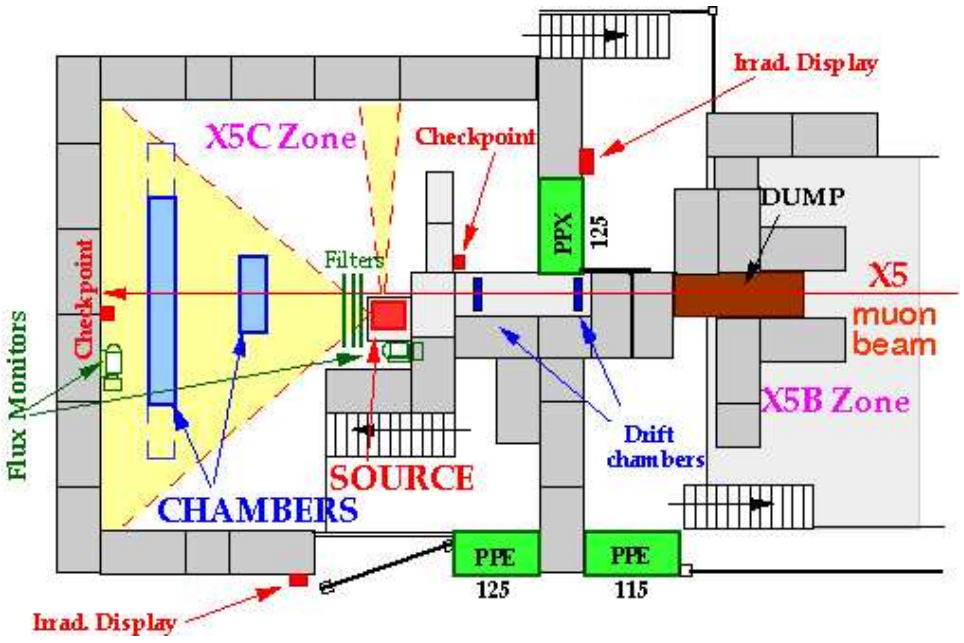

Fig. 7.1: Top view of the Gamma Irradiation Facility at CERN.

and reported in Section 5.3.2 and in reference [3].

7.2 Experimental setup for the ageing tests at GIF

To simulate the effect of a long working period at LHC, we have performed a serie of tests at the Gamma Irradiation Facility (GIF) [4] at CERN exposing the RPCs to a high γ ray flux from the ^{137}Cs source (610 GBq); the flux can be varied by means of lead filters and reduced by factors up to 1000. The top view of the GIF is sketched in Fig. 7.1.

The experimental setup is shown in Fig. 7.2: the RPC under test is put in front of the ^{137}Cs source in a mechanical structure that also supports two scintillator pairs to identify the cosmic ray for the efficiency measurement. The four–fold scintillator coincidence covers a 10×30 cm^2 area on the tested RPC. The mechanical support can house up to three RPCs at a time.

The tested RPCs, read by means of two orthogonal strips planes, have been equipped with the FEE cards with the ADULT chip: the two thresholds have been set at 10 mV and 80 mV for the tests in streamer mode whereas in maxi–avalanche mode both thresholds have been set at 10 mV.

Data acquisition and signal processing are the same used for the beam

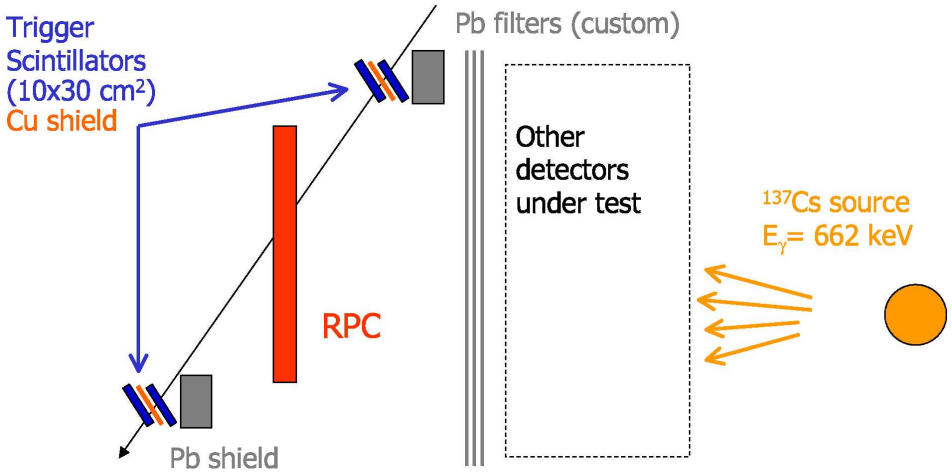

Fig. 7.2: Side view of the setup for the ageing tests at GIF. The cosmic ray trigger is given by the four–fold scintillator coincidence: the two scintillator pairs (one upstream the chamber and the other downstream) are protected from source irradiation by lead blocks (5 cm thick). The copper plate interposed between the scintillators of each pair protects the downstream scintillator from electrons emitted from interaction of γ–ray in the upstream one. The γ flux on the RPCs can be varied by means of the GIF lead filters, nevertheless a "custom shielding" can be put in front of the chambers to obtain the desired irradiation pattern.

test and are described in Section 6.3.

To study the ageing effects, the RPC current, rate and efficiency are continuously monitored during the test, alternating long irradiation periods (source on) and short ones without irradiation (source off).

There are three different trigger types:

- "Cosmic Ray" trigger (given by the coincidence of 2 pairs of scintillators) is the normal trigger used during ageing operation to monitor the efficiency, the rate and the current of the RPC;
- "Autotrigger[1]"(given by the coincidence of the logic OR of the 2 strips planes, X and Y) gives the local counts distribution when the source is off and the irradiation pattern when the source is on, these kind of run lasts few minutes;
- "Pulse Generator" to check the acquisition and to monitor the rate quickly and independently from scaler overflow due to the low frequency

[1] This type of trigger is not available for some of the ageing test described in the following sections.

of the cosmic ray trigger (about 2 events per minutes) coupled with a high γ induced rate.

In Fig. 7.3 is shown how these different trigger types are implemented: Cosmic Ray, Autotrigger and Pulse Generator enter in a discriminator which can be enabled/disabled by writing a mask, in this way only one trigger type at the time is enabled. The trigger is then distributed to the CAMAC modules (TDC, Coincidence Register and Status A for the interrupt handling).

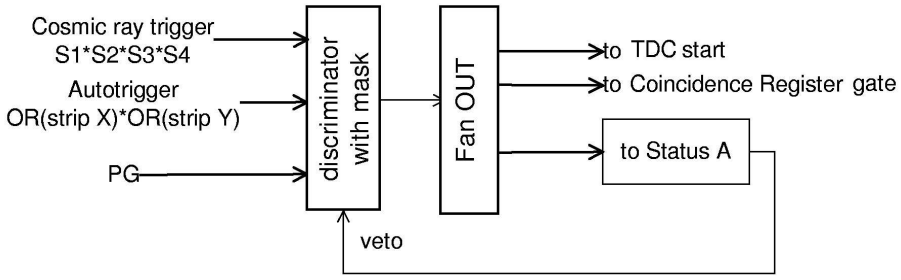

Fig. 7.3: Block scheme of the trigger distribution for the ageing test.

Temperature and pressure for the high voltage correction, accessible on the web [5], are provided by three stations dedicated to the environmental data taking installed in the GIF area and in the gas distribution zone. Since Spring 2004, the tests have been performed operating the chambers at fixed effective voltage with a temperature/pressure correction each 15 minutes.

7.3 Data analysis

The analysis depends on the trigger type:

- **Cosmic Ray**

  The efficiency of the chamber is calculated using the Coincidence Register information. With a preliminary analysis, the range of strips X and Y covered by the trigger is defined: the RPC is considered efficient if there is at least one hit on these strips. We have also implemented an event selection considering only the events with number of cluster less than 9 on the 2 strip planes, in such a way it is possible to reject cosmic ray showers or problems on the FEE cards.

- **Autotrigger**

We evaluate the rate (dark rate or γ induced rate) distribution on the whole surface of the RPC: each trigger is given by the coincidence of one strip X with one strip Y (around 2×2 cm^2 cell) and the rate of each cell is given by:

$$\text{rate} = \frac{\text{cell counts}}{\text{area(cm}^2) \times \text{time(s)}} \text{dead time} \tag{7.1}$$

where the dead time is the ratio between the number of trigger without veto and the number of acquired trigger. The obtained value is nevertheless affected by a systematic error given by the cluster size: in fact a fraction of the "cell counts" is due to the counts of the 8 nearby cells, this fraction is obviously proportional to the cluster size.

When the source is off we have an information related to the noise distribution, while, at source on, the rate distribution should remains the same, if nothing changes in the setup of the detectors between the source and our chambers, any other change can be related to a loss of efficiency.

- the **Pulse Generator trigger** provide an additional method to calculate the rate on the RPC.

7.4 Streamer mode ageing tests

In Section 5.1 are reported the requirements for the detector lifetime: working in streamer mode and estimating the charge of each streamer to be 500 pC, the ageing requirement of 100 Mhit/cm^2 for the heavy–ion program corresponds to an integrated current of 50 mC/cm^2.

The streamer mixture has already been tested on four small prototypes (50×50 cm^2) in different conditions (wet/dry gas mixture, number of linseed oil layers ...). Despite an increase of the dark current, the efficiency for cosmic rays was stable up to about 100 Mhit/cm^2 (50 mC/cm^2) as described in Section 5.3.2.

7.4.1 RPC1 ageing tests

We describe here the ageing test of RPC1 (210×70 cm^2), a pre–production chamber already tested in the September 2003 beam test and described in Section 6.5.

As said before, in ALICE we expect a not uniform irradiation on the RPCs planes, with high rates near to the beam pipe and decreasing ones in

the external parts: to recreate these conditions, a custom lead plates shielding has been installed between the RPC and the source; this shielding, sketched in Fig. 7.4, gives rates from 6 to 60 Hz/cm^2, i.e. about a factor 10 higher than the ones expected in ALICE, but with a very similar irradiation distribution. Efficiency was monitored in the most irradiated section of RPC1.

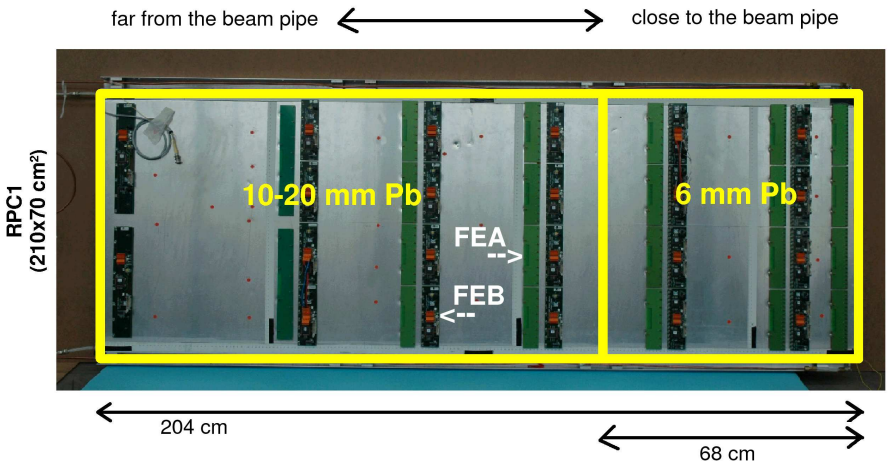

Fig. 7.4: Front view of the ageing setup. RPC1 (in the Figure background) has been shielded with lead plates of different thickness (from 6 mm to 20 mm, indicated by the yellow boxes) to reproduce the counting rates distribution expected in ALICE: high rates (up to 60 Hz/cm^2) near to the beam pipe and the lower ones (~10 Hz/cm^2) far from the beam pipe. RPC1 is totally equipped with Front End Board (FEB) and Front End Adapter (FEA) cards. The scintillator hodoscopes are not shown in this figure.

After protracted operation (~100 Mhit/cm^2 in the most irradiated area), the detector has shown a slight dark current increase up to 13 μA, while the dark rate remained lower than 0.4 Hz/cm^2 (see Fig. 7.5). Fig. 7.6 shows the efficiency plateaux obtained with ~60 Hz/cm^2 of γ induced rate at the beginning of the ageing test and after having integrated 100 Mhit/cm^2: the displacement of the efficiency plateau, due to the bakelite resistivity increase, is the cause of the efficiency loss observed in Fig. 7.5. Nevertheless, at the end of the test, RPC1 has a 97% efficiency without induced gamma irradiation, condition that is more similar to the one we will have in the ALICE environment (Table 5.1) that the one with a maximum rate of about 60 Hz/cm^2.

At the end of the ageing test, RPC1 has been tested on the test bench built in Turin for the validation of the final RPCs: a description of the setup and of the testing procedure has been provided in Section 5.5.

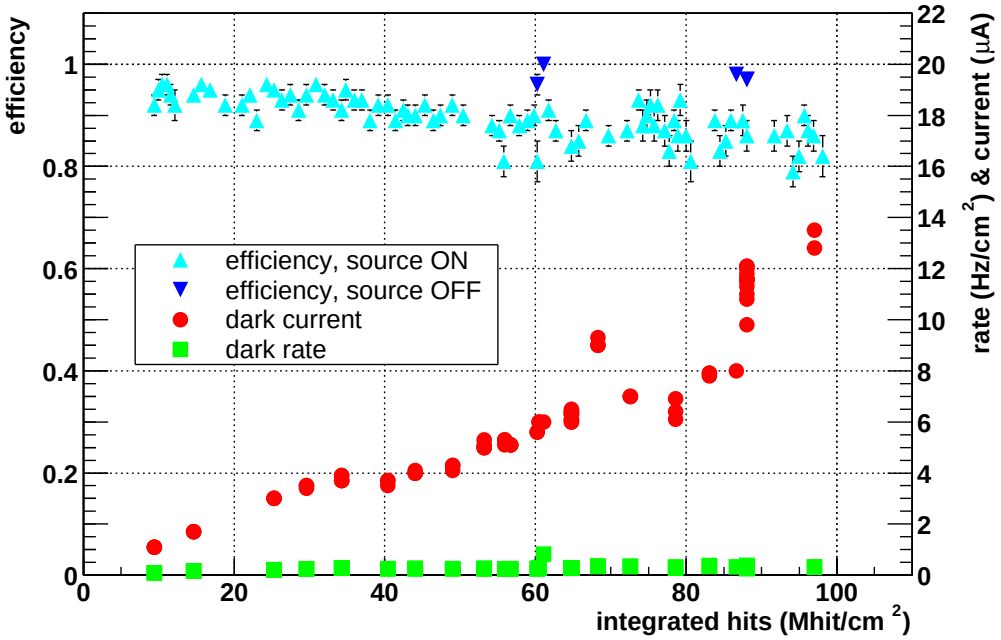

Fig. 7.5: RPC1 tested in streamer mode at GIF: efficiency (with - 60 Hz/cm^2, azure points - and without γ irradiation - blue point), dark current and dark rate as a function of the integrated hits. The working voltage ranged between 8050 and 8250 V.

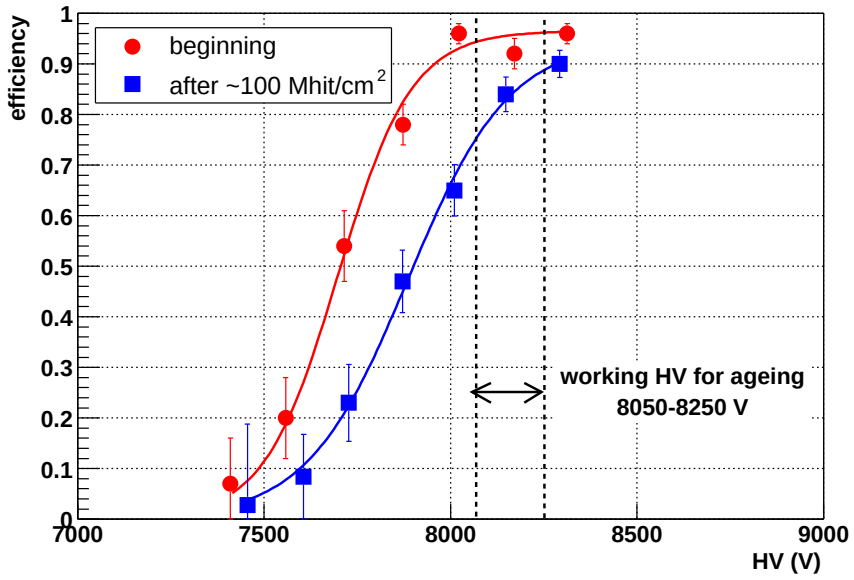

Fig. 7.6: RPC1 tested in streamer mode: efficiency plateaux for the detection of cosmic rays with $\sim$60 Hz/cm^2 of γ induced rate at the beginning of the ageing test (red circle) and after 100 Mhit/cm^2 (blue square). During the ageing test, the working voltage ranged between 8050 and 8250 V.

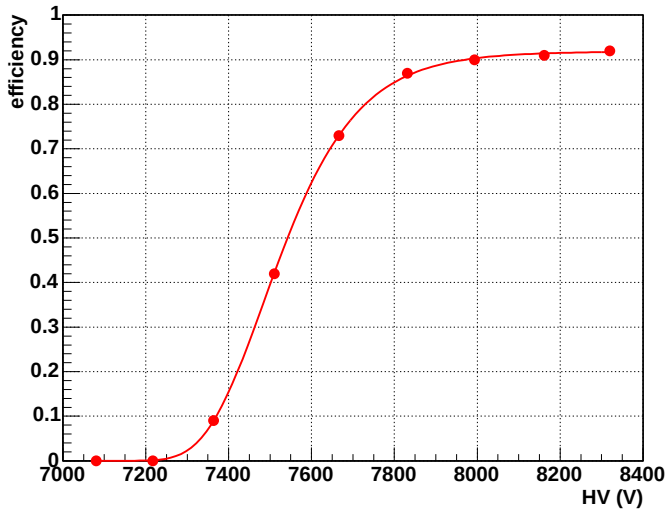

Fig. 7.7: RPC1 tested on the Turin test bench: efficiency plateau of a 20×20 cm^2 cell.

The efficiency of RPC1 has been measured over the whole surface of the chamber with 20×20 cm^2 cells: in Fig. 7.7 is reported one of the obtained plateau. A maximum efficiency of 92% (geometrical ineffiency of the spacers included) is achieved, this value is in reality affected by a systematic error due to fake triggers of about 3–4% less.

The distribution of the HV giving a 50% efficiency for the 21 tested positions is plotted in Fig. 7.8, the mean value is 7550 V, with a RMS=40 V: the RMS/mean ratio is therefore equal to 0.5%.

The map of the efficiency at constant high voltage (HV=8300 V) is shown in Fig. 7.9: the dimension of each cell is about 1.2×1 cm^2. The mean efficiency at 8300 V is ∼94% (value not corrected for fake triggers); it has to be noticed that the efficiency in the extreme left side is affected by a very low statistics; the yellow–green dot grid (efficiency ∼50%) is due to the geometrical inefficiency caused by the spacers.

The main result of this test is that after protracted operation (equivalent to 10 years of heavy–ion collisions), RPC1 is still fully efficient with an excellent uniformity in the plateau position over the whole surface of the chamber (RMS/mean=0.5%).

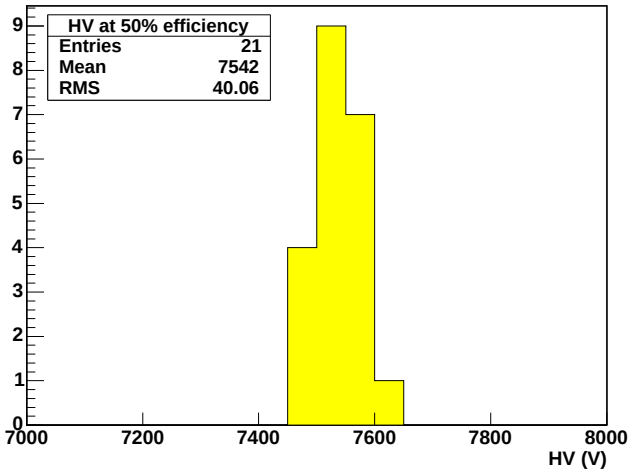

Fig. 7.8: RPC1 tested on the Turin test bench: 50% efficiency high voltage distribution.

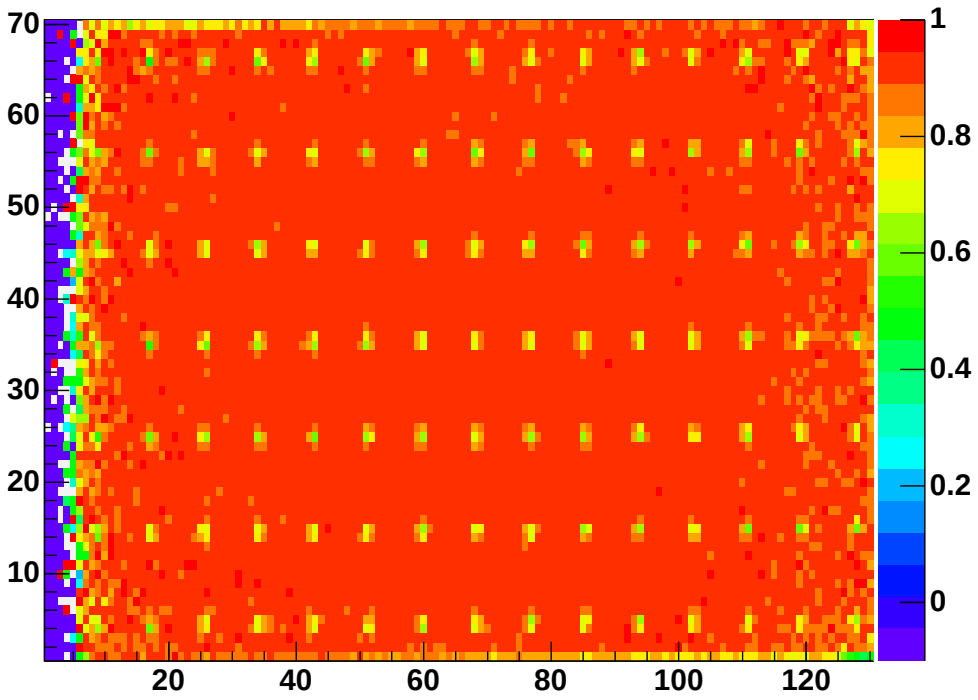

Fig. 7.9: RPC1 tested on the test bench: efficiency map at HV=8300 V. The dimension of each cell is about 1.2×1 cm^2. The efficiency in the left side is affected by a very low statistics and the yellow–green grid (efficiency ∼50%) corresponds to the geometrical inefficiency caused by the spacers.

7.4.2 Streamer gas mixture without tetrafluorethane

In the last years, great attention has been addressed to the understanding of the ageing effects due to polluting substance production inside the gas gap. The project "Common Effort for RPCs" at GIF of CERN has been created to puts together the studies of different research teams, related to different experiments at LHC, that will use RPC detectors.

In this framework, chemical analysis both of the electrodes surface and of the gas mixture have been carried out. In particular, the analysis of the exhaust gas provides percentage of impurities and the concentration of HF (μg/l), one of the most aggressive acid for the bakelite surface.

One of the first hypothesis is that the HF production occurs in presence of tetrafluorethane ($C_2H_2F_4$), while the SF_6 presence is not relevant. We have therefore undertaken a study of a streamer gas mixture without $C_2H_2F_4$.

Previous tests on ALICE RPC prototypes, have shown that the streamer gas mixture 80% Ar, 20% C_4H_{10} with an added quantity of SF_6 ($\sim$4%) has a good time and spatial resolution [6]; nevertheless it was not selected for the use because of the signal amplitude, which is greater with respect to the usual streamer gas mixture.

Ageing tests performed in the past have as well demonstrated that reducing the SF_6 percentage it is possible to increase the lifetime of the detector [3]. To choose the gas mixture to be used for the ageing test, we have first investigated the behaviour with different percentage of SF_6: 1%, 2% and 4%.

The results for the efficiency plateaux and the mean cluster size trend are plotted in Fig. 7.10 and Fig. 7.11, as we can notice, the trend of the cluster size does not change changing the SF_6 percentage.

We have thus decided to perform an ageing test in the following conditions:

- the RPC flowed with the gas mixture 78% Ar, 20% C_4H_{10} and 2% SF_6 (RH=50%, 60 cc/min corresponding to 7.2 vol/hour);
- the working voltage set at 5700 V;
- the irradiation rate of about 50 Hz/cm^2.

The tested RPC is a small prototype (50$\times$50 cm^2) called RST1.

We observed that, since the beginning, the current had a tendency to grow fast; furthermore, switching on or off the source, the current followed the trend shown in Fig. 7.12.

At the end of the ageing, RST1 integrated $\sim$100 Mhits/cm^2, corresponding to the total heavy–ion program at LHC. In Fig. 7.13 are plotted the trends of current, rate and efficiency with respect to the integrated hits:

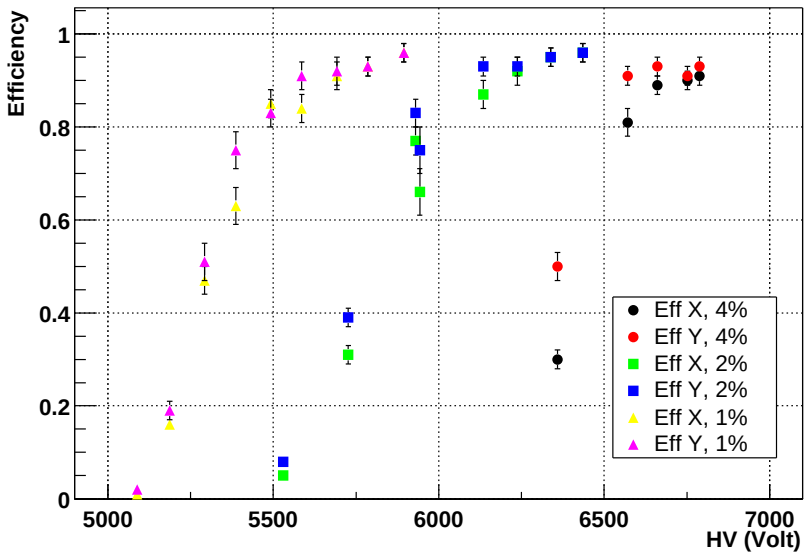

Fig. 7.10: Efficiency plateaux for streamer gas mixture 80% Ar, 20% C_4H_{10} with different percentages of SF_6 (1% pink and yellow triangle, 2% blue and green square and 4% black and red circle).

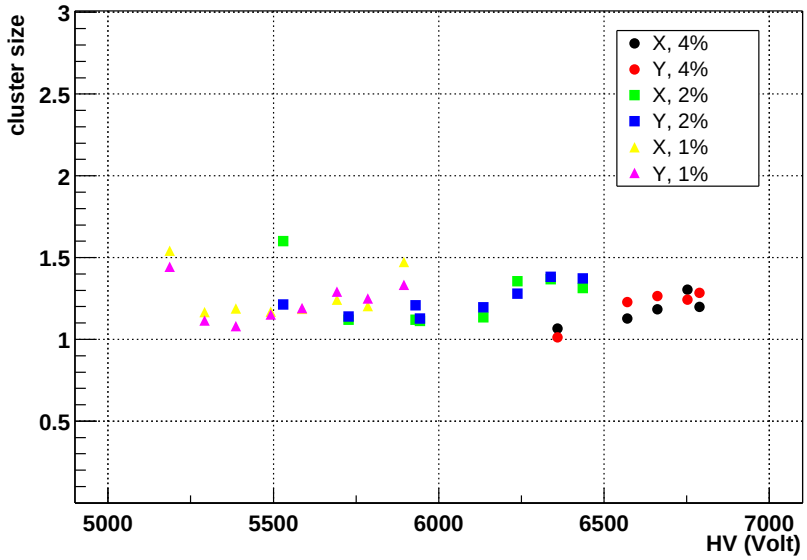

Fig. 7.11: Mean value of the cluster size for streamer gas mixture 80% Ar, 20% C_4H_{10} with different percentages of SF_6 (1% pink and yellow triangle, 2% blue and green square and 4% black and red circle).

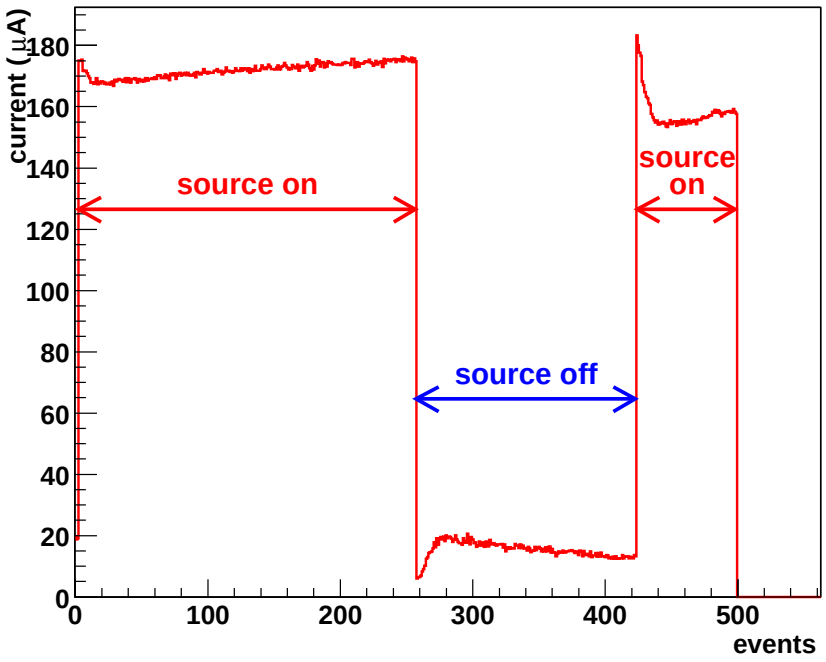

Fig. 7.12: Current behaviour of RST1 during a typical 500 events run (∼3 hours), switching on and off the source.

- as said before, the dark current started suddenly to grow reaching at the end $\sim$100 μA;
- the dark rate had the same trend, reaching at the end $\sim$20 Hz/cm^2;
- the efficiency is quite constant through the whole period, except a little loss of efficiency at source on.

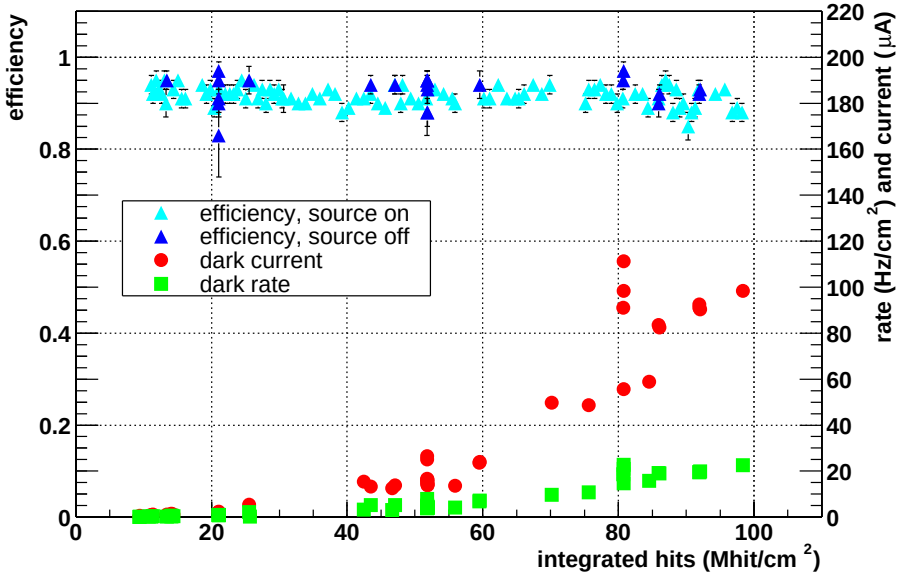

Fig. 7.13: RST1 tested with the streamer gas mixture without tetrafluorethane: efficiency (with - 50 Hz/cm^2 - and without γ irradiation), dark current and dark rate as a function of the integrated hits.

As last operation, we have taken a sample of exhaust gas to check if the tetrafluorethane absence results in exhaust gas without HF, but an amount of 0.017 mg/l of HF was found. The value, even if it is lower that the typical one obtained with the ALICE streamer gas mixture (0.03 mg/l), indicates that it is not sufficient to eliminate the tetrafluorethane to prevent the acid formation, as a matter of fact the HF production occurs probably in presence of SF_6. The results of the analysis, as well as the working voltage, current and rate conditions during the gas sampling are reported in Table 7.1.

We thus tested, for a short period, a second small prototype (RST2, 50$\times$50 cm^2 area) with a new streamer mixture without fluorine (neither tetrafluorethane nor SF_6): 80% Argon and 20% C_4H_{10}. Considering the

	source on
HV_{eff}	5350 V
mean rate	55 Hz/cm^2
mean current	initial 250 μA final ~300 μA
HF	0.017 mg/l gas
total impurities	0.431 %

Tab. 7.1: HF and impurity contents in a sample of exhaust gas from RST1 flowed with 78% Ar, 20% C_4H_{10} and 2% SF_6.

efficiency plateau shown in Fig. 7.14, we have chosen 5100 V as working voltage.

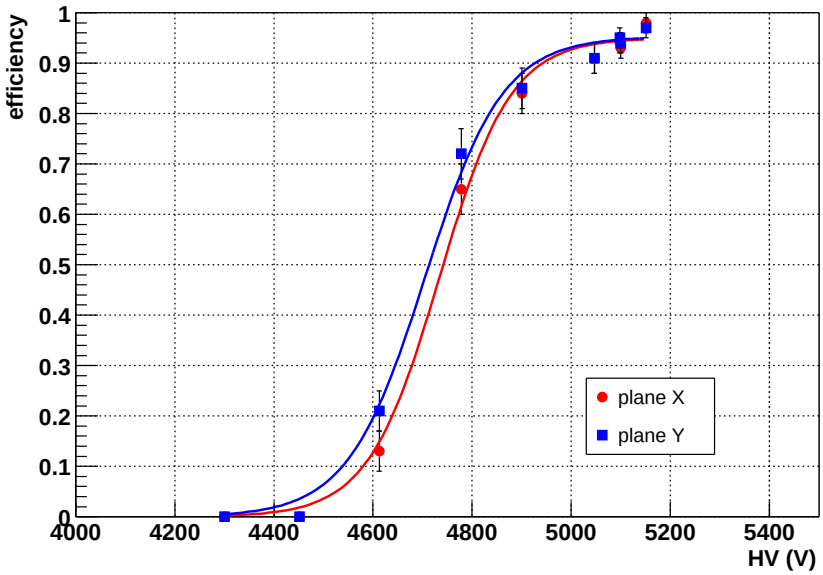

Fig. 7.14: Efficiency plateau of RST2 operated with a streamer gas mixture without tetrafluorethane (80% Ar and 20% C_4H_{10}).

Also with this new gas mixture the dark current and the dark rate started to increase from the very beginning.

We performed two gas sampling at source on and at source off: in Table 7.2 are listed the results of the chemical analysis, as well as the working voltage, current and rate conditions during the gas sampling. As expected, no HF has been found.

	source on	source off
HV_{eff}	5100 V	5100 V
mean rate	50 Hz/cm^2	1 Hz/cm^2
mean current	initial 160 μA final $\sim$300 μA	$\sim$10 μA
HF	0 mg/l gas	0 mg/l gas
total impurities	0.253%	0%

Tab. 7.2: HF and impurity content of samples of exhaust gas from RST2 fluxed with 80% Argon + 20% C_4H_{10}.

Despite the constant efficiency measured over the test period, the increase of the dark current and of the dark rate as a function of the integrated hits (Fig. 7.13) and the current trend at source on/off switch, show that these streamer gas mixture without tetrafluorethane is not appropriate for long term operation.

7.4.3 Conclusions and remarks

Ageing test with the streamer gas mixture (50.5% Ar, 41.3% $C_2H_2F_4$, 7.2% C_4H_{10}, 1% SF_6, RH=50%) have been undertaken on RPC1, a pre–procuction chamber of area 210×70 cm^2, to corroborate the results of the ageing test performed on small RPC prototypes (50×50 cm^2).

The test has been carried out with custom shielding in front of the RPC to reproduce a pattern irradiation with a distribution similar to the one expected in the ALICE environment. RPC1 works satisfactorily up to 100 Mhit/cm^2 (50 mC/cm^2) corresponding to the heavy–ion program for the first 10 years of data taking in ALICE, thus confirming the results obtained with small prototypes.

The efficiency of RPC1 has been measured at the end of the test on the Turin test bench on the whole surface of the chamber with 1.2×1 cm^2 cells: the RPC was found efficient with an excellent uniformity.

Moreover, this result is relevant in comparison with the ones obtained in the beam test during which a disuniformity in the efficiency plateau position was observed, as described in Section 6.5. This disuniformity, mainly due to the use of a dry gas mixture, was solved by flushing the chamber with a wet gas mixture, allowing a quick decrease of the resistivity with a consequential recovery of the rate capability: a partial recovery was already noticed during the last part of the beam test, while, during the test in Turin, a total recovery has been found.

These results can be explained considering the dependence of the bakelite resistivity on temperature and humidity as reported in Appendix A. In Fig. A.2 is reported the trend of the bakelite resistance as a function of the time after relative humidity changes at constant temperature: the humidity change causes a rapid resistance increase/decrease followed by a long period necessary to reach stable condition. This mean that the effect of humidity change is soon evident, but it take few months to get a total recovery, as experimentally verified with RPC1.

Ageing tests have been undertaken with a streamer gas mixture without tetrafluorethane (78% Ar, 20% C_4H_{10}, 2% SF_6, RH=50%) trying to prevent the HF formation (i.e. the most aggressive agent for linseed oil coating).

The efficiency measured over the test period has remained constant, but the increase of the dark current and of the dark rate as a function of the integrated hits and the current trend at source on/off switch, indicate that this streamer gas mixture is not appropriate for long term operation.

7.5 Highly–saturated avalanche mode ageing test

As mentioned in Section 5.4, test results demonstrated that it is possible to work in highly–saturated avalanche mode with the same Front End Electronics foreseen for the streamer operations. Moreover, the results of the September 2003 beam test (Section 6.5.2, 6.5.3) showed that the performance, in term of time resolution and cluster size, are similar to the ones obtained with the ALICE streamer gas mixture, exception made for a slightly higher cluster size.

On the basis of these results, we decided to perform an ageing test with the maxi–avalanche gas mixture.

The correspondence between charge and hit for the maxi–avalanche mixture is about 150 pC/hit: this means that the requirement of 100 Mhit/cm^2 per year for the p–p program corresponds to 15 mC/cm^2 per year. The ageing test in maxi–avalanche mode has been carried out on small prototypes of 50×50 cm^2, they are equipped with two orthogonal strip plane (24 strip of 2.215 cm for plane) that cover the whole surface of the chamber, including the borders and the corners.

A preliminary test has been undertaken in November 2003 on one chamber: a total of 100 Mhit/cm^2 have been integrated without noticing any ageing effect. Nevertheless we decided to stop the test because the RPC had only one linseed oil layer, instead of the two of the final production chambers.

7.5.1 Spring 2004 ageing test

During Spring 2004 we have undertaken an ageing test on one small prototype, hereafter RAV1, with two linseed oil layers. The chamber is flushed with 100 cc/min of the maxi–avalanche gas mixture (88% $C_2H_2F_4$, 10% C_4H_{10} and 2% SF_6, RH=50%, 100 cc/min corresponding to 12 vol/hour).

The efficiency plateau of RAV1 is reported in Fig. 7.15: the knee is at 10600 V so that a working point of 10900 V has been chosen for the ageing. During the test, the chamber has been irradiated with a γ induced rate ranging from 125 to 170 Hz/cm^2, with limited periods at lower rate.

The trend of dark current and dark rate as a function of the integrated hits are plotted in Fig. 7.16: after having integrated about ∼225 Mhit/cm^2, the RPC dark current always remains low (∼1 μA) though showing some instabilities; the dark rate remains under 1 Hz/cm^2, apart from few oscillations in the first period. In the same Figure, the efficiency for cosmic rays detection measured at 10900 V is stable at 94% during the whole test period,

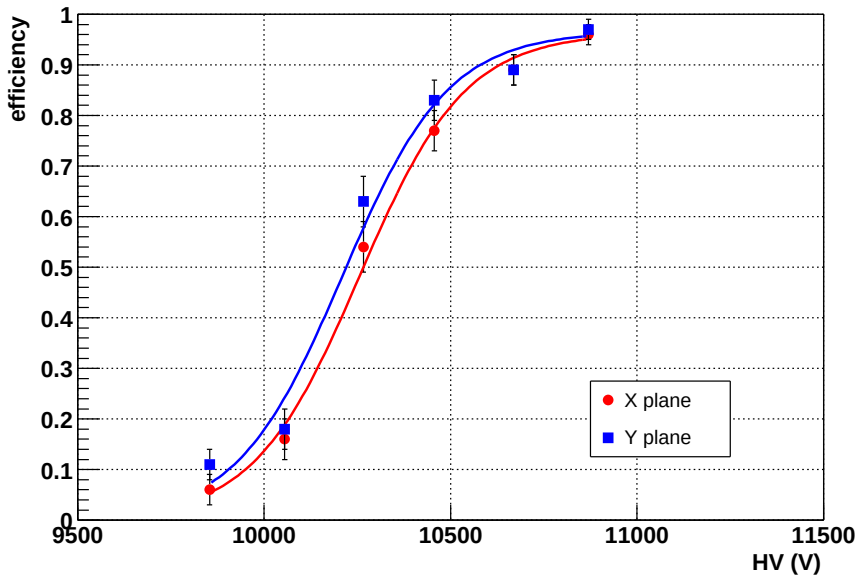

Fig. 7.15: RAV1 efficiency plateau with the maxi–avalanche mixture (88% $C_2H_2F_4$, 10% C_4H_{10}, 2% SF_6, RH=50%).

both without and with γ irradiation (120 Hz/cm^2).

Despite these good results, after having integrated about 100 Mhit/cm^2, from time to time, the current of the RPC starts to grow quickly and eventually passes the limit imposed by the HV power supply (hundreds of μA): in this case we define the condition as "trip". After a period with the high voltage off, the RPC totally recovers its normal behaviour, with high efficiency, low dark current and low dark rate.

After a series of test in different operating conditions (gas flow, gas relative humidity, ...), we can argue that:

- the trips are not induced by insulation problems, as a matter of fact the insulation between the RPC and the external mechanics has been improved during the test. Moreover, it has been measured that the current passes totally through the gas gap;
- the trip occurrence does not depend on the humidity of the gas mixture flowing inside RAV1 as it has been varied from 50 to 25%;
- trips are favored by high rates but there is no evident difference between 170 Hz/cm^2 and 125 Hz/cm^2 (for instance), whereas at 70 Hz/cm^2 trip occurrence is reduced;

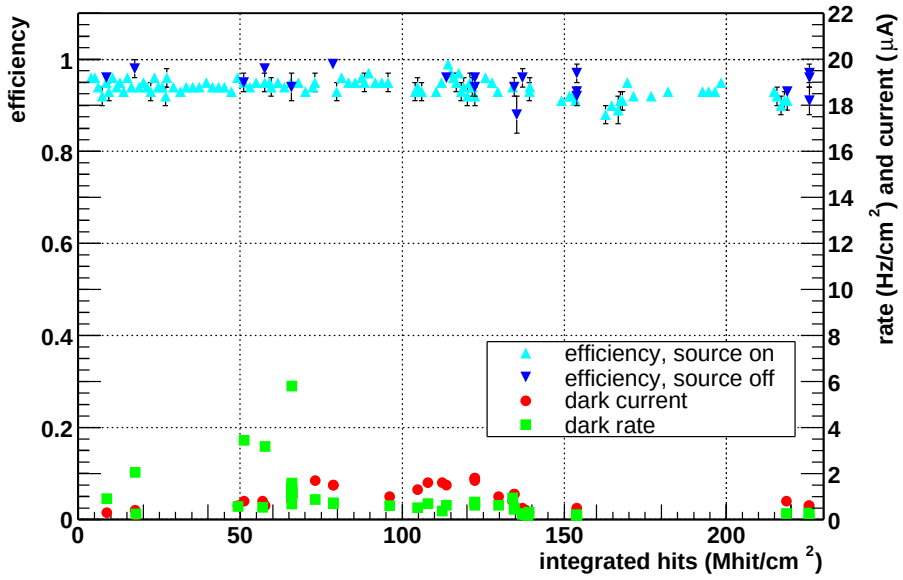

Fig. 7.16: RAV1 tested in maxi–avalanche mode: efficiency (with - 120 Hz/cm^2 rate - and without γ irradiation), dark current and dark rate as a function of the integrated hits.

- once induced, trip condition is maintained even switching off the GIF source as can be seen in Fig. 7.17;

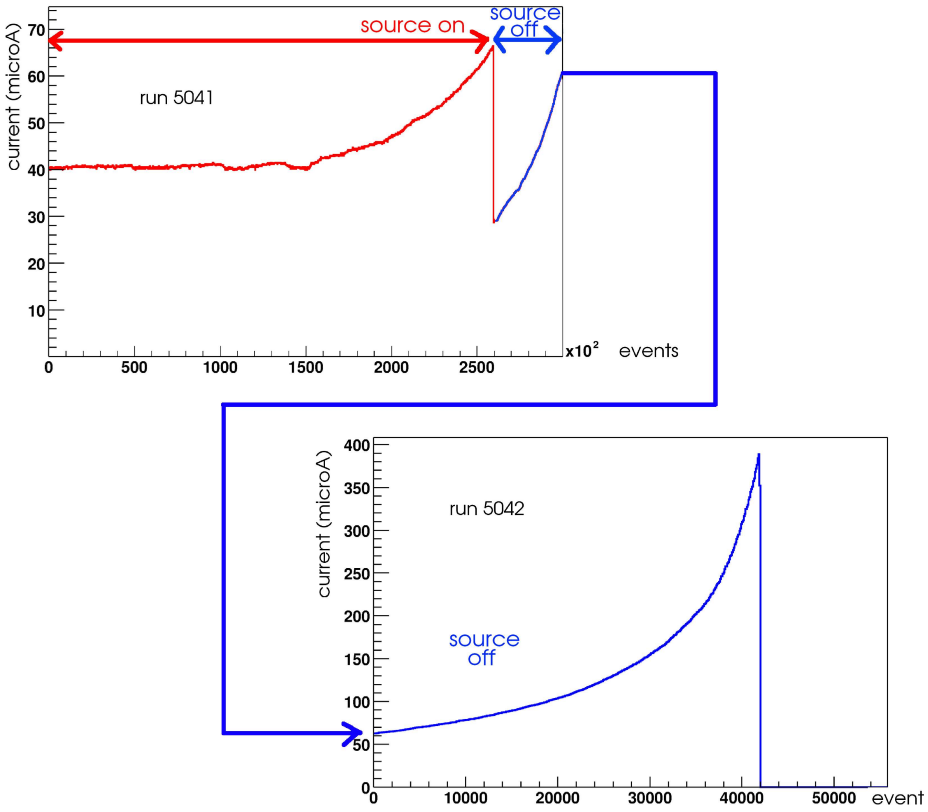

Fig. 7.17: Current trend during a trip: the source is initially on (red curve), after the first increase of current the source was switched off (blue curve). The current has a sudden decrease of ∼40 μA but then it starts again to increase up to 400 μA going in trip (I_{max} was set at 400 μA). On the horizontal axis 100 events correspond to about one second.

- during the trip there is a clear dependence on HV, once induced the trip, we lower the high voltage at different values:
  - if the effective HV is around 9500–9700 V (RPC totally inefficient) the current is higher than the value the RPC should have, but it slowly decreases to the normal value; once reached stable conditions the RPC can be put in working condition and the normal values of efficiency, dark current and dark rate are completely

restored;

– if during the trip we put an effective HV greater than 10000–10200 V (efficiency ∼10-15%), the current continues to increase.

In Fig. 7.18 is shown the current trend as a function of the elapsed time during three trip occurrences: the slope is always the same.

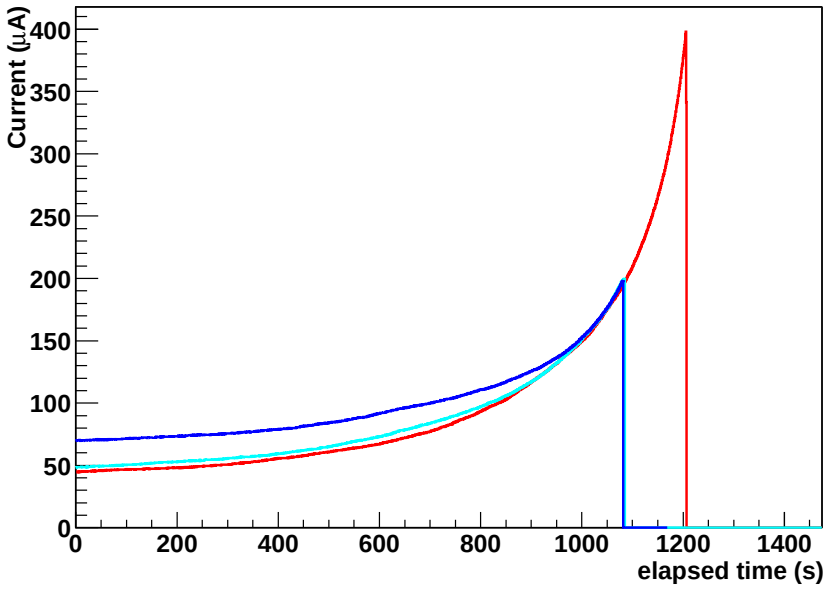

Fig. 7.18: Current trend as a function of the elapsed time during three trip occurrences.

On the basis of these results we hypothesized that the current increase could be due to a local discharge: in this case the temperature in correspondence of the discharge point should increase appreciably. To corroborate this hypothesis we have covered the ground side of the RPC with thermosensitive adhesives as shown in Fig. 7.19. The RPC without the external mechanics has been left under irradiation and we observe that:

- in normal operation condition the temperature on the surface of RAV1 was about 25°C (measured by mean of an infrared thermometer);
- during a sudden current increase, one of the thermosensitive adhesives reached a temperature of 35°C (Fig. 7.20);

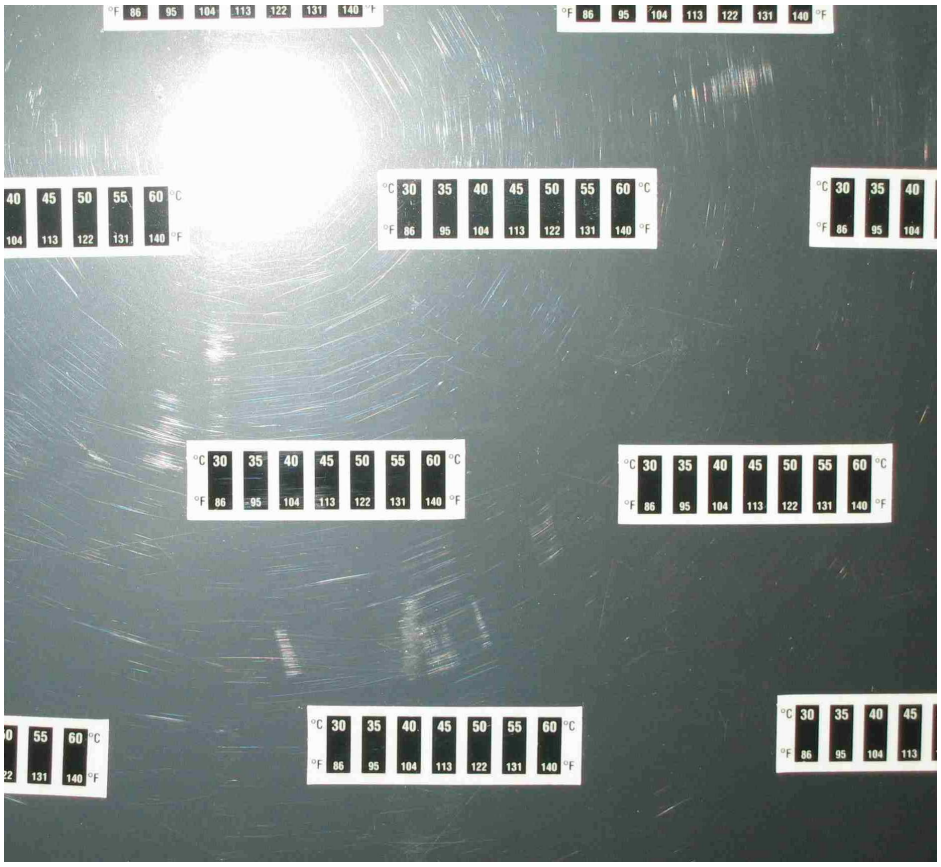

Fig. 7.19: Partial image ($\sim$10$\times$10 cm^2) of RAV1 ground side covered with thermosensitive adhesives.

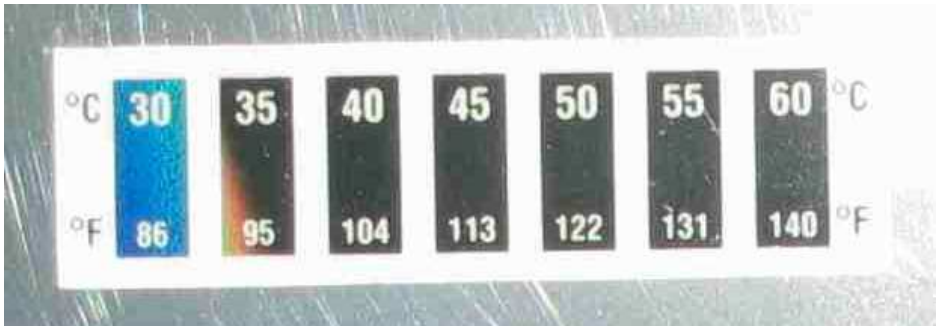

Fig. 7.20: Picture of the thermosensitive adhesive near to the hot spot at high current: the temperature reached is about 35°C

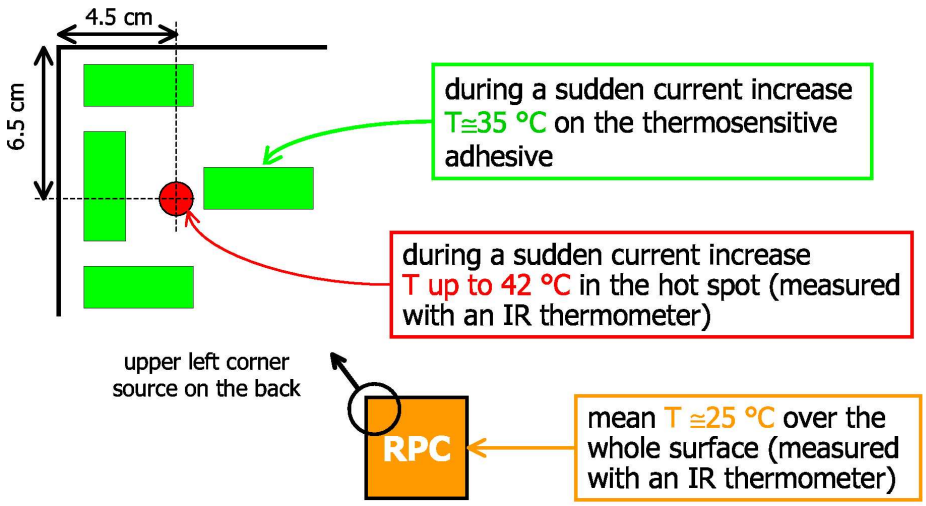

Fig. 7.21: Schematic sketch of the area around the hot spot.

- measuring the temperature with the infrared thermometer in the area around this adhesive we found a spot of radius ∼1 cm with a temperature of 42°C. A sketch of the position of the hot spot is reported in Fig. 7.21.

After the ageing test we have measured the chamber efficiency with the muon beam from CERN SPS–X5 (with the same setup of the other beam test already described in Chapter 6) scanning the whole surface of the chamber with a 10×10 cm^2 trigger. The goal of the test is to check the uniformity of the RPC with respect to the plateau position in absence of γ irradiation: the mean efficiency at HV=10900 V (that we have defined as working value) is 0.95±0.01 and it is uniform on the whole surface (see Fig. 7.22).

7.5.2 Spring 2005 ageing test

The ageing test performed in Spring 2004 shows that the current trend during the instability periods seems to have a strict correlation with high rates conditions and with the high voltage the RPC must work with (10900 V).

We thus tried to reduce the working voltage of the RPC by decreasing the percentage of SF_6 from 2% to less than 1%. To this aim, in November 2004, a beam test has been undertaken to study the performance of the RPCs with the following gas mixtures:

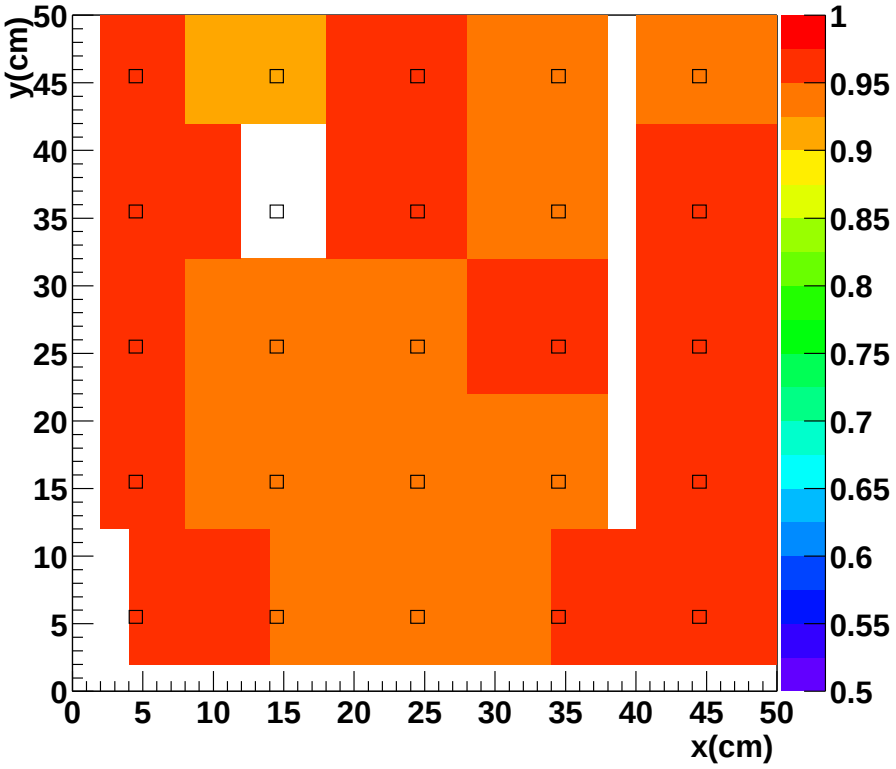

Fig. 7.22: Efficiency map of RAV1 tested in maxi–avalanche mode in the beam test. For each tested position (displayed with a colored square at the given X and Y chamber coordinates) the efficiency of the RPC at fixed HV=10900 V is represented. The white areas have not been tested; the small squares correspond to the spacers. The hot spot at high current is at coordinates (x=4.5 cm, y=43.5 cm).

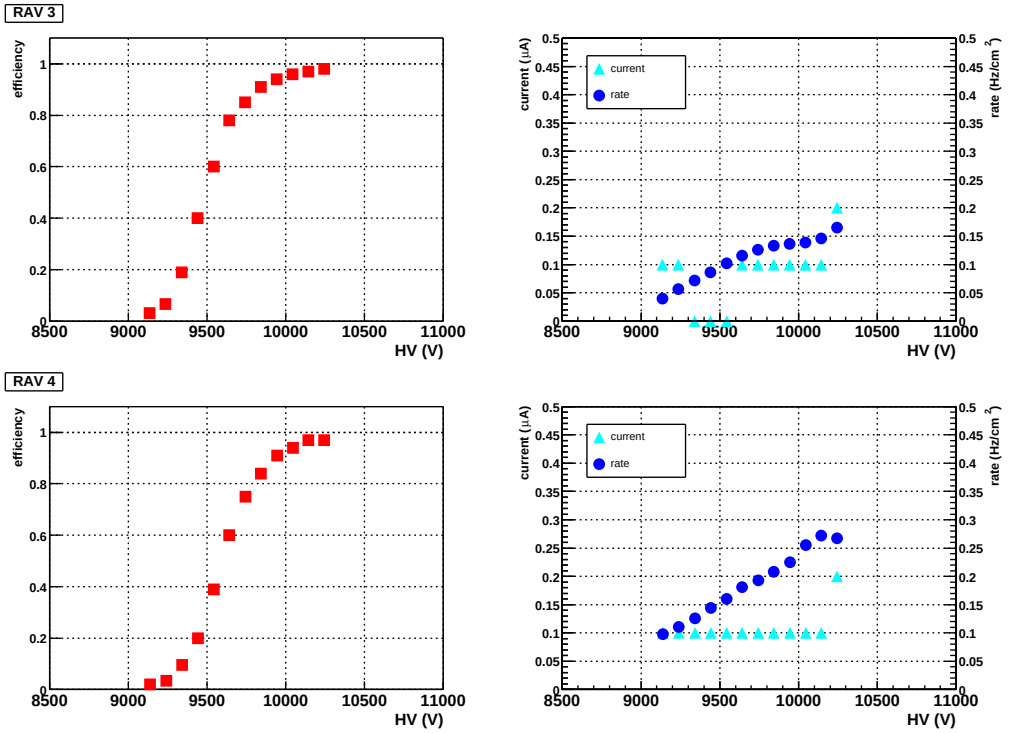

Fig. 7.23: Efficiency plateaux (left), current and rate (right) of RAV3 (top) and RAV4 (bottom) with the gas mixture 89.7% $C_2H_2F_4$, 10% C_4H_{10} and 0.3% SF_6, in absence of induced gamma irradiation.

- 89.7% $C_2H_2F_4$, 10% C_4H_{10}, 0.3% SF_6, RH=50%;
- 89.4% $C_2H_2F_4$, 10% C_4H_{10}, 0.6% SF_6, RH=50%.

November 2004 beam test

The experimental setup, the same used in the beam tests described in Section 6.3, allows us to measure the efficiency scanning the whole surface of the RPC with a 10×10 cm^2 trigger area (coincidence of four scintillators). The test has been carried out with two small RPC prototypes (50×50 cm^2) called RAV3 and RAV4.

Gas mixture with 0.3% SF_6

The efficiency plateaux for the detection of muons (in absence of irradiation) of RAV3 and RAV4 are reported in Fig. 7.23.

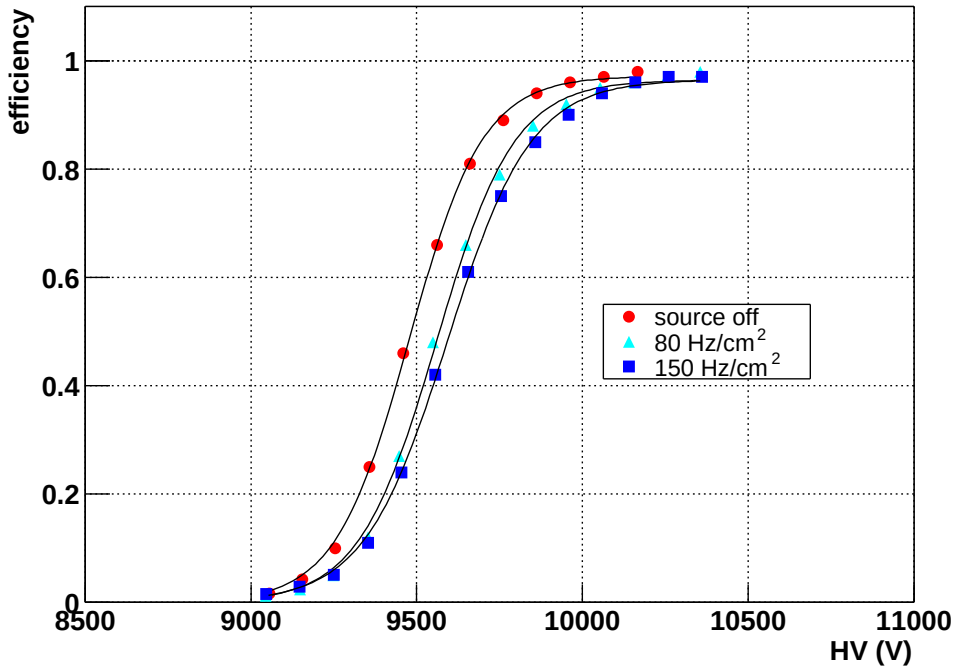

Fig. 7.24: RAV3 efficiency plateaux with the gas mixture 89.7% $C_2H_2F_4$, 10% C_4H_{10} and 0.3% SF_6 in different irradiation conditions: absence of irradiation (source off), 80 and 150 Hz/cm^2 of γ induced irradiation.

In Fig. 7.24 are plotted the efficiency plateau of RAV3 in different source condition: absence of irradiation (source off), 80 and 150 Hz/cm^2 of induced gamma irradiation (ABS=5 and ABS=2 respectively). The high voltage giving 50% efficiency is:

- 9480 V for the plateau with the source off;
- 9560 V for the plateau with 80 Hz/cm^2 of γ irradiation;
- 9590 V for the plateau with 150 Hz/cm^2 of γ irradiation.

The displacement ($\sim$100 V) between the two extreme conditions is the one expected considering the high voltage drop caused by the particle rate.

The dependence of the single counts on the threshold value has been studied too, both with the source on and with the source off. The threshold for the negative signals (Y) has been varied between -10 mV and -80 mV, while the threshold for the positive signals (X) has been kept fixed as reference: in

source	threshold (mV)		ratio Y/X	
	positive signals, X	negative signals, Y	RAV3	RAV4
off	+10	-80	25 %	30 %
on	+10	-80	20 %	22 %
on	+10	-60	28 %	30 %
on	+10	-40	47 %	50 %
on	+10	-25	80 %	83 %

Tab. 7.3: Study of the dependence of the single counts on the threshold value: the ratio between the rate of signals greater than 10 mV and the ones greater than the threshold for the negative signals is given for HV at working point (10100 V).

this way it is possible to obtain the ratio between the rate of signals greater than -80 mV (or -60 mV, -40 mV and -25 mV) and the ones greater than 10 mV. All these information are summarized in Table 7.3.

Furthermore, as an example, in Fig. 7.25 are reported the rates (with source on) of RAV3 and RAV4 with the threshold set to +10 mV and -80 mV: in this specific case the ratio correspond to the percentage of streamer signals, whose typical amplitude is of the order of 100-150 mV.

The study on the threshold dependence has been carried out also measuring the efficiency of the RPCs for the detection of muons: tests has been done varying the threshold for negative signals (Y) between -10 and -80 mV and keeping fixed the threshold for the positive signals (X) at 10 mV; the results for RAV3 are reported in Fig. 7.26; in particular, the efficiency with the threshold set at 80 mV is 6–8% at working point (10100 V). The difference between this measurement and the one performed with the single count (20% at working voltage) could be due to the fact that, for this test, the strip planes cover totally the gas gap, including the borders and the corners where high dark rate is localized. It must be remarked that the strip planes for the final RPCs have a guard frame of about 2 cm.

The performances of the RPCs have been widely investigated with two discrimination thresholds: 7 and 10 mV. In Fig. 7.27 and Fig. 7.28 are reported the results for the efficiency plateaux, cluster size and time resolution as a function of the high voltage for RAV3 and RAV4. The threshold reduction from 10 to 7 mV yields to a decrease in the plateau position of 150–175 V accompanied by a slight degradation of the cluster size.

Fig. 7.29 and 7.30 show the trend of the mean cluster size as a function of the applied voltage shifted by the knee voltage: this means that the zero

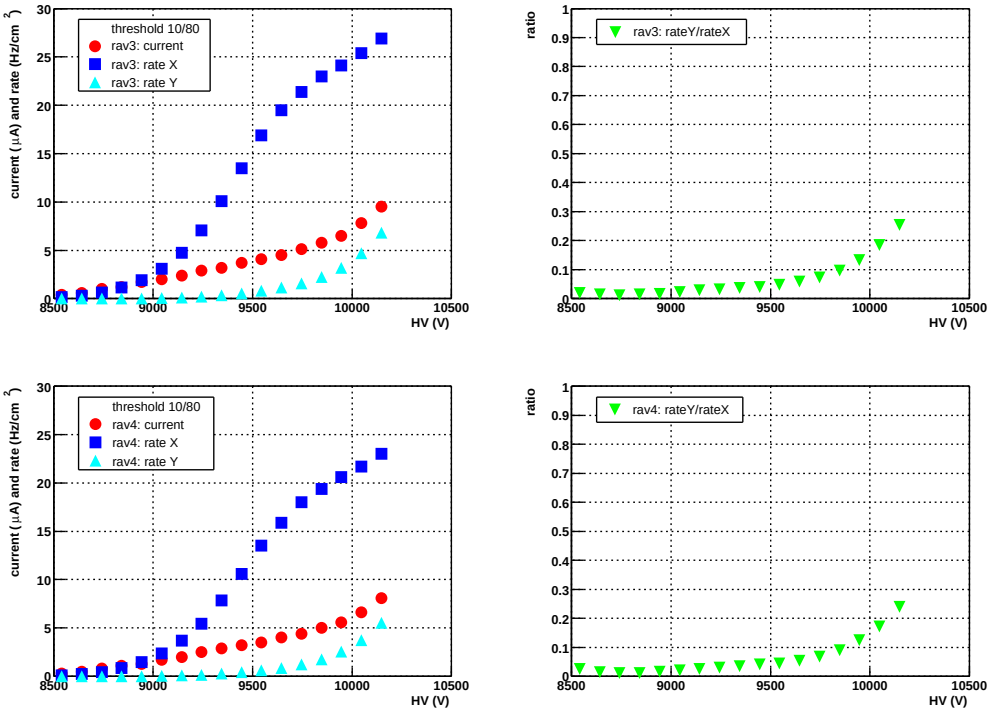

Fig. 7.25: Current and rates trend with threshold set at +10 mV (positive signals, X) and -80 mV (negative signals, Y) at source on (25 Hz/cm^2). On the right side, the green curves show the streamer contamination as a function of the high voltage.

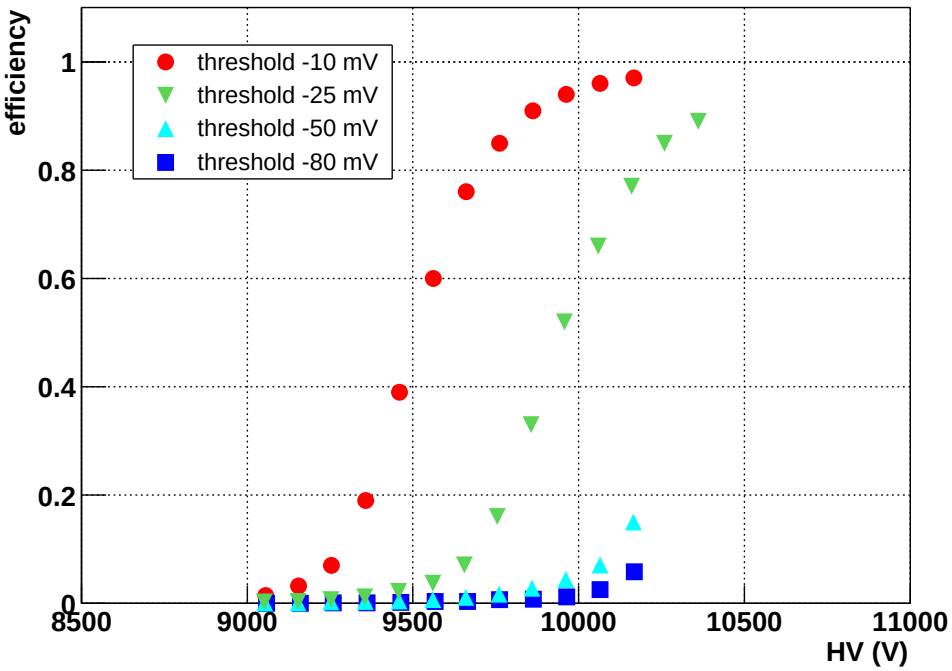

Fig. 7.26: RAV3 efficiency curves with the gas mixture 89.7% $C_2H_2F_4$, 10% C_4H_{10} and 0.3% SF_6 for different threshold values ranging between -10 and -80 mV.

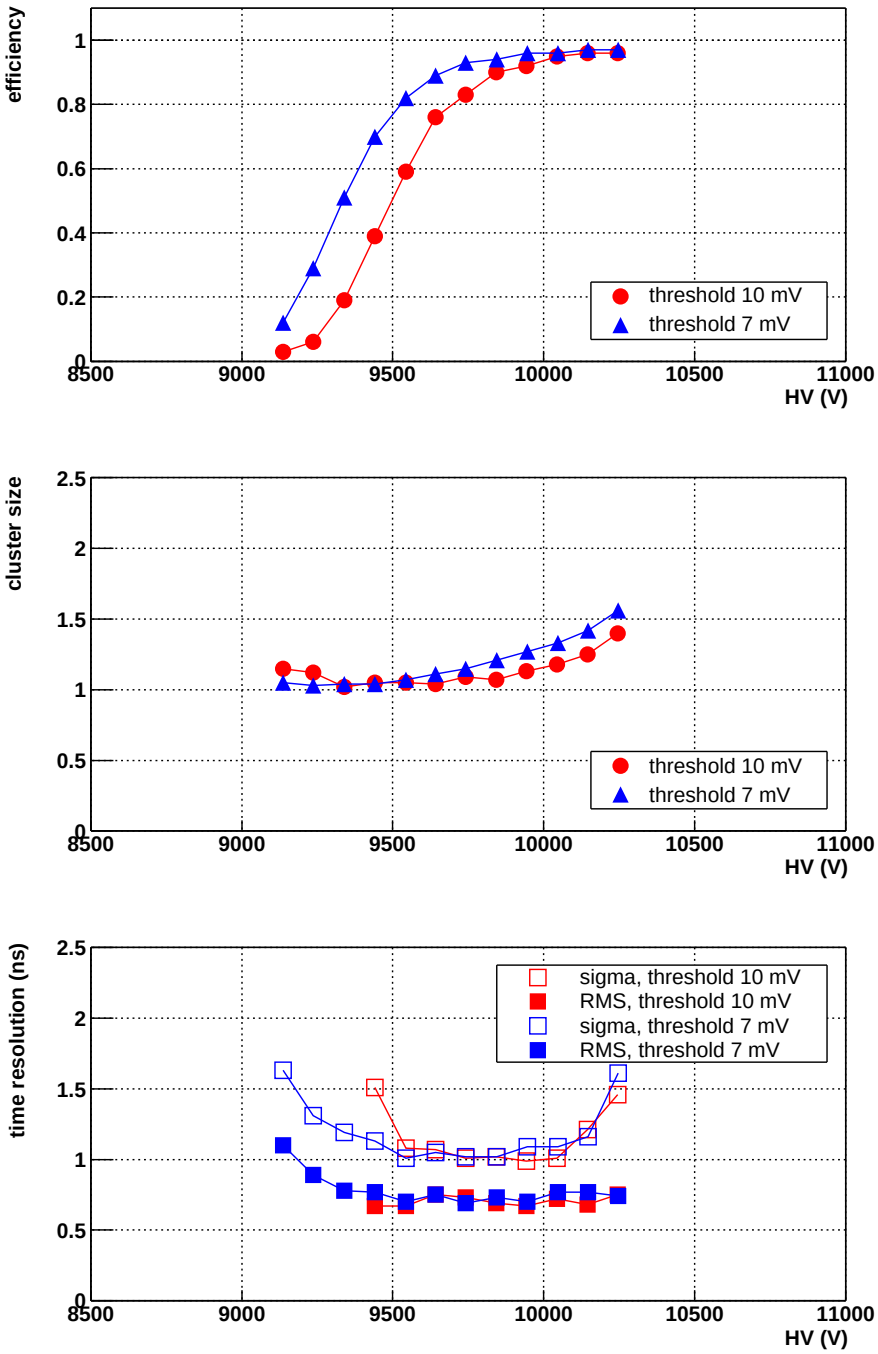

Fig. 7.27: RAV3 performances with the gas mixture 89.7% $C_2H_2F_4$, 10% C_4H_{10} and 0.3% SF_6 for two different discrimination threshold values, 7 and 10 mV: efficiency plateaux (top), cluster size (center) and time resolution (bottom) as a function of the high voltage.

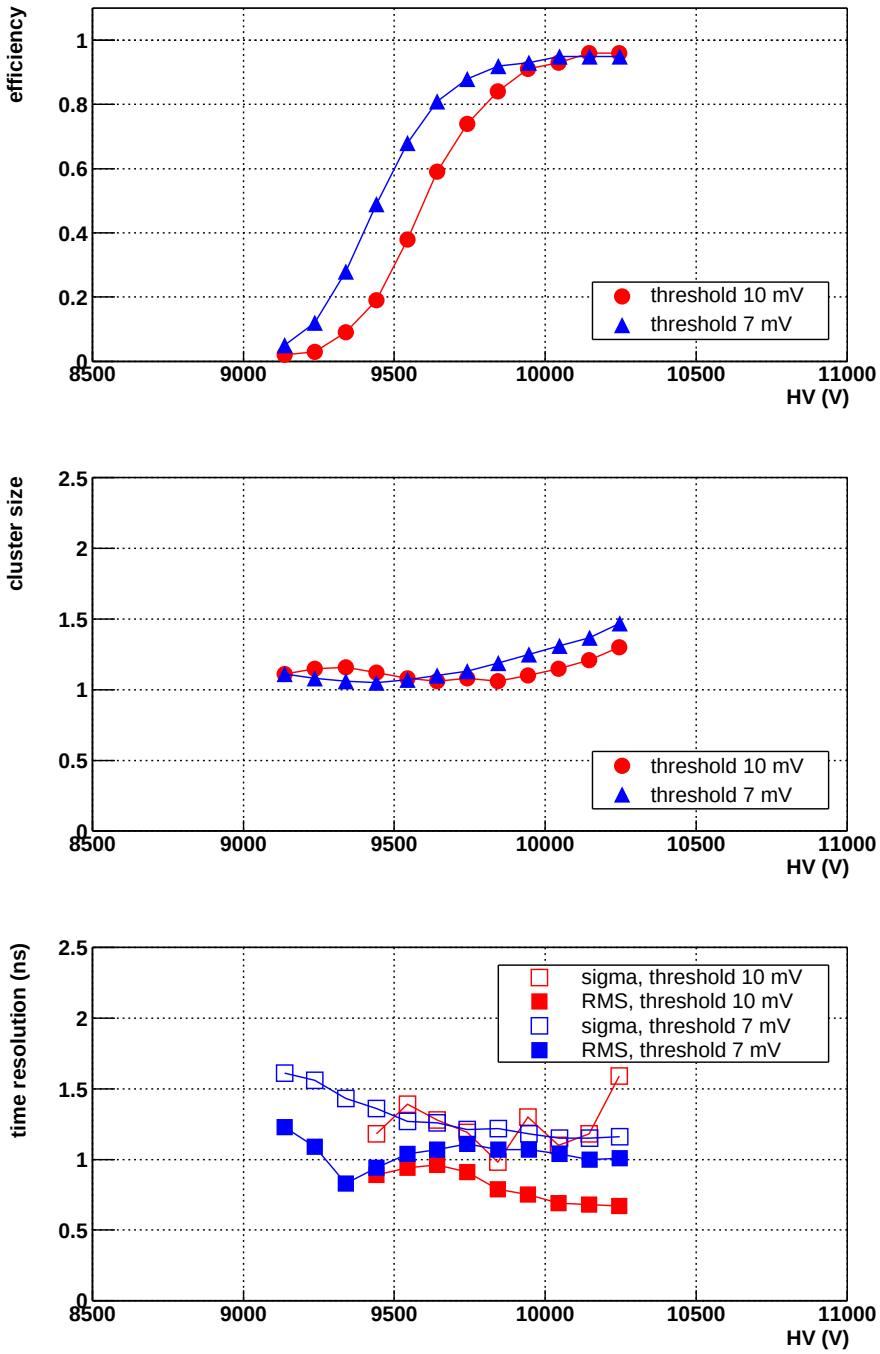

Fig. 7.28: RAV4 performances with the gas mixture 89.7% $C_2H_2F_4$, 10% C_4H_{10} and 0.3% SF_6 for two different discrimination threshold values, 7 and 10 mV: efficiency plateaux (top), cluster size (center) and time resolution (bottom) as a function of the high voltage.

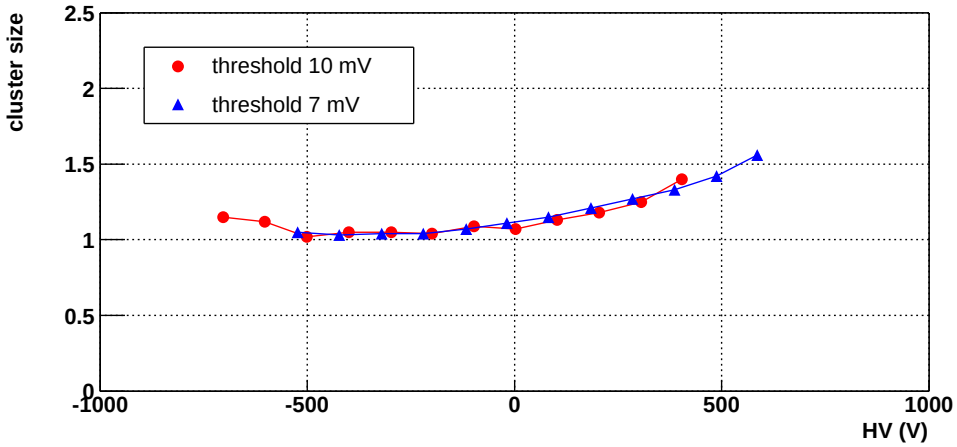

Fig. 7.29: RAV3: cluster size as a function of the applied voltage for two different discrimination threshold values, 7 and 10 mV. The applied voltage is shifted by the knee voltage (i.e. zero correspond to the knee of the plateau).

corresponds to the knee. In the same Figures are plotted the curves obtained with the two threshold setting (7 and 10 mV): the shift of the knee voltage to zero allow to overlap the two set of data to better compare them. It can be noticed that the cluster size at working point is 0.1 greater when the threshold is set at 7 mV.

No significant differences concerning the time resolution, which is $\sim$1 ns at working point for both thresholds setting, can be noticed.

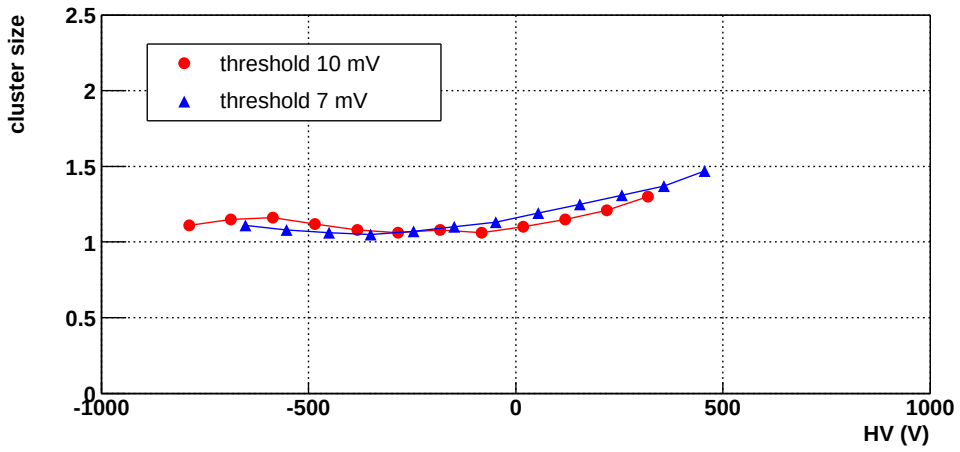

Fig. 7.30: RAV4: cluster size as a function of the applied voltage for two different discrimination threshold values, 7 and 10 mV. The applied voltage is shifted by the knee voltage (i.e. zero correspond to the knee of the plateau).

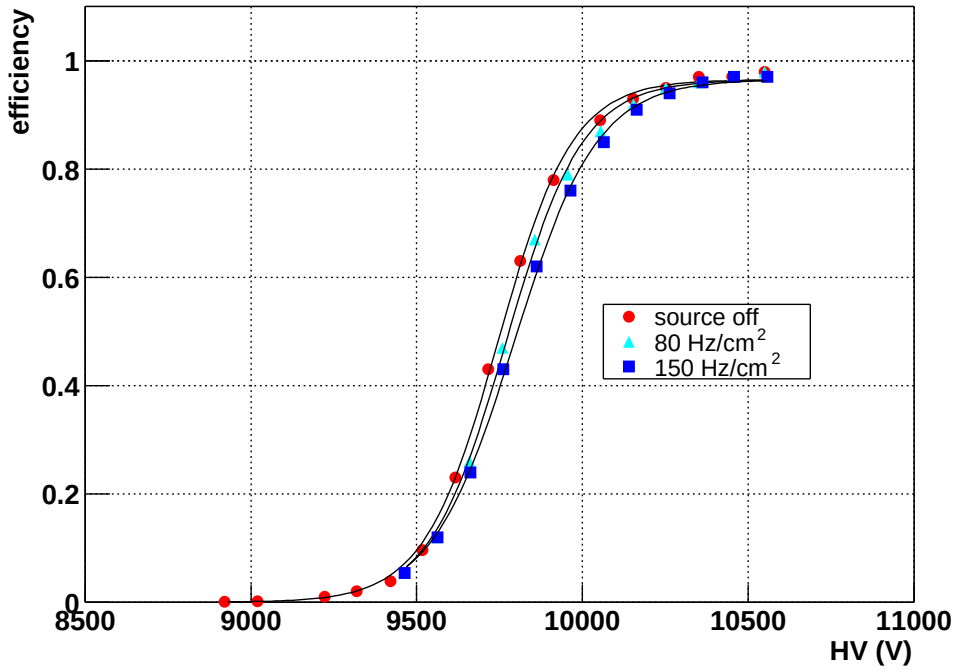

Fig. 7.31: RAV3 efficiency plateaux with the gas mixture 89.4% $C_2H_2F_4$, 10% C_4H_{10} and 0.6% SF_6 in different irradiation condition: absence of irradiation (source off), 80 and 150 Hz/cm^2 of induced gamma irradiation.

Gas mixture with 0.6% SF_6

The same series of tests has been done with the 0.6% SF_6 gas mixture. In Fig. 7.31 are plotted the efficiency plateau of RAV3 in different source conditions: absence of irradiation (source off), 80 and 150 Hz/cm^2 of γ irradiation (ABS=5 and ABS=2 respectively). The high voltage giving 50% efficiency is:

- 9745 V for the plateau with the source off;
- 9770 V for the plateau with 80 Hz/cm^2 of γ induced rate;
- 9795 V for the plateau with 150 Hz/cm^2 of γ induced rate,

$\sim$200 V higher than the ones obtained with the 0.3% SF_6 gas mixture.

In Fig. 7.32 are shown the efficiency obtained with the study on the threshold dependence varying the threshold of negative signals (Y) between

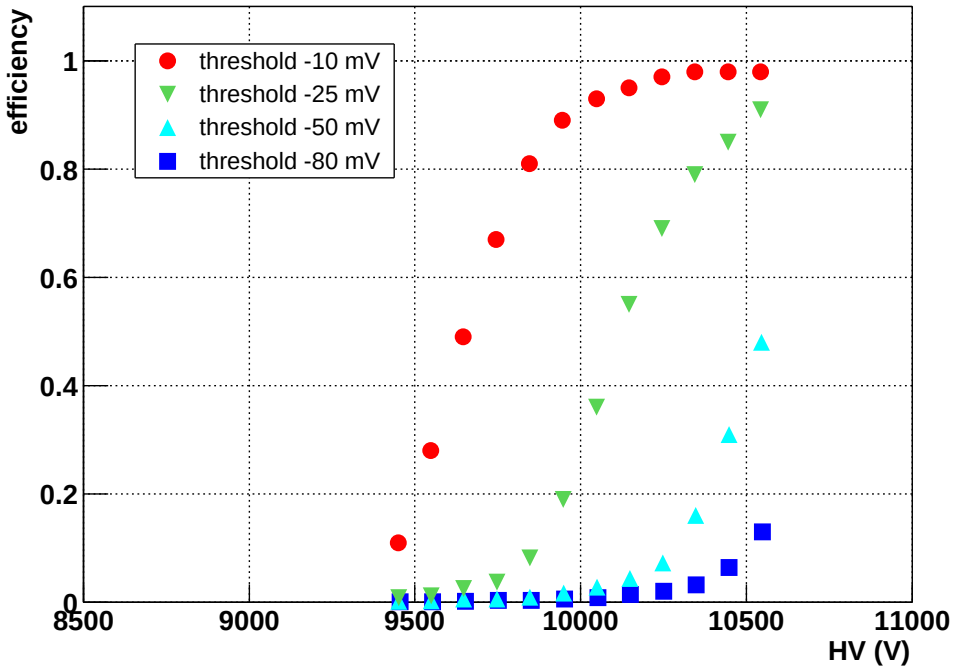

Fig. 7.32: RAV3 efficiency curves with the gas mixture 89.4% $C_2H_2F_4$, 10% C_4H_{10} and 0.6% SF_6 for different threshold values ranging between -10 and -80 mV.

-10 and -80 mV and keeping fixed the threshold of the positive signals (X) at 10 mV: the efficiency at working point (10300 V) with the threshold set at -80 mV is 3-4%.

The performances of the RPCs in term of cluster size and time resolution are quite the same with respect to the 0.3% SF_6 gas mixture:

- cluster size at working HV = 1.4 for 2.125 cm wide strips;
- time resolution at working HV $\sim$1 ns (RMS=0.8 ns, σ=1 ns).

Furthermore no significant differences between the two gas mixture under study and the one with 2% SF_6 have been pointed out. However, the 0.3% SF_6 gas mixture allow a reduction of the working high voltage of 200 V with respect to the 0.6% SF_6 gas mixture and of 900 V with respect to the 2% SF_6 one.

A displacement of the plateau position (about 150 V), without degradation of the RPC performance, is obtained lowering the threshold from 10 mV

to 7 mV, but this displacement is not significant enough to justify operations in a worse signal to background ratio condition.

Concluding, the chosen gas mixture is the one with 0.3% SF_6 and the working point is about 10000–10100 V with the discrimination threshold at 10 mV. With this percentage of SF_6, we perform a complete test to check the uniformity of the RPCs with respect to the plateau position: the surface of the chambers is scanned with a 10×10 cm^2 trigger. The efficiency map of RAV3 and RAV4 at HV=10100 V are reported in Fig. 7.33 and Fig. 7.34:

- in all positions the plateaux reaches ∼95–96% of efficiency;
- the mean efficiency at HV=10100 V (that we have defined as working value) is 0.95 ± 0.01 for both RPCs.

For each of the 25 tested positions we also estimate the percentage of streamer contamination measuring the efficiency of RAV3 and RAV4 with the threshold for negative signals (Y) set at -80 mV, while the one for the positive signals (X) has been left at 10 mV. The distributions of the streamer contamination (simply defined as the efficiency of the Y plane) have been plotted at three different voltages in Fig. 7.35: the difference in the streamer percentage can be ascribed to small differences in the gas gap or to local impurities.

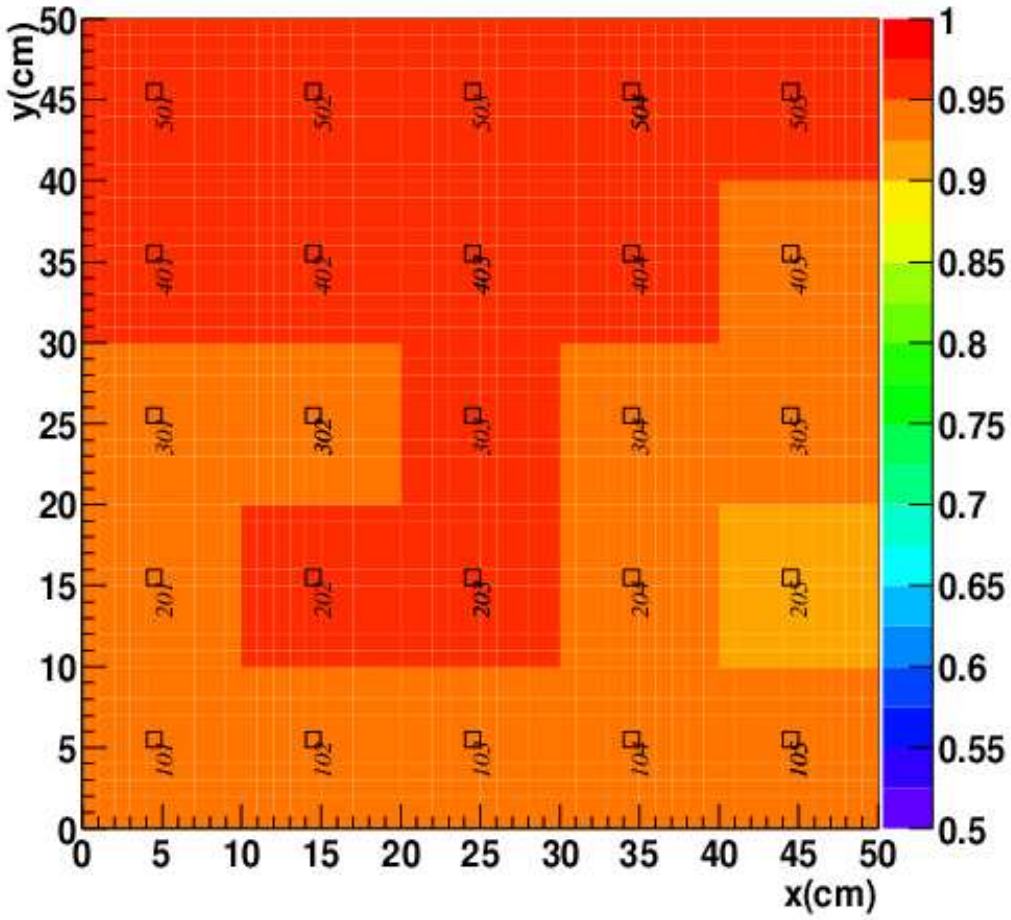

Fig. 7.33: Efficiency map of RAV3. For each tested position (displayed with a colored square at the given X and Y chamber coordinates) the efficiency of the RPC at fixed HV=10100 V is presented. The small squares correspond to the spacers.

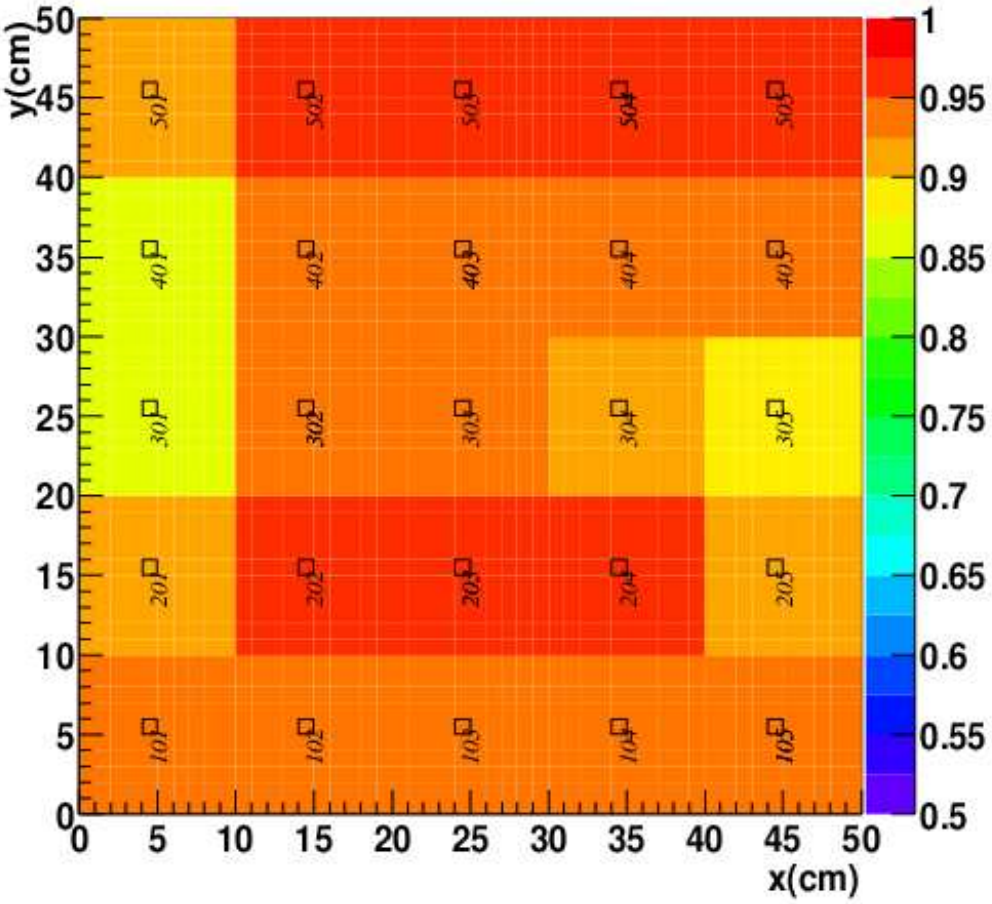

Fig. 7.34: Efficiency map of RAV4. For each tested position (displayed with a colored square at the given X and Y chamber coordinates) the efficiency of the RPC at fixed HV=10100 V is presented. The small squares correspond to the spacers. The low efficiency of position 301 and 401 (87%) is due to geometrical problem related to the trigger alignment.

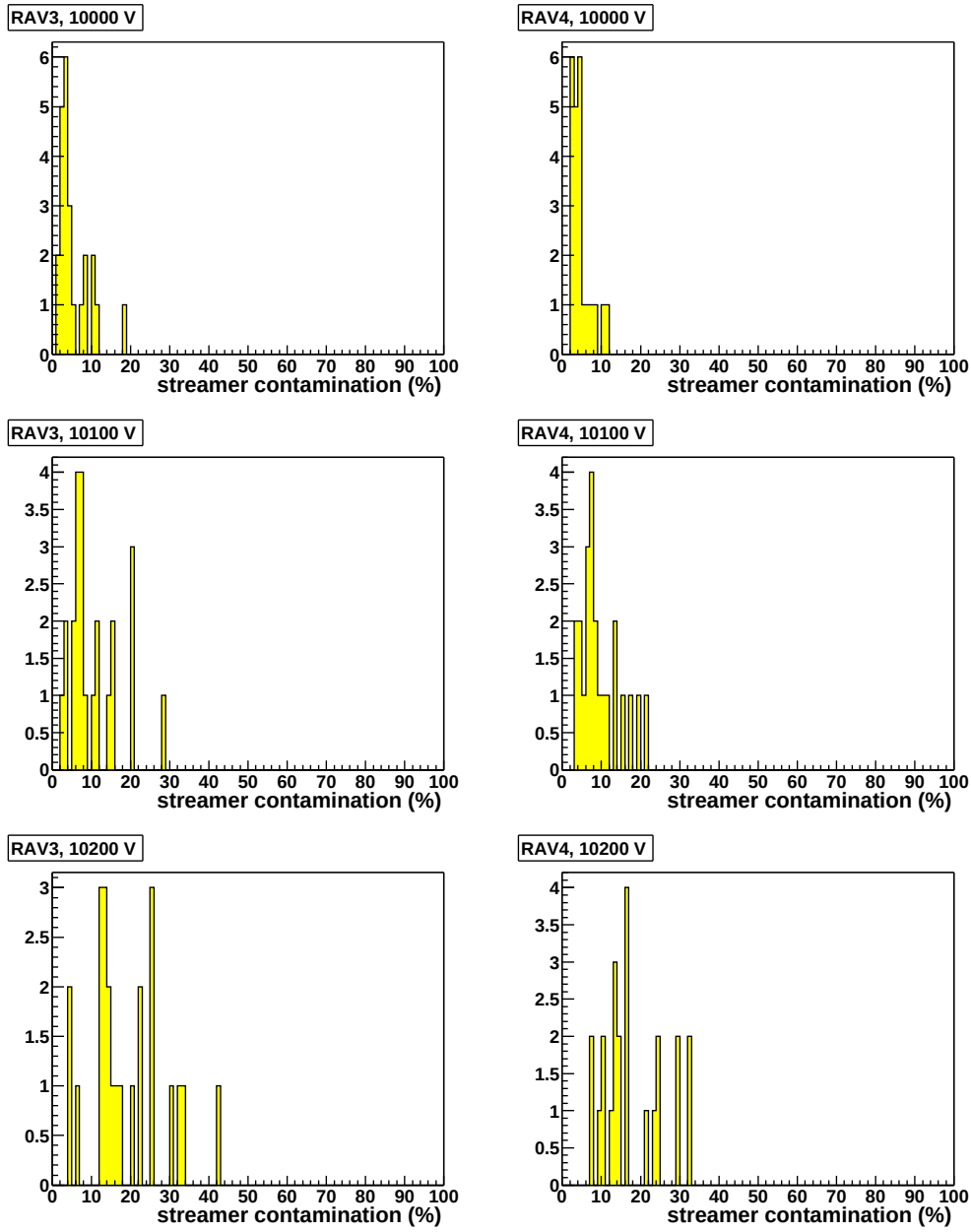

Fig. 7.35: Streamer contamination distribution of RAV3 (left side) and RAV4 (right side) at HV = 10000, 10100 and 10200 V for the 25 tested position

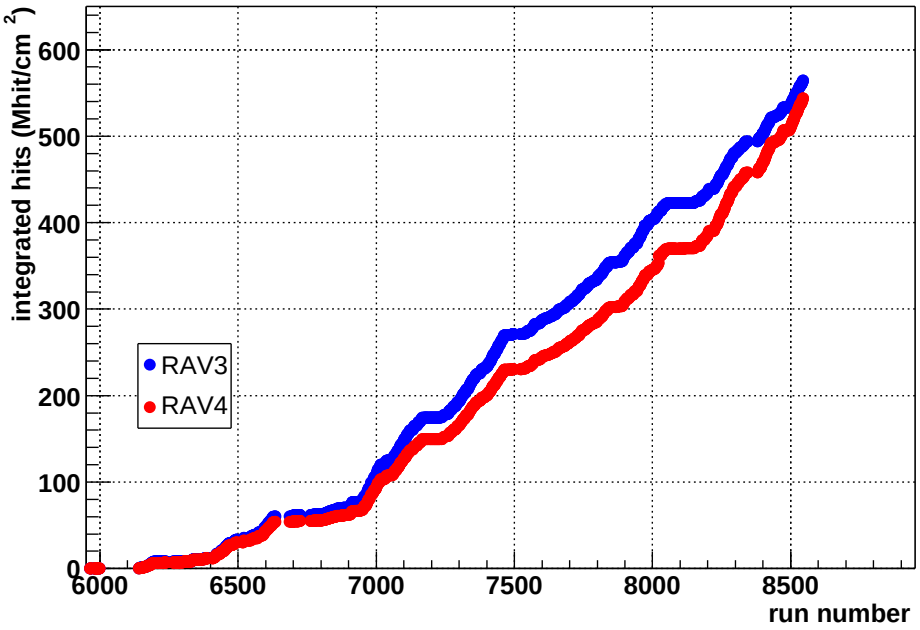

Fig. 7.36: Integrated hits as a function of the run number for the Spring 2004 ageing test.

Ageing test

On the basis of these results, correlated with the efficiency curves (Fig. 7.23), we set the working point for the two RPCs to have full efficiency and a streamer contamination less than 20% over the whole chamber:

- working HV = 10050 V for RAV3;
- working HV = 10100 V for RAV4.

The ageing test currently going on, has started in February 2005. Up to now, as can be seen in Fig. 7.36, about 550 Mhits/cm^2 have been integrated.

The γ induced irradiation on both RAV3 and RAV4 ranged from 50 to 100 Hz/cm^2; the most important changes during the ageing test have been:

- at the beginning of July 2005 the temperature inside the GIF area went up to 28°C so that the working point has been lowered by 100 V to avoid problems related to the bakelite resistivity decrease caused by the temperature increase. The chosen working points are still 200 V

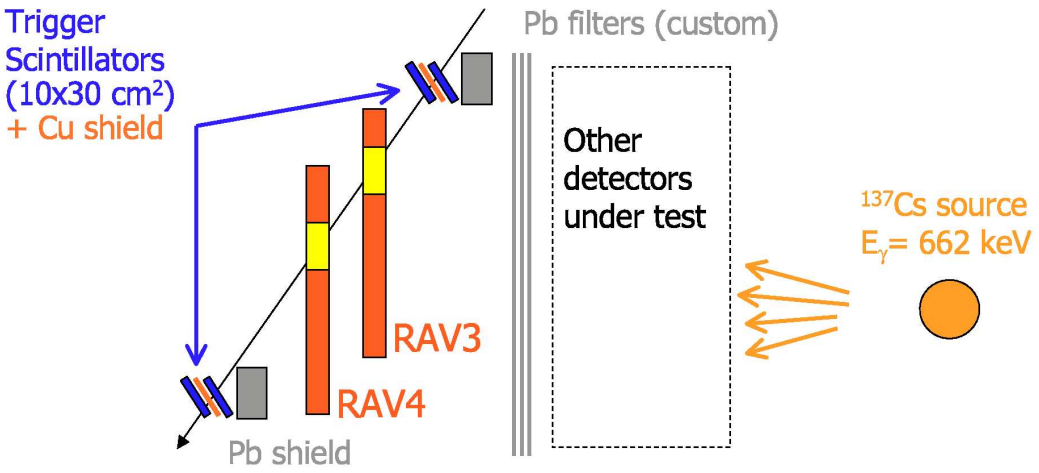

Fig. 7.37: Side view of the setup for the ageing tests of RAV3 and RAV4 until the end of September 2005, then the position of the two chamber has been inverted. The yellow boxes on the RPCs indicate the area covered by the cosmic ray trigger.

above the plateau knee, and therefore, the two RPCs are full efficient at these voltages.

- At the end of September 2005, the position of the two RPCs has been inverted. As can be seen in Fig. 7.37, the chamber closer to the source shields the one far from the source: the difference of the γ irradiation (about 10%) results in the difference between the total amount of integrated hits by the two RPCs reported in Fig. 7.36. To have a similar ageing effect for the two RPCs, RAV3 has been put far from the source and RAV4 close to it. The most relevant consequence of this operation is that the area covered by the cosmic ray trigger (10×30 cm^2, corresponding to the yellow boxes in Fig. 7.37) has changed.

During the ageing test, the streamer contamination has been measured simply considering the ratio between the rate of the signals greater than 80 mV on the ones greater than 10 mV. To this aim the threshold for the negative signals (Y) has been set at -80 mV, leaving the positive signal thresholds at +10 mV as reference. This method allow to obtain the streamer contamination as a mean value over the whole surface of the chamber (including borders), and, repeating the measurement during the ageing test, we monitor the streamer contamination a as a function of the integrated hits.

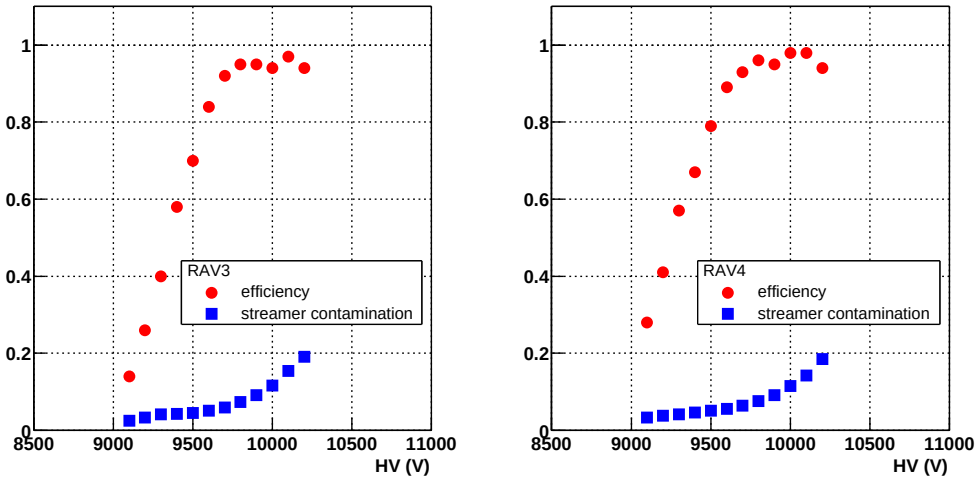

Fig. 7.38: Streamer contamination and efficiency plateau as a function of the applied voltage for RAV3 after 370 Mhit/cm^2 (left) and for RAV4 after 410 Mhit/cm^2 (right).

In Fig. 7.38 is plotted, together with the efficiency values, the streamer contamination for RAV3 (after 370 Mhit/cm^2) and for RAV4 (after 410 Mhit/cm^2): at working point (HV=10100 V) the streamer contamination is about 15% for both tested RPCs, value similar to the one obtained at the beginning of the ageing test and listed in Table 7.3.

The illumination of the two tested RPCs has been monitored with the "Autotrigger" which provide the local counts distribution when the source is off and the irradiation pattern when the source is on. The presence of some "hot spots" have been revealed: as expected, most of them are localized on the borders of the chambers. As a matter of fact, for this ageing test, both RPCs are equipped with strip plane covering 50×50 cm^2, that is the whole surface of the detector, including the frame and the gas inlets and outlets. Concerning the pattern irradiation, no relevant changes have been noticed.

The trend of dark current and dark rate of RAV3 as a function of the integrated hits are plotted in Fig. 7.39: after having integrated about 565 Mhit/cm^2 (85 mC/cm^2), the RPC dark current always remains low (∼2 μA) and the dark rate remains under 1–2 Hz/cm^2. In the same Figure, the efficiency for cosmic rays detection both without and with γ irradiation is reported: a slight efficiency loss can be noticed with high irradiation rate (100 Hz/cm^2), while the efficiency is stable with the source off. The box encloses a period

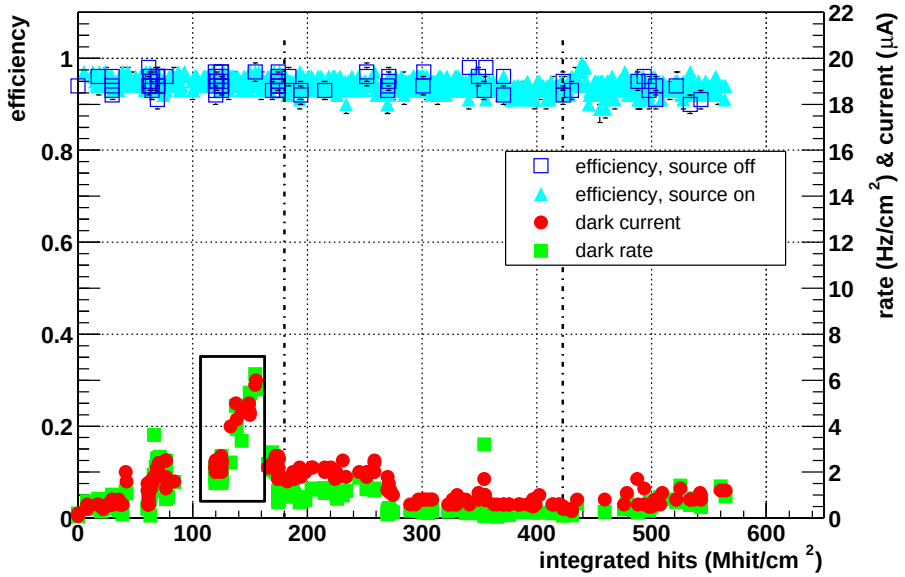

Fig. 7.39: RAV3 tested in maxi–avalanche mode: efficiency (with and without γ irradiation), dark current and dark rate as a function of the integrated hits. The HV change and the inversion of the two RPCs are indicated by the vertical black lines. The box encloses the period with the refrigerator problem.

in which the dark current, dark rate as well as the ohmic current (current at HV=7000 V) increased: this was due to a problem with the refrigerator used to add water in the gas mixture to get a 50% of relative humidity. During this period the temperature inside the refrigerator went up to room temperature (about 18°C) thus increasing the relative humidity of the gas mixture. Unfortunately, we could not solve the problem in a brief time because the test is monitored in remote from Turin and from Clermont–Ferrand.

Concerning the RAV4, the trend of dark current and dark rate as a function of the integrated hits are plotted in Fig. 7.40: also for this chamber, after about 545 Mhit/cm^2 (82 mC/cm^2), the dark current remains low ($\sim$2 μA) and the dark rate remains under 2 Hz/cm^2. In the same Figure, the efficiency for cosmic rays detection both without and with γ irradiation is reported: a slight efficiency loss can be noticed with high irradiation rate (80 Hz/cm^2), while the efficiency is stable with the source off. The box encloses a period in which only the dark current increased, while both the dark rate and the ohmic current were low: the problem was due to an external discharge and disappears after having improved the insulation.

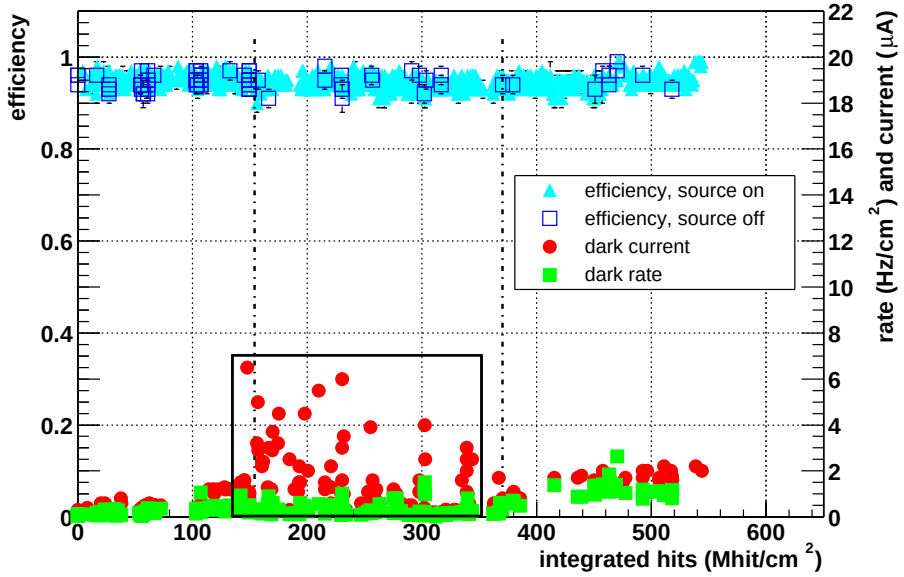

Fig. 7.40: RAV4 tested in maxi–avalanche mode: efficiency (with and without γ irradiation), dark current and dark rate as a function of the integrated hits. The HV change and the inversion of the two RPCs are indicated by the vertical black lines. The box encloses the period in which dark current increased due to an external discharge.

Both chamber show a slight efficiency loss at high rate, nevertheless, a comparison between the efficiency plateau at the beginning of the ageing test (after about 30 Mhits/cm^2) and after 255–310 Mhits/cm^2, is plotted in Fig. 7.41: the efficiency has been measured with 60–50 Hz/cm^2 and no displacement of the plateau position is observed.

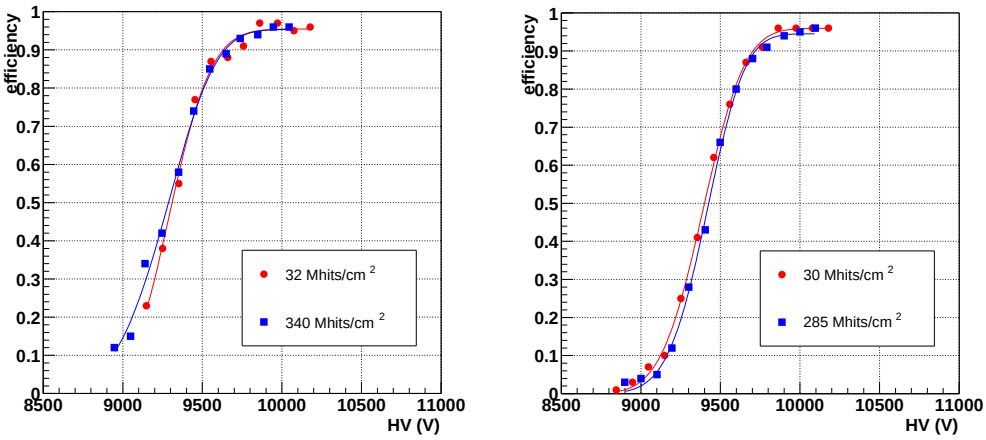

(a) RAV3 (b) RAV4

Fig. 7.41: Comparison between the efficiency plateau at the beginning of the ageing test (after about 30 Mhits/cm^2) and after 255–310 Mhits/cm^2 for RAV3 (a, left) and RAV4 (b, right).

In conclusion we can affirm that no particular ageing effects are observed after 550 Mhits/cm^2 (83 mC/cm^2), corresponding to 5.5 year of p–p data taking for the RPCs covered by the high rate area described in Section 3.6.1:

- dark current and dark rate are low (2 μA, 2 Hz/cm^2);
- the efficiency is stable for rate below 50–60 Hz/cm^2 while a slight efficiency loss can be noticed at high rate (80–100 Hz/cm^2);
- the streamer contamination does not change, remaining at the level of the beginning of the ageing test;
- no current increase (trip) has occurred with this gas mixture and in these working conditions.

7.5.3 Conclusions and remarks

The first 50×50 cm^2 RPC prototype (RAV1) was tested in Spring 2004 with the maxi–avalanche gas mixture 88% $C_2H_2F_4$, 10% C_4H_{10} and 2% SF_6 (RH=50%). After having integrated 225 Mhit/cm^2 (34 mC/cm^2), no ageing effects were observed but after 100 Mhit/cm^2 we incurred in some current instabilities strictly correlated with the high working voltage (HV=10900 V).

After decreasing the SF_6 percentage (from 2 to 0.3%) to lower the working point, and after having controlled that he performance with the maxi–avalanche gas mixture 89.7% $C_2H_2F_4$, 10% C_4H_{10} and 0.3% SF_6 (RH=50%) still fullfill the requirements for the p–p data taking, an ageing test has been performed on two RPC prototypes (RAV3 and RAV4) since February 2005: after 550 Mhits/cm^2, corresponding to 5.5 years of the p–p program, no particular ageing effects have been observed. The test is presently in progress.

References

[1] R. Arnaldi *et al.*, Nucl. Instr. and Meth. A 508 (2003) 106-109

[2] R. Arnaldi *et al.*, Nucl. Instr. and Meth. A 451 (2000) 462-473

[3] R. Arnaldi *et al.*, Nucl. Instr. and Meth. A 533 (2004) 112-115

[4] S. Agosteo *et al.*, Nucl. Instr. and Meth. A 452 (2000) 94-104
http://pcessgif04.cern.ch/

[5] *http://pcessgif04.cern.ch/*
http://pcessgif04.cern.ch/datadesc.html
http://pcessgif04.cern.ch/envdata.html

Conclusions

To fulfill the requirements related to the ALICE running scenario, and having demonstrated the possibility to use the same FEE both in streamer and in highly–saturated avalanche mode, ageing and beam tests have been performed with different gas mixtures:

- a quenched streamer mixture (50.5% Ar, 41.3% $C_2H_2F_4$, 7.2% C_4H_{10} and 1% SF_6, RH=50%) appropriate to the heavy-ion operations;
- a highly–saturated avalanche mixture (90% $C_2H_2F_4$, 10% C_4H_{10} and different percentages of SF_6, RH=50%) suitable for the p–p program.

Beam and ageing tests in streamer mode for the heavy–ion data taking

The results obtained in the beam test of the pre–production RPC (RPC1, 210×70 cm^2) show that the performance in term of efficiency, cluster size (1.5 for 1 cm wide strips) and time resolution (1 ns) with the streamer gas mixture are in agreement with the one obtained with small RPC prototypes (50×50 cm^2).

The same performance results have been obtained testing three RPCs belonging to the final production: each chamber has a uniform behaviour over the whole active area and the behaviour is quite the same for the three RPCs.

An ageing test at GIF with the streamer gas mixture has been undertaken on RPC1: the chamber works satisfactorily up to 100 Mhit/cm^2 (50 mC/cm^2), corresponding to the heavy–ion program for the first 10 years of data taking in ALICE, thus confirming the results obtained with small prototypes. The detector has shown a slight current increase up to 13 μA, while the dark rate remains lower than 0.4 Hz/cm^2. A slight efficiency loss has been found with high irradiation rate (60 Hz/cm^2), while the efficiency without irradiation is constant. The efficiency of RPC1 has been measured at the end of the test on the Turin test bench on the whole surface of the

chamber with 1.2×1 cm^2 cells: the RPC was found efficient with an excellent uniformity.

In conclusion, RPCs working in streamer mode can fulfill the requirements for the heavy–ion data taking, both in term of performance and of lifetime.

Beam and ageing tests in highly–saturated avalanche mode for the p–p data taking

On the basis of the results obtained with the beam test of the pre–production RPC1 we can conclude that it is possible to work in highly–saturated avalanche mode with the same FEE used for the streamer mode simply by lowering the threshold to the value of 10 mV by means of the external control. Moreover, the achieved performance cope with the p–p data taking obtaining, as expected, a larger cluster size (1.8 for 1 cm wide strips) with respect to the streamer mode; the time resolution is 1 ns, the same as in streamer mode.

The ageing tests performed in maxi–avalanche mode are presently in progress. Up to now 550 Mhits/cm^2, corresponding to 5.5 years of the p–p program, have been integrated without noticing particular ageing effects.

Ageing test with a streamer and highly–saturated avalanche mode alternation, are foreseen for the near future.

Appendix A

Dependence of the bakelite resistivity on temperature and humidity

The performance of RPCs, in particular their rate capability, strongly depends on the bulk resistivity of the electrodes. Since the bakelite resistivity changes as a function of temperature and humidity, we have performed resistivity measurements of bakelite samples in order to carefully investigate these dependences.

The bakelite sample under study is 2 mm thick and 20×20 cm^2 large, it is housed in a climatic cell (Challenge 500–V, Angelantoni S.p.A) able to control temperature (in the range -20°C$\div$70°C, 1°C accuracy) and relative humidity (in the range 25%$\div$95%, 5% accuracy) for temperatures between 10°C and 70°C.

The resistance is measured by means of a high resistance meter (HP 4339B, Hewlett Packard) with an accuracy of 0.6% in the range 10^3–10^{16} Ω. In order to obtain a better quality of the electrical contact for long period measurements, a few μm thick silver layer has been deposited on both bakelite surfaces between the high resistance meter electrodes and the sample. In Fig. A.1 is reported a picture of the bakelite sample inside the climatic cell.

Two sets of measurements were performed:

- the resistance of the bakelite sample has been monitored after fast relative humidity (RH) changes at constant temperature (25°C), and then after temperature changes at constant humidity (55%) for about one year. After each environmental change the bakelite sample has been conditioned for a period long enough to get stable resistance values. The conditioning time, defined as the time in which the resistance un-

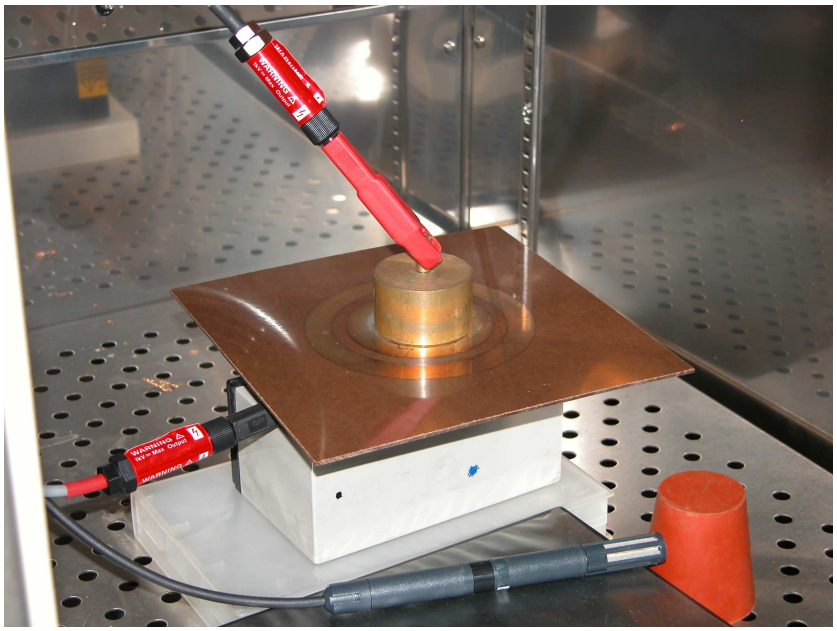

Fig. A.1: The bakelite sample under study with the silver coating and the high resistance meter electrodes.

dergoes 90% of its variation after each environmental condition change, has been evaluated;

- the resistance of the bakelite sample was measured as a function of temperature in the range from 15°C to 35°C at 3 values of relative humidity: 20%, 55% and 80%.

In Fig. A.2 is reported the trend of the resistance as a function of the time after relative humidity changes at constant temperature (25°C):

- the humidity drop from 80% to 55% causes a resistance increase of a factor 3.5, 40 days are necessary to reach stable condition with a conditioning time of 30 days;

- the resistance increase after the second humidity drop (from 55% to 20%) is even more evident, a raise of a factor 22 occurs in 140 days with a long conditioning time of 100 days;

- when the humidity has been newly set at 55%, the resistance achieves a value 50% higher than its previous one at the same humidity. A conditioning time of only 7 days shows that the slope of the resistance decrease is higher than the one of the correspondent increase (100 days).

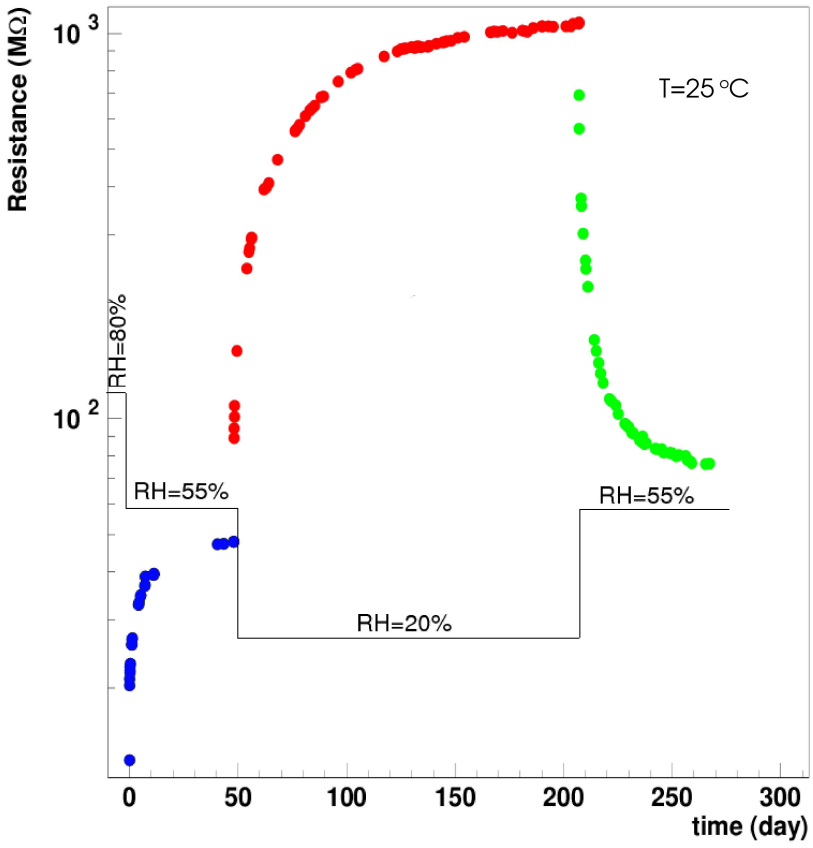

Fig. A.2: Bakelite resistance as a function of time for relative humidity changes at constant temperature (25°C). At time=0 day humidity drops from 80% to 55%, at time=50 day from 55% to 20% and at time=210 day it rises from 20% to 55%. Relative humidity changes take less that an hour.

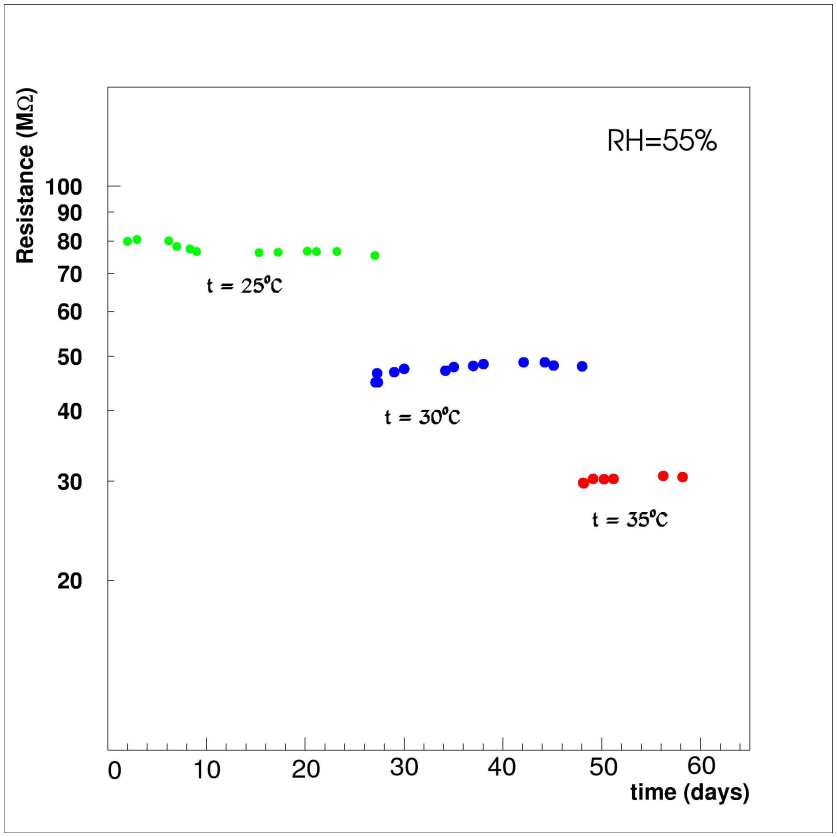

Fig. A.3: Bakelite resistance as a function of time after temperature changes at constant relative humidity (55%). Temperature has been increased from 25°C to 30°C (time=25 day) and to 35°C (time=45 day). Temperature changes take a few hours.

The same measurements have been performed changing the temperature at constant relative humidity (55%): the results as a funcion of time are plotted in Fig. A.3. The decrease of the bakelite resistance due to the temperature increase is a fast process and stable values are achieved in the same time the environmental conditions are stabilized (∼2 hours).

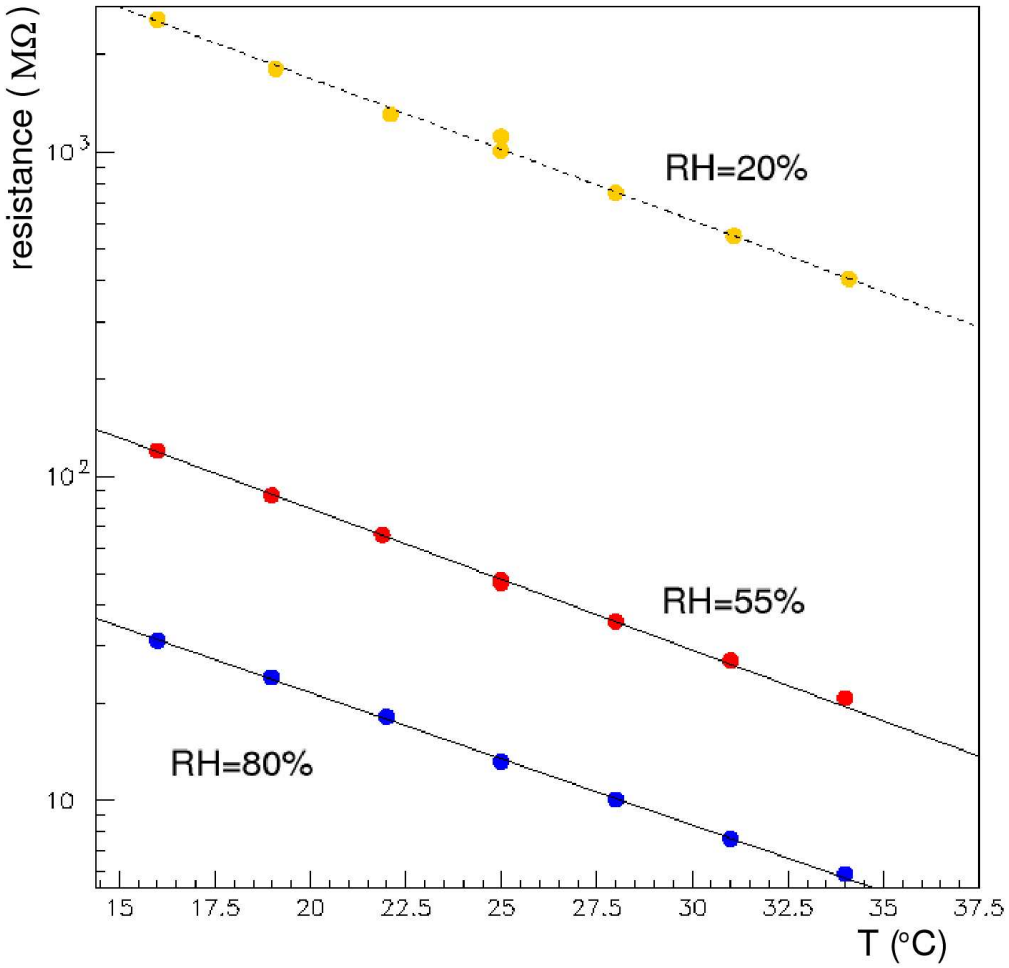

Fig. A.4: Bakelite resistance as a function of temperature at three values of relative humidity: 20% (yellow), 55% (red) and 80% (blue).

The dependence of resistance as a function of temperature has been measured for three values of relative humidity: 20%, 55% and 80%. The measurements are performed when the resistance reaches a stable value after humidity change. In Fig. A.4 are plotted the results together with the fit to experimental data obtained with the function:

$$R = e^{(a \cdot temp + b)} \tag{A.1}$$

In Table A.1 are shown the value of the slope of the exponential fit. The slight difference between the three value can be attributed to a no long enough conditioning time after temperature changes.

relative humidity	a	σ_a
20%	-1.0×10^{-1}	$2\times\ 10^{-3}$
55%	-9.8×10^{-2}	10^{-3}
80%	-9.3×10^{-2}	10^{-3}

Tab. A.1: Slope of the exponential fit of the resistivity dependence as a function of the temperature.

This study shows that the humidity strongly affects the bakelite resistivity through a slow process (several months): a resistivity increase of a factor 100 has been found in the investigated interval (20÷80%). Finally, there is an evident exponential dependence of bakelite resistivity on temperature: it decreased of a factor 5 within a 20°C interval (15÷35°C).

Taking into account these considerations, it must be concluded that a strict control of the environmental conditions is mandatory to keep constant the bakelite resistivity and thus the rate capability of the detector, especially for long tem operations.

Appendix B

RPC16 and RPC18 beam test results

In this Appendix are shown the results of RPC16 and RPC18 as measured in the beam test described in Section 6.6.

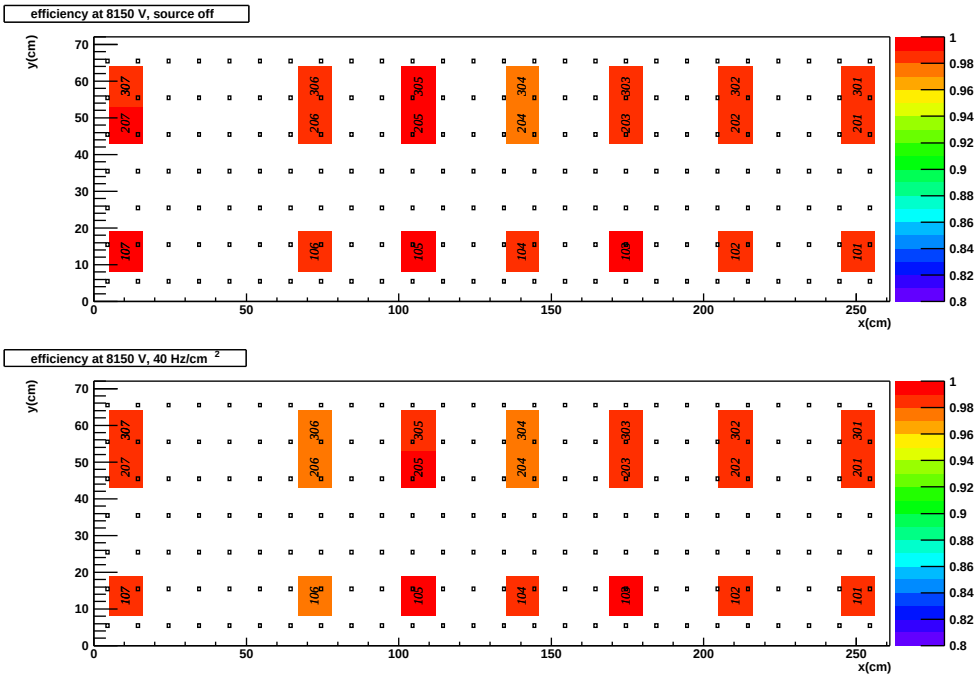

Fig. B.1: RPC16 efficiency map: for each tested position (displayed with a colored square at the given X and Y chamber coordinates) the efficiency of the RPC at working point (HV=8150 V), without γ induced rate (top) and with $\sim$40 Hz/cm^2 γ induced rate (bottom) is represented.

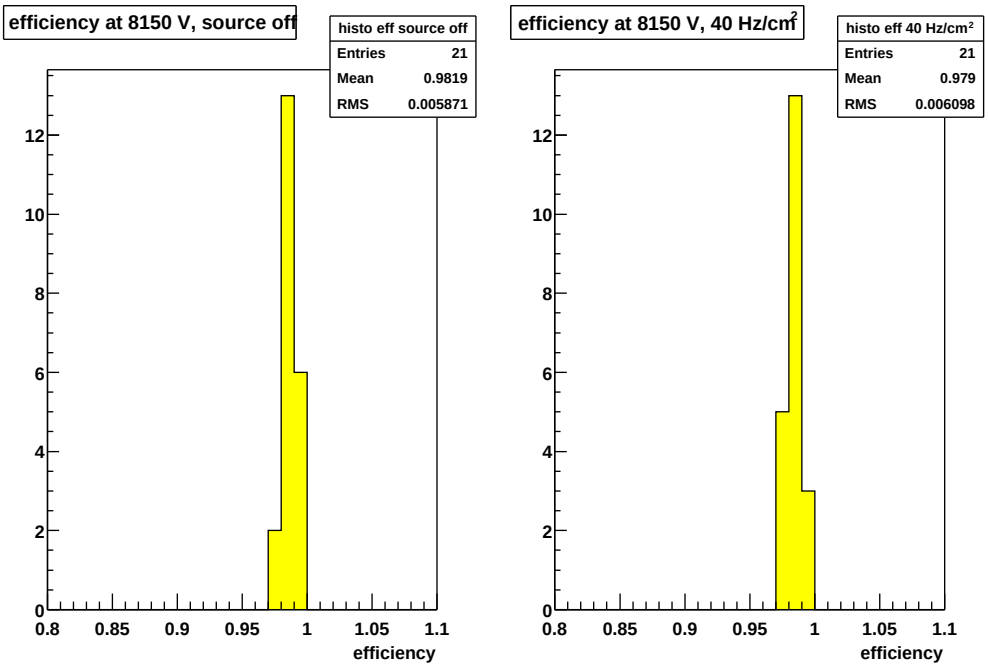

Fig. B.2: RPC16 efficiency distribution at working point (HV=8150 V), without γ induced rate (top) and with $\sim$40 Hz/cm^2 γ induced rate (bottom).

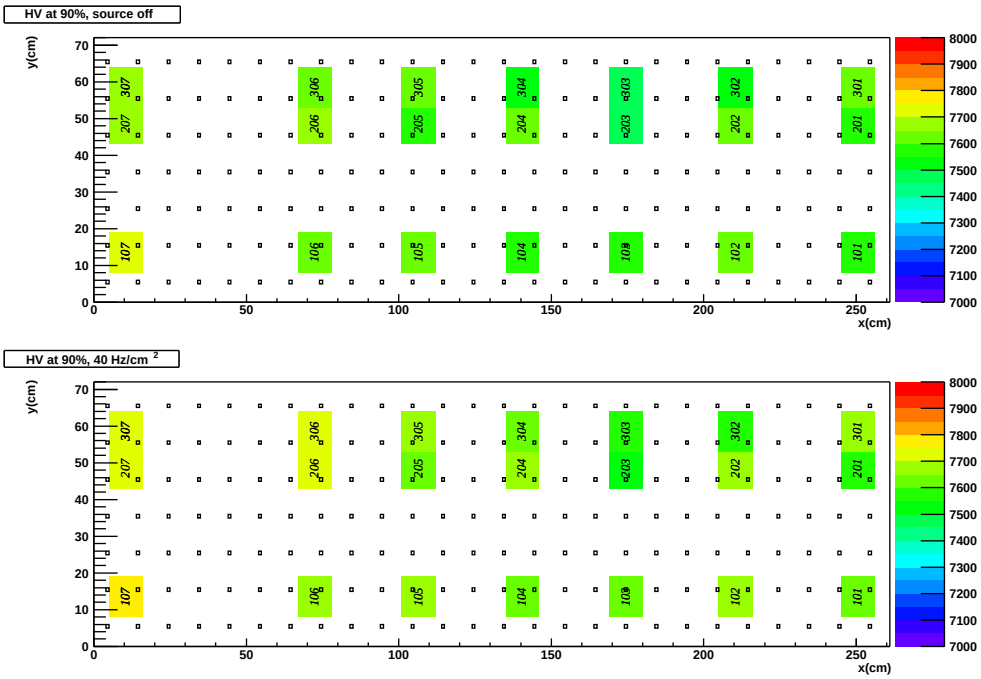

Fig. B.3: RPC16 high voltages map: for each tested position (displayed with a colored square at the given X and Y chamber coordinates) the value of the effective voltage that gives an efficiency of 90%, without γ induced rate (top) and with $\sim$40 Hz/cm^2 γ induced rate (bottom) is represented; the small squares correspond to the spacers.

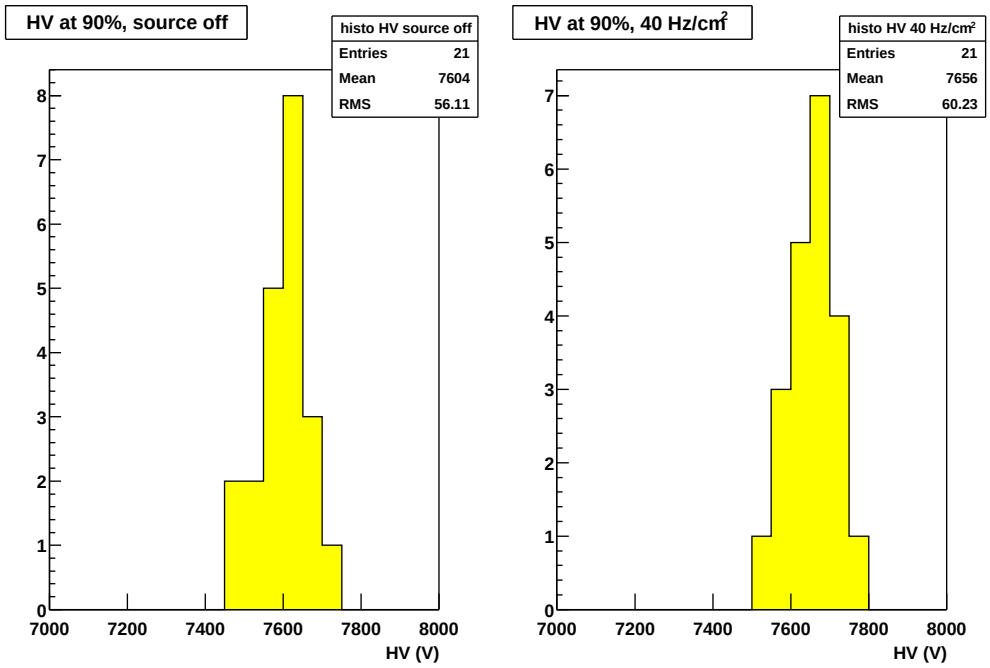

Fig. B.4: RPC16 high voltages at 90% efficiency distribution, without γ induced rate (top) and with $\sim$40 Hz/cm^2 γ induced rate (bottom).

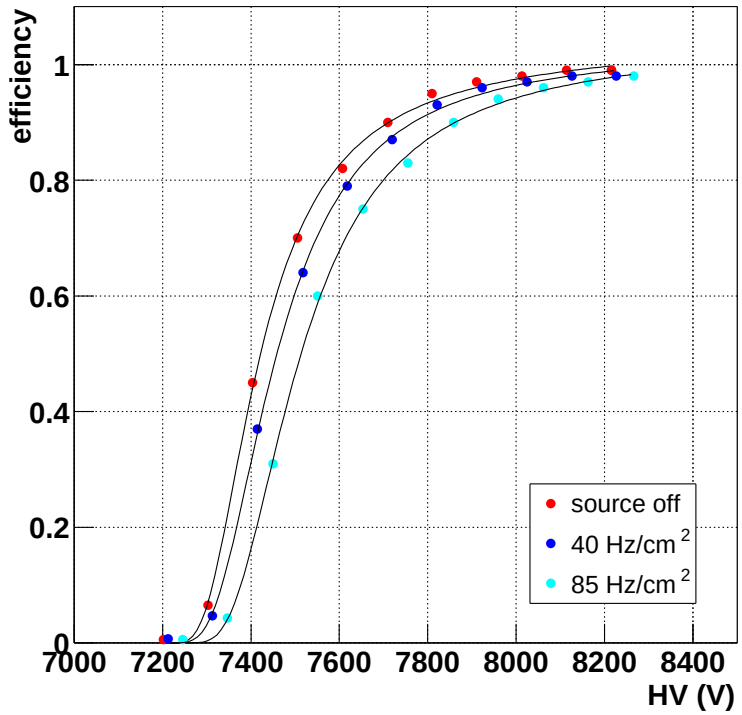

Fig. B.5: RPC16 efficiency plateaux without γ induced rate (red), with $\sim$40 Hz/cm^2 of γ induced rate (blue) and with $\sim$85 Hz/cm^2 of γ induced rate (azure).

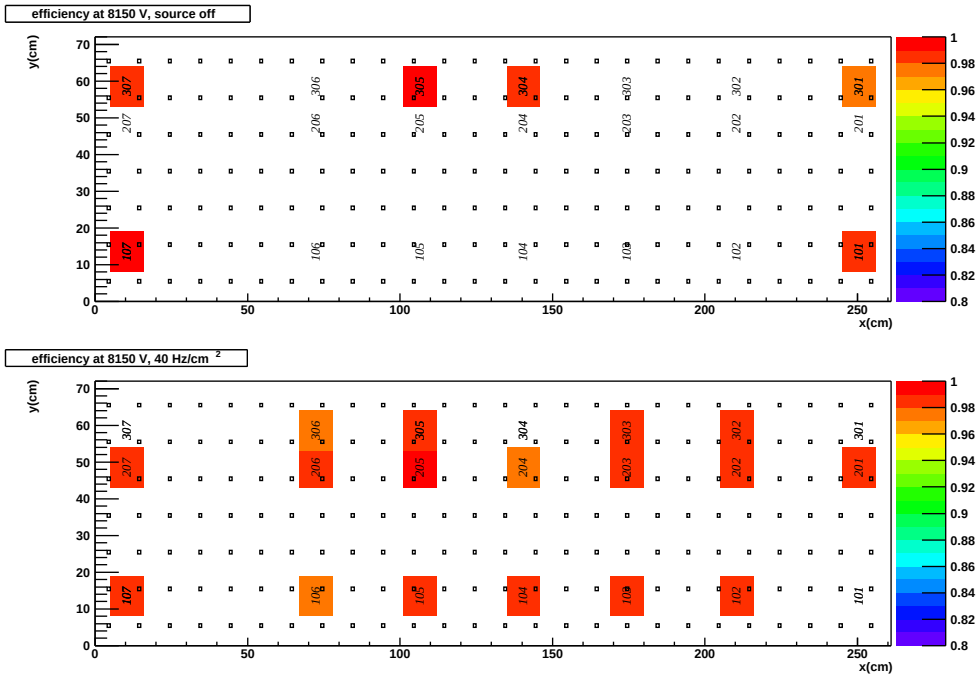

Fig. B.6: RPC18 efficiency map: for each tested position (displayed with a colored square at the given X and Y chamber coordinates) the efficiency of the RPC at working point (HV=8150 V), without γ induced rate (top) and with $\sim$40 Hz/cm^2 γ induced rate (bottom) is represented.

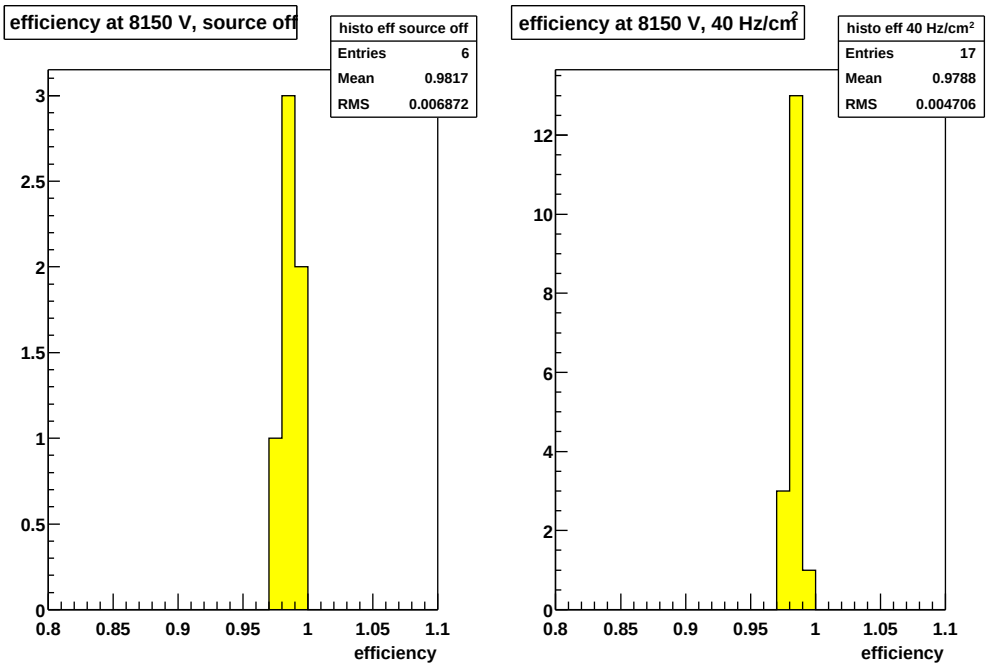

Fig. B.7: RPC18 efficiency distribution at working point (HV=8150 V), without γ induced rate (top) and with $\sim$40 Hz/cm^2 γ induced rate (bottom).

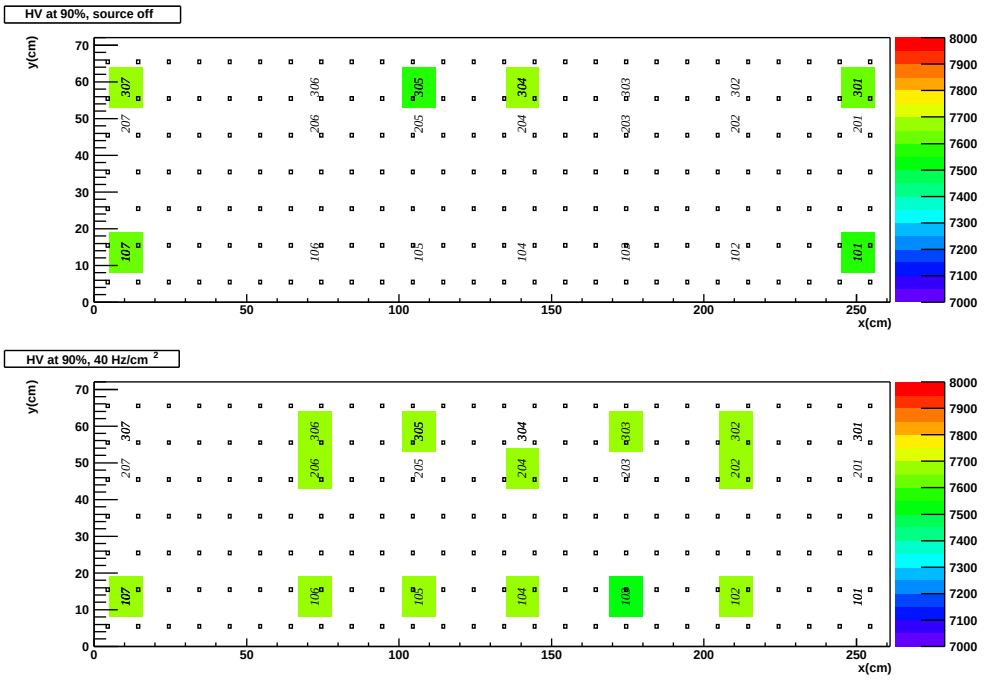

Fig. B.8: RPC18: high voltages map: for each tested position (displayed with a colored square at the given X and Y chamber coordinates) the value of the effective voltage that gives an efficiency of 90%, without γ induced rate (top) and with $\sim$40 Hz/cm^2 γ induced rate (bottom) is represented; the small squares correspond to the spacers.

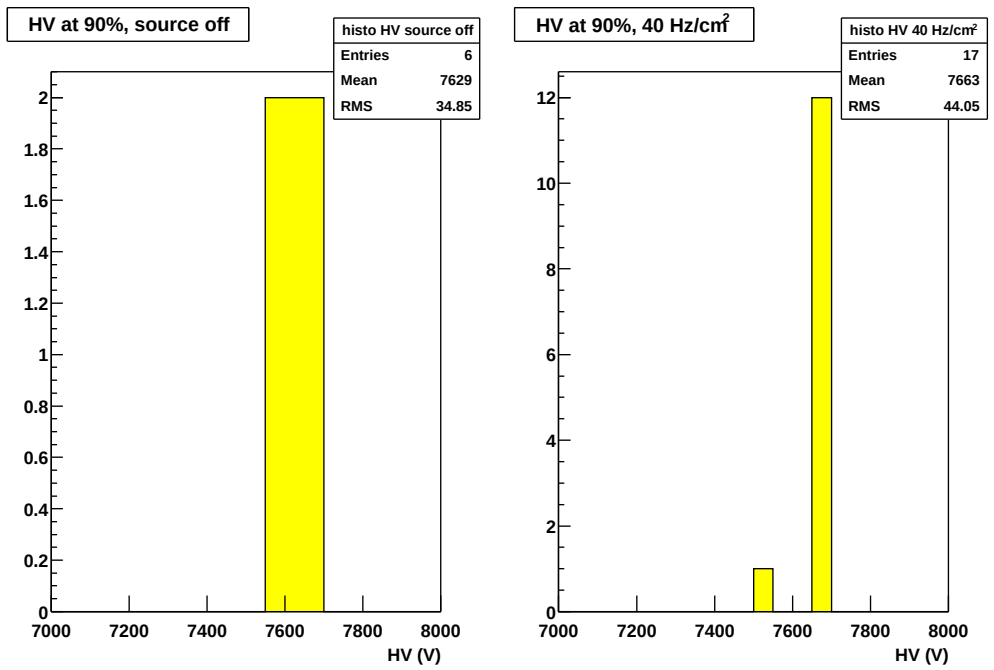

Fig. B.9: RPC18 high voltages at 90% efficiency distribution, without γ induced rate (top) and with $\sim$40 Hz/cm^2 γ induced rate (bottom).

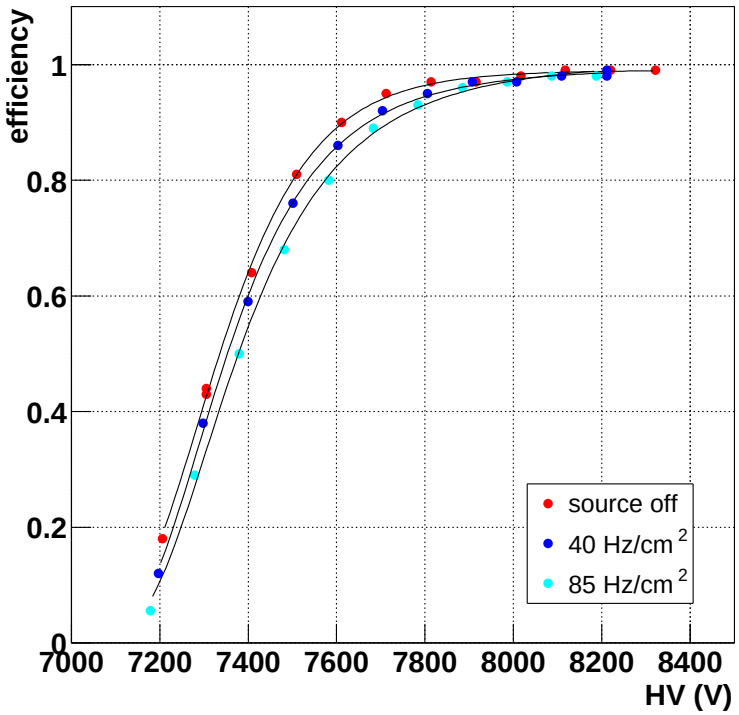

Fig. B.10: RPC18: efficiency plateaux without γ induced rate (red), with $\sim$40 Hz/cm^2 of γ induced rate (blue) and with $\sim$85 Hz/cm^2 of γ induced rate (azure).

Appendix C

Trigger System efficiency

C.1 Trigger System efficiency rough simulation

The aim of this simple simulation is to evaluate the efficiency for the detection of a single muon provided by the four RPCs planes composing the Trigger System. This simulation take into account the detector efficiency without considering the eventual inefficiency related to the trigger algorithm as well as the inefficiency due to the p_t cut (Section 3.6).

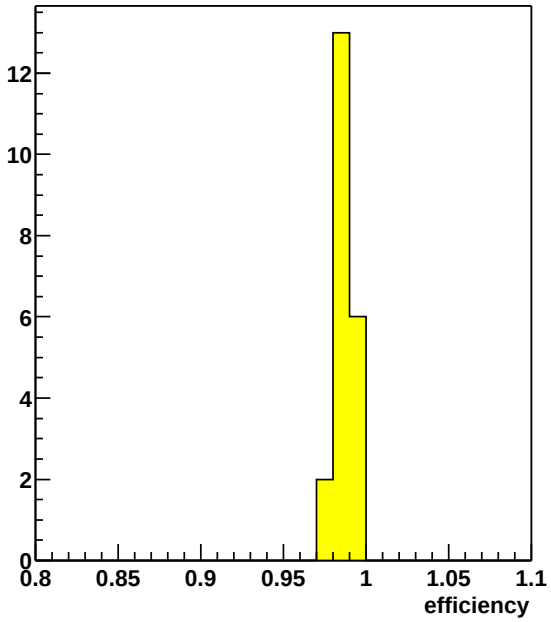

Fig. C.1: Efficiency distribution in working condition obtained in a beam test.

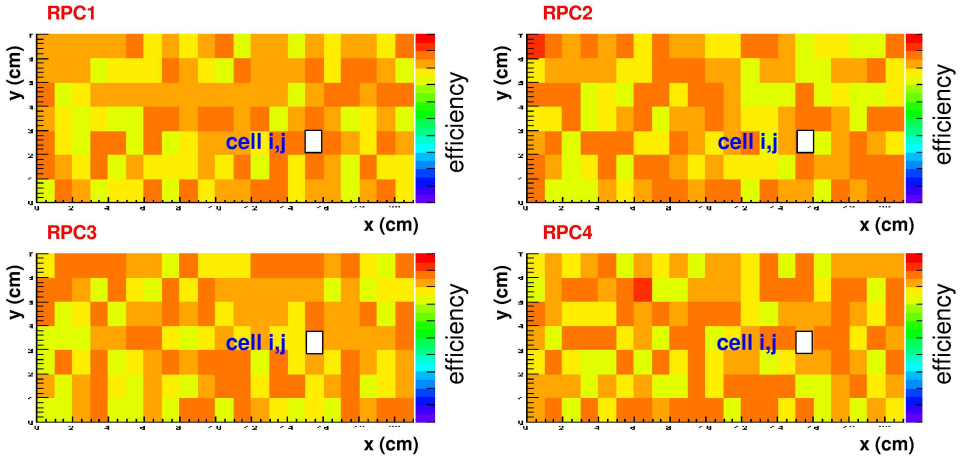

Fig. C.2: Efficiency map of 4 RPCs. For each position (displayed with a colored square at the given X and Y chamber coordinates) we represent the efficiency of the RPC directly extracted from the experimental efficiency distribution.

The base of this simulation are the RPC efficiency distributions as a function of the HV obtained with the analysis of a beam test: in Fig. C.1 is shown the one at HV=8150 V, i.e. in working condition. We consider 4 RPCs and we follow the procedure described below:

- we divide each RPC in cells of 10×10 cm^2;
- we assign an efficiency value to each cell of each chamber with a direct extraction from the experimental efficiency distribution. In this way we obtain the efficiency maps shown in Fig. C.2 and we can calculate the expected efficiency of the Trigger System with equation C.1

$$\begin{aligned} eff(i,j) &= eff_1(i,j)\times eff_2(i,j)\times eff_3(i,j)\times eff_4(i,j) \\ &+ \{(eff_1(i,j)-1)\times eff_2(i,j)\times eff_3(i,j)\times eff_4(i,j)\} \\ &+ \{eff_1(i,j)\times (eff_2(i,j)-1)\times eff_3(i,j)\times eff_4(i,j)\} \\ &+ \{eff_1(i,j)\times eff_2(i,j)\times (eff_3(i,j)-1)\times eff_4(i,j)\} \\ &+ \{eff_1(i,j)\times eff_2(i,j)\times eff_3(i,j)\times (eff_4(i,j)-1)\} \end{aligned} \quad \text{(C.1)}$$

  where eff$_n$(i,j) is the efficiency of the cell (i,j) of the n–th RPC and the Trigger System efficiency is calculated requiring hits on 3 out of 4 RPCs;
- we assume that each track is perpendicular to the Trigger System and hits always the same cell (i,j) (see Fig. C.2);

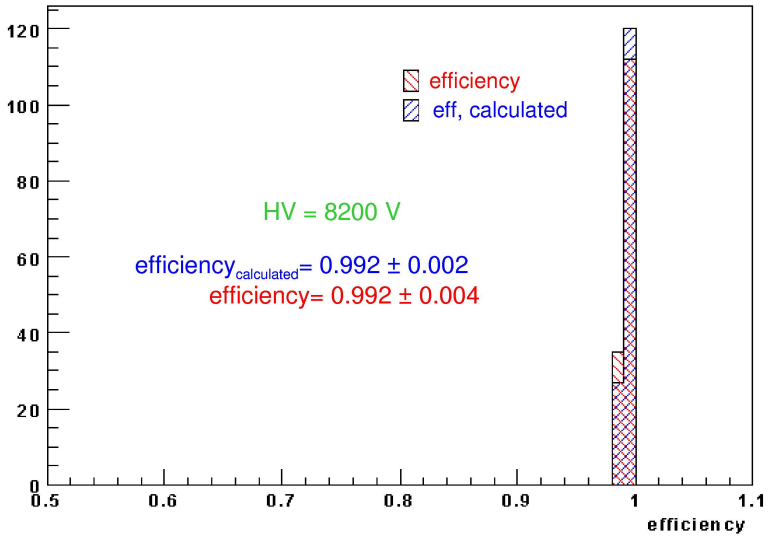

Fig. C.3: Efficiency of the Trigger System for the detection of a single muon: the efficiency simulated is plotted in red while the one calculated with equation C.1 is in blue

- we simulate 1000 events, i.e. 1000 muons, for each cell:
  - for each cell of each chamber we extract a random number in the interval [0,1];
  - the cell (i,j) of n–th RPC is considered efficient if the extracted random number is smaller than eff$_n$(i,j);
  - the Trigger System is efficient if at least 3 upon 4 RPC are efficient.

At the end we obtain the map and the distribution of the Trigger System efficiency for the single muon detection, furthermore we can repeat the simulation at different applied voltages. In Fig. C.3 is plotted the efficiency distribution at HV=8200 V compared with the efficiency distribution (always at HV=8200 V) calculated with equation C.1: no significant difference emerges from the comparison.

In table C.1 are summarized the results of this simulation as a function of the applied voltage. It is important to notice that the plateau of the 3/4 Trigger System efficiency is displaced toward lower voltage with respect to the one of the RPC efficiency; this means that it is possible to work at 99% Trigger System efficiency at a high voltage about 250 V under the RPC working point. These results are also shown in the graphic in Fig. C.4.

HV (V)	RPC efficiency	Trigger System efficiency
7800	0.938	0.979
7900	0.956	0.988
8000	0.964	0.991
8100	0.966	0.992
8200	0.967	0.992
8300	0.967	0.992

Tab. C.1: RPC and Trigger System efficiency with respect to the HV. The RPC efficiency is the mean value of the experimental efficiency distribution.

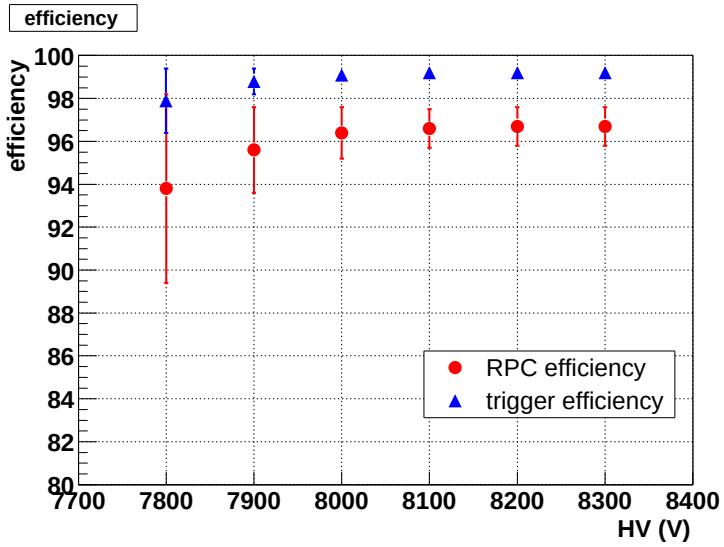

Fig. C.4: RPC (red circles) and Trigger System (blue triangle) efficiency as a function of HV.

C.2 Global performance of a prototype of the ALICE Muon Trigger

The performance of a small–scale prototype of the dimuon trigger system has been tested with the CERN/SPS muon beam at the Gamma Irradiation Facility, during June 2002 [1,2]. The experimental setup is shown in Fig. C.5.

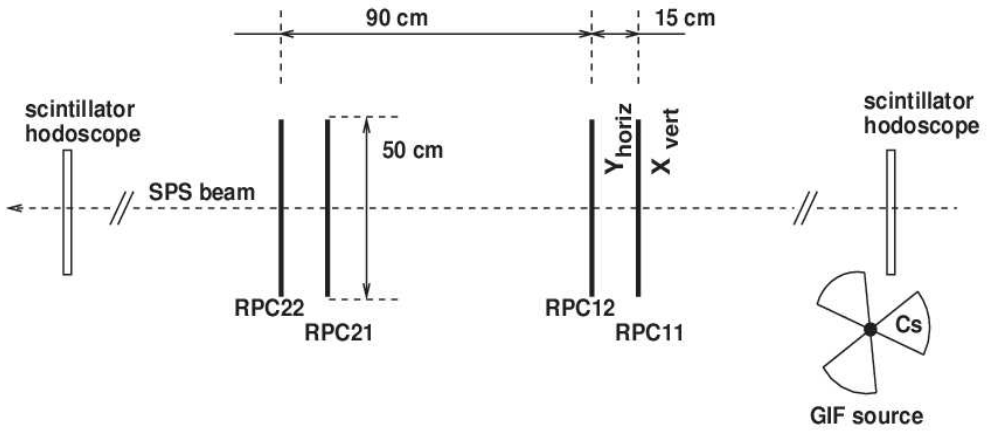

Fig. C.5: Experimental setup at GIF.

Four 50×50 cm^2 RPCs, geometrically spaced as foreseen for the four trigger planes in ALICE, are positioned in the GIF area perpendicularly to the muon beam. Two 30×30 cm^2 scintillator hodoscopes are used for efficiency measurements. The chambers are flowed in parallel with the standard ALICE streamer gas mixture (50.5% Ar, 41.3% $C_2H_2F_4$, 7.2% C_4H_{10},1% SF_6). Each RPC is readout by 16 strips, 2 cm wide and 50 cm long, in the two orthogonal directions. The Front End Electronics uses the ADULT chip.

The X-Y patterns of the fired strips are transmitted to a prototype of the Local Trigger Board (see Section 3.5) in LVDS standard with a 25 m long cable. Since no magnetic field was present, no cut on the measured deviation was applied by means of the Look-Up Table implemented in the Local Trigger Board.

In ALICE working conditions, the LHC clock, which will synchronize the interactions within less than ±1 ns, will be distributed to the trigger electronics. To have a similar situation, we have developed a system to synchronize the beam muons with the clock.

The background is provided by the uncorrelated γ–background from the GIF. At the setup location, the maximum background rate is 320 (110) Hz/cm^2

on the detector close to (far from) the source; this exceeds by far the expected background level in ALICE (24 Hz/cm^2 at maximum).

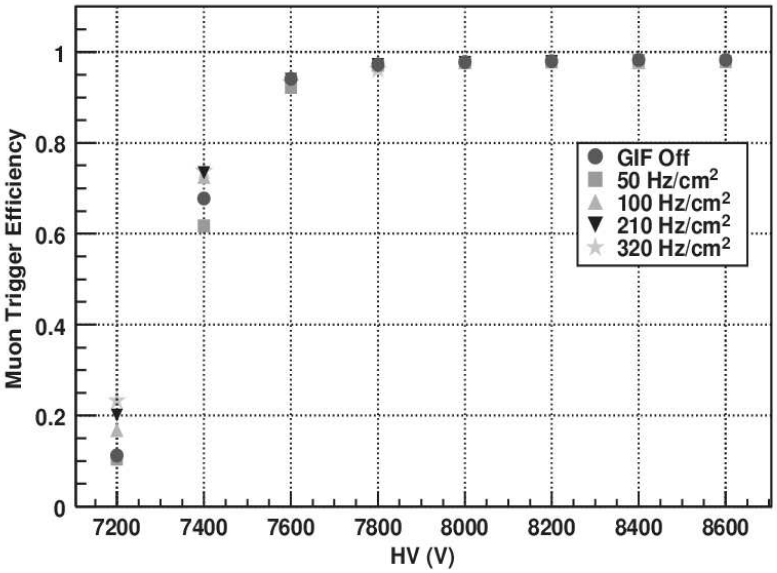

Fig. C.6: Muon trigger track–finding efficiency for different background rate.

The muon trigger track–finding efficiency has been investigated with and without the uncorrelated γ–background; the results are illustrated in Fig. C.6. The trigger efficiency (measured with the scintillator hodoscope as reference) reaches a 98% plateau, up to a background rate of 320 Hz/cm^2.

We also measured the fake trigger rate at various background levels, with beam off, in order to check the robustness of the system to uncorrelated background. The obtained values are shown in Table C.2: we had less than 3 fake trigger per minute at the maximum background level.

	background rate (Hz/cm^2)	fake trigger rate per minute
GIF source with attenuation	50	< 0.3
GIF source without attenuation	320	< 3

Tab. C.2: Fake trigger rate (upper limits) for two GIF attenuation settings, with beam off, obtained with a 3/4 coincidence level. The operating voltage was set at 8000 V and the indicated rates refer to the RPC close to the source.

References

[1] R. Arnaldi *et al.*, Performances of a prototype for the ALICE muon trigger at LHC, IEEE-TNS-00055-2003

[2] B. Forestier, Nucl. Instrum. Meth. A 533 (2004) 22-26

grazie, grazie, mille grazie!

Eccoci qui, la stesura è completata! In queste pagine c'è il lavoro di tre anni della mia vita durante i quali molte persone hanno *camminato* al mio fianco, mi hanno aiutata e sorretta.

Il primo ringraziamento è per Alfredo, per tutti i manuali che mi ha fatto leggere e per le cose che mi ha insegnato.

Grazie anche al mio 'referee esterno', il Prof. Salvatore Nuzzo, per i consigli che mi ha dato e per aver letto la mia tesi, che a 'a vista' è di proporzioni considerevoli.

Voglio poi ringraziare tutti gli inquilini che sono passati dall'ufficio in questi tre anni: Giovanna e Alberto (in ordine di cavalleria!!!), Martino e Diego. Ringrazio anche Fred, che da questo ufficio è stato scacciato! Grazie anche a Roberto, relegato da sempre nel Lingottino ...

Un ringraziamento speciale a tutto il gruppo Pinot, per l'accompagnamento scientifico e personale. Grazie al prof. Emilio Chiavassa, al prof. Mauro Gallio e al prof. Ermanno Vercellin. Grazie a Chiara, Roberta e Alessandro, grazie a Enrico, a Nora e a Pietro. Un grazie particolare ad Anna e al Prof. Beppe Dellacasa per avermi dato l'opportunità di continuare a divertirmi con le RPC del progetto ANNA. Grazie anche a Paolo Mereu, e insieme a lui un grazie di cuore a tutto il Laboratorio dei Sette Comuni e a Ruggiero Farano.

Grazie a tutta la mia famiglia, che da quando ho sposato Carletto si è allargata! Grazie in particolare a mamma, a papà e alla mia nonnina, grazie a Federica, la mia sorellina speciale, e a Giangi. Lancio poi la palla 'scrittura tesi' a Marilena, la mia cognata preferita.

Grazie a tutti gli amici che ho incontrato in questi anni, ai Tracollari, alle matrone e alle magnifiche cene.

Grazie a Mara per aver condiviso con me le gioie e i dolori della scrittura in questa Torino pre–Olimpica.

Grazie a Elena, per l'amicizia premurosa e allegra.

E *the last, but not the least*[1], grazie a Stefano, per il dottorato mi ha abbandonata ... ma è stato al mio fianco in modo speciale negli ultimi dieci anni della mia vita.

Grazie a Carletto, il mio sorriso e la mia forza.

[1] Questa volta non è banale!

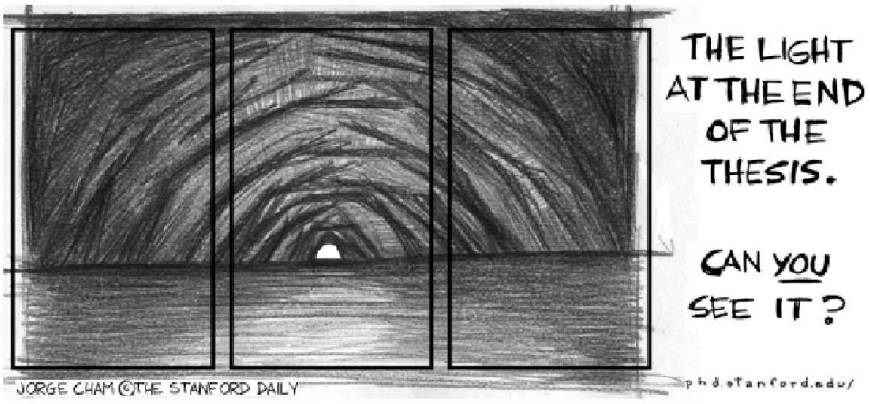
THE LIGHT AT THE END OF THE THESIS.
CAN YOU SEE IT?
JORGE CHAM ©THE STANFORD DAILY
phdcomics.stanford.edu/